



HAL
open science

Steerable antenna design based on liquid metal actuation

Denis Le Goff

► **To cite this version:**

Denis Le Goff. Steerable antenna design based on liquid metal actuation. Other. Université de Bretagne occidentale - Brest, 2017. English. NNT : 2017BRES0152 . tel-01809047

HAL Id: tel-01809047

<https://theses.hal.science/tel-01809047>

Submitted on 6 Jun 2018

HAL is a multi-disciplinary open access archive for the deposit and dissemination of scientific research documents, whether they are published or not. The documents may come from teaching and research institutions in France or abroad, or from public or private research centers.

L'archive ouverte pluridisciplinaire **HAL**, est destinée au dépôt et à la diffusion de documents scientifiques de niveau recherche, publiés ou non, émanant des établissements d'enseignement et de recherche français ou étrangers, des laboratoires publics ou privés.

UBO

université de bretagne
occidentale

UNIVERSITE
BRETAGNE
LOIRE

Lab-STICC

CiNTRA
UMI 3288
CNRS-NTU-THALES

THÈSE / UNIVERSITÉ DE BRETAGNE OCCIDENTALE

sous le sceau de l'Université Bretagne Loire

pour obtenir le titre de

DOCTEUR DE L'UNIVERSITÉ DE BRETAGNE OCCIDENTALE

*Mention : Sciences et Technologies de l'Information et de la
Communication*

Spécialité : Télécommunications

École Doctorale : Maths-STIC 601

présentée par

Denis Le Goff

Préparée au Lab-STICC, CNRS UMR 6285,
Laboratoire des Sciences et Techniques de
l'information, de la Communication et de la
connaissance & à CINTRA, CNRS UMI 3288, CNRS
International NTU Thales Research Alliance

Steerable antenna design based on liquid metal actuation

Thèse soutenue le 20 Décembre 2017

Devant le jury composé de :

Renaud LOISON

Professeur, IETR, INSA Rennes, Rennes / **Président**

Corinne DEJOURS

Professeur, IMS, Bordeaux INP / ENSEIRB-MATMECA, Talence / **Rapporteur**

Jean-Marc RIBERO

Professeur, LEAT, Université de Nice – Sophia Antipolis, Sophia Antipolis / **Rapporteur**

Eric RIUS

Professeur, Lab-STICC, Université de Bretagne Occidentale, Brest / **Directeur de thèse**

Philippe COQUET

Professeur, CINTRA, Université de Lille 1 - Nanyang Technological University, Singapore / **Directeur de thèse**

Yves QUERE

Maître de conférences, Lab-STICC, Université de Bretagne Occidentale, Brest / **Encadrant**

Azar MAALOUF

Ingénieur de recherche, Lab-STICC, Université de Bretagne Occidentale, Brest / **Encadrant**

Fabrice COMBLET

Maître de conférences, Lab-STICC, ENSTA Bretagne, Brest / **Invité**

Edwin TEO HANG TONG

Assistant professor, Nanyang Technological University, Singapore / **Invité, Encadrant**

Acknowledgments

This work was done in the Lab-STICC laboratory (UMR 6285) of the University of Bretagne Occidentale (UBO), in Brest France as well as in the CINTRA laboratory (UMI 3288) of the Nanyang Technological University, in Singapore. I thank their directors, Gilles COPPIN & Philippe COQUET for welcoming me in their respective laboratories.

I express my sincere thanks to Renaud LOISON professor at INSA Rennes who did me the honor of chairing my dissertation jury. I also express my gratitude to Corinne DEJOUS, professor at INP/ENSEIRB & Jean Marc RIBERO, professor at the University of Nice Sophia Antipolis, for the honor they have done me to accept to report on my PhD work as well as for their very constructive remarks. I would also like to thank Edwin TEO, assistant professor at the Nanyang Technological University & Fabrice COMBLET, lecturer at ENSTA Bretagne for their participation to my dissertation jury and for their questions.

I would like to express my deepest gratitude to my supervisors for these three years where their support was absolutely key to the success of this project. I have learned a lot thanks to them, both scientifically and humanly.

I thank Eric RIUS, professor at the UBO, for his continuous and precious support and his unfailing sense of humor. I thank Philippe COQUET, adjunct professor at the Nanyang Technological University (NTU), and Edwin TEO, assistant professor at NTU for their support and advice while I was in Singapore. I thank Yves QUERE, lecturer at the UBO, for his help, pertinent remarks and support throughout the whole project. I thank Azar MAALOUF, research engineer at the UBO, for his invaluable help, his technical expertise and his constant availability which have greatly contributed to the success of this project.

This work wouldn't have been possible without all the implicated people and companies, such as the Micro-Liquid, GTID and 3D Alchemy companies and of course people like Fabrice COMBLET of the ENSTA Bretagne, Alexandre MANCHEC of ELLIPTIKA to cite just a few.

I would also like to thank all the people of the UBO, NTU, Lab-STICC & CINTRA who helped me at one moment or another and for their warm welcome.

I would now like to thank all of my fellow Ph.D students and colleagues, both in the UBO & the Lab-STICC; by starting with Sarra, Younes, Mahdi, Mohammed, Luc, Adrien, Mira, Norbert, Mohammed, Allan, Vinod, Christophe, Nathan, Vassidiki, Ruben, Julie, Ishan, Petros, Anaïg, Rozenn, Tony, Jean-François, Vincent, Philippe, Michèle ... as well as in NTU & CINTRA; Etienne, Mathieu, Ange, Nicolas, Umar, Nicolas, Olivier, Matthieu, Marc, Aravind, Quyen, Hasman ...

Finally, Marie, I would like to thank you very much for supporting me in this project, especially during the last year which was quite challenging. I would like to thank my family for their constant support and their help during those years and to express my gratitude to all my friends for their support.

Table of content

Introduction.....	15
I. General context & objective.....	15
II. Structuring technological choices & key performances criteria.....	16
III. Research areas.....	18
IV. Organization of the manuscript.....	18
1) State of the art of liquid metal actuation for antenna applications.....	18
2) System's design.....	19
3) System's electromagnetic simulations.....	19
4) System's tests & measures.....	20
5) Conclusion & perspectives.....	20
Chapter 1 : State of the art of liquid metal actuation for antenna applications:.....	21
I. Problematic.....	21
II. Performances criteria & applications.....	23
III. Bibliographic study.....	25
IV. Key points & bottlenecks extracted from literature.....	44
V. Bibliography.....	47
Chapter 2 : System's design.....	51
I. Singled out technological solutions.....	51
II. Choice among the technological solutions.....	52
1) Horizontally polarized Yagi-Uda antenna.....	55
2) Vertically polarized antenna.....	61
III. Chosen characteristics of the system.....	69
IV. Bibliography.....	70
Chapter 3 : Electromagnetic simulations.....	73
I. Design approach and guidelines for the simulations.....	73

II. Progressive validation of the architecture.....	74
1) Simulation of the wire dipole based system.....	74
2) Simulation of the coaxial dipole and Alford-loop dipole based system.....	79
3) Simulation of the coaxial dipole based system embedded in a COP cylinder.....	84
4) Simulation of the coaxial dipole based system embedded in COP slides.....	88
5) Simulation of the coaxial dipole based system embedded in COP slides with electrolyte	92
6) Simulation of the coaxial dipole based system embedded in COP slides with electrolyte & tanks.....	97
7) Simulation results analysis.....	106
III. Bibliography.....	107
Chapter 4 : Fabrication, tests & measures.....	109
I. Central antenna fabrication architecture.....	109
II. Development of fluidic chip fabrication technologies.....	114
1) Introduction to fluidic chip fabrication.....	114
2) Fluidic channels fabrication on COP substrate.....	115
a) <i>Micro-machining</i>	116
b) <i>Laser engraving</i>	117
c) <i>Hot embossing</i>	117
3) Fluidic channels fabrication on PDMS substrate.....	118
4) Fluidic channels characterization.....	120
5) COP & PDMS fluidic chips bonding.....	122
COP bonding technologies.....	123
a) <i>Mechanical & toluene bonding</i>	123
b) <i>Thermal bonding</i>	124
PDMS bonding technologies.....	125
a) <i>Oxygen plasma bonding</i>	125
b) <i>Curing agent bonding</i>	125
6) Electrodes fabrication.....	127
a) <i>Gold evaporation with e-beam on top of photo-resist masked substrates</i>	129
b) <i>Gold electroplating on top of selective copper metallization obtained through an auto-catalytic process on top of tape-masked substrates</i>	130

c) Gold electroplating on top of selective Au-Pt metallization obtained through sputtering on top of tape-masked substrates.....131

III. Test of the prototype's fluidic system.....	131
1) First COP fluidic chip testing.....	132
2) Second COP fluidic chip testing.....	137
3) Third COP fluidic chip testing.....	142
IV. Test of the system's proofs of concept.....	148
1) Test of the non-fluidic proof of concept.....	148
2) Test of the fluidic proof of concept.....	158
V. Microfluidic actuation system applied to an autonomous system.....	168
VI. Bibliography.....	172
Conclusions & perspectives.....	174
I. Conclusion.....	174
II. Perspectives.....	175

Table of figures

Figure 1) : 20*20 patch elements antenna phased array capable of 120° beam steering with a top view of the system (left) and scanning patterns [1] (right) for +5°, +30° & +60° illustrating the limits of the beam steering angle.....	21
Figure 2) : Thales RDY-2 radar featuring mechanical beam steering.....	22
Figure 3) : Example of an of autonomous sensor network equipped with our reconfigurable antenna system used for dynamic situation and threats mapping for ground troops.....	24
Figure 4) : [21] Design of a microfluidic antenna based on a low profile Yagi-Uda antenna with liquid metal parasitic. The center antenna is called an Alford type loop antenna.....	27
Figure 5) : [24] Radiation pattern of the microfluidic reconfigurable antenna presented in figure 4) for three different angular positions: (A) 0°, (B) 22.5° and (C) 45°.....	28

Figure 6) : [20] 5 elements configuration of a 7 elements reconfigurable Yagi-Uda monopole array based on syringe actuated vertical columns filled with Galinstan, with the feed element being the L4 column.....	28
Figure 7) : [20] Filling mechanism (not to the scale) of one vertical Galinstan filled column. By applying pressure on the syringe, the Galinstan rises in the column.....	29
Figure 8) : [20] Radiation pattern for the 7 elements Yagi-Uda reconfigurable monopole array presented on figure 6), with a) $\varphi=+90^\circ$ and b) $\varphi=-90^\circ$ and for: red; 3 elements, blue; 4 elements & black; 5 elements.....	29
Figure 9) : [29] CAD depiction of a cooling system based on MHD micro-pump with Galinstan as cooling fluid).....	30
Figure 10) : [33] CAD depiction of a thermally driven variable capacitor.....	31
Figure 11) : [35] Illustration of the working principle of the EW actuation; with in (a) the initial situation, where the charge distribution is even on the surface of the droplet which is therefore in position of energetic equilibrium. Then in (b), after applying a voltage, the charge distribution changes, driving the droplet towards the negative electrode.....	33
Figure 12) : [36] Series of picture showing the motion of a Galinstan slug in a channel filled with NaOH based electrolyte when is applied a 7V DC command. The result is a slug displacement through CEW actuation. Voltage is applied in (a) until (d).....	35
Figure 13) : [35] Illustration of the concept of a liquid-metal based micro-motor.....	36
Figure 14) : [35] Illustration of the working principle of the electrical command of the CEW actuation with the channel on top and the evolution of the command signal on each electrode bellow.....	37
Figure 15) : [35] Picture of the micro-motor view from the top (right), with a detailed view of the Mercury filter (left), which prevent the mercury slug to get to the electrode.....	37
Figure 16) : [36] Series of picture comparing the motion of a Galinstan slug in a channel filled with NaOH based electrolyte when is applied: (a) 8V DC signal, (b) 8 VPP AC 30 Hz square signal, with a +3V DC bias.....	38
Figure 17) : [36] Top view illustration of the interlocked chambers. Each chamber has the same radius R and constant spacing S from the other chambers. The metal slug length is expressed in terms of number of chambers occupied, N, with here N=3.....	39

Figure 18) : [36] A $N=2$ metal slug is moving (in five steps) one chamber further to the right under the action of the square signal. Picture of each step with the corresponding MATLAB simulation in a) to e).....	39
Figure 19) : [37] Schematic of the slot antenna tuning device based on Galinstan's DEW along an horizontal channel with top view (left), a side view (bottom) & a detailed view of the overlapping channel on top of the antenna's slot aperture (right).....	40
Figure 20) : [37] Return losses (S_{11}) evolution for different liquid metal coverage length of the slot antenna's aperture (left), Radiation pattern for a) : no coverage (2.52 GHz) & b) full coverage (2.88 GHz) of the antenna's aperture (right).....	40
Figure 21) : [18] Illustration of the electro-capillary actuation (top) and electrochemical actuation (bottom) with in each case the different phases of the phenomenon.....	41
Figure 22) : [19] Illustration of the vertical Galinstan made frequency tunable monopole antenna controlled via electrochemical actuation. By applying a voltage, authors are able to raise or lower the Galinstan inside the channel, which is a glass capillary, hence tuning the length of the resonating elements, and therefore tuning the antenna's frequency.....	43
Figure 23) : Schematic example of a 3+1 dipole Yagi-Uda antenna (left) and an example of its typical radiation pattern (right).....	53
Figure 24) : Horizontally polarized planar Yagi-Uda antenna.....	55
Figure 25) : [11] 2+1 Yagi-Uda based antenna made of an Alford-loop inspired low profile dipole antenna surrounded by copper parasitic elements.....	56
Figure 26) : [11] Yagi-Uda based antenna made of an Alford-loop inspired low profile dipole antenna surrounded by mercury parasitic elements inside a water filled plastic tube actuated by a mechanical micro-pump.....	57
Figure 27) : [20] Picture of the micro-motor view from the top (right), with a detailed view of the Mercury filter (left).....	58
Figure 28) : Schematic views (from left to right: top, side and bottom view) of a horizontally polarized Yagi-Uda based fluidic antenna system.....	59
Figure 29) : [23] Illustration of an example of a drop manipulation device based on EWOD displacement method.....	60
Figure 30) : Concept of a vertical fluidic Yagi-Uda based antenna system with its two working phases, the "OFF" phase (left) the "ON" phase (right).....	61

Figure 31) : Diagram depicting the architecture capable of a 360° beam steering based on the columns architecture as well as it's working principle.....	62
Figure 32) : Schematic sectional side view of a vertical Yagi-Uda based fluidic antenna system capable of a 360° beam steering with a coaxial dipole feed antenna.....	63
Figure 33) : Plain (left) and sectional (right) view of a folded half wave dipole antenna.....	64
Figure 34) : Plain (left) and sectional (right) view of a sleeve dipole antenna.....	64
Figure 35) : Sectional side view of a sleeve dipole antenna with a sleeve support ring made of dielectric material.....	65
Figure 36) : 3D CAD view of a vertically polarized Yagi-Uda based fluidic antenna system.....	66
Figure 37) : Illustration of the system's dimensions guidelines.....	75
Figure 38) : Wire dipole Yagi-Uda antenna system in a unidirectional "narrow beam" configuration in vacuum (red rectangle figuring the propagation plan).....	76
Figure 39) : Evolution of S11 of the wire dipole Yagi-Uda antenna system in unidirectional configuration.....	77
Figure 40) : Evolution of impedance of the wire dipole Yagi-Uda antenna system in unidirectional configuration.....	77
Figure 41) : 2D radiation diagram of the wire dipole Yagi-Uda antenna system in unidirectional configuration.....	78
Figure 42) : 3D radiation diagram of the wire dipole Yagi-Uda antenna system in unidirectional configuration.....	78
Figure 43) : Dimensions of the central antenna of the coaxial dipole system (left) & the Alford-loop based system (right).....	79
Figure 44) : Coaxial dipole Yagi-Uda antenna system (left) and Alford-loop based dipole Yagi-Uda antenna system, both in unidirectional "narrow beam" configurations.....	80
Figure 45) : Evolution of S11 of the wire (red) / coaxial (blue) / Alford-loop based (green) dipole Yagi-Uda antenna system in unidirectional configuration.....	81
Figure 46) : Evolution of impedance of the wire (red) / coaxial (blue) / Alford-loop based (green) dipole Yagi-Uda antenna system in unidirectional configuration.....	82
Figure 47) : 2D radiation pattern of the wire (red) / coaxial (blue) / Alford-loop based (green) dipole Yagi-Uda antenna system in unidirectional configuration.....	82

Figure 48) : 3D radiation pattern of the coaxial dipole antenna system (left) & the Alford-loop based dipole antenna system (right) dipole both in unidirectional configuration.....	83
Figure 49) : Coaxial dipole Yagi-Uda antenna system in a unidirectional “narrow beam” configuration embedded in COP cylinder in vacuum.....	85
Figure 50) : Evolution of the S11 of the coaxial dipole antenna system in COP (red) & in vacuum (blue) both in unidirectional configuration.....	86
Figure 51) : Evolution of the impedance of the coaxial dipole antenna system in COP (red) & in vacuum (blue) both in unidirectional configuration.....	86
Figure 52) : 2D radiation pattern of the coaxial dipole antenna system in COP (red) & in vacuum (blue) both in unidirectional configuration.....	87
Figure 53) : 3D radiation pattern of the coaxial dipole antenna system in COP (right) & in vacuum (left) both in unidirectional configuration.....	87
Figure 54) : Coaxial dipole Yagi-Uda antenna system in a unidirectional “narrow beam” configuration embedded in COP slides in vacuum.....	89
Figure 55) : Evolution of the S11 of the coaxial dipole antenna system with COP slides (red), with COP cylinder (blue) & in vacuum (green) all in unidirectional configuration.....	90
Figure 56) : Evolution of the impedance of the coaxial dipole antenna system with COP slides (red), with COP cylinder (blue) & in vacuum (green) all in unidirectional configuration.....	90
Figure 57) : 2D radiation pattern of the coaxial dipole antenna system with COP slides (red), with COP cylinder (blue) & in vacuum (green) all in unidirectional configuration.....	91
Figure 58) : 3D radiation pattern of the coaxial dipole antenna system with COP slides (left) & with COP cylinder (right) both in unidirectional configuration.....	91
Figure 59) : Coaxial dipole Yagi-Uda antenna system in a unidirectional “narrow beam” configuration embedded in COP slides containing electrolyte in vacuum.....	93
Figure 60) : Evolution of the S11 of the coaxial dipole antenna system with COP slides containing electrolyte (red), without electrolyte (blue) both in unidirectional configuration.....	94
Figure 61) : Evolution of the impedance of the coaxial dipole antenna system with COP slides containing electrolyte (red), without electrolyte (blue) both in unidirectional configuration.....	94
Figure 62) : 2D radiation pattern of the coaxial dipole antenna system with COP slides containing electrolyte (red), without electrolyte (blue) both in unidirectional configuration.....	95

Figure 63) : Top view of the coaxial dipole antenna system with COP slides containing electrolyte	96
Figure 64) : 3D radiation pattern of the coaxial dipole antenna system with COP slides containing electrolyte (right) & without electrolyte (left) both in unidirectional configuration.....	96
Figure 65) : Illustration of the working principle of the fluidic system.....	97
Figure 66) : Illustration of the overlapping tanks in the two “activated” configurations used in the simulation with the two directors ON (left) and the reflector ON (right).....	98
Figure 67) : Coaxial dipole Yagi-Uda antenna system in a unidirectional “narrow beam” configuration embedded in COP slides containing electrolyte and Galinstan tanks in vacuum.....	100
Figure 68) : Evolution of the S11 of the coaxial dipole antenna system with COP slides containing electrolyte and tanks (red), with electrolyte & no tanks (blue) both in unidirectional configuration	101
Figure 69) : Evolution of the impedance of the coaxial dipole antenna system with COP slides containing electrolyte and tanks (red), with electrolyte & no tanks (blue) both in unidirectional configuration.....	101
Figure 70) : 2D radiation pattern of the coaxial dipole antenna system with COP slides containing electrolyte and tanks (red), with electrolyte & no tanks (blue) both in unidirectional configuration	102
Figure 71) : 3D radiation pattern of the coaxial dipole antenna system with COP slides containing electrolyte & tanks (right) & with electrolyte and no tanks (left) both in unidirectional configuration	102
Figure 72) : Radiation pattern for four system’s configurations, omnidirectional 1), unidirectional narrow beam 2), unidirectional large beam 3) & four-way multi-directional 4).....	103
Figure 73) : 360° beam steering capable coaxial dipole Yagi-Uda antenna system actuated by microfluidic technology.....	109
Figure 74) : Evolution of the dimension of the system’s antenna before (left) and after (right) recalculation for 3D printing.....	111
Figure 75) : 3D CAD plans for the “external coating” (left) and “central coating” (right).....	111
Figure 76) : 2D & 3D CAD plans for the SMA connector of the antenna (from RADIALL) (left) and its 3D printed fitting base (right).....	112

Figure 77) : Sectional schematic view of the assembled 3D printed and metallized antenna.....	113
Figure 78) : From left to right, the 3D printed antenna non metallized and disassembled, non metallized and assembled, metallized and assembled.....	113
Figure 79) : Basic COP fluidic channel design.....	114
Figure 80) : COP injection press (left) and COP granules (right).....	115
Figure 81) : LPKF S103 CNC (left) and micro-machined COP fluidic channel (right).....	116
Figure 82) : EPILOG fusion CO2 cutting laser (left) and laser engraved COP fluidic channel (right)	117
Figure 83) : From left to right, aluminum milled hot embossing imprint, hot embossing process before start & a hot embossed COP fluidic channel.....	118
Figure 84) : Aluminum PDMS with the plastic bridge (left) and a molded PDMS fluidic channel	119
Figure 85) : Redesigned 3D printed PDMS molding bridge with additional purple plastic slide (left) & resulting PDMS chip (right).....	119
Figure 86) : From left to right, micro-machined COP, hot-embossed COP, molded PDMS & COP laser engraved fluidic chip.....	120
Figure 87) : Profilometer profile of the chips presented on figure 86).....	120
Figure 88) : 3D CAD view of an assembled mechanically bonded COP fluidic chip (left) and two of these same chip after fabrication & assembling (right).....	123
Figure 89) : COP thermal bonding support holding a COP chip before bonding (left) and a bonded chip (right).....	124
Figure 90) : RIE system used for the oxygen plasma bonding in Singapore (left) and PDMS/glass bonded fluidic chip (right).....	125
Figure 91) : Illustration of the curing agent bonding process used by us.....	126
Figure 92) : Spin-coater used to deposit the curing agent on top of glass and COP slides (left) and two PDMS chip bonded on top of glass (right-front) and COP slides(right-back).....	127
Figure 93) : Illustration of the problem posed by the use of metallic wire as electrodes.....	128
Figure 94) : Results of the gold deposition on top of COP and glass slides (left), with a COP slide (right-top) and glass slide (right-bottom).....	129

Figure 95) : Results of the lift-off and scalpel grinding operations on COP slides (left) and glass slides (right).....	130
Figure 96) : COP slides after metallization with copper.....	131
Figure 97) : COP slides with copper electrodes after the gold electroplating.....	131
Figure 98) : Summary of the fluidic chips working principle.....	132
Figure 99) : 3D (left) & 2D (right) CAD views of the first fluidic system test chip.....	133
Figure 100) : Detailed view of the experimental set-up of the first chip.....	134
Figure 101) : From left to right, sequential rise of the Galinstan inside the first test chip.....	135
Figure 102) : Schematic top view of the chip design sent to MicroLIQUID for realization.....	137
Figure 103) : MicroLIQUID PDMS/glass fluidic chip (left) and inside its holder (right).....	138
Figure 104) : From left to right, sequential rise of the Galinstan inside the second test chip.....	139
Figure 105) : Detailed view of the rise of the Galinstan inside the second test chip.....	139
Figure 106) : Example of an incomplete filling scenario of the chip.....	141
Figure 107) : COP fluidic channel after injection and electrodes access holes drilled through it....	142
Figure 108) : COP fluidic chip with gold plated copper electrodes after thermal bonding.....	142
Figure 109) : Kapton (polyimide) film coated COP chip.....	143
Figure 110) : Kapton filmed COP chip with wires soldered (left) without & with the filling tubing sections (right).....	144
Figure 111) : Kapton filmed COP chips with wires soldered & filling tubing sections after being sealed up by glue.....	144
Figure 112) : Test bench of the fluidic chips.....	145
Figure 113) : Rise sequence of the Galinstan inside the chip 3.....	146
Figure 114) : Detailed view of the initial setup of the chip 3.....	146
Figure 115) : Evolution of the current in the chip as a function of the voltage applied.....	147
Figure 116) : Schematic view of the non-fluidic proof of concept (left) and picture of the real device (right).....	149
Figure 117) : Pictures of the non-fluidic system Rohacell support without (left) & with (right) the system installed.....	150

Figure 118) : Simulated non-fluidic proof of concept in unidirectional configuration.....	150
Figure 119) : Illustration of the main simulation/measure modelling difference.....	151
Figure 120) : S11 comparative evolution of the non-fluidic system for simulation & measure.....	153
Figure 121) : S11 comparison for the various feeding system models.....	154
Figure 122) : Impedance evolution of the simulated non-fluidic system.....	154
Figure 123) : Picture of the measured non-fluidic system inside the anechoic chamber.....	155
Figure 124) : Illustration of the calibration horn antenna & its properties.....	156
Figure 125) : Polar radiation pattern of the simulated non-fluidic system at 4.86 GHz for a system tilted of 0° (red) & +10° (blue).....	156
Figure 126) : Rectangular radiation pattern of the simulated non-fluidic system at 4.86 GHz for a system tilted of 0° (red) & +10° (blue).....	157
Figure 127) : Comparison of the rectangular radiation patterns of the non-fluidic system at 4.86 GHz for measure & simulation.....	157
Figure 128) : Illustration of the general architecture of the fluidic proof of concept.....	158
Figure 129) : Simulated fluidic proof of concept in unidirectional configuration.....	160
Figure 130) : CAD views of the COP slides assembled (left) & disassembled (right).....	160
Figure 131) : Pictures of the fabricated, injected & sealed slides with two Galinstan directors (left) & one Galinstan reflector (right).....	161
Figure 132) : CAD view of the fluidic system Rohacell support (left) & picture of the same system post-fabrication (right).....	161
Figure 133) : S11 comparative evolution of the fluidic system for simulation & measure.....	162
Figure 134) : Impedance evolution of the simulated fluidic system.....	163
Figure 135) : S11 comparative evolution of the fluidic & non-fluidic system for simulation & measure.....	163
Figure 136) : Picture of the measured non-fluidic system assembled (left) & inside the anechoic chamber (right).....	164
Figure 137) : Polar radiation pattern of the simulated fluidic system at 4.48 GHz (red) and for the non-fluidic system at 4.86 GHz (green).....	165

Figure 138) : Rectangular radiation pattern of the simulated fluidic system at 4.48 GHz (red) and for the non-fluidic system at 4.86 GHz (green).....	165
Figure 139) : Comparison of the rectangular radiation patterns of the fluidic system at 4.48 GHz for measure & simulation.....	166
Figure 140) : Comparison of the measured rectangular radiation patterns of the fluidic system not tilted at 4.48 GHz & of the non-fluidic system tilted +10° at 4.86 GHz.....	167
Figure 141) : Simplified embeddable antenna system.....	169
Figure 142) : Simplified system with on top the solar cell array and at the bottom the battery pack needed for a continuous 24/7 actuation of the fluidic system.....	171

Table of tables

Table 1:[7] Comparison between the properties of the Galinstan & of the Mercury.....	25
Table 2: Performances comparison of the liquid metal displacement technologies studied.....	44
Table 3 : Electromagnetic performances of the 4 configuration at 5 GHz (realized gain looked at the main lobe).....	105
Table 4 : Classification of the impact on the gain of the system's design modifications.....	106
Table 5: Fluidic chips profilometer measures sum-up.....	121
Table 6: Sum up of the performances achieved during the chips testing.....	148
Table 7: Fluidic system's performances emulator.....	170

Introduction

I. General context & objective

The work presented in this manuscript was supported by a PhD scholarship from the Minister de l'Éducation nationale, de l'Enseignement supérieur et de la Recherche. The goal of that PhD was to realize a prospective work on the use of microfluidic technologies, applied to the problematic of the development of beam steering capable microwave antenna system. We aimed at providing an innovative & original alternative to mechanic & electronic beam steering technology. It was established from the beginning of this work that we would developed a microfluidic technology focused on the microfluidic actuation of liquid metal, Galinstan more precisely.

This subject is a follow-up of the previous COCORICO (Cyclo Olefin Polymer (Co)-polymer for the design of millimeter wave wireless components and associated autonomous sensors) ANR ASTRID 2012 project funded by the DGA, which aimed at the realization of a communicating object including a fixed self directing antenna working on the principle of the compass.

This work aim at replacing this fixed antenna by one able to rotate on 360° . This is a technological work requiring specific means (but not necessarily heavy equipment) and various skills. Given the already established relations between the Lab-STICC & the UMI 3288 CINTRA, located inside the Nanyang Technological University (NTU), in Singapore, it has been decided to split the 36 months of the project in three successive stays in Brest, Singapore, and Brest again. Those stay were respectively of 8 months, 18 months & 10 months, meaning that I have spend a total of 18 month in each countries.

In the long term, this skill sharing should allow researchers off these two laboratories to developed new subjects and allow the doctorate student to be immersed in different cultures & practices.

Moreover, that microfluidic technology was to be developed based on the use of Cyclo-Olefin Polymer (COP). This material is already used by the technological center SIMtech (from A*STAR, in Singapore) to realize microfluidic chips. It very quickly become a subject of interest for the Lab-STICC due its RF properties, especially in terms of dielectric constant and loss tangent. In addition, COP presents also very good electrical characteristics, while being a rigid (in opposition of the Polydimethylsiloxane or PDMS for example) & a relatively easy to be shaped material. This set of characteristics make for an interesting material for such a hybrid microwave & microfluidic system as the one we want to develop.

The tangible objective was to demonstrate the concept and the feasibility of a microwave antenna system able to perform a COP based 360° horizontal beam steering through microfluidic actuation and to realize proofs of concept of it. This will encompass the development of a microwave antenna device & its microfluidic actuation mechanism, of the relevant fabrication processes of that antenna & of the COP microfluidic chips constitutive of the actuation system. These processes comprise the

3D printing & metallization of part of the antenna, the patterning of the microfluidic channel as well as the deposition of electrodes on the surface of the chip or their hermetic bonding, a crucial step in order to seal the chips.

We insist on the fact that this study is very upstream or even exploratory. That is why, in order to fulfill that objective, we will need to realize proofs of concepts of the different subsystems & to provide data on the performances of the systems, both as an RF systems & as a microfluidic system. These data will help us to determine the field of possible applications for this kind of system.

The application which is our main target is autonomous surveillance or detection system. This require to have a device which is going to be low-cost and with a power consumption low enough to allow its deployment in an isolated place, where the only energy available is the one it is able to harvest in its environment. These two aspects, the energy sobriety & the low cost of the system, are the core of our approach. The integration of our sub-system inside a larger autonomous surveillance device for example, pleads also for a compact design, which takes the best advantage possible of the volume. We need to take into consideration the fact that in such device, space is a limited resource that we need to use wisely. This choice of application combined with what our will to work with microfluidics led us to define an operating frequency of 5 GHz, which we considered a good trade-off between the size of the microfluidic system and the antenna's dimensions.

Regarding our positioning towards other types of systems, we can already say that given the structuring technological choices made, especially working with microfluidic, we cannot expect to be a competitor in terms of speed of actuation to the electronic beam steering systems. Indeed, this is their main advantage, for which they has been optimized. On the other hand in terms of cost & design simplicity, we can definitely hope to be a serious challenger, given that these systems relies on expensive & extremely sophisticated electronics. Regarding our positioning towards the other family of beam steering capable systems, the mechanical beam steering ones, we are going to be in the same range in terms of actuation speed. Here also we can hope to challenge them in the field of cost of the device, design simplicity & of the power consumption.

II. Structuring technological choices & key performances criteria

As it was said in the previous part, at the very beginning of the PhD, a certain number of structuring decisions were made in terms of system architecture and technological choices. These decisions have guided our conception approach. In addition, the electromagnetic and fluidic aspect of the system being intermingled, choices in one domain, affects the other, which generate more complexity for the conception of the system.

The first structuring decision we have made was to work with COP fluidic chips encapsulating Galinstan, which is considered currently a non-toxic liquid metal. The goal was to have a strong

interaction between the RF emitting part of the system and its fluidic part thanks to the Galinstan but also to minimize the losses due to the fluidic system itself thanks to the use of COP.

The second structuring decision was to select an electrical only actuation for the fluidic system in order to have the simpler the command system possible and ease its interfacing with an electronic system. That actuation system is necessary in order to control the Galinstan position inside the system and therefore enable its capability to produce a 360° beam steering. This choice imposes us the filling of the chips with Galinstan but also a basic electrolyte (needed to prevent Galinstan oxidation & convey the electrical charges), which is going to be aqueous, as well as the addition of electrodes to our fluidic chips.

Finally, the third structuring decision was to chose a general system architecture of a Yagi-Uda antenna. This choice was later on precised by the selection of a vertically polarized Yagi-Uda antenna architecture centered around the use of a 3D printed vertical coaxial dipole antenna, whose specifications will be further detailed later. The interest of this choice is to have a more agile system as well as exploiting the occupied space more efficiently, not only in the plan but in 3D.

These decisions had for consequences to imposes on us the mastering of key technological steps in order to realize our system. These key steps are the following:

- Patterning of COP microfluidic channels
- Bonding & sealing of COP microfluidic chip
- Injecting Galinstan and basic conductive electrolyte inside fluid chips
- Understanding and mastering of Galinstan electrofluidics vertical actuation
- Depositing metal electrodes on COP
- Precise 3D printing of an antenna's dielectric
- Metallization of a 3D printed antenna

The work presented in this manuscript will demonstrate how these steps have been implemented. It will also look into the performances of the system which came out of this conception approach, based on four criteria of evaluation. These criteria are the following:

- 1) Response time of the system
- 2) Power consumption of the system
- 3) Electromagnetic performances of the system
- 4) Cost of the system

The answer of the system to each of these criteria will be determining in terms of potential applications. Indeed, for example a fluidic system's response time of the order of the second would disqualify for electronic warfare. On the other hand, such system would be much adapted for area surveillance for example.

III. Research areas

Given the width of the scope of the problematic and the structuring technological choices made early in the PhD, the range of research fields investigated was narrow down to two main domains. These are the microfluidic & the millimeter frequency antenna system.

The work done in the microfluidic domain was mainly focus on conception and development of polymer based fluidic chips, essentially chips made of COP and PDMS. This development comprise the various design of chips (electromagnetic, fluidic), the development and the implementation of their fabrication process (patterning, bonding, electrode deposition) and finally the set up of testing methods in order to evaluate their performances. The work on these chips was focused on providing technological solution to the general antenna system and qualifying their behavior in the same optic.

The work done in the domain of the centimeter wave frequency antenna was mainly focused on the conception design simulation, fabrication and testing of a microwave antenna actuated via microfluidic technology. This include the choice of the system architecture, the design of the central antenna of the Yagi-Uda architecture, the selection of the fabrication process and subsequent realization of this central antenna, the validation of the architecture through measurements & the investigation of the impact of the fluidic actuation mechanism elements on the whole system's electromagnetic performances.

IV. Organization of the manuscript

The manuscript is divided on four chapters, entitled:

- 1) State of the art of liquid metal actuation for antenna applications
- 2) System's design
- 3) System's electromagnetic simulations
- 4) System's tests & measures

We will now detail the content of each of these chapters:

1) State of the art of liquid metal actuation for antenna applications

A general overview on the various actuation methods of liquid metal presented in the literature. The choice was made to focus mainly on the fluidic aspect on chapter one given the

specificity of the antenna actuation method chosen by us and presented in the first part of the introduction. Indeed, that specificity is going to impact heavily our system's design as well as its performances, especially in terms of response time and power consumption. Therefore it is extremely important for us to single out from the literature the best suited actuation method for our system based on its performances but also the constraints it will impose further on our conception of the system. The selection criteria of the method is of course largely influenced by projected application which is an autonomous surveillance system. The chapter concludes by a general recommendation in favor of an all electrical actuation method, and more specifically the electrofluidics actuation method.

2) System's design

That chapter focus on the final system's design and architecture retained for our application. While the fluidic system's technologies has been selected at the end of chapter one, we still have to choose between two competing system's architectures inspired from the literature, both based on that same fluidic technology. This chapter outline the pros and cons of each based on elements from the literature. It concludes this investigation by stating the superiority for our application of the second architecture investigated, the vertically polarized Yagi-Uda antenna, especially in terms of system's agility. Finally is presented a general preliminary delimitation, based on the fluidic actuation method and system's architecture retained, of the potential application domains of our system.

3) System's electromagnetic simulations

Electromagnetic performances of the system is of paramount importance in this work. It is especially true for the ability of the system to focus the beam of the central antenna in a specific direction and from there to rotate that beam inside the horizontal plan, all that while retaining that important directivity and maintaining a high gain for the main lobe. This chapter outline the system's conception approach of the antenna and the fluidic part from an electromagnetic point of view. This approach heavily relies on finite elements electromagnetic simulations done with ANSYS HFSS. While it brings additional elements justifying our conception choice of architecture presented on chapter two (arbitration between vertical and horizontal polarization), it also provide us with a good estimation of the RF performances of the system. In particular, it is investigated through simulations the impact of the Galinstan vertical columns on the antenna, as well as of the COP fluidic system presence & geometry. The specific impact of the electrolyte's presence on the RF performances of the system, especially gain, is also investigated.

4) System's tests & measures

This chapter presents the work done in terms of fabrication & measurements. The fabrication work includes of course the realization of the fluidic system and the antenna. It also includes all the developmental work done in order to design and validate the fabrication processes for the COP and PDMS chip manufacturing and bonding. This work is very important because it has for result to provide the laboratory with reliable and validated fabrication process for future works in the same domain. This chapter includes the qualification tests of the fluidic system based on the vertical actuation of liquid metal, important because they give us two of the validation criteria, the response time and power consumption of the system. These tests were run on several prototypes, with their results compared. Also presented are the RF measurements of two antenna system's proofs of concept, one validating the general system architecture from the perspective of the antenna, the other the combination of the fluidic system and the central antenna. This chapter also features a comparison of the performances demonstrated by the RF proofs of concepts & the corresponding simulations.

5) Conclusion & perspectives

We will conclude our this thesis by summing up the work done during this PhD on this system. The adequacy between our findings and the application targeted at the very beginning of our work will be examined. Finally, we will also be giving out potential leads to enhance the performances of our system.

Chapter 1 : State of the art of liquid metal actuation for antenna applications:

I. Problematic

The original idea behind this work was to conceive and design a system able to achieve a 360 degrees electromagnetic (EM) beam steering using microfluidic technologies.

With the advent of autonomous connected objects, especially sensors networks, the need for on the fly reconfigurable antenna, energetically sober, low cost is more and more important. The interest of beam forming is justified by the optimization of the link budget and the directional selectivity it gives to the antenna. Dynamic beam reconfiguration, especially the possibility to realize a 360 degree azimuthal sweep in order to give the system the capability to detect static/mobile objects visible in its accessible frequency band is another wanted characteristic.

Systems able to perform such function are already existing, with two main technologies, electronic beam steering and mechanical beam steering, both with their advantages and disadvantages.

Indeed, the electronic beam steering systems have very low response time, are easy to integrate inside devices, but they are inherently limited, in their planar configuration, in terms of their steering angle (± 60 degrees usually), as we can see on the figure 1) below:

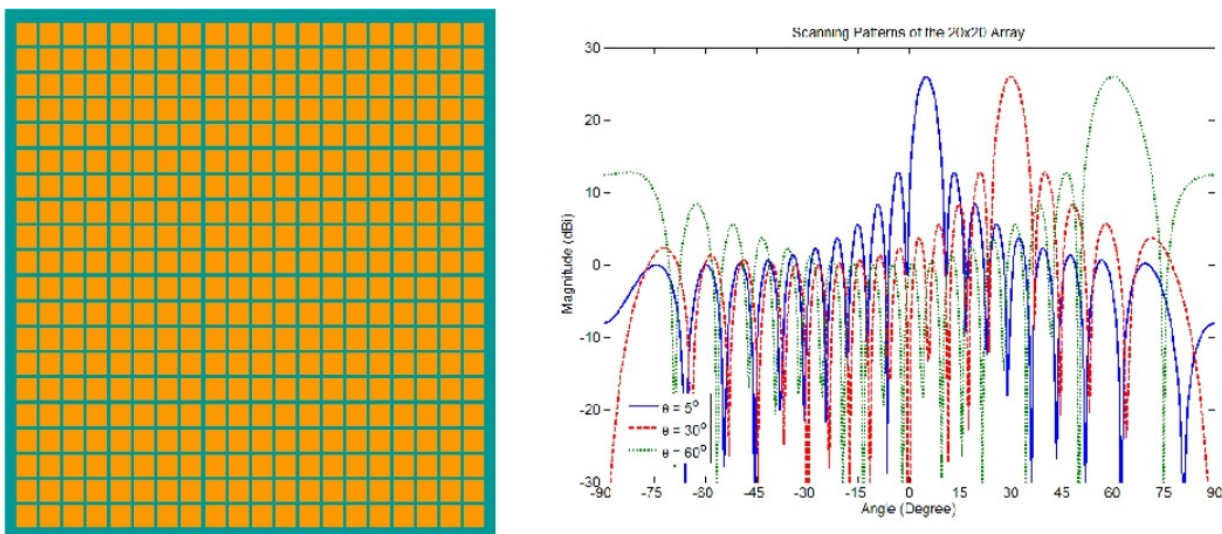


Figure 1 : 20*20 patch elements antenna phased array capable of 120° beam steering with a top view of the system (left) and scanning patterns [1] (right) for +5°, +30° & +60° illustrating the limits of the beam steering angle

As we can see on this figure, the beam cannot go farther than 50° , at the risk of severely deteriorate itself as it closes on the edge of the array. This derives from the fact that the effective surface of the antenna tends towards zero as we get closer to a 90° angle. This also means that the beam obtain is not isotropic along the emission plan, but is varying as a function of the beam steering angle, the “zero” being the plane perpendicular to the antennas’ array. The system’s radiation maximal efficiency is reached at that “zero plan”, and deteriorate as long as we increase the angle and move further away from that plan. At best we could materially hope to cover 180 degrees (by reaching 90 degree on each side, with a beam parallel to the planar array), but these values are theoretical and currently impossible to achieve.

Of course, we still have the possibility to take that planar array and to conform it to a substrate of cylindrical, spherical or conic form in order to overcome this limitation. The inconveniences of such system is nonetheless that it remains a complex system, with an important size relatively to the frequency and a high cost due to that complexity.

It also must be precised that the electronic command and control elements, like diodes or MEMS actuators are limiting the electrical performances of the RF systems in general, be it antennas, filters, phase sifters etc... Theses elements generally possess mediocre quality factors, which has the effect of lowering the quality factor of the whole system. They tend to degrade the noise factor and to generate inter-modulation, and are a limiting factor in term of power in emission. It must also be noted that they play a key role in increasing the power consumption of the system due to their poor energy efficiency.

On the other hand, the mechanical systems do not have any limit of steering angle, they usually have an isotropic beam and do not have the electrical limitations inherent to the electronic elements mentioned earlier. That came from the fact that the antenna used is usually a directive one which the mechanical system makes pivot around an axis without any alteration of the beam. That is another advantage of that design, its simplicity. On the other hand, because of that reason, they rely heavily on a mechanical system to operate their sweeping, which makes them more subject to wear (because of moving parts), as we can see on the figure 2).

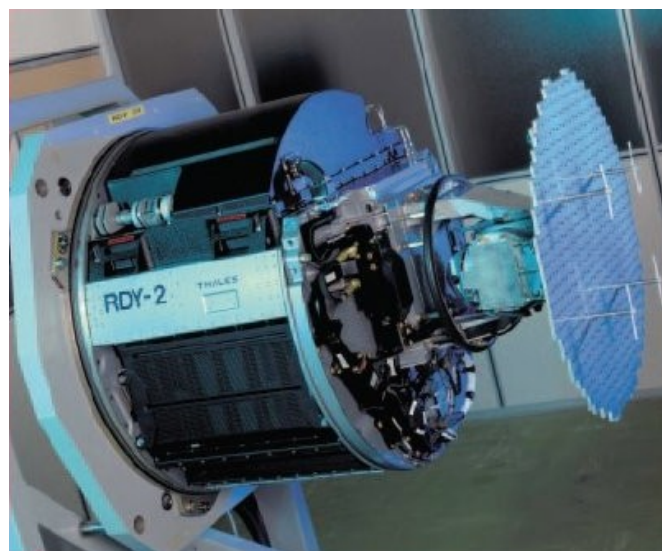


Figure 2 : Thales RDY-2 radar featuring mechanical beam steering

Indeed, we see on this figure that the whole antenna is fitted on servomechanisms which are necessary to make it move inside the various rotation planes for which the system is programmed for. These servomechanisms, aside from being relatively complex and costly systems, could also be quite volume consuming. Miniaturizing them can also be a rather complicated task, especially because below a certain scale, their fragility have a tendency to increase inversely to their miniaturization, making them more expensive to produce and most importantly potentially less reliable. The response time of such system is going to be it's weak point in comparison to the electronic beam scanning, because a mechanical system cannot compete in term of speed of a mechanic displacement against the commutation time of a diode for example. The order of magnitude for the response time is going to be from hundreds of milliseconds to seconds for such mechanical system, when it is in the order of ten nanoseconds for a diode.

The innovation of our system lies in our proposition of an intermediate way, which is a compromise in favor a greater beam steering domain at the expense of the speed of the steering process itself. To obtain that greater beam steering domain, we resort to a technology with no moving mechanical parts but liquid metal. Its working principle is based on fluidic actuation, and it is controlled through a very simple electrical command. With this configuration we manage to integrate some of the respective advantages of the two previous systems: we have an isotropic beam on the 360 degrees of the steering, we have a simple electronics command but we potentially do not have mechanical wear and our system is rather easy to miniaturize.

For our system to be attractive despite its medium to low performances in terms of commutation speed, we looked for ways to make the system as cheap to produce as possible. Hence, we have chosen to realize it in Cyclo-Olefin-Polymer (COP) from Zeonex, a relatively cheap thermoplastic showing good electric performances ($\epsilon_r = 2,3$, $\tan \delta = 3.10^{-4}$ at 1 GHz from the manufacturer [2], and confirmed by measurement in [3]), already in use at our laboratory for RF applications and on which we already have an experience in terms of molding and processing. Its glass transition temperature is about 130°C. For higher temperature (150°C) of work, we could also use special Cyclo-Olefin-Polymer (COP) from Topas. The COP's electric performances are comparable to those of Polydimethylsiloxane (PDMS) ($\epsilon_r = 2.68$, $\tan \delta = 1.33 \cdot 10^{-3}$ at 100 kHz from the manufacturer [4], and measured at $\epsilon_r = 2.77$, $\tan \delta = 5.4 \cdot 10^{-2}$ at 5 GHz in [5]). The two materials present comparable dielectric constant, but while the PDMS is more flexible than the COP, the later have lower losses at higher frequencies.

II. Performances criteria & applications

The creation of a prototype, in order to prove the viability of the concept, is the main objective of this PhD work.

In order to fully characterize our system's performances and evaluate it, we will need to determine some key parameters, such as; the response time, the power consumption, the EM performances and

the device cost. These characterization will be done throughout EM simulations and measurements the subsystems.

We can already define, based on the technological choices of the fluidic actuation & the use of liquid metal, a general frame of use for our system. This frame will exclude applications such as electronic warfare & all other applications requiring a very fast reaction time simply because such actuation system will turn out to be slow for them. We can add to this the fact the presence of moving liquid metal inside the system and the need to control its position with a relative precision has consequences. In particular, it forbid us applications where important mechanical constraints, brutal acceleration variations from multiple direction, which is especially the case for system for airborne & space applications. Therefore we can also exclude them from our scope.

Nonetheless, the interest of such a system is evident for a certain number of applications, especially in the defense & security field. We can envision potential applications for land & sea based surveillance/detection systems. In particular, its integration inside deployable autonomous sensors networks or in fixed stations for area monitoring. Indeed we can use such system to make either a continuous sweep of the environment, either enabling a communication channel following only one specific direction, and so limiting the detectability of the communication as well as lowering the device power consumption through the directivity of the device. Our target is going to be applications which don't focus on the steering speed of the antenna but more on the width of the scanned zone coupled with a small size device

An example of such application in the maritime context could be to have this system integrated inside anchored buoys to achieve a real time and relatively cheap monitoring network system of a country exclusive economic zone (EEZ) in order, for example, to protect it more efficiently against smuggling, illegal fishing and human born environmental threat.

We can also mention distributed autonomous sensors networks for military purposes, to perform discrete area's surveillance (for the detection of vehicles and personnel) or enable narrow beam point to point reconfigurable communication channels. It's obvious that the miniaturization possibility of our system makes it a suitable candidate to couple it with energy harvesting systems in order to package them inside fully autonomous sensor unites, and for a very wide range of environments. An example of the use of such system can be seen on the following figure 3):

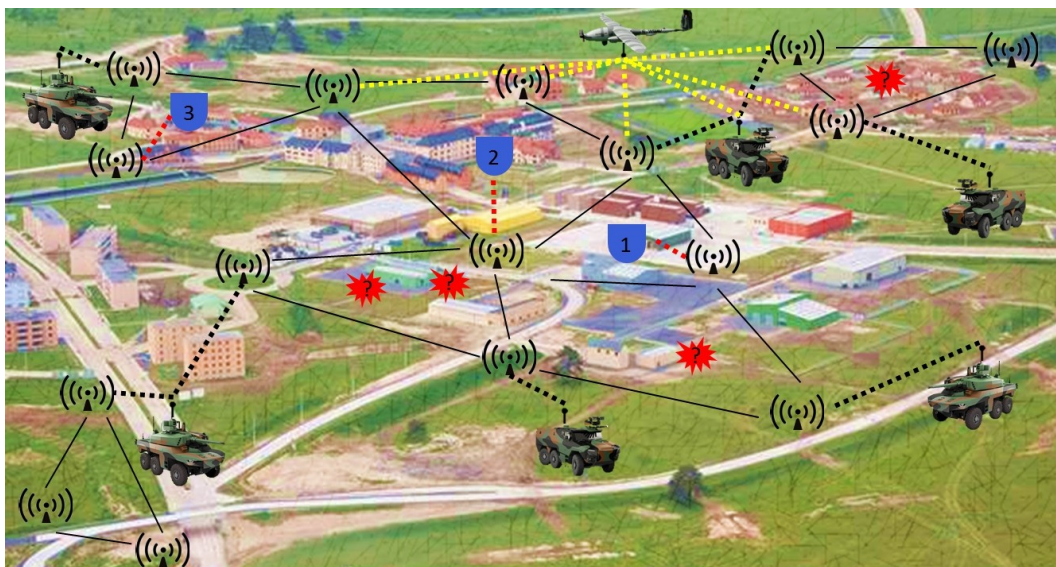


Figure 3 : Example of an of autonomous sensor network equipped with our reconfigurable antenna system used for dynamic situation and threats mapping for ground troops

As we can see in the prospective example of use above, our micro fluidic based reconfigurable antenna system is deployed packaged in communicating nodes of an autonomous sensors networks. It is used to provide a continuous 360° scanning of a large zone, meshed in few smaller sub-networks, in order to detect movement of unidentified vehicles and personnel to provide a real time dynamic operation theater mapping for the disembarked ground units and the support vehicles units (APCs, IFVs...), operating on the ground or in the air (airplanes, drones...).

III. Bibliographic study

The justification of the use of Galinstan [6], which was imposed at the beginning of the PhD lies in the nature of its direct competitor, which is the most commonly known liquid metal available, Mercury (Hg). This metal has the fatal flaw of being toxic and having its use heavily regulated today but still present very interesting characteristics. In particular it is liquid at room temperature (as opposed to Field's metal for example) and atmospheric pressure. It is also a fully metallic compound, as opposed to a solution containing metallic particles in suspensions, which would have far less good conductivity and would be mainly composed of a dielectric solvent. Therefore, the use of Galinstan, which is very close to Mercury in terms of characteristics, most notably the one of being liquid a room temperature, should allow us to enjoy the advantages of Mercury, without its inconveniences. Galinstan is an eutectic alloy of Gallium, Indium and Stannum, the name "Galinstan" being a commercial designation from its main producer, Geratherm Medical AG. Its composition is the following : 68.5% Ga, 21.5% In, and 10.0% Sn as indicated in [7]. Galinstan is non toxic, has a very low vapor pressure and is already used in a variety of applications, such as thermal management [8] temperature sensors [9], geophysics [10], MEMS power generator [11] or for applications in the same domain we are working on, RF [12][13], as these few example demonstrate it. We can see on the table 1) under a comparison between it and Mercury, as well as some of its most notable characteristic.

Table 1:[7] Comparison between the properties of the Galinstan & of the Mercury

Property	Galinstan [®] [1]	Mercury [2]
Color	Silver	Silver
Odor	Odorless	Odorless
Boiling point	> 1300°C	356.62°C
Melting point	-19°C	-38.83°C
Vapor pressure	<10 ⁻⁶ Pa at 500°C	0.1713 Pa at 20°C
Density	6440 kg/m ³	13533.6 kg/m ³
Solubility	Insoluble	Insoluble
Viscosity	2.4×10 ⁻³ Pa•s at 20°C	1.526×10 ⁻³ Pa•s at 25°C
Thermal conductivity	16.5 W•m ⁻¹ •K ⁻¹	8.541 W•m ⁻¹ •K ⁻¹
Electrical Conductivity	2.30×10 ⁶ S/m	1.04×10 ⁶ S/m

One which is not mentioned above but will be of importance is the fact that the Galinstan, when in contact with O_2 , oxidize itself, with a very fine layer of oxide creating on its surface [14], oxide which has very different physical characteristics, most notably it becomes hydrophilic, quite the opposite of the non-oxidized Galinstan which is hydrophobic. Indeed the oxide layer on the Galinstan is extremely thin (2-3nm) [15] and has the particularity of acting as a surfactant [16], lowering drastically the Galinstan's surface tension. When it happens, the Galinstan no longer behave as a Newtonian fluid. This state should therefore be avoided if we want to use the Galinstan for classic fluidic applications, such as circulation inside a channel for example, but we will see that we can take advantage of this phenomenon to develop specific displacement methods and application such as in [16][17][18] and [19].

It should be noted than none of the publications cited above report a modification of the electrical conductivity of the Galinstan due to its oxidation. We will therefore consider in our work, like these authors, that the oxidation phenomenon has no effects on the Galinstan electrical conductivity. We could also add that given our will to realize a system working in the 1-10 GHz band, the oxide layer should be invisible. Indeed, in this range of frequency, the thickness of the skin depth is comprised between $3.32 \mu\text{m}$ & $10.5 \mu\text{m}$, which is three order of magnitude higher than the reported thickness of the Galinstan layer.

In order to design our system, we first started to investigate the different technologies existing in the literature which could allow us to displace liquid metal (and more specifically Galinstan, since there is the potential obstacle of the oxidation), especially in the frame of RF applications. The second point was for us to look at how can we use these technologies to achieve the forming of the beam of an omnidirectional antenna. Our main criteria would be the simplicity of the command and its miniaturization prospects.

These technologies are the following:

Mechanical micro-pumps or syringe pumps; with the condition that the Galinstan is not being put in contact with the O_2 contained in the air. The pumping circuit and the outside environment should be separated to avoid any oxidation which would end up making the Galinstan a non Newtonian fluid.

Several sources in the literature mention the use of such technology, as in [20][21][22][23]. The main advantages of this system are its simplicity & its ruggedness. It must also be noted that this technology is not sensible to the actuation plan (horizontal or vertical), giving us more flexibility to design the fluidic system. On the other hand this technology is highly volume consuming (fluidic circuit, pump itself, power transformation unit etc.), which will necessarily negatively impact the miniaturization of our system. It potentially constrain us in terms of architecture to have a continuous actuation circuit, especially if we want to minimize the number of pumps, such as in [21][24], where only one pump is used, (figure 4)), to reach a displacement speed of $160\text{mm}\cdot\text{s}^{-1}$.

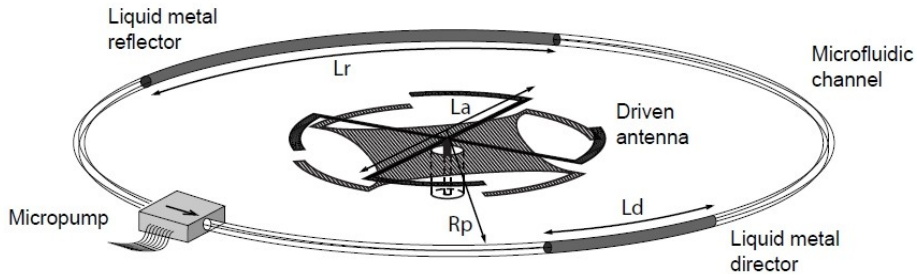


Figure 4 : [21] Design of a microfluidic antenna based on a low profile Yagi-Uda antenna with liquid metal parasitic. The center antenna is called an Alford type loop antenna.

This example shown above actually highlights another problem: we cannot allow the liquid metal (Mercury (Hg)) in the example, but the problem is the same, if not more acute for Galinstan because of the sealing constraint) to circulate inside the pump in order to; 1) Not tamper with the length of the parasitic liquid metal elements, or even break them & 2) Prevent damages to the pump on the long run. Indeed, most pump, a piezoelectric pump in this case, are not designed to accommodate the pumping of liquid metal. Even with an adapted pump, such as a peristaltic pump, there might be a blind spot in our radiation pattern because of the presence of the pump on the parasitic elements path, as it is specified in [21]&[24].

That is problematic to us because, as we can see on the figure 4) above, it limits the beam steering angle of this system. Here the angle can be calculated by the following formula:

$$\theta = 180 * \left(1 - \frac{L_R + L_D}{2 * \pi * R} \right) \quad (1)$$

Where θ is the total angle (in degree) of the beam steering achievable without crossing the pump, R the distance of the circular channel to the center of the antenna, L_D is the length of the director and L_R the length of the reflector of the antenna. In the example showed in [24], for the same system shown on figure for a 1.8GHz operating frequency, we have an $R = 80\text{mm}$, $L_D = 62\text{mm}$ and an $L_R = 217\text{mm}$. Therefore θ value is of 80 degrees in this case.

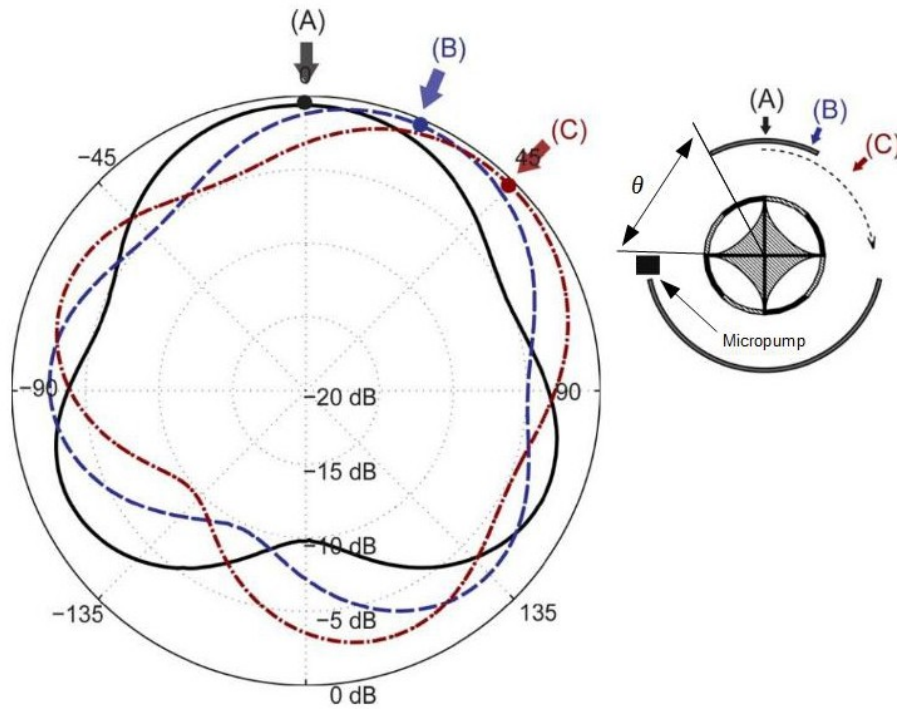


Figure 5 : [24] Radiation pattern of the microfluidic reconfigurable antenna presented in figure 4) for three different angular positions: (A) 0° , (B) 22.5° and (C) 45° .

As we can see, the figure 5), which is displaying the radiation pattern corresponding to the system showed in figure 4), is validating our previous assumption, the max angle realized is 45° , well below the 80° limit calculated above. This is making this technology no better than the planar electronic beam steering, with a steering angle of, here also, ± 40 degree in each direction. This is rendering it therefore less attractive than the very technology we seek to improve because these performances are obtained with a difficulty to miniaturize technology and the use of microfluidic technology, which is more troublesome to use.

We could avoid that obstacle of the pump by using multiple pumps instead of a single one. But if we shift to a system with multiple discrete actuations, we will need to have multiple power and command circuits in order to control and power each pump's subsection, as in [23] for example, which is illustrated in figure 6).

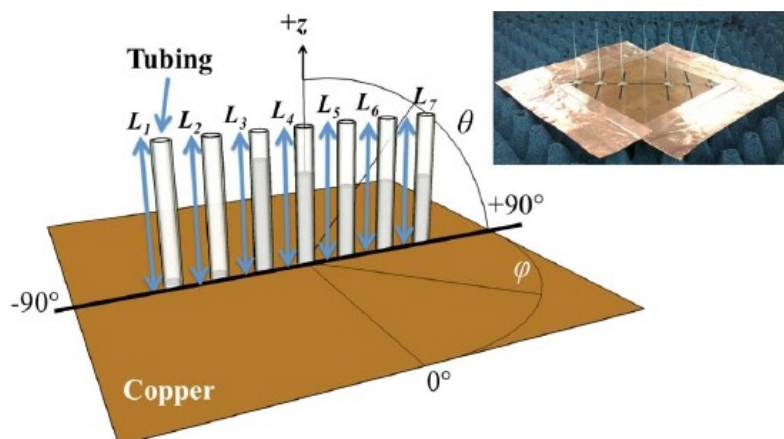


Figure 6 : [20] 5 elements configuration of a 7 elements reconfigurable Yagi-Uda monopole array based on syringe actuated vertical columns filled with Galinstan, with the feed element being the L_4 column.

We can also see that the volume consumption problem become even more acute in this case (as we can see from figure 6), despite the fact that the architecture in figure 7) has potentially solve the problem of the angular blind spot in the beam steering if we are to increase the number of columns.

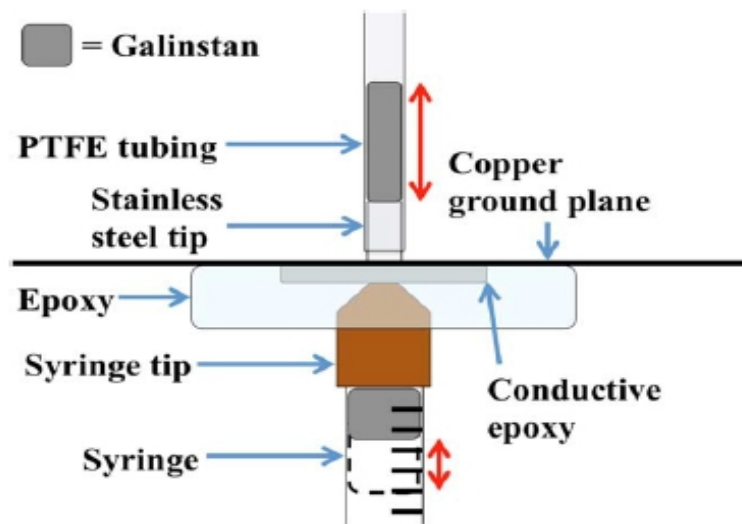


Figure 7 : [20] Filling mechanism (not to the scale) of one vertical Galinstan filled column. By applying pressure on the syringe, the Galinstan rises in the column.

On a more general note, mechanical pumps will also make the system more prone to failure, less reliable on the long run as well as less discrete in terms of acoustics signature, which can be a problem for certain applications, and which was one of the drawback we propose to solve in our system. Finally, the expected power consumption tend to be non negligible, with actuation voltage for the piezoelectric technology pump being between 100 to 250V [21], with power consumption being up to 200mW [25], allowing a displacement speed of $160\text{mm}\cdot\text{s}^{-1}$. The power consumption is not indicated in [20] and [23] since the actuation is still manual.

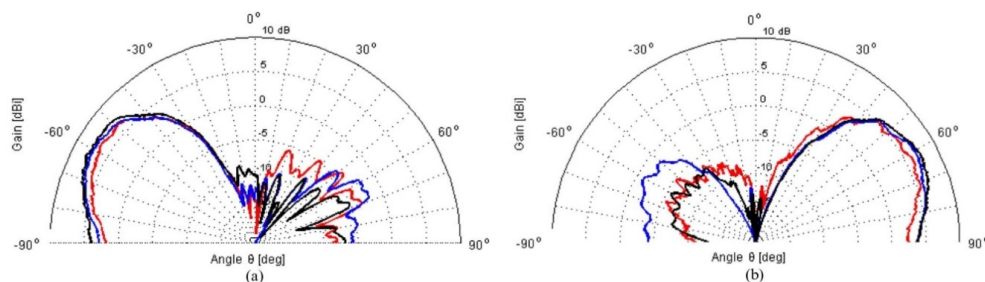


Figure 8 : [20] Radiation pattern for the 7 elements Yagi-Uda reconfigurable monopole array presented on figure 6), with a) $\varphi=+90^\circ$ and b) $\varphi=-90^\circ$ and for: red; 3 elements, blue; 4 elements & black; 5 elements.

As we can see on the figure above, we have the radiation pattern in the vertical plane of the design presented on figure 6), and where we clearly see that, at the difference of a dipole where it would be null, the monopole array's azimuth of the beam has an angle of around $+30^\circ$ from the horizontal plane.

There is of course other mechanical pump technologies available, with example such as [26][27][28], but their characteristics either makes them too big for embedded systems (which is our target

application), either results of technological choices which do not suit some of our Galinstan related exigences, especially its handling without any contact between it and the pump internal parts as well as a complete sealing of the Galinstan circulation channel from the outside environment to prevent oxidation.

Magneto-Hydro-Dynamic (MHD) pumps; which allow an easy circulation of the Galinstan inside a closed sealed loop and with a contact-less actuation, being based on the magnetic field of a magnet. At least one example in the literature can be found in [29], but some studies have also been done about the behavior of the liquid-metal flow under MHD actuation, as in [30], and also one example of the use of what is called an “electromagnetic pump” for forcing the Galinstan circulation, also for cooling purposes in [31]. An example of such a pump can be seen on figure 9).

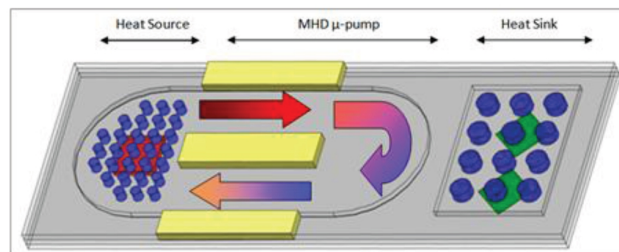


Figure 9 : [29] CAD depiction of a cooling system based on MHD micro-pump with Galinstan as cooling fluid)

Interest of such a system is of course the complete sealing of the Galinstan circulation channel, as well on its insensitivity to the actuation plan, as for mechanical pumps. But on the other hand the size of the device could be very problematic (especially because of we need a powerful magnet above our pump to make it work), as well as its power consumption, which is important, 2W for a tension of 0.5V DC in [29], rendering it very difficult to integrate into an autonomous system. The speed reachable for such high power consumption is of $10\text{mm}\cdot\text{s}^{-1}$, which while being a relatively average performance compared to the rest of the liquid metal displacement technologies, is very low in regards to the power injected in the system. All these factors are making it difficult for us to envision the use of this technology.

Thermal expansion based actuation; which allow the moving of Galinstan inside a sealed channel through its heating, via the exploitation of its thermal expansion properties. This method presents the advantage of operating in a complete sealed environment and the thermal actuation makes it particularly easy to integrate into autonomous devices, the heat energy being specifically easy to harvest and, in general, to produce from an electrical source. Here also, a relative insensitivity to the actuation plan is to be noted. At least one example of this technology applied to the active control of water can be found in [32], and applied to liquid metal in [33]. We can also find an example where that property is passively exploited in [9], in this case for Galinstan itself, but another very well known application is the use of Galinstan in replacement of Mercury in “Mercury thermometers”.

The drawbacks of this technology are that even though the volumetric thermal dilatation coefficient (β) of the Galinstan (which could be estimate at 3 times the linear dilatation coefficient α , which can be found in [9], by neglecting the α^2 and α^3 terms) could be qualified as high compared to the

majority of materials, at $34.5 \cdot 10^{-5} \text{ K}^{-1}$ (for example for Mercury it is roughly half at $18.2 \cdot 10^{-5} \text{ K}^{-1}$), it will translate into a relatively low volume variation ΔV for a given variation of the temperature ΔT , following the bellow formula:

$$\Delta V = \beta * V_0 * \Delta T \quad (2)$$

Where V_0 is the initial volume of the heated fluid, β the volumetric thermal dilatation coefficient. Therefore for a $\Delta T = 1 \text{ K}$ we'll have a ΔV of 0.0345% of V_0 . This means that we will need an initial Galinstan volume which will have to be important in order to have a significant volume variation, which, if the system is appropriately designed, will translate into a displacement, as the result of its heating. We can also see that the higher our temperature gradient will be, the more important the volume expansion will be, for example to have a 3% volume variation, we need a temperature gradient of 87K. We can see an illustration of this on figure 10), with a Mercury tank which is significantly bigger than the channel it's feeding because of the value of β , and with a system designed in a way that volume expansion of the tank, translates into the filling of the longitudinal channel.

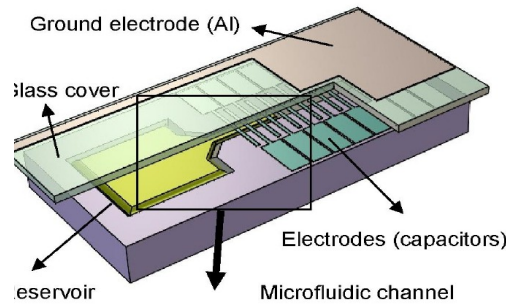


Figure 10 : [33] CAD depiction of a thermally driven variable capacitor

In this example, Pottigari et al. are using a tank filled with mercury which they heat in order to expand the liquid metal inside the channel, contacting the electrodes, and therefore modifying the capacity of the system. They've created a thermally driven variable capacity.

We can see that this technology will be volume consuming, which is something we want to avoid. The use of this technology will also make it necessary for us to pay attention to the heat transfer problematic, because the speed at which the heat will be transferred to the Galinstan will determinate the actuation speed of the device. That speed is not specified, but can be calculated based on the data provided inside the paper. Indeed, the volume $V_0 = V_T$ of the tank is of $2 \text{ mm} * 2 \text{ mm} * 400 \mu\text{m} = 1.6 \cdot 10^{-9} \text{ m}^3$. If, in first approximation, we consider the heat transfer to be isochoric (occurring at a constant volume), we know that we have the following equation:

$$Q = \rho * V_T * C_p * \Delta T \quad (3)$$

Where Q is the heat, ρ the density of the Mercury at $13533.6 \text{ kg.m}^{-3}$, V_T the volume of the tank of $1.6 \cdot 10^{-9} \text{ m}^3$, C_p the specific heat capacity, here measured at $125.6 \text{ J.kg}^{-1}.\text{K}^{-1}$ and ΔT the temperature gradient. For a ΔT of 1K, we have a Q of 2.72mJ. We also know that we can calculate the time necessary for this energy to be transferred to the liquid metal in the ideal scenario, meaning without any electrical, thermal, viscous losses. This will give us a rough estimation of the performances of

the system, performance very difficult to reach but which will give us a maximum speed achievable theoretically by this device. We have the following equation:

$$t = \frac{Q}{P} \quad (4)$$

Where t_R is the time needed to transform the power P into the heat Q . If we postulate an electrical power P of 10 mW, in the perfect scenario, $t_R=272$ ms. We know from [33] that a ΔT of 1K equals a rise in the channel of a length $l_R=55\mu\text{m}$. Therefore we can calculate the speed of the that rise in the perfect scenario, with the following formula:

$$V_R = \frac{l_R}{t_R} \quad (5)$$

Where V_R is the speed of liquid metal displacement achieved in the perfect scenario, which is equal to $0.2\text{mm}\cdot\text{s}^{-1}$. As we can see, doubling the power will lead to the doubling of this theoretical speed. But in order to have speeds of $20\text{mm}\cdot\text{s}^{-1}$, which would be interesting for us, we would have to inject 1W in the system, again assuming the transformation of the electrical power into heat is perfect.

As we can see the achievable speed with this device is rather low. This is achieved with very narrow channel of $40\mu\text{m}$, where for our application in the GHz band we will need a channel diameter of $500\mu\text{m}$ to 1mm, with a width ratio of the tank diameter above the channel diameter of 50, which highlight the volume consumption of this technology. Indeed, if we take a channel diameter of $700\mu\text{m}$, it gives us, if we keep the same geometry of the tank, a tank diameter of 35mm, which is extremely important.

Of course we could decide to lower the tank dimensions, but this would be detrimental to the speed of actuation because it would mean we would have to reduce the area of thermal exchange, which would lower to heating process. This would also diminish the amplitude of the liquid displacement for each additional degree of elevation of the temperature, because of the formula showed previously, where the volume variation depends on the initial fluid volume V_0 .

Additionally, if we were to properly evaluate the speed of system with our requirements (meaning with Galinstan in place of mercury), we would have to calculate the diffusivity D of the Galinstan, which can be calculated with the following formula:

$$D = \frac{\lambda}{\rho * C_p} \quad (6)$$

where λ is the thermal conductivity in $\text{W}\cdot\text{m}^{-1}\cdot\text{K}^{-1}$, here 16.5 [7], ρ the density in $\text{kg}\cdot\text{m}^{-3}$, here 6440 [7], and the C_p specific heat capacity in $\text{J}\cdot\text{kg}^{-1}\cdot\text{K}^{-1}$, here measured at 296 [34]. This gives us a value for D of $8.65 \text{ mm}^2\cdot\text{s}^{-1}$. That value can be considered low, compared to those of Copper (Cu) and Gold (Au), respectively $111 \text{ mm}^2\cdot\text{s}^{-1}$ & $127\text{mm}^2\cdot\text{s}^{-1}$, but high compared those of Mercury (Hg), at $4.52\text{mm}^2\cdot\text{s}^{-1}$. Just by knowing this value, we can assess that the response time of our thermal system, even if better with Galinstan than mercury, will still be relatively long, which further limits our interest in this technology for our application, because, as specified above, response time is one of the key points we're going to look at.

And finally, the problem of heat leaks and general thermal isolation will also be critical. Depending on the operating frequency chosen for our device (most likely in the GHz band), we might end-up with a relatively small device, making the management of this problem even more crucial and difficult to solve. Indeed such a system could be prone to a “cooling off” time, especially given the rather low diffusivity of Galinstan and the fact that the system will be realized in polymer (usually insulating materials), which would further curtail the response time, which we saw might already be problematic for surveillance applications for example.

Electro-wetting, continuous electro-wetting and discrete electro-wetting (EW, CEW & DEW); which allow an all electrical command of the liquid metal, in our case Galinstan, which move along channels equipped with electrodes. Galinstan is drowned in an electrolyte solution and thereby it is permanently surrounded by this solution. The literature is quite rich when it comes to that technology applied to the transportation of liquid-metal, and a lot of publications explore the possibilities of continuous [35] or what we could call “discrete” electro-wetting [36] for liquid metal displacement, some in the frame of RF devices, as in [36][37][38][39], or other application such as MEMS DC switch [40], pumps [26] and micro-motor [35].

First of all, we will explain the working principle of electro-wetting (EW) actuation. The following figure 11) will be very useful for this objective:

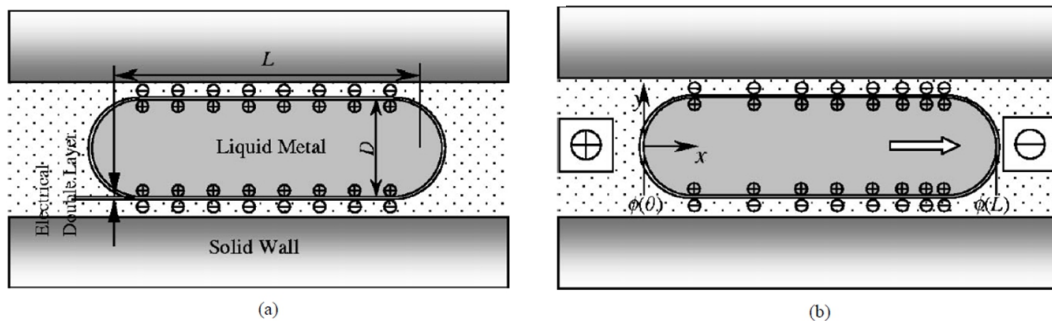


Figure 11 : [35] Illustration of the working principle of the EW actuation; with in (a) the initial situation, where the charge distribution is even on the surface of the droplet which is therefore in position of energetic equilibrium. Then in (b), after applying a voltage, the charge distribution changes, driving the droplet towards the negative electrode.

As we can see on figure 11), when we apply an electrical tension between the two ends of an electrolyte filled channel in which is immersed a droplet of liquid metal (Mercury, Galinstan, etc.), we create a charges displacement. We know that the interface between the two media (liquid metal and electrolyte) is electrically charged because of the various electrochemical activities which takes place at this interface. According to [35], this interface is called an electrical double layer or (EDL). Always according to [35], thickness of that EDL varies depending on the electrolyte/liquid metal couple, as well as on the environment, inside a range of 1-100 Å. When the voltage is applied, a current flow inside the small channel between the liquid metal droplet and the fluidic channel wall, thus creating a disequilibrium in the charges distribution along that EDL (initially in an equipotential state). That disequilibrium leads to the creation of a voltage gradient along the X axis (as shown on figure b), with voltage being greater on the right side than on the left side. That came from the difference in charges density along the EDL. Due to a phenomenon called electro-capillary

and which can be expressed through the following equation (also known as the Lippman's equation):

$$\gamma = \gamma_0 - \frac{C}{2}(V - V_0)^2 \quad (7)$$

Where γ_0 is maximum value of surface tension (for $V=V_0$), C the capacitance per unit area of the EDL, V_0 the initial voltage applied between the electrodes, and V applied voltage across the interface between the liquid metal and the electrolyte, we have that voltage gradient which translate into a surface tension gradient, which in turn translates into a motion of the liquid metal droplet. Indeed, in order to minimize its surface energy, the liquid droplet is inclined to move in the direction where the surface tension is the lowest, for it to reach a new equilibrium position of lower surface energy. While this phenomenon is the one triggering the EW actuation, the continuation of it is based on another phenomenon, which is the Marangoni effect.

It might be necessary here to clarify what is the Marangoni effect. This is the a phenomenon which arise when we put in contact two liquids with a high surface tension gradient at their interface, as explained in [40]. What happens is that the liquid having the lower surface tension will “flee” away from the other liquid, which has the highest surface tension. In our case, it's translating into the aqueous electrolyte trying to flee the contact of the side of the leading edge of the slug in the channel (right side). The initial movement of advance of the slug in the channel has been trigger by the lowering of the surface tension due to the change in the charges surface distribution, but the continuation of the motion is due to the triggering of the Marangoni flow. Indeed, by introducing a gradient of surface tension, we break the initial equilibrium. That translate into the electrolyte, under the action of these Marangoni flows, being evacuated from along the side of the slug towards the rear, acting as a “conveyor belt” [42] for the electrolyte, and also increasing the “activated” region of the EDL.

When the DC voltage is shut off, the charges distribution changes to become even again, which means all gradients disappear, ending all movements. The slug having reached a state of energetic equilibrium stands still in the channel in its new position. We can see that through this technology of actuation we managed to displace the liquid-metal droplet only by using a simple DC electrical command.

What is described above is what happen in theory, now let's see how this translates into experiment. An example can be found in [36], as shown on figure 12), which explore the dynamics of the EW actuation through a series of pictures, for a configuration very similar to the theoretical example described above, with in this case a droplet of Galinstan and an electrolyte which is basic and which is a 1% NaOH solution:

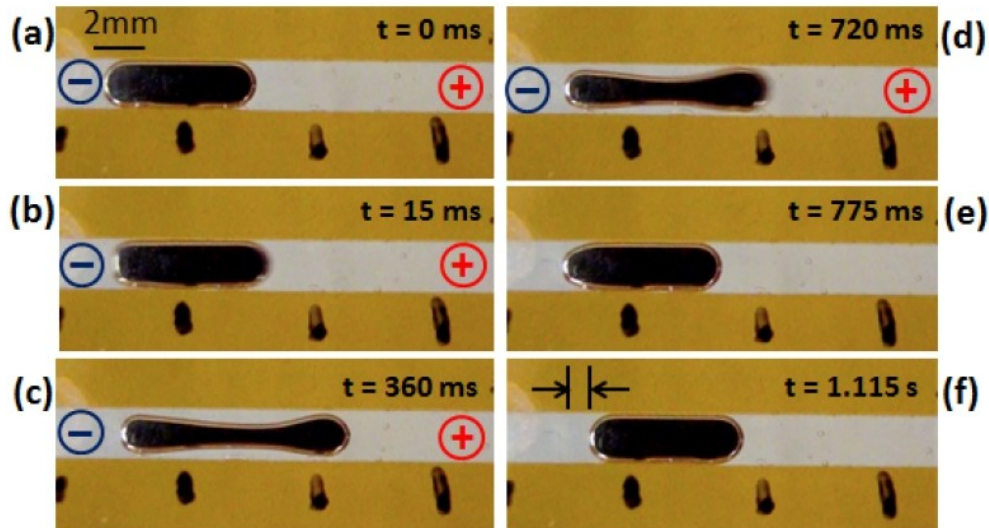


Figure 12 : [36] Series of picture showing the motion of a Galinstan slug in a channel filled with NaOH based electrolyte when is applied a 7V DC command. The result is a slug displacement through CEW actuation. Voltage is applied in (a) until (d).

As we can see on this figure, Gough et al. performed a test on a Galinstan slug trapped inside a horizontal channel filled with an electrolyte solution and fitted with two electrodes, one at each end, exactly like the example use in theory. The sequence of events is the following: when the voltage is applied the EW actuation starts and is first and foremost “pulling” the leading edge of the slug forward as a consequence of the charges redistribution along the surface. This is the case from (a) to (d). We clearly see the metal slug being elongated with the end of it, on the left, trailing behind and slowly advancing. Once we shut off the DC voltage (d), we see almost immediately the left side catching up (less than 55 ms) (e) and the leading edge retracting from an elongated and thinned slug to a slug of the same shape as initially (f). The accumulated advance of the slug is now around 1mm (so a total displacement of roughly 16% of the initial droplet length. if we take an initial length of the droplet of 6mm) for 1.115 s, which give a speed of roughly $0.9 \text{ mm}\cdot\text{s}^{-1}$. The maximum elongation length of the droplet is 3 mm, reached in 360 ms, meaning the droplet in (c) measure around 9 mm long. This give an elongation speed of roughly $8.3\text{mm}\cdot\text{s}^{-1}$. This is a 50% elongation which in turn give a 17% displacement. These results are obtained for a 7 V DC command.

These results highlight two facts:

First, we can see that this method does not have a very important speed of displacement if we look at the final position difference between (a) and (f), it is slightly less than $1 \text{ mm}\cdot\text{s}^{-1}$. It compares rather poorly in terms of speed to the $160 \text{ mm}\cdot\text{s}^{-1}$ obtained in [21], (for the pump actuated Mercury displacement inside the tube loop) even if we do have other advantages such as a low power consumption, very good miniaturization perspectives of our system and the all electrical command.

For a dynamic use on the other hand, where the total elongation is more important than the ability to hold the droplet elongated for a long period of time, this EW method is more interesting. Indeed, in this case, from (a) to (c), we reach a speed of $8.3 \text{ mm}\cdot\text{s}^{-1}$, which is significantly higher.

Second, this results highlight that the position control of the slug with such an actuation method is rather complicated. Indeed it is very difficult to predict the exact distance the slug will have travel inside the channel at the end of the actuation sequence, therefore it cannot be considered reliable on this point. Even if we would be able to predict this distance, nothing tells us if the droplet is going to stay in its position because the channel offer no asperity on which the droplet could block its motion.

Of course these problems have been addressed in the literature. We'll start by the first problem, which is the motion speed.

We can find in [35][36][37] potential solutions of these problems, through the use of "Continuous electro-wetting" and "Dynamic electro-wetting".

In order to better understand what we're talking about, we'll take a closer look at the work presented in [35] with the help of figures 13) to 15). Indeed, this publication presents a very interesting solution to the first problem not anymore based on a linear but a circular channel for a system called by Kim et al. a micro-motor. The principle of the device is presented on figure 13):

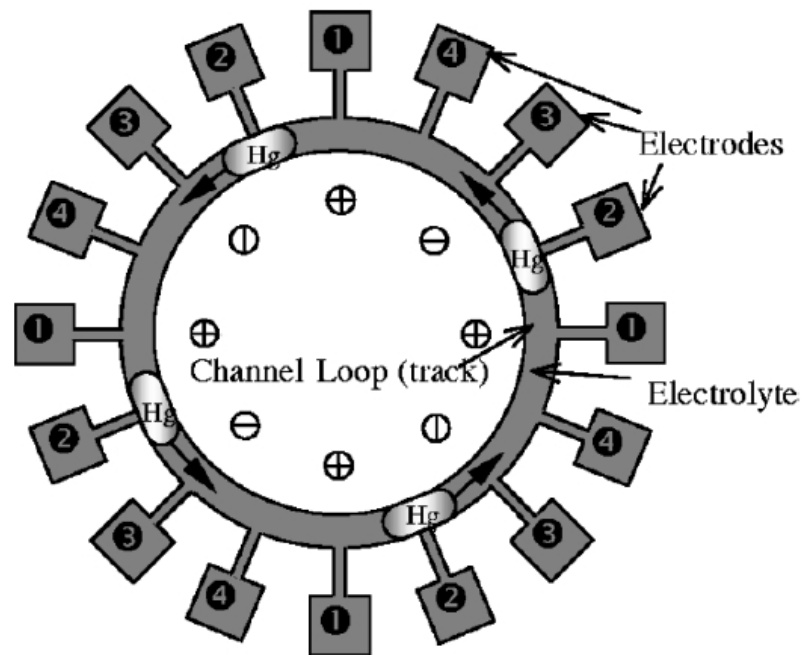


Figure 13 : [35] Illustration of the concept of a liquid-metal based micro-motor

In this example Kim et al. use a mercury slug placed inside a circular channel etched inside a silicon wafer with multiple electrodes (distributed by pairs) positioned regularly along that channel, inside dedicated cavities, and in contact with the slug through the electrolyte. By activating the electrodes following a well thought sequence, as shown in figure 13), they're able to enable the continuous displacement of the slug, therefore avoiding the phenomenon spotted in [18]. As a byproduct of their system, they're also able to actively control the droplet speed inside the channel. The figure 14) bellow shows the electrical control sequence allowing the continuous electro-wetting of the mercury slug, therefore its continuous displacement. This method of displacement is called CEW.

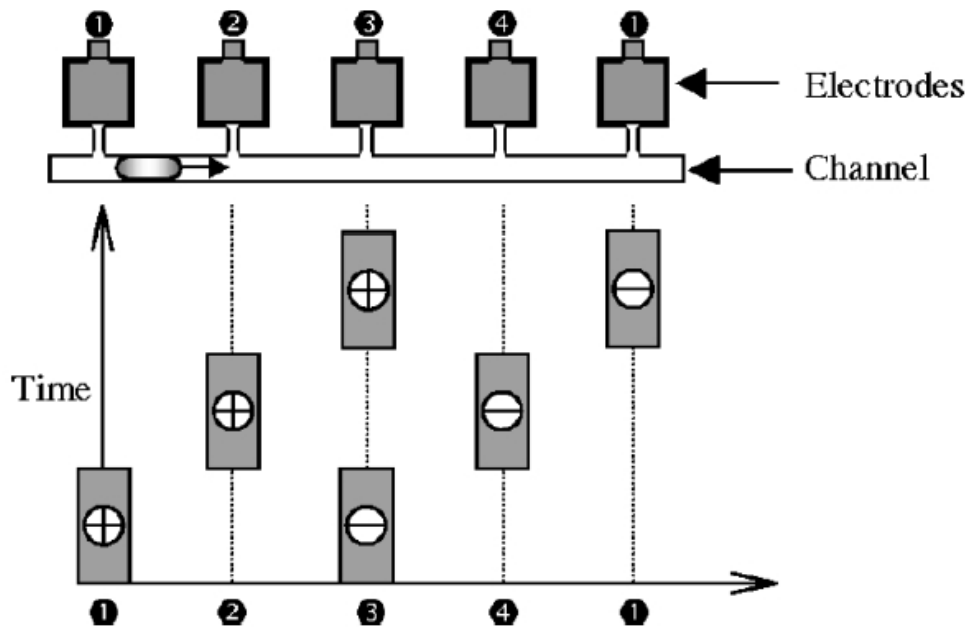


Figure 14 : [35] Illustration of the working principle of the electrical command of the CEW actuation with the channel on top and the evolution of the command signal on each electrode below.

As we can see on the figure 14), a DC signal is sequentially applied to the electrodes in order to continuously displace the metal slug. The sequence is the following: “+” on 1) with “-” on 3) to push the slug away from the electrode 1 and pull it closer towards the electrode 3. Then when it passes in front of the electrode 2), electrodes 1) & 3) power is shut off and “+” is applied on the electrode 2) and “-” on the electrode 4), etc. By alternating quickly the powering of the appropriate electrodes, it is possible to continuously drive the metal slug inside the channel for as long as necessary.

As we can see, the second problem is not fully addressed on this system, because while the authors are able to control the position rather precisely (resolution depending on the number of electrodes) with the power on, if the power is shut off, that ability is lost, given that here also the channel is slick. Therefore when the power is cut off, the slug is free to move according to all mechanical impulse or oscillation the system will be submitted to, as it is the case for the example showed previously in [36]. In terms of achievable speed with such a system, Kim et al. are close to $40 \text{ mm} \cdot \text{s}^{-1}$ for a channel of 2 mm of diameter, as we can see in figure 15).

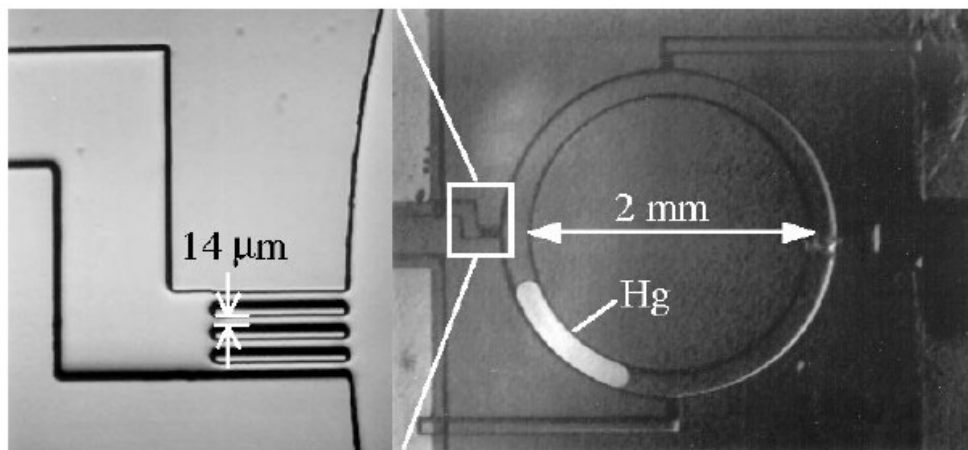


Figure 15 : [35] Picture of the micro-motor view from the top (right), with a detailed view of the Mercury filter (left), which prevent the mercury slug to get to the electrode.

The power consumption is ranging from $10 \mu\text{W}$ to $30 \mu\text{W}$ (1 to 3 V for $10 \mu\text{A}$). As we can see the speed in this configuration is 40 times the speed of effective displacement achievable with the first method, and still faster than the dynamic elongation of the first system, approximately 4.8 times faster.

We will now turn to the second example, presented in [36] & [37] which manage to solve the two problems by combining the use of an AC control signal and a new linear channel geometry.

The first system they proposed is the same system as in the figure 12), but this time they changed the actuation signal, from a 7 V DC signal to an 8 V peak to peak square AC signal, with a 30 Hz frequency and a +3 V DC bias. The results of this change on the performances of the system can be seen on figure 16):

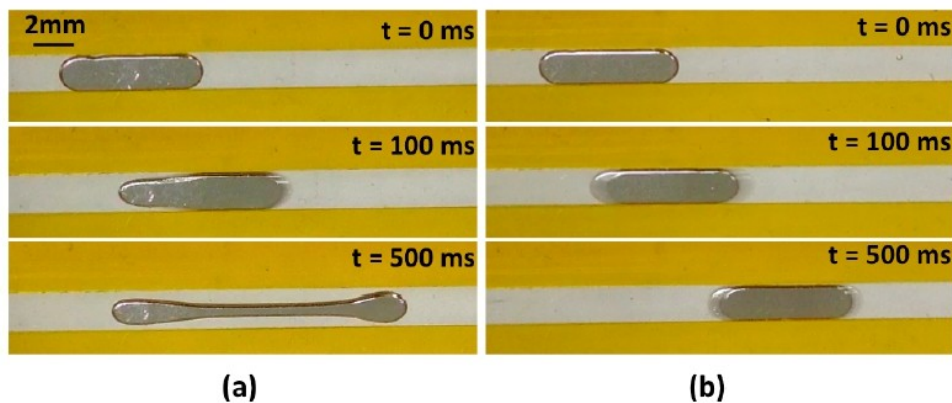


Figure 16 : [36] Series of picture comparing the motion of a Galinstan slug in a channel filled with NaOH based electrolyte when is applied: (a) 8V DC signal, (b) 8 VPP AC 30 Hz square signal, with a +3V DC bias.

The difference is obvious between the two actuation mode. When the droplet elongate itself under the action of the DC voltage, it moves forward with minimal deformation under the action of the square signal. We can calculate the speed of the droplet with the second method, it give us a speed of $18 \text{ mm}\cdot\text{s}^{-1}$, which is slightly more than the double of the elongation speed of the first method and 20 times more important than it's effective displacement speed.

So as we can see, either with multiple electrodes and by keeping a DC only signal, either with only two electrodes but by switching to an AC signal we're capable of addressing the problem of the low displacement speed of Galinstan with an only electrical command.

As for the problem of the position control, a solution has been proposed as well in [36], and named "discrete electro-wetting". It is the combination of a new geometry of the channel in which circulate the liquid metal, which change from a simple linear trench as in figure 16), to a trench made of interlocked circular chambers which are perpendicular to the channel's direction, as figure 17) is showing it.

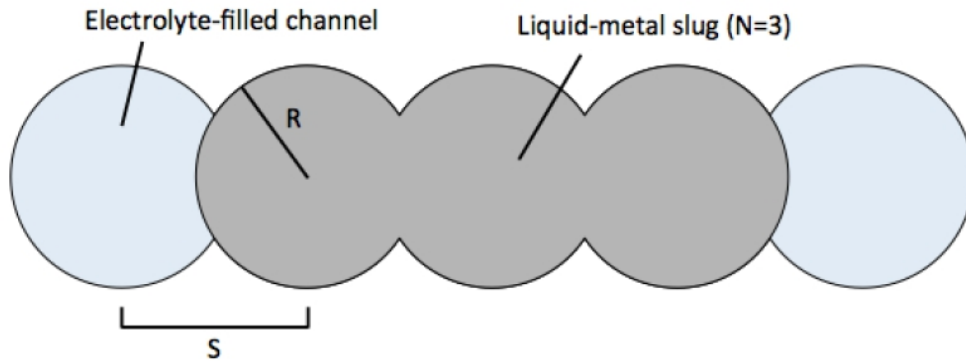


Figure 17 : [36] Top view illustration of the interlocked chambers. Each chamber has the same radius R and constant spacing S from the other chambers. The metal slug length is expressed in terms of number of chambers occupied, N , with here $N=3$.

The term of “discrete” electro-wetting is coined by using the findings found in [36], but this technology is also used in [37], which is from the same authors. The functioning is basically the same as for figure 16), unless this time the channel is “serrated”, which allow the slug to stay in it’s position when the power is shut.

Indeed, since the slug is trying to minimize its free surface energy, and since the cylindrical chambers offers to the droplet a shape to conform which minimize it, then without an external intake of energy in the system, here under the form of an electrical potential difference, the slug stays trapped inside the chambers. With this simple mean, Gough et al. are able to control, within the resolution of one chamber, the position of the slug inside the channel. The immediate drawback of this technology is that its power consumption compared to those of systems with a slick channel increase. Indeed, more energy is now necessary to dislodge the slug from the chamber, because it amount to increase its free surface energy in order to push it in the next, as we can see on figure 17). The control signal applied to the channel is the same as for figure 16) (b), a 30 Hz 8 VPP square signal with a + 3 V DC bias.

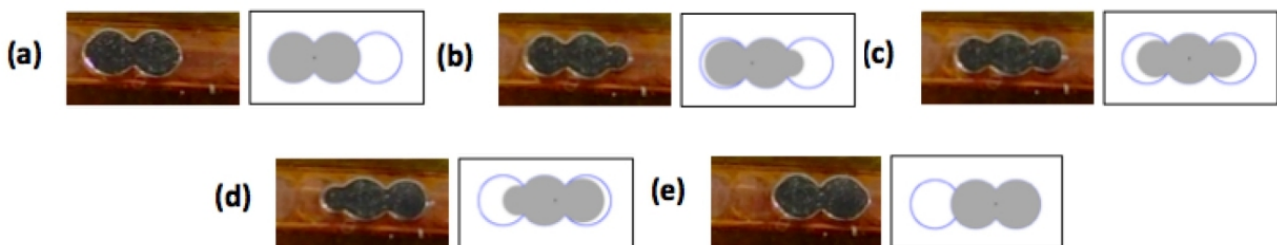


Figure 18 : [36] A $N=2$ metal slug is moving (in five steps) one chamber further to the right under the action of the square signal. Picture of each step with the corresponding MATLAB simulation in a) to e)

The speed of displacement of the slug for this channel configuration is not specified in [36], but we can expect a lower speed than in figure 16) given that it’s the same signal, but it is more energy costly to move the slug from chamber to chamber. On the other hand, on [37], with a 4 V DC signal, applied on the device in figure 18) bellow, we have a speed of 6.4mm.s⁻¹. The power consumption is of less than 10 mW according to Gough et al. for a similar device presented in [36], and not specified for the case of [37]. As for the dimensions, the chambers have a 1.8mm diameter and are

spaced by 1.5mm for [36], & have a 3.7mm diameter and are spaced by 3mm for [37]. For the purpose of illustration, we can see an example of the application of this principle in the figure 19), applied to a radio-frequency application (RF):

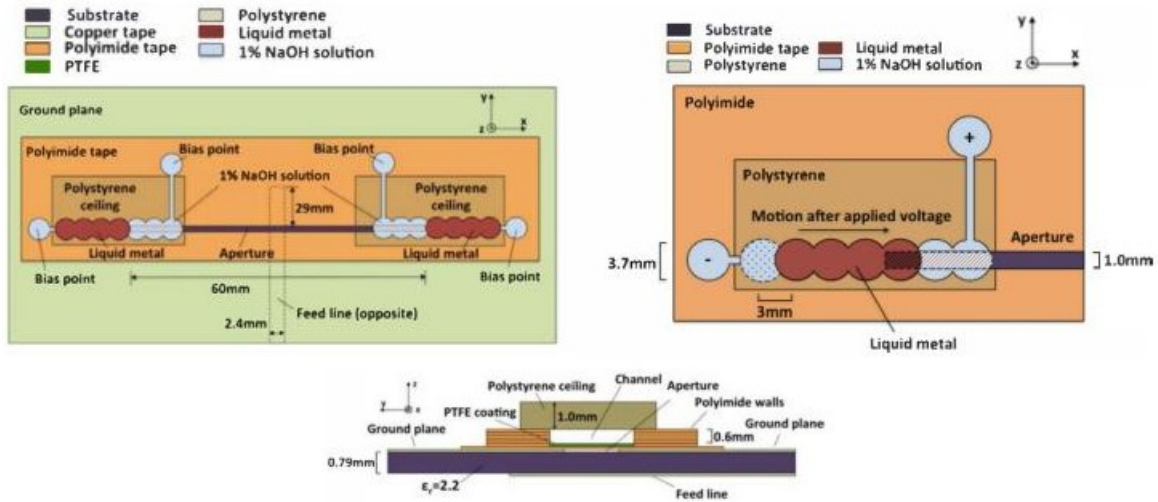


Figure 19 : [37] Schematic of the slot antenna tuning device based on Galinstan’s DEW along an horizontal channel with top view (left), a side view (bottom) & a detailed view of the overlapping channel on top of the antenna’s slot aperture (right)

In this example [37], Gough et al. use a horizontal serrated polyimide channel topped with a polystyrene sealing filled with electrolyte and Galinstan placed above the aperture of a slot antenna. This slot antenna, consisting of a 60mm*1mm aperture inside a copper ground plane topped by a layer of PTFE coating. Initially, the Galinstan slug is standing by the edge of the aperture, above the ground plane. By activating the DEW actuation (with a 4 V DC voltage) they can move the metal slug above the slot (with a speed of $6.4 \text{ mm}\cdot\text{s}^{-1}$), diminishing the length of the aperture & hence enhancing the resonant frequency of the antenna, as we can see in figure 20) bellow.

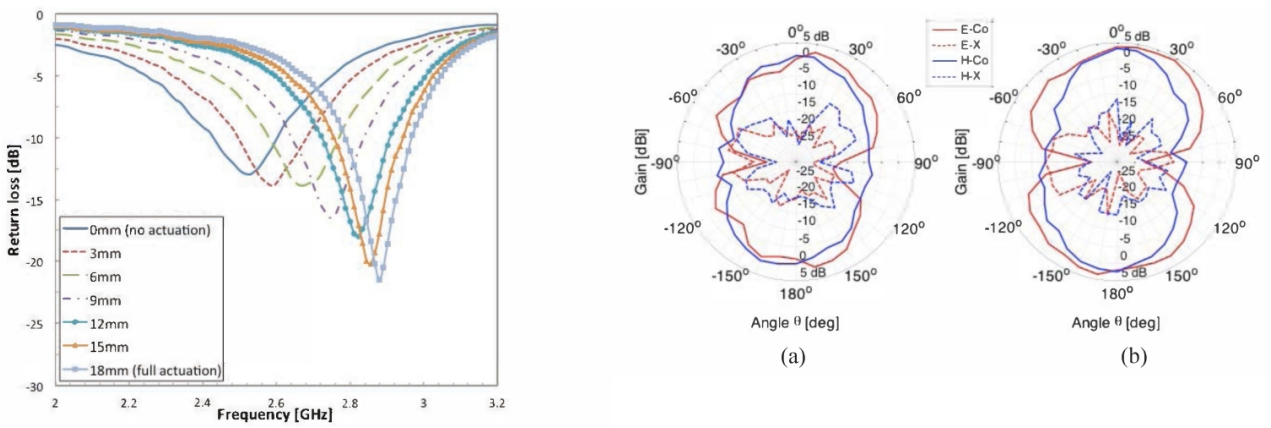


Figure 20 : [37] Return losses (S_{11}) evolution for different liquid metal coverage length of the slot antenna’s aperture (left), Radiation pattern for a) : no coverage (2.52 GHz) & b) full coverage (2.88 GHz) of the antenna’s aperture (right)

As the channel is serrated, there is therefore only a limited number of possible position for the metal slug to adopt, which limits the different frequencies obtainable with this device. That limitation of

the possible lengths renders the process completely repeatable due to the finer position control of the droplet.

The performances in terms of miniaturization of the CEW based systems are excellent because that technology come in large part from the MEMS background, the power consumption is also quite low (up until 10 mW documented in [36] for the design presented above, but could be as low as 30 μ W). The speeds of displacement achievable are rather high for CEW and DEW actuation, 18mm.s⁻¹ to 40 mm.s⁻¹ as in [35] & [36], with documented speed of 100 mm.s⁻¹ in [18]. It must be noted that the displacement speed tends to go up as we reduce the size of the systems, while at the same time the power consumption tends to go down.

Electrochemical actuation (ECA): which also allow an all electrical command of the Galinstan, in a similar fashion as the CEW, but which also rely on some of the specific characteristics of the Galinstan, namely the formation of the oxide layer on the droplets, and therefore is exclusive to this specific liquid metal. The term ECA itself was coined in [18], but we can also in [19] find the term “electrically controlled capillarity” ECC. CEW and ECA devices are relying on the same working principle, the application of a DC signal to a liquid metal slug (specifically Galinstan) inside an electrolyte filled channel, as in [42]. But, the two phenomenons differs because of the sign of the voltage applied to the droplet in the electrolyte solution. Indeed, for the same setup, if we apply a positive voltage, we can trigger the electrofluidics actuation, and with a negative one, we can trigger the electrochemical actuation. The dual nature of this phenomenon is highlighted in [18], as shown on figure 21) below:

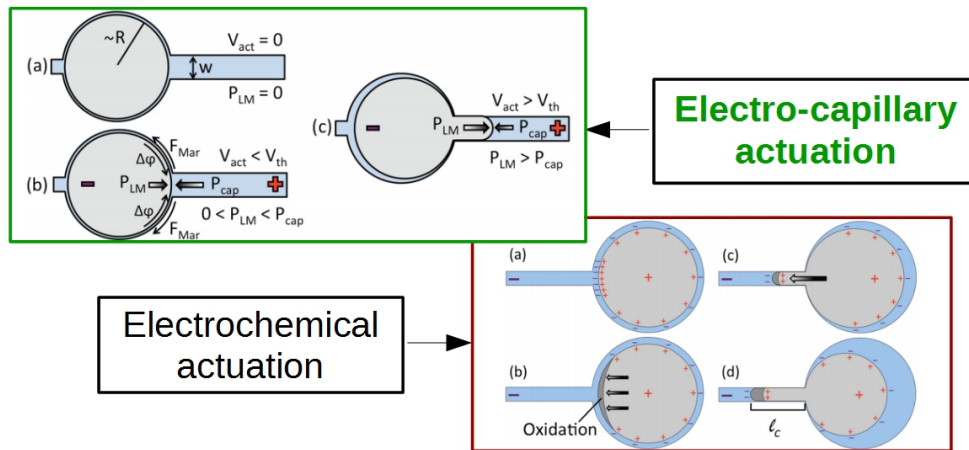


Figure 21 : [18] Illustration of the electro-capillary actuation (top) and electrochemical actuation (bottom) with in each case the different phases of the phenomenon.

As a reminder, for the electro-capillary actuation (top), initially the Galinstan sits in the tank (on the left), as in (a), when we apply a positive actuation voltage (V_{act}) to the chip (b), we create a surface tension gradient on the Galinstan droplet’s surface near the channel entrance (noted as $\Delta\phi$ in the figure). This triggers the Marangoni flows (F_{Mar}), which drain the electrolyte from the channel (on the right) to the bottom of the tank (on the left), building up the pressure inside the channel (P_{LM}). Once the activation voltage reach the threshold value (V_{th}), P_{LM} overcome the capillary pressure (P_{cap}) inside the channel and therefore the Galinstan advance in the channel (c).

For the electrochemical actuation (bottom), initially the Galinstan sits in the tank (on the left), as in (a), when we apply a negative voltage, to the chip (b), a layer of oxide will form on the Galinstan's droplet's surface near the channel entrance. As we said before, Galinstan oxide behave as a surfactant [16], therefore the oxide coated Galinstan shift from hydrophobic to hydrophilic behavior. Hence the capillary effect is triggered and the coated Galinstan advance inside the channel (c). Capillarity is the name of the phenomenon which allow a liquid to advance inside a thin enough channel, without any visible application of force. The capillary effect is in fact the result of the minimization of the surface free energy (via a change in the liquid's meniscus shape) of a liquid combined with the molecular interaction between the liquid and the wall of the channel, as described in [43] & [44].

The phenomenon's behavior has been modeled by James Jurin [45], which has established the following law for the rise of a liquid inside a vertical tubular channel, called the Jurin's law:

$$h = \frac{2 * \gamma * \cos(\theta)}{\rho * r * g} \quad (8)$$

Where h is the height of the rise, γ the surface tension of the liquid, θ the contact angle between the liquid and the wall of the channel, ρ the liquid density, r the radius of the channel and g the gravitational acceleration (9.81 m.s^{-2}).

This law is true only if the tube radius is smaller than the capillary length, λ_c , which can be calculated by the following formula:

$$\lambda_c = \sqrt{\frac{\gamma}{\rho * g}} \quad (9)$$

Where γ is the surface tension of the liquid, ρ the liquid density and g the gravitational acceleration (9.81 m.s^{-2}). If the $r < \lambda_c$ then the Jurin's law is valid.

It must be noted that since the Galinstan's oxide is a very thin layer (few nm) [15], it is very prone to break under the pressure of the advancing metal behind it. That layer reconstitute itself almost immediately because of the presence of the oxidation voltage. Therefore as the droplet is advancing, more and more Galinstan get oxidized, keeping the slug coated with a very hydrophilic oxide layer, which allow it to advance in the channel thanks to the capillary effect. When the oxidation potential at the leading edge of the slug becomes too high, the oxide layer become too thick to be broken by the incoming liquid metal pressure. At this moment (d) the rise is blocked, and the length reached at this point is called l_c for "critical length". That length is of course depending of the geometrical characteristics of the channel and of the value of the applied voltage. It has been shown in [15] that the critical length is inversely proportional to the value of the applied voltage. It has to be noted that this drawback of the critical length is intrinsic to this Galinstan displacement method.

A very interesting example of the application of this technology can be found in [19]. In this example Wang et al. use the electrochemical actuation to raise or lower the height of their antenna,

and therefore realizing frequency tuning of their antenna. This antenna itself is a simple monopole, bottom fed with a coax cable, as we can see in figure 22).

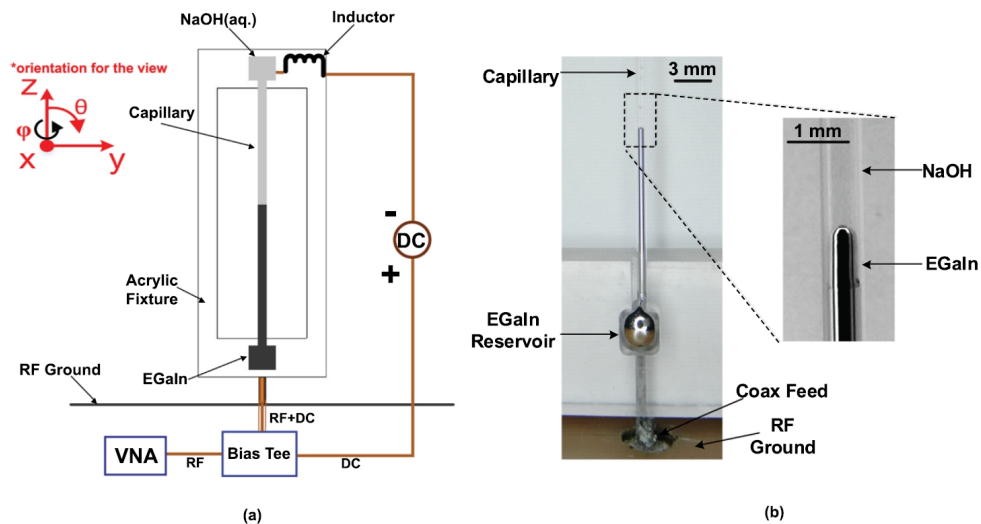


Figure 22 : [19] Illustration of the vertical Galinstan made frequency tunable monopole antenna controlled via electrochemical actuation. By applying a voltage, authors are able to raise or lower the Galinstan inside the channel, which is a glass capillary, hence tuning the length of the resonating elements, and therefore tuning the antenna's frequency.

In this example, the Galinstan is stored inside a tank at the bottom of a glass 0.7mm diameter capillary filled with a 1 mol.L⁻¹ NaOH aqueous solution. By applying a negative voltage between the tank and the capillary, they're able to make the Galinstan rises inside the channel, for very important length, starting to 4mm up until 75mm in this case. This is realized by tuning the hydrophilicity of the Galinstan by the phenomenon explained above, the ECA. The speed of such actuation is asymmetrical, meaning that the rise is significantly slower than the withdrawal, 0.6 mm.s⁻¹ against 3.6mm.s⁻¹. This asymmetry is linked to the fact that in order to withdraw the Galinstan, we just need to remove the surfactant oxide layer from the Galinstan and let the Galinstan return to a position of lower free surface energy, in which case the gravity is helping, when to make it rise, we need to oxidize the Galinstan and let the capillarity elevate the liquid metal. Since the density of Galinstan is quite high, at 6440 kg.m⁻³, in this case the gravity is playing against the rise.

We find again this asymmetry in the power consumption, when the voltage needed to rise the Galinstan is of +7 V DC (with respect to the polarity shown in figure 22), it is only of -0.7 V DC to withdraw it. It is actually non compulsory to apply a negative voltage to withdraw the Galinstan, but it speeds up the procedure. It must be noted that the elevation inside the column can be blocked at the desired length value simply by maintaining a small positive (again, with respect to the polarity shown in figure 22).











As we can see from the example of the devices presented in the literature for the CEW & ECA actuation, most of them displace the Galinstan (or Mercury) in the horizontal plan. While it is not specified if these technology couldn't work in the vertical plan, there is here a potential limitation we need to take into account in our design of the whole RF fluidic system. Namely, if we want to

design a Yagi-Uda based antenna, it would be easier for us to chose a horizontally polarized central antenna, hence we would not need to have any vertical channels in our design because the parasitic elements would be horizontal as well. On the other hand, the use of a vertically polarized antenna would allow us more original designs, a better optimized use of the available space and potentially more flexibility for the system's on the fly reconfiguration, which is a major advantage of the use of liquid metal in our design. It is also noteworthy that the fact that the Galinstan is completely immersed into the electrolyte solution prevents its oxidation, therefore allow it to stay completely hydrophobic.

IV. Key points & bottlenecks extracted from literature

As a conclusion, we can say that among the various technologies investigated, the EW/CEW/DEW technology, as well as the ECA/ECC technology seems very interesting and the present the most balanced compromise in order to fulfill to our objectives in terms of integration, miniaturization, power consumption and response time. These technologies being very close from one another, we have the possibility to work with both with minimal if not any changes in our system's architecture to accommodate them both. We can find on table 2) bellow a summary of the performances of all the technologies surveyed:

Table 2: Performances comparison of the liquid metal displacement technologies studied

Liquid metal displacement technics performances (order of magnitude)					
Technology	Speed	Tension	Power consumption	System complexity	Size
Mechanical pump	100- 200 mm/s	100 V	100 mW		
MHD pump	10 mm/s	1V	1W		
Thermally driven actuation	1-10 mm/s	/	10 - 100 mW		
CEW/DEW	10-100 mm/s	1V	10 μ W - 10mW		
ECA	1-10 mm/s	10V	10mW		

As we can see on the figure above, the CEW/DEW as well as the ECA (which are extremely close

in terms of architecture and command) are the most adapted liquid metal displacement methods for systems which are designed to be part of an autonomous device. The choice of these technologies was based on their matching with the key points developed earlier, namely: the response time achievable, the power consumption, the EM performances and the cost of the device. They represent the best compromise for us in terms of simplicity of the architecture, volume consumption, speed of actuation and power consumption. We will be using the Galinstan as liquid metal inside our system, in place of Mercury, because of the non-toxicity of Galinstan. That being said, we can identify some hard points from the literature for our design to take into account if we are to use this displacement method with this material:

First of all, as we have seen, the literature mention mostly liquid metal displacement inside the horizontal plan associated with the use of the aforementioned displacement method, as in [11][13][35][36], with the notable exception of [19] for the ECA technology. This problem is rather specific to this method, as it is obviously not a problem with the use of syringe pump for example, as in Morishata et al. in [23]. For various reason, namely antenna architecture, space saving, device agility, reconfigurability and effectiveness, we might want to move the Galinstan inside the vertical plan, both with CEW/DEW and ECA methods. While nothing in the literature said it's actually impossible or problematic, as [19] proves it, we will be mostly in uncharted territory for the CEW/DEW actuation method for vertical liquid metal displacement.

Second, we need to take into account the fact that the Galinstan and the electrolyte (being either basic or acidic) might damage the electrodes needed to actuate the liquid metal, particularly if the electrodes are made of metal. If the electrodes are damaged, it might impact the performances of the system, and most of all its reliability on the longer term. For the Galinstan (and mercury), the phenomenon of the amalgamation of the liquid metal with the electrodes can be considered as a problem in [38][46] & [47] for the long term durability of the device, but also part the solution to avoid the formation of a battery cell in the liquid due to the acidic/basic nature of the electrolyte reacting with the metal of the electrodes, such as copper, as shown in [48]. This alloying behavior of the Galinstan is actually mentioned in its safety data sheet, at the paragraph 10, [6]. One solution could be the use of non-metallic but conductive electrodes, such as graphite for example, as in [49].

Third, the problem of the generation of hydrogen gas bubbles, is documented in [35][47][48] & [49]. This occurs because the passage of a current inside the aqueous electrolyte generate an electrolysis of the water, and also if, like in [47], the Galinstan is put in contact with aluminum, in which case a chemical reaction occur, as underlined in the Galinstan data sheet, [6]. These two phenomenon generate hydrogen gas which forms bubbles inside the channel if this channel is sealed, and accumulate. The volume of gas generated stays low compared to the overall volume of electrolyte, and since our system should contain relatively small amounts of electrolyte, the total volume of H₂ released would also be small, therefore rendering risks of explosions negligible if placed in a well vented environment.

The use of Galinstan require for us to work in a dioxygen free environment. Because of the method of displacement chosen, that's not a problem, the presence of electrolyte, completely encasing the Galinstan will prevent oxidation, unless, by applying the adequate voltage, we create the condition for the oxide layer to appear, which is at the base of the functioning of the ECA, as in [19] and [42]

for example. But this means that the sealing of the system is of great importance, because if the electrolyte was to leak outside the system, it would render it inoperable and the Galinstan would become totally oxidized.

One very important potential hard point is a consequence of the fact that we need to use this fluidic system for an RF application. It happens that our electrolyte is going to be an aqueous one, due to the fact that we need to dissolve ionic salts inside a solvent in order to realize a conductive electrolyte, and because water is an excellent solvent for ionic salts, solvent which is also cheap, easily available and non toxic. Because of this, we need to take into account the impact of water on the RF performances, which is really negative due to its characteristics ($\epsilon_R = 80.4$ at 20°C , $\tan \delta = 0.154$ at 3 GHz). Particularly, its dielectric losses, through which the water is absorbing an important part of the radiated power from the antenna, are very significant. Ions in the solution will also, because of their presence in the solution and because their electrical conductivity, disrupt the radiation propagation inside the antenna system, through conduction losses. This problem is highlighted in [19], where it is also said that there is a compromise to make between a low conductivity electrolyte & a highly conductive electrolyte. Indeed, while a low conductivity of that electrolyte will negatively impact the response time of the fluidic system (because the electric charges will move slower, take more time to unbalance the charges distribution along the EDL of the liquid metal slug), it will positively impact the RF radiation propagation inside the whole system (because from a RF point of view, the electrolyte behavior become closer to a dielectric). On the other hand, a high conductivity electrolyte will lower the response time of the fluidic actuation, at the detriment of the radiation propagation efficiency inside the system (by making the electrolyte further diverting away from a dielectric behavior).

Finally, since we're going to make Galinstan circulate inside channels, we need to ensure that the surface state of the channels is as good as possible, in order to facilitate the displacement of the metal slug inside it. This is illustrated in [13][35] & [48], where they've coated the channels with Teflon in order to minimize the energy losses due to the contact between them and the Galinstan, the Teflon coating allowing the channel surface to stay as hydrophobic as possible. Other solutions to minimize the friction forces could include the use of channel's fabrication technologies which don't deteriorate excessively the surface state of the channels, such as laser engraving, hot embossing, injection molding etc., as opposed to more "aggressive" technologies like micro-machining for example. Given that we're going to work with the COC/COP polymer to fabricate our fluidic system, we will be able to investigate the impact of each of these fabrications on that material, which is also naturally hydrophobic.

V. Bibliography

- [1] Y.-J. Ren and C.-P. Lai, "Wideband Antennas for Modern Radar Systems," G. B. T.-R. T. Kouemou, Ed. Rijeka: InTech, 2010, p. Ch. 17.
- [2] Zeon corporation, "ZEONEX® - Cyclo Olefin Polymer (COP)," Tokyo, 2016.
- [3] A. Glise, "Application des Cyclo-Oléfine Polymère et Copolymère (COP/COC) pour la mise en œuvre de microsytèmes communicants autonomes et des capteurs associés," *Univ. Bretagne Occident. Brest*, 2015.
- [4] Dow Corning, "Sylgard ® 184 Silicone Elastomer," 2014.
- [5] P. Y. Cresson *et al.*, "1 to 220 GHz complex permittivity behavior of flexible polydimethylsiloxane substrate," *IEEE Microw. Wirel. Components Lett.*, vol. 24, no. 4, pp. 278–280, 2014.
- [6] S. D. Sheet, G. Medical, A. G. Fahrenheitstra, and G. Telephon, "Safety Data Sheet acc , to Guideline 93 / 112 / EC Safety Data Sheet acc , to Guideline 93 / 112 EC," *Direct*, pp. 2004–2007, 2004.
- [7] T. Liu, P. Sen, and C. Kim, "Characterization of nontoxic liquid-metal alloy galinstan for applications in microdevices," ... *Syst. J.*, vol. 21, no. 2, pp. 443–450, 2012.
- [8] R. Zhang, M. Hodes, N. Lower, and R. Wilcoxon, "High heat flux, single-phase microchannel cooling," *2014 Semicond. Therm. Meas. Manag. Symp.*, pp. 1–7, Mar. 2014.
- [9] A. Traille, S. Bouaziz, S. Pinon, P. Pons, H. Aubert, and A. Boukabache, "A Wireless Passive RCS-based Temperature Sensor using Liquid Metal and Microfluidics Technologies," *Eur. Microw. Conf.*, no. October, pp. 45–48, 2011.
- [10] T. Alboussiere, P. Cardin, F. Debray, P. La Rizza, J.-P. Masson, F. Plunian, A. Ribeiro, and D. Schmitt, "Experimental evidence of Alfvén wave propagation in a Gallium alloy," *arxiv*, p. 19, Jun. 2011.
- [11] S. K. T. Ravindran, M. Roulet, T. Huesgen, M. Kroener, and P. Woias, "Performance improvement of a micro thermomechanical generator by incorporating Galinstan® micro droplet arrays," *J. Micromechanics Microengineering*, vol. 22, no. 9, p. 94002, Sep. 2012.
- [12] S. Cheng, Z. Wu, P. Hallbjörner, K. Hjort, and A. Rydberg, "Foldable and stretchable liquid metal planar inverted cone antenna," *IEEE Trans. Antennas Propag.*, vol. 57, no. 12, pp. 3765–3771, 2009.
- [13] C. H. Chen and D. Peroulis, "Liquid RF MEMS wideband reflective and absorptive switches," *IEEE Trans. Microw. Theory Tech.*, vol. 55, no. 12, pp. 2919–2929, 2007.

- [14] M. R. Khan, "Engineering the Yield Properties of the Oxide Skin on a Liquid Metal Alloy," 2011.
- [15] L. Cademartiri, M. M. Thuo, C. A. Nijhuis, W. F. Reus, S. Tricard, J. R. Barber, R. N. S. Sodhi, P. Brodersen, C. Kim, R. C. Chiechi, and G. M. Whitesides, "Electrical Resistance of $\text{Ag}^{\text{TS}}-\text{S}(\text{CH}_2)_{n-1}\text{CH}_3//\text{Ga}_2\text{O}_3/\text{EGaIn}$ Tunneling Junctions," *J. Phys. Chem. C*, vol. 116, no. 20, pp. 10848–10860, 2012.
- [16] M. R. Khan, C. B. Eaker, E. F. Bowden, and M. D. Dickey, "Giant and switchable surface activity of liquid metal via surface oxidation.," *Proc. Natl. Acad. Sci. U. S. A.*, vol. 111, no. 39, pp. 14047–51, Sep. 2014.
- [17] M. D. Dickey, "Emerging applications of liquid metals featuring surface oxides," *ACS Appl. Mater. Interfaces*, vol. 6, no. 21, pp. 18369–18379, 2014.
- [18] R. C. Gough, A. M. Morishita, J. H. Dang, M. R. Moorefield, W. A. Shiroma, and A. T. Ohta, "Rapid electrocapillary deformation of liquid metal with reversible shape retention," *Micro Nano Syst. Lett.*, vol. 3, no. 4, pp. 1–9, 2015.
- [19] M. Wang, C. Trlica, M. R. Khan, M. D. Dickey, and J. J. Adams, "A reconfigurable liquid metal antenna driven by electrochemically controlled capillarity," *J. Appl. Phys.*, vol. 117, no. 19, p. 194901, 2015.
- [20] C. Kitamura and A. Morishita, "A liquid-metal reconfigurable Yagi-Uda monopole array," ... *Dig. (IMS), 2013 ...*, pp. 65–67, 2013.
- [21] D. R. López, "Reconfigurable pixel antennas for communications," Universitat Politecnica de Catalunya (UPC), 2013.
- [22] A. M. Morishita, R. C. Gough, J. H. Dang, A. T. Ohta, and W. a. Shiroma, "A liquid-metal reconfigurable log-periodic balun," *2014 IEEE MTT-S Int. Microw. Symp.*, no. 1, pp. 1–3, Jun. 2014.
- [23] A. Morishita, C. Kitamura, A. Ohta, and W. Shiroma, "A Liquid-Metal Monopole Array With Tunable Frequency, Gain, and Beam Steering," *IEEE Antennas Wirel. Propag. Lett.*, vol. 12, pp. 1388–1391, 2013.
- [24] D. Rodrigo, S. Member, L. Jofre, and B. A. Cetiner, "Circular Beam-Steering Reconfigurable Antenna With Liquid Metal parasitic," *IEEE Trans. Antennas Propag.*, vol. 60, no. 4, pp. 1796–1802, 2012.
- [25] Bartels Mikrotechnik GmbH, "Bartels Micropumps," Dortmund, Germany, 2016.
- [26] S.-Y. Tang, K. Khoshmanesh, V. Sivan, P. Petersen, A. P. O'Mullane, D. Abbott, A. Mitchell, and K. Kalantar-Zadeh, "Liquid metal enabled pump.," *Proc. Natl. Acad. Sci. U. S. A.*, vol. 111, no. 9, pp. 3304–9, 2014.
- [27] O. O. Osman, H. Shintaku, and S. Kawano, "Development of micro-vibrating flow pumps using MEMS technologies," *Microfluid. Nanofluidics*, vol. 13, no. 5, pp. 703–713, May 2012.

- [28] M. Du, X. Ye, K. Wu, and Z. Zhou, "A peristaltic micro pump driven by a rotating motor with magnetically attracted steel balls.," *Sensors (Basel)*, vol. 9, no. 4, pp. 2611–20, Jan. 2009.
- [29] W. Irshad and D. Peroulis, "A silicon-based galinstan magnetohydrodynamic pump," ... *9th Int. Work. ...*, pp. 127–129, 2009.
- [30] E. Gedik, H. Kurt, and Z. Recebli, "CFD Simulation of Magnetohydrodynamic Flow of a Liquid-Metal Galinstan Fluid in Circular Pipes," *FDMP Fluid Dyn. Mater. ...*, vol. 9, no. 1, pp. 23–33, 2013.
- [31] R. Wilcoxon, N. Lower, and D. Dlouhy, "A compliant thermal spreader with internal liquid metal cooling channels," *Annu. IEEE Semicond. Therm. Meas. Manag. Symp.*, no. Lm, pp. 210–216, 2010.
- [32] O. Faitas and O. Matviykov, "Simulation of liquid thermal expansion effect for wireless passive microfluidic temperature sensor," in *2014 20th International Conference on Microwaves, Radar and Wireless Communications, MIKON 2014*, 2014.
- [33] S. Pottigari and J. Kwon, "An ultra wide range MEMS variable capacitor with a liquid metal," *Device Res. Conf. 2008*, no. 4, pp. 153–154, 2008.
- [34] M. Hodes, R. Zhang, L. S. Lam, R. Wilcoxon, and N. Lower, "On the potential of galinstan-based minichannel and minigap cooling," *IEEE Trans. Components, Packag. Manuf. Technol.*, vol. 4, no. 1, pp. 46–56, 2014.
- [35] H. Lee and C. Kim, "Surface-tension-driven microactuation based on continuous electrowetting," *Microelectromechanical Syst. J.*, vol. 9, no. 2, pp. 171–180, 2000.
- [36] R. Gough, A. Morishita, J. Dang, and W. Hu, "Continuous Electrowetting of Non-Toxic Liquid Metal for RF Applications," *IEEE access*, vol. 2, pp. 874–882, 2014.
- [37] R. C. Gough, J. H. Dang, A. M. Morishita, A. T. Ohta, and W. a. Shiroma, "Frequency-tunable slot antenna using continuous electrowetting of liquid metal," *2014 IEEE MTT-S Int. Microw. Symp.*, pp. 1–4, Jun. 2014.
- [38] S. C. Yee, "A Frequency Reconfigurable Circularly Polarized Microstrip Patch Antenna Using Liquid Metal Microswitches," United States Naval Academy, 2011 L, 2013.
- [39] Y. Damgaci and B. a Cetiner, "A frequency reconfigurable antenna based on digital microfluidics.," *Lab Chip*, vol. 13, no. 15, pp. 2883–7, 2013.
- [40] E. Cagatay, "Design, fabrication and characterization of liquid solid microelectromechanical switches," Bilkent university, 2012.
- [41] C. V. Sternling and L. E. Scriven, "Interfacial turbulence: Hydrodynamic instability and the marangoni effect," *AIChE J.*, vol. 5, no. 4, pp. 514–523, 1959.
- [42] S.-Y. Tang, Y. Lin, I. Joshipura, K. Khoshmanesh, and M. Dickey, "Steering Liquid Metal Flow in Microchannels using Low Voltages," *Lab Chip*, vol. 15, pp. 3905–3911, 2015.

- [43] D. Juncker, “Capillary Microfluidic Systems for Bio / Chemistry,” *Scientist*, p. 97, 2002.
- [44] B. Zhmud, F. Tiberg, and K. Hallstensson, “Dynamics of Capillary Rise.,” *J. Colloid Interface Sci.*, vol. 228, no. 2, pp. 263–269, 2000.
- [45] K. S. Birdi, D. T. Vu, a. Winter, and a. Nørregård, “Capillary rise of liquids in rectangular tubings,” *Colloid Polym. Sci.*, vol. 266, pp. 470–474, 1988.
- [46] M. A. H. Khondoker and D. Sameoto, “Fabrication methods and applications of microstructured gallium based liquid metal alloys,” *Smart Mater. Struct.*, vol. 25, no. 9, p. 93001, 2016.
- [47] B. Zhang, Q. Dong, C. E. Korman, Z. Li, and M. E. Zaghoul, “Flexible packaging of solid-state integrated circuit chips with elastomeric microfluidics,” *Sci. Rep.*, vol. 3, pp. 1–8, Jan. 2013.
- [48] A. Zavabeti, T. Daeneke, A. F. Chrimes, A. P. O’Mullane, J. Zhen Ou, A. Mitchell, K. Khoshmanesh, and K. Kalantar-zadeh, “Ionic imbalance induced self-propulsion of liquid metals,” *Nat. Commun.*, vol. 7, no. May, p. 12402, 2016.
- [49] S.-Y. Tang, V. Sivan, K. Khoshmanesh, A. P. O’Mullane, X. Tang, B. Gol, N. Eshtiaghi, F. Lieder, P. Petersen, A. Mitchell, and K. Kalantar-zadeh, “Electrochemically induced actuation of liquid metal marbles,” *Nanoscale*, vol. 5, no. 13, pp. 5949–5957, 2013.

Chapter 2 : System's design

I. Singled out technological solutions

As we saw on chapter one, we can already lay down the first design guidelines of our antenna system:

- Should allow beam steering on 360 degrees
- Should use microfluidic technologies to guide liquid metal
- Should adopt an omnidirectional central antenna based architecture
- Should use that liquid metal to steer the beam of a central antenna
- Should use Galinstan for the liquid metal because of its non toxicity
- Should be designed to work in the GHz band (at 5GHz more precisely)
- Should be made of COC/COP because of the good dielectric properties of this polymer ($\epsilon_r = 2,3$, $\tan \delta = 3.10^{-4}$ at 1 GHz [1]) and the fact that we master its fabrication and processing in our laboratory.

Based on these guidelines, there is a number of solutions to displace the Galinstan which exist in the literature. We tried in the first chapter to single out one of these technologies based on four key parameters defined at the beginning of the manuscript, these criteria being: the response time of the system, the power consumption, the electromagnetic (EM) performances and the overall cost of the system. By narrowing of the range of available technologies capable of answering to that objective through bibliographic study, we can say that two technological solutions really emerged:

- Continuous Electro-Wetting / Dynamic Electro-Wetting (CEW/DEW)
- Electro-Chemical Actuation (ECA)

These two solutions are we think the most appropriate because of series of reasons:

- Based on an electrochemical phenomenon
- Simple system, requiring a simple command
- Very good miniaturization perspectives
- Relatively high speed
- Low power consumption
- Low volume consumption for the technology implementation
- Electrical only command (easy to integrate in a RF system)

- Are compatible with the use of COC/COP fluidic chips

We choose to retain two and not one because these two technologies are extremely close in terms of material requirements, the main difference between them being basically the sign of the applied electrical potential needed for the actuation. It must be noted that the second one have the particularity to work specifically with the Galinstan, being based on an electrochemical reaction and the creation of an oxide layer along the surface of the Galinstan droplet, oxide layer acting as a surfactant.

II. Choice among the technological solutions

As we said above, we settled at the beginning for an architecture based on a central antenna, surrounded by a number of elements on each side of it. These elements will be the fluidic circuit of our system, and will be made of liquid metal, specifically Galinstan in our device. The architecture of the antenna will be the architecture of a Yagi-Uda antenna, as described in [2], where are described the design guidelines for such antennas. These rules are rather simple, and state that:

- The length of the reflectors L_R should be of $0.51 \lambda_{EFF}$ ($>0.5 \lambda_{EFF}$)
- The length of the directors L_D should be $0.41 \lambda_{EFF}$ ($<0.5 \lambda_{EFF}$)
- The spacing of the directors S_D should be of $0.3 \lambda_{EFF}$ (min $0.3 \lambda_{EFF}$)
- The spacing of the reflector and the feed S_{RF} should be $0.25 \lambda_{EFF}$
- The spacing between the director and the feed S_{DF} should be $0.3 \lambda_{EFF}$ (min $0.3 \lambda_{EFF}$)
- The diameter of the reflectors & the directors D should be inferior to $0.024 \lambda_{EFF}$

The Yagi-Uda architecture is build around a central omnidirectional antenna, usually a dipole or a monopole, around which is disposed a number of directors and reflectors (called parasitic elements in [3]), as we can see on the schematic example of figure 1) bellow. The Yagi-Uda architecture has been chosen because it is a simple architecture which separate the feed antenna from the rest of the elements, making it easier for us to compartment the system, which is imperative since we're using a liquid metal inside a liquid electrolyte. The following figure 23) shows an example of a 3+1 dipole Yagi-Uda antenna system.

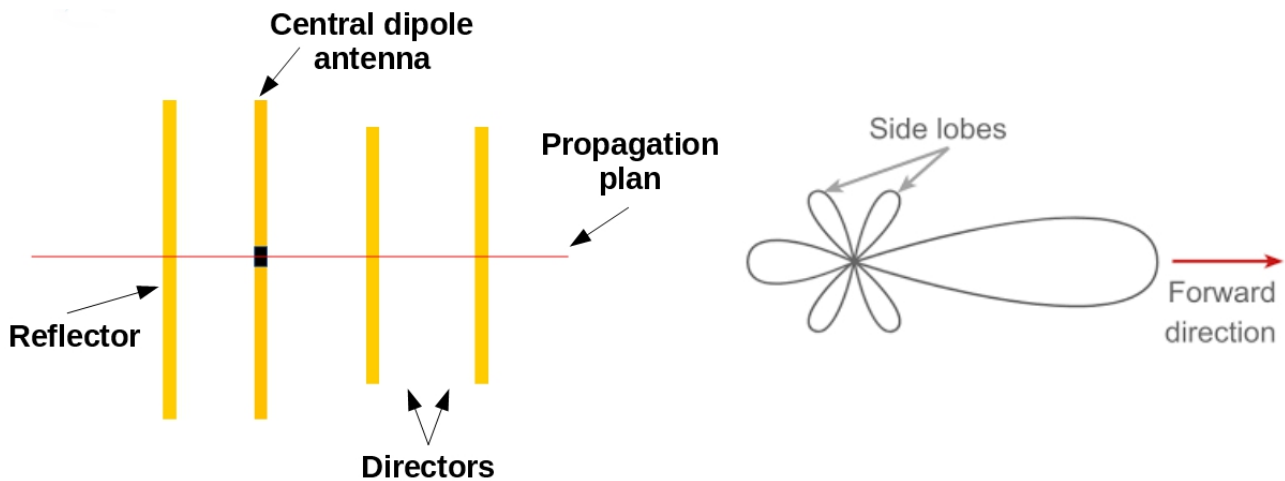


Figure 23 : Schematic example of a 3+1 dipole Yagi-Uda antenna (left) and an example of its typical radiation pattern (right)

As we can see here on figure 23) we have a dipole Yagi-Uda antenna, with two directors and one reflector. This makes therefore 3 parasitic elements for 1 central feed elements, hence the “3+1” designation. Only the central antenna is fed electrically, the parasitic elements only act as reflector (left on figure 23)) and directors (right on figure 23)) of the field generated by the central antenna. The resulting beam is inside the horizontal propagation plan indicated on the figure, and is directed toward the right, in the direction of the 2 directors.

Placed at a certain distance of it, the reflector is reflecting the incident beam coming from the feed antenna towards that same antenna and the directors, which in turn are channeling the incident beam away from the feed antenna (towards the right of figure 23)). Therefore the resulting beam is oriented along the alignment of reflectors and directors, and channeled towards the direction of the directors with a directivity depending on the characteristics of the system, namely the number of director & reflectors as well as their geometric parameters (length, position, spacing...).

More precisely, the number of parasitic elements in the antenna is going to determine how directive the antenna is going to be, as stated in [2]. The number of reflectors impact the efficiency of the reflection, and it is the same thing for the number of directors, which impact the narrowness of the resulting beam. It is important to note that the total number of elements is the result of a trade-off between the efficiency between the directivity of the antenna and size compatible with the application targeted (in our case an autonomous system). As it is stated in [2], the 3+1 architecture is the best compromise in terms of size and performances for a unidirectional antenna, which is the reason why we chose that architecture. In this case, by applying the rules cited above, the size of the system shown in figure 1) is: $2 * 0.3 * \lambda_{EFF} + 0.25 * \lambda_{EFF} = 0.85 * \lambda_{EFF}$. We can see that the operating frequency and the material in which will be made (responsible fro the value of λ_{EFF}) the system will have an overwhelming influence on the size of the device.

As we explained above, the principle of the Yagi-Uda antenna is rather simple. The central antenna's beam is omnidirectional and its beam channeled through the parasitic elements. The main criteria we set for the choice of the design of the antenna are the following:

- For practical reasons it has been chosen to use a dipole for the central antenna.
 - Indeed, a monopole based Yagi-Uda architecture imposes us to connect the ground plane to the parasitic elements, as it is shown in [4][5][6] & [7]. This is a problem for us because we choose to use a liquid metal, Galinstan, and a displacement technology based on electro-wetting, which uses extensively an electrolyte. From these two characteristics arise the problem of the prolonged contact and subsequent degradation of the ground plane (usually made of copper or similar material) with the electrolyte (which is usually very acidic or basic), as well as the contact of that same ground plane with Galinstan itself, which is an eutectic alloy, as this was diagnosed as a potential problem in [8][9] & [10]. These problems of degradation are occurring under the separate action of each of these two components of our system on the ground plane, and are even more acute if actions of these two components are combined. Therefore, this would render the system difficult to realize.
 - On the contrary, for dipoles, we do not need to connect the parasitic elements to the ground plane, because there is no need for a ground plane. Therefore, the fluidic circuit playing the role of the parasitic elements can easily be completely sealed, which voids the problematic of the ground plane degradation. Remains the problematic of the electrodes potential degradation, but leads of solutions can be found in the literature, as already explained in chapter one.
- The polarization of the antenna is going to have a decisive impact the design of the antenna.
 - Indeed, if we built a horizontally polarized antenna system, then the parasitic elements are going to be inside the propagation plan, as it is the case in figure 25), extracted from [11]. Therefore the maximum height of the device (antenna+parasitic elements) will be dictated by the height of the substrate on which is the antenna system + the height of the taller element of the system, either the parasitic elements, as it is the case in [11] (but where that height is very low), or the antenna. Therefore, having a low profile antenna is interesting in order to have a system which is also low profile, as in [12][13] & [14] because the height of the antenna can be easily dominant, as it would be the case with the use of the antennas presented in [15][16] or [17]
 - On the other hand, if we built a vertically polarized antenna system, then the parasitic elements are perpendicular to the propagating plan, as it is the case in figure 25). Therefore, since we know from [2] that the taller element is the reflector, with $L_{REF} > 0.5\lambda_{EFF}$, and that the theoretical dipole antenna length is $0.5\lambda_{EFF}$, then we know that the height of the system is determined by the length of the reflector, and therefore by the operating frequency and the material of the system. Since the system is poised to have an important height, we should try to take advantage of that volume and have a bottom fed antenna which design is the closest possible from its theoretical design, in order to maximize the EM performances of the whole system.
- The feeding of the antenna must imperatively be from the bottom of it, ideally with a coax cable. Indeed, since we want to achieve a 360 degree beam steering, we must have a central

antenna which have of course an omnidirectional radiation pattern, but also having the surroundings of the antenna not blocked by any feed line, as it is the case in [12]. The reason is that would result in creation of a blind spot in the beam steering domain of the antenna, especially if the antenna is as in [11][12][13] & [18].

So we could sum-up by saying that we will need to have a dipole based central antenna design, bottom fed through coaxial cable and with a polarization (either vertical, either horizontal) which will be determining of the general architecture of the whole system design.

1) Horizontally polarized Yagi-Uda antenna

We could see above in figure 23) an example of a vertically polarized antenna (if we consider the propagation plan to be horizontal), which is the most practical polarization for us to use a Yagi-Uda antenna. Indeed, if we chose a vertical antenna like the example presented bellow on figure 24), we can see that we will very quickly be limited by the surface area occupied by the device and that the resulting device will not be able to perform a true 360 degree beam steering.

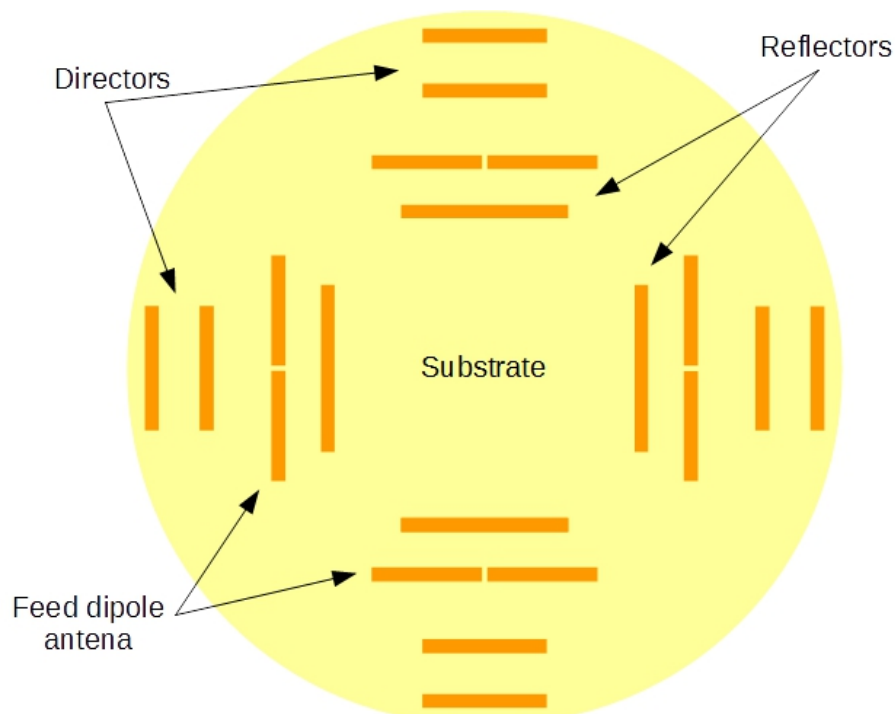


Figure 24 : Horizontally polarized planar Yagi-Uda antenna

Therefore, in order to choose the best possible antenna for our system, we should also look at horizontally polarized antenna which are not based on the same kind of Yagi-Uda architecture presented on figure 23) & 24). The antenna system presented in figure 25) bellow use a different architecture and shows an example from the literature of a liquid metal based horizontally polarized antenna capable in theory of a 360° beam steering & which has a more optimized use if the available surface:

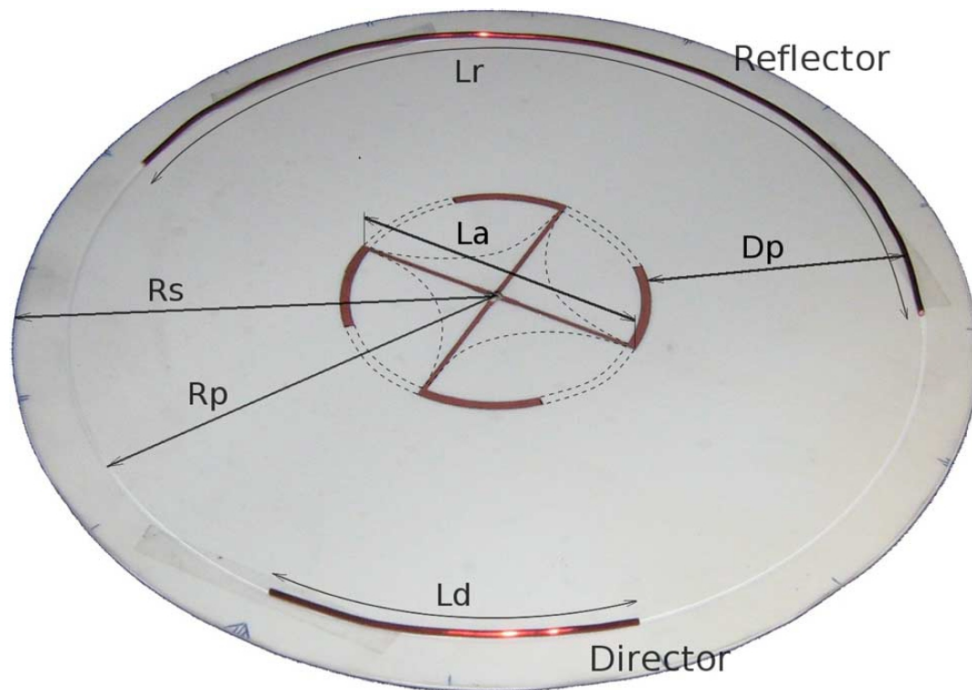


Figure 25 : [11] 2+1 Yagi-Uda based antenna made of an Alford-loop inspired low profile dipole antenna surrounded by copper parasitic elements

In the example above, we have a 2+1 Yagi-Uda based antenna made of a central Alford-loop inspired low profile dipole antenna combined with one reflector and one director made of copper wire inside plastic tubing. The reason for the use of copper is because this system is just a proof of concept of the one presented next, on figure 26). Since the system works at 1.8 GHz we have $\lambda_0 = 166$ mm and for reasons detailed in [11], the diameter of the dipole element, L_a , is $0.35 \lambda_0$ which gives $L_a = 58.5$ mm. The antenna is realized on a substrate with a dielectric constant of $\epsilon_R = 1.41$, which gives λ_{EFF} 140 mm. Given the constraint of having only one tubing loop, the reflection and the director are placed at the same distance D_p from the antenna, with $D_p = 0.3 \lambda_0$ and $\lambda_0 = 50.75$ mm. Finally we have the director (L_d) and the reflector (L_r) length, respectively of $L_d = 0.45 \lambda_{EFF}$ and $L_r = 1.5 \lambda_{EFF}$ (because the reflector is operating at his second resonance). While these distances are not exactly fitting the rules established for the design of such antennas, as we have seen in the paragraph above, this is an acceptable compromise in order to simplify the system by reducing the number of tubing loop and the size of the system.

The example depicted above is also very interesting because it shows an example with copper parasitic of a structure which is designed to use mercury and a mechanical pump for the displacement of that mercury inside the channel, as we can see on figure 26):

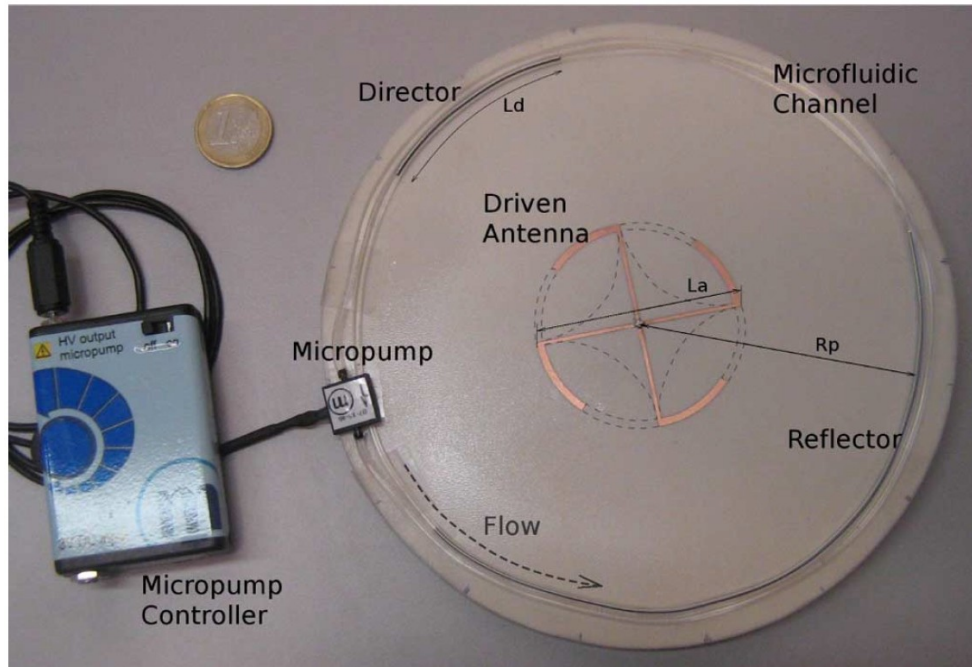


Figure 26 : [11] Yagi-Uda based antenna made of an Alford-loop inspired low profile dipole antenna surrounded by mercury parasitic elements inside a water filled plastic tube actuated by a mechanical micro-pump

In this figure we see the micro-pump driving the motion of the liquid metal inside the plastic channel and therefore realizing wide beam steering, with the constraint already shown in chapter I of the maximum angle allowed for such a system.

That being said, we could imagine combining this antenna design with the CEW or ECA technologies, as it is shown in [19] & [20] for the first one or as in [21] & [22] for the second one, and obtain a planar antenna system capable of an electrically controlled 360° beam steering, so without the angular limitation of the pump system presented above. If we imagine a system in which the metal slugs travel inside slick channels, the main drawback of such a system would be that it would be difficult to precisely control the position of the metal slugs inside the channel, especially during the movement, to prevent them to collide and merge, which would severely degrade the system's response.

An immediate upgrade could consist into applying the same architecture as presented in [20] for the driving of the micro-motor presented there. By having multiple electrodes evenly distributed along the channel, we could rather precisely control the position of the slugs and prevent them to merge as long as the power is on. Figure 27) bellow shows an example of a realization of such micro-motor:

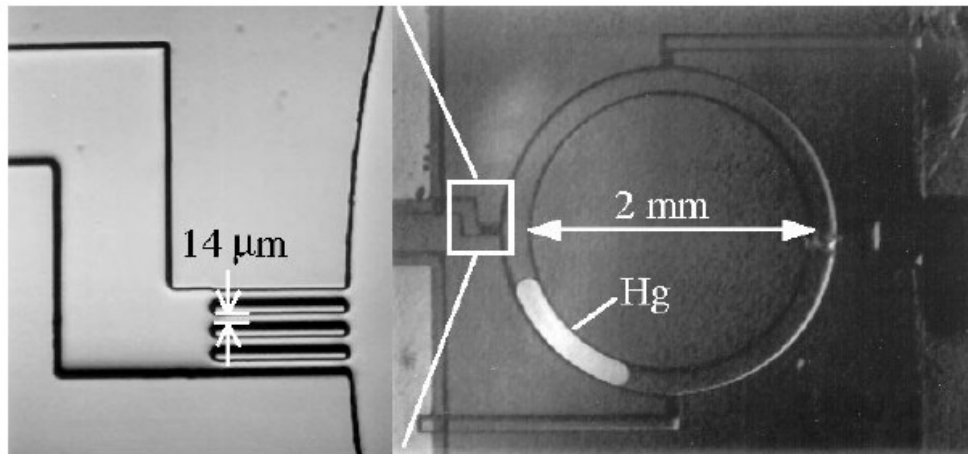


Figure 27 : [20] Picture of the micro-motor view from the top (right), with a detailed view of the Mercury filter (left)

As we can see, between each couple of electrodes, we have enough control on the slug's position. The choice of such architecture means we choose the CEW actuation method, even if the ECA is still usable, but most likely at the detriment of the operation speed. This figure also shows us a detail of the electrodes implantation on such system, which is important regarding the degradation problem underlined in [8] & [9] for example. The solution consist in separating the electrodes from the metal slug by having a "filter" separating the liquid metal from the electrodes but allowing the electrolyte to flow from them to the metal slug.

While the addition of electrodes as presented above would help to improve the controllability of the liquid metal position inside our device, this controllability stops when the power is shut off. This could be a problem, especially for nomad devices, where the power is a limited commodity and we cannot afford to let the system run continuously, we can think of autonomous sensors networks for example. This would mean that the function our system is supposed to perform is not done if the power is off.

If controllability of the position is a greater importance than the operation cost in terms of power, one solution could be find by the addition of the kind of channel design presented in [19]. This mean shifting from CEW and ECA actuation method to DEW actuation. In this case the ECA method will most likely not work, because relying primarily on capillary effect, effect contradicted by the intricated chambers design of the new channel. The design of such channels was presented in chapter one, and consist of the substitution of a serrated channel to a slick channel. This would allows the overcoming of that problem, by restricting the number of fixed position possible and increasing the operating power consumption, because it would be more difficult to dislodge the slug from its initial position and make it move to another chamber of the channel.

A sketch of such a system, combining the low-profile Alford loop antenna inserted inside a 2+1 Yagi-Uda system and a serrated channel for the DEW actuation method, which has been designed by us to be realized in COP, can be found in figure 28) bellow, with different views of the system:

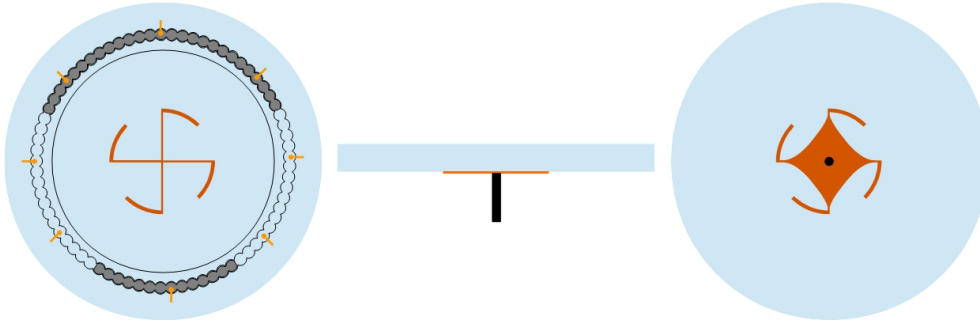


Figure 28 : Schematic views (from left to right: top, side and bottom view) of a horizontally polarized Yagi-Uda based fluidic antenna system

As we can see the figure above is depicting a full low profile horizontal fluidic 2+1 elements Alford-loop based Yagi-Uda antenna system capable of controllable beam directivity and 360° degree beam steering. It is composed of a COP planar disc at the center of which is positioned the Alford-loop antenna on the top face, with its balun on the bottom face, surrounded by an electrolyte filled circular channel, in which sit two Galinstan slugs serving as the parasitic elements of the Yagi-Uda system. The system is bottom fed through a coaxial cable. This sketch also shows us that the system is really a low profile system for the vertical direction, but that it is a rather large one. We see that the maximum height of the system is determined by the height of the channel, which is embedded in the COP substrate ($\epsilon_R = 2,3$: $\tan \delta = 5 \cdot 10^{-4}$ at 1 GHz [1]), and the thickness of the COP layer between the two part of the Alford-loop antenna. This represent a few millimeters. In terms of dimensions, for an operating frequency in the gigahertz band of 5 GHz and by taking a channel width of 1 mm, we have a diameter of the system D_{SYSTEM} from the external wall of the channel to the external wall of the channel of 41mm. As a reminder we have the following rule which can be extracted from [11]:

$$D_{SYSTEM} = 2 * D_{CHANNEL} + L_a + 2 * D_p = 2 * D_{CHANNEL} + 0.95 \lambda_0 \quad (10)$$

Where L_a is the diameter of the Alford loop antenna at $0.35 \lambda_0$, $D_{CHANNEL}$ the diameter of the channel and D_p the distance between the parasitic elements and the central antenna at $0.3 \lambda_0$. This distance of $0.3 \lambda_0$ represents a compromise in the Yagi-Uda antenna's design rule presented in [2], and is an averaged value of the distance between the director and the central antenna and the distance between the reflector and that same central antenna. These distances are normally different, but given that we only have one channel, we need to do otherwise. Also given that the channel diameter is going to be between one and two order of magnitudes smaller than the wavelength, we could approximate in order to compare our system to other that D_{SYSTEM} is equal to $0.95 \lambda_0$.

To that D_{SYSTEM} diameter we need to add the space to place the electrodes, which will be contacting the channel, as well as the command and control electronics. So we can estimate the final system dimensions in such way that it would fit in the worst case in a cylinder with a maximum diameter of 60mm for a maximum height of 20mm.

These dimensions are bigger than the ones of the antenna showed in figure 23), but it is because the antenna in this figure is only unidirectional. It is relatively difficult to compare the dimensions of these two antennas, given the Alford-loop architecture chosen above. What we could say is that

comparatively to the theoretical wire dipole architecture of the figure 23), the Alford-loop based architecture is going to be larger at a given frequency.

The reason for it lies in the fact that we have to account for the central Alford-loop antenna length, L_a , when on the classic vertical dipole Yagi-Uda configuration, the diameter of the central dipole is comparatively very small.

The second point about the dimensions of the system presented in figure 28) is that we compromise on the design rules by fitting the 2 parasitic elements inside one single channel is costing us again directivity and antenna efficiency. These two choices, the 2+1 architecture and the unique tube loop have for consequence a reduction of the size of the antenna, but at the cost of degraded RF performances.

A possible drawback, mentioned earlier, of this system would be that once the configuration of the Yagi-Uda antenna would be set it would be very difficult to change this configuration. If we take the configuration proposed in [3] & [11] or on figure 28) for example, with a 2+1 elements Yagi-Uda antenna (one director, one reflector & one feed antenna), it would be very difficult to change this configuration, to let's say a 4 parasitic elements, 4 directors for example.

Though, by using the technology shown in [23], and with the serrated channel design of the DEW method [4], it might be possible to partly overcome this limitation. But we will need to drastically enhance the number of electrodes inside the channel as shown in figure 29), to be able to manipulate the droplet with enough precision.

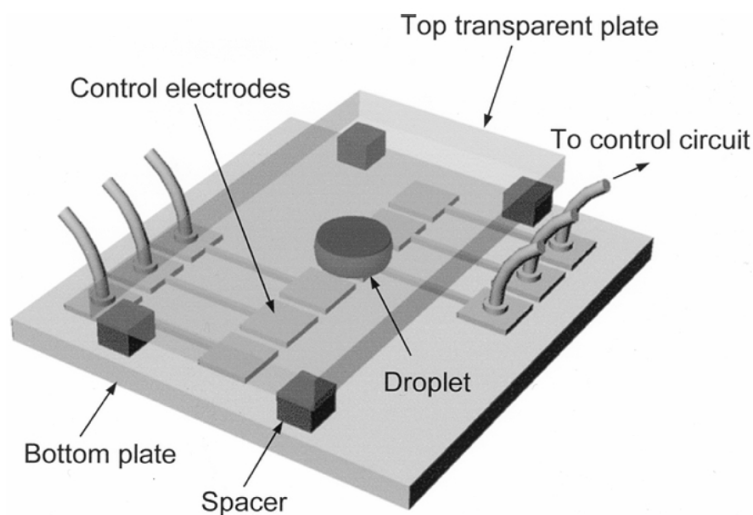


Figure 29 : [23] Illustration of an example of a drop manipulation device based on EWOD displacement method

As we see in the figure 29) above, we need to have the bottom of the channel paved with electrodes, coated with a layer of dielectric (not visible on the figure), which are necessary in order to control efficiently the droplets position and size. The complexity of this system is evident, the high number of electrodes and their closeness make the system potentially difficult to realize. Therefore, while technically feasible, the use of this technology of droplet manipulation inside our system would render it increasingly complex, and would add an additional architecture of command. It must be

noted that if we were to add the technology presented in [23] by Cho et al. we would have a wider system because of the addition of all the command part of the droplets manipulating system.

The fact is that even with this technology, the amount of liquid metal inside the channel initially present cannot vary, we cannot have more or less of it inside, which limits the number of possible configurations possible. Therefore the adaptability of the system is inherently limited by the first configuration installed, which could be a problem for certain applications where the mission is susceptible to change rapidly and often.

We should also consider the impact of the presence of electrolyte inside the antenna as in [11], where they had to take into account the losses due to the water.

Finally, we also need to point out that given the system is working in the horizontal plane, it is more subject to vibrations and mechanical movements which might disturb the position of the droplets inside the channels or render it inoperable if tilted on one side for example.

2) Vertically polarized antenna

We saw above an example with a horizontally polarized antenna. Now, if we take a vertically polarized antenna, and if we design our system according to the guidelines and constraints that we have managed to gather from [2], the design must be as close as possible of the one presented on figure 23), a centrally fed dipole antenna and vertical parasitic elements (needed to interact with the beam of the vertically polarized antenna).

Since we need to conjugate the Yagi-Uda design and the microfluidic technology, based on that architecture, it means we need to replace the parasitic elements by vertical fluidic channels, like in [24]. If we apply this rule to the design presented in figure 23), we obtain the design of figure 30) below:

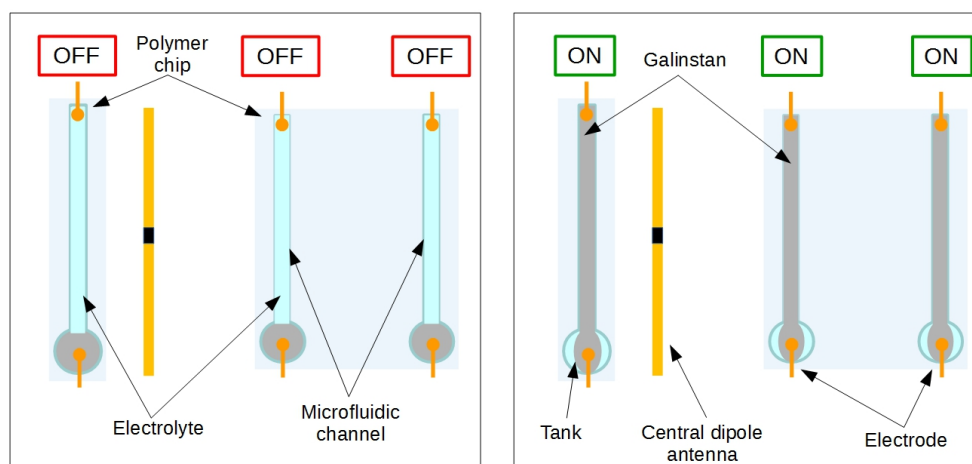


Figure 30 : Concept of a vertical fluidic Yagi-Uda based antenna system with its two working phases, the "OFF" phase (left) the "ON" phase (right)

In this figure we see that vertical fluidic channels, embedded inside polymer made fluidic chips (in our case COP), replace the parasitic elements of the figure 23). We see that each channel is

equipped with electrodes, and that we can activate or deactivate the channels by switching ON or OFF the voltage between the electrodes. These channels are filled with a mix of liquid metal which sits in a tank at the bottom of them when the voltage is OFF, due to gravity, and a conductive electrolyte, which must also be acidic or basic, in order to be able to prevent the oxidation of the Galinstan, as explained in chapter 1. The phenomenon responsible for the rise of the metal can be, depending on the sign of the voltage, CEW (as in [19]) or ECA (as is [24]).

We have the following behavior for the system. If we are in OFF phase, the radiation diagram stays identical in shape to the diagram of stand alone sleeve (or coaxial) dipole antenna, which means an omnidirectional diagram. If we are in the ON phase, the radiation diagram becomes unidirectional. In the case of figure 30), it points towards the right of the figure, and has the aspect of a classic 3+1 elements Yagi-Uda antenna. We can therefore see that by switching ON or OFF fluidic columns and filling them on demand with liquid metal, we can alter significantly the radiation diagram of an omnidirectional antenna.

The design presented above is a simplified design, but if we want to achieve our objective of 360° degree beam steering, we need to be able to design an array of tunable elements in such way that by switching "ON" or "OFF" these elements we are able to make the beam rotate on the entirety of the horizon. Such a design would work as illustrated on the figure 31) bellow:

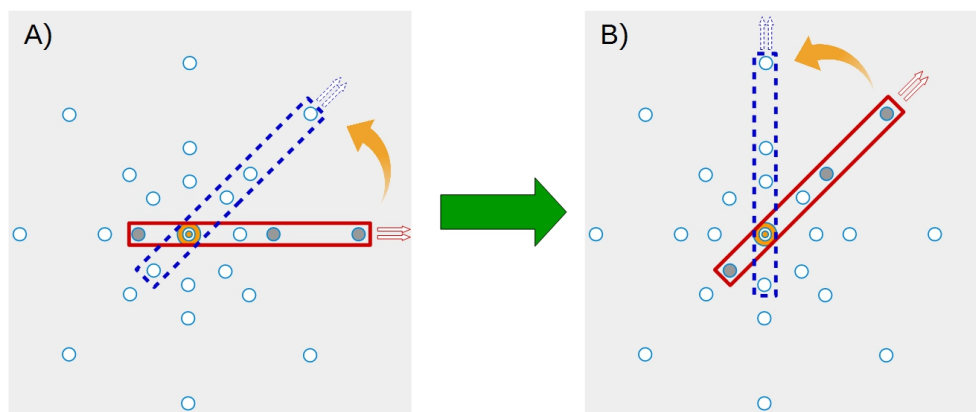


Figure 31 : Diagram depicting the architecture capable of a 360° beam steering based on the columns architecture as well as its working principle.

As we can see on this diagram, if we build an architecture where the channels used as parasitic elements are spread around three concentric circles (one circle for reflectors, one circle for first directors and one circle for second directors), we now have the ability to make the beam rotate with discrete steps, here wide of 45 degrees. The activation sequence is the following:

In A), the beam is focused along the columns alignment inside the red rectangle. This is our "active segment". The next step is to switch OFF this segment and switch ON the one figured by the dashed blue rectangle, at +45° above. This give us B), where the beam has been tilted +45° and is now focused again along the new red segment's direction. The next step is again to switch the beam +45° left by switching OFF the columns inside the red segment and switching ON the cones inside the new dashed blue segment.

By repeating the procedure the appropriate number of time (here eight times), we will come back to our starting point by having performed a 360° beam rotation, and by doing this continuously, we have the ability to perform a discrete 360° horizontal sweep. That sweep spatial resolution depends on the number of "segments" in the design. In this case we have 8 segments, therefore a resolution of 45° . Of course we can increase or decrease the width of the step by changing the number segments. But we can also perform various configurations, like switching OFF all columns, and therefore going back to an omnidirectional beam, or we can configure the column pattern to have whatever configuration required for a specific application.

The versatility of this system is specific to this architecture of discrete distribution of the liquid metal. We cannot achieve the same level of agility with the horizontally polarized central antenna, or at least not within the same area, the system would be considerably larger. Therefore this is a specific advantage to this system.

We decided to investigate more this kind of system because of the system potential in terms of agility. The next figure, figure 32), shows a side schematic view of a system we designed capable of performing the same tasks as presented on figure 31):

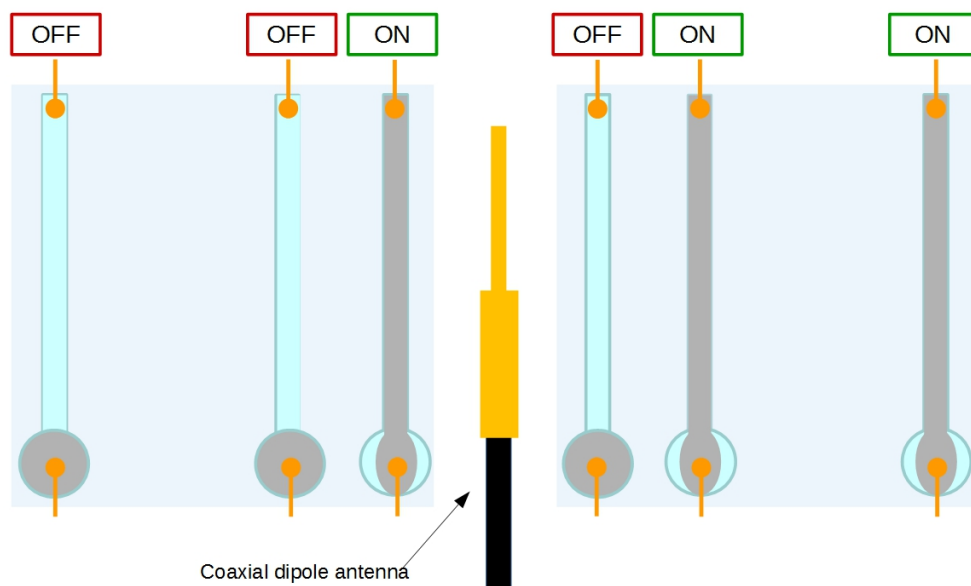


Figure 32 : Schematic sectional side view of a vertical Yagi-Uda based fluidic antenna system capable of a 360° beam steering with a coaxial dipole feed antenna.

On this drawing, we can see that the general layout is very similar to the architecture presented on figure 30), but combined with the columns distribution of figure 31). This explain why we have now 6 columns but only 3 "ON". The 3 "OFF" are the columns which will be switched "ON" when we will want to steer the beam 180° towards the left instead of the right, as it is the case on figure 32). The other main difference with the system of figure 30) is the central feed antenna. Indeed, in this design we use a coaxial dipole antenna, also called a sleeve antenna. The reason why we use this antenna is to fit the antenna requirements established earlier, in particular the bottom feeding of the antenna through a coax cable.

We can see on this figure that the whole fluidic system is also embedded inside the COP. The simplest geometry we can think for the COP substrate is a tube with very thick walls with the coaxial dipole antenna at the center and the channels of the fluidic systems drilled inside the walls, parallel to the central hole.

This antenna is a relatively old concept, and is explored in the literature, as in [25][26][27][28][29][30][31] & [32]. The base of the design is a derivative of a classic folded dipole architecture presented in [2], and on the figure 33) bellow:

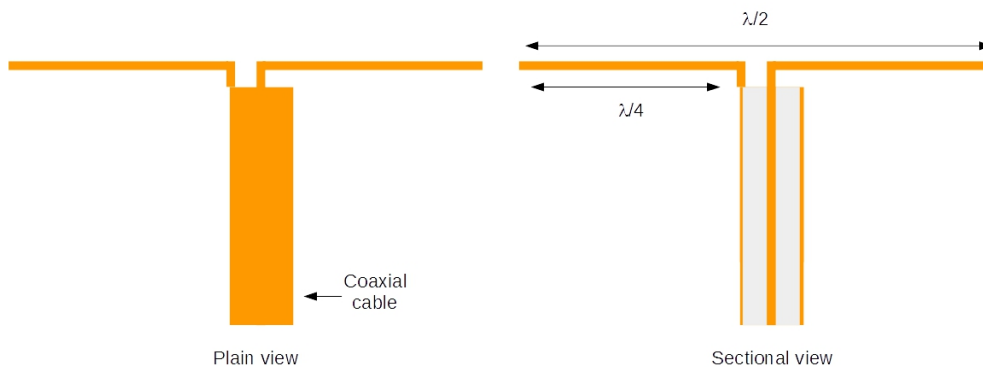


Figure 33 : Plain (left) and sectional (right) view of a folded half wave dipole antenna

As we can see on figure 33), the dipole antenna is made of two folded quarter wave length metallic rods, one of which is connected to the coax central conductor, the other to the coax outer conductor. The coaxial dipole antenna is simply this architecture, but modified, in such way that the rod connected to the outer coax conductor is folded 90° towards the bottom (parallel to the coax cable), and changed from a rod to a cylindrical metallic sleeve, as illustrated on the figure 34):

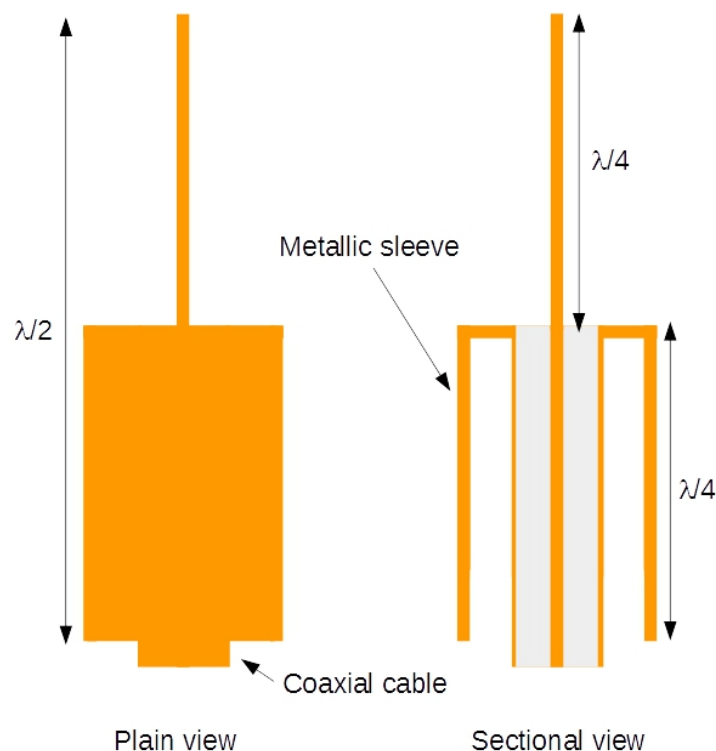


Figure 34 : Plain (left) and sectional (right) view of a sleeve dipole antenna

We see that the antenna is composed of one quarter wavelength metal rod connected to the central conductor of a coaxial cable and a quarter wavelength tall cylindrical metallic sleeve connected to the outer conductor of the same coaxial cable. We still have a dipole architecture, but which is now bottom fed (relatively to the direction of the antenna) through a coaxial cable, which was our requirement for the feed antenna of our Yagi-Uda system, as specified above. Of course, since we need mechanical support for the sleeve, the space between the sleeve and the coaxial cable can be filled with a solid material which will support the sleeve. A solution for the sleeve mechanical support could be to have a dielectric ring (most likely made of polymer) put around the coaxial cable, a ring which is then metallized and electrically connected to the outer coax, as shown in figure 35).

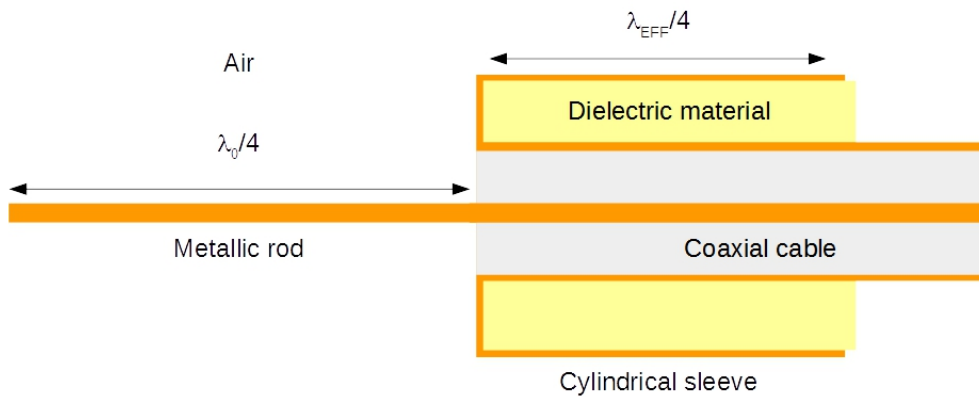


Figure 35 : Sectional side view of a sleeve dipole antenna with a sleeve support ring made of dielectric material.

The main difference between this design and the one presented on figure 34) is that the length of the sleeve is not anymore of $\lambda_0 / 4$ but of $\lambda_{EFF} / 4$. That's because the effective dielectric constant of the polymer material is different from the air. We now have:

$$\lambda_{EFF} = \frac{C}{f * \sqrt{\epsilon_{EFF}}} \quad (11)$$

Where λ_{EFF} is the effective wavelength, f the frequency of the wave and ϵ_{EFF} the effective dielectric constant of the propagation material. If we were to change the filling material of the interstitial volume from air to a material with a higher value of ϵ_{EFF} the value of ϵ_{EFF} will be smaller. Hence, we would obtain a different length for the sleeve, depending of the filling dielectric material, as shown on figure 35).

Given that we have clarified the design of the general system as well as the one of the antenna, we can now introduce the design we have produced in order to fit our requirements. The figure 36) bellow shows the result of our design process:

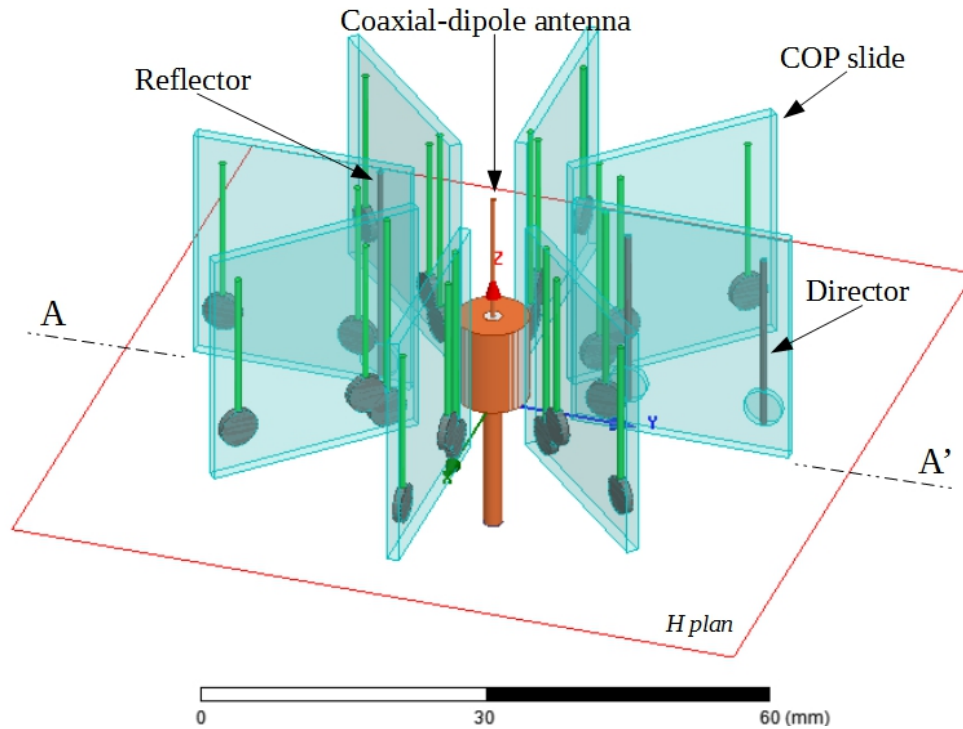


Figure 36 : 3D CAD view of a vertically polarized Yagi-Uda based fluidic antenna system

As we can see the figure 36) depicts an entire reconfigurable 3D Yagi-Uda based antenna system actuated through vertical microfluidic channels. The antenna system is based on a 3+1 elements architecture, centered on the use of a sleeve dipole antenna. That system is capable of controllable beam directivity, advanced beam forming, on the fly radiation diagram reconfiguration and 360° degree beam steering. It features a central sleeve dipole antenna surrounded by eight vertical slides of COP (as required) in which are embedded in each slide 3 electrolyte filled vertical fluidic channels on top of a Galinstan tank. These channels serves as the parasitic elements of the Yagi-Uda system. The central antenna is bottom fed by a coaxial cable. A cut along the **AA'** section plan would give us something very close to the figure 32) presented above. The use of COP slides instead of a whole cylinder of COP in which would have been drilled the columns and the tanks, as mentioned earlier, has been dismissed because of fabrication constraints but also because of the unavailability of such COP substrate, in our lab and on the market.

Indeed, if we select an operating frequency of 5 GHz, as for the system presented on figure 5), then the diameter of this system is of 66 mm, for a height of 27 mm, for a 3+1 elements Yagi-Uda antenna system able to perform 360° degree beam steering and on the fly beam reconfiguration. The dimensions of the system are calculated based on the recommendations of [2] and the effective dielectric constant of the structure, $\epsilon_{EFF\ TOTAL}$, which gives us a $\lambda_{EFF\ TOTAL}$ at 50 mm for a λ_0 of 60 mm, with $\epsilon_{EFF\ TOTAL}$ and $\lambda_{EFF\ TOTAL}$ determined through EM simulations.

The impossibility to modify the initial parasitic elements configuration mentioned in the case of the low profile system build around the Alford-loop antenna does not occur here, due to the architecture of the system which allows it to be very agile. Indeed, it can render almost invisible (from an RF point of view) to the central antenna some or all of those elements, thus rendering it capable of complete reconfiguration of its radiation pattern. Also, it must be noted that this system is bigger

(volume of a cylinder with a 66 mm diameter and a height of 27 mm) than the previous system (volume of a cylinder with a 60 mm diameter and a height of 20 mm), by almost 64%. That might be compensated by the fact that it should be less sensitive to low tilting angles. The reason why it shouldn't be an as important problem as for the horizontal system, is that the Galinstan is this not moving in the horizontal plane, but in the vertical one. That edge will likely disappear for tilting angles from moderate to high, given the density of Galinstan and the impact of the gravitational acceleration on it.

Indeed, we might encounter other difficulties linked to the fact that the displacement of the metal will now occur in the vertical plan, which mean we will have to fight against the gravitational acceleration, and given the important density of the Galinstan, at 6440 kg/m^3 [33], the resulting force may not be negligible. Combined to this, there is also the fact that vertical Galinstan displacement is something which has been rarely done in the literature, with the notable exception of [24], where the rise is driven by the ECA method, but also of a more widespread object, the medical Galinstan based thermometer, as in [34]. In this application, the thermometer can be positioned with its bulb towards the ground, in which case the rise occurs against gravity, driven by thermal expansion. So we know for sure that vertical Galinstan displacement is possible, but we do also know that the speed noted so far are inferior to what we can expect in the case of horizontal displacement, as in [24], where the Galinstan speed ranges from 0.6 mm.s^{-1} to 3.6 mm.s^{-1} .

Another difficulty we prepared for is the EM losses due to the presence of electrolyte inside the channels, as it was the case in the planar architecture presented above. Two types of losses occurs in the electrolyte:

The first type is the losses due to the conductivity of the electrolyte, which is a water based solution in which is dissolved salts (here NaOH). The second type is link to the very high value of dielectric constant of water. The resulting high value of index of the water induce a reflection of incident waves, which of course lower the overall performances of the system. It might be difficult to tackle the first kind of losses due to the fact that we need to have a conductive electrolyte. This problem was studied by Wang et al. [24] for a similar situation, and it appears that there is a trade-off to be made between the losses due to the conductivity of the electrolyte and the speed of rise of the Galinstan in the column.

The more conductive the electrolyte is the faster the rise is but also the higher the conductivity linked losses are. The reason for it is that the more conductive the electrolyte, the more charges are available to modify the surface tension of the Galinstan droplet, which occur therefore faster.

Regarding the reflection losses in the water due to the brutal traveling medium index change, a potential solution lies in the fact that as explained by A. Glise in [35], there is two types of dielectric liquids, the polar & apolar ones. The difference between them lies in the presence or the absence of dipoles inside the liquid, dipoles which are in facts the molecules of the liquid. It is the geometry of the molecules which will determine if the liquid is or not polar. Water is of the polar kind.

The polar liquid have dielectric properties which are frequency dependent and tend to have higher dielectric loss when the frequency goes up. The reason for it is that the rotation of the molecules inside it follow the frequency of the RF signal going through it. After a certain threshold frequency

(around 1 GHz for water), these molecules cannot rotate fast enough, the dielectric constant escalate and consequently the index also. The direct effect is to increase the losses by reflection inside that polar liquid. It should be added that polar liquids also tend to have a higher dielectric constant for starter as well as a higher loss tangent than the apolar liquid. Given these elements, we can see that a potential improvement leads would be for us to replace the water, which is a polar liquid, by an apolar liquid.

The conditions for such replacement would be that this new apolar liquid should be non-toxic, or at least no more than the initial NaOH aqueous solution, that it would have a lower dielectric constant and loss tangent. This apolar liquid would ideally be conductive and basic, or at least should allow us to dissolve in it salts in order to make it basic and slightly electrically conductive, within the same order of magnitude as the current solution, which have a conductivity of $\sigma = 24.88 \text{ S.m}^{-1}$. An alternative to that last point would be that the new apolar liquid is naturally basic, but can have its conductivity enhance by dissolving salts in it.

The major problem we would run into with our approach here, is that it is almost impossible to dissolve an ionic crystal inside an apolar liquid. Therefore unless we can find an apolar liquid which is both naturally basic *and* conductive, we will have the worst difficulties to replace our current aqueous solution. In the absence of such liquid, we are forced to stick with our previous solution, which also present the advantage of being relativity safe. Indeed, most apolar liquids are hydrocarbons, and therefore tends to be volatile and flammable, in addition of most of them being toxic to various degrees. We should also add that we don't know how well these chemical would react with Galinstan and COP (or PDMS) chips.

With all these questions unresolved, we have chosen to stick with our NaOH aqueous solution, because of the lack of time for us to investigate such complicated and specific matter. Nonetheless, as we will see later, improvement of the dielectric properties of the electrolyte would be a very interesting for our system in order to boost its RF performances.

That specific point is detailed in [24], where it is stated that a compromise must be found between the conductivity of the electrolyte and the speed of rise of the Galinstan column. Indeed, a low conductivity electrolyte will have lower EM conductivity losses but a slower rise speed, when a high conductivity electrolyte will do the opposite to our system, high EM conductivity losses for a higher rise speed. In [24] is also precised that one of the best electrolyte composition is according to them the 1Mol/L NaOH aqueous solution, which is easy to come by, relatively inexpensive and which provide a good compromise in terms of reductive power of the Galinstan oxide and electrical conductivity.

It's going to be especially critical in our case since we operate vertical columns as well and because as we can see on figures 32) & 36), we have a column filled with electrolyte right in the middle of our Yagi-Uda antenna, therefore its impact is going to be significant.

III. Chosen characteristics of the system

If we sum up what we have said so far about this system, we can lay out its following characteristics:

- Dipole based antenna system
- Vertically polarized central feed antenna
- Coaxial-dipole antenna or sleeve antenna for the radiating element
- Fluidic system working in the vertical plane
- CEW or ECA technologies used for the liquid metal displacement
- Dimensions of the system within the order of magnitude of the wavelength of the system.

We chose the vertical displacement for the fluidic system because we thought it was offering more in term of flexibility and agility to the system. The reconfigurability achievable with such fluidic system, as shown on figure 31), is far greater than the one achievable with the horizontal displacement based fluidic system, as shown on figure 28).

Nonetheless, that flexibility and agility might comes at a cost, which could especially be a decrease of the response time of the system, as well as its power consumption. Indeed, the speed of vertical displacement is likely to be inferior to the speed of horizontal displacement, based on the literature, as a comparison between [19] & [24] tells us. In that case, even if the phenomenon driving the rise is different (CEW vs ECA), the speed of the vertical displacement presented in [24] is an order of magnitude inferior to the speed of the horizontal displacement presented in [19].

On the other hand, the systems based on the horizontal displacement tend to occupy a larger surface than vertical displacement based systems, for the same configuration. Of course the vertical displacement based system have a 3D architecture, when the architecture of the horizontal displacement based systems is at best 2.5D. We are also not taking a great deal of risk by saying that the vertical displacement based design can also very probably work in intermediate positions between the horizontal and the vertical. This could give the device ease of use in motion for example.

IV. Bibliography

- [1] Zeon corporation, "ZEONEX® - Cyclo Olefin Polymer (COP)," Tokyo, 2016.
- [2] C. Balanis, *Antenna theory: analysis and design*. 2012.
- [3] D. R. López, "Reconfigurable pixel antennas for communications," Universitat Politecnica de Catalunya (UPC), 2013.
- [4] J. K. Sungyong Cha, Tae-Soon Yun, "Pillar Array-type Parabolic Reflector Antenna Driven by Air-lifted Monopole Fed by CB-CPW for 2.4 GHz Applications," *IEEE Antennas Propag. Soc. Int. Symp.*, pp. 5–8, 2008.
- [5] M. R. O. Mofolo, A. a. Lysko, T. O. Olwal, and W. a. Clarke, "Beam steering for circular switched parasitic arrays using a combinational approach," *IEEE AFRICON Conf.*, no. September, pp. 13–15, 2011.
- [6] D. Nascimento and R. Schildberg, "Low-cost Yagi-Uda monopole array," *Antennas Propag. Soc. Int. Symp. 2008. AP-S 2008. IEEE*, pp. 1–4, 2008.
- [7] A. Morishita, C. Kitamura, A. Ohta, and W. Shiroma, "A Liquid-Metal Monopole Array With Tunable Frequency, Gain, and Beam Steering," *IEEE Antennas Wirel. Propag. Lett.*, vol. 12, pp. 1388–1391, 2013.
- [8] M. A. H. Khondoker and D. Sameoto, "Fabrication methods and applications of microstructured gallium based liquid metal alloys," *Smart Mater. Struct.*, vol. 25, no. 9, p. 93001, 2016.
- [9] B. Zhang, Q. Dong, C. E. Korman, Z. Li, and M. E. Zaghoul, "Flexible packaging of solid-state integrated circuit chips with elastomeric microfluidics," *Sci. Rep.*, vol. 3, pp. 1–8, Jan. 2013.
- [10] A. Zavabeti, T. Daeneke, A. F. Chrimes, A. P. O'Mullane, J. Zhen Ou, A. Mitchell, K. Khoshmanesh, and K. Kalantar-zadeh, "Ionic imbalance induced self-propulsion of liquid metals," *Nat. Commun.*, vol. 7, no. May, p. 12402, 2016.
- [11] D. Rodrigo, S. Member, L. Jofre, and B. A. Cetiner, "Circular Beam-Steering Reconfigurable Antenna With Liquid Metal parasitic," *IEEE Trans. Antennas Propag.*, vol. 60, no. 4, pp. 1796–1802, 2012.
- [12] R. D. Hasse, W. Hunsicker, K. Naishadham, A. Z. Elsherbeni, and D. Kajfez, "Design of a planar segmented circular loop antenna for omnidirectional radiation at 5.8 GHz," *IEEE Antennas Wirel. Propag. Lett.*, vol. 11, pp. 1402–1405, 2012.
- [13] C.-C. Lin, L. Kuo, and H. Chuang, "A horizontally polarized omnidirectional printed antenna for WLAN applications," *Antennas Propagation, IEEE ...*, vol. 54, no. 11, pp. 604–605, 2006.

- [14] W. Hong and K. Sarabandi, "Low-profile, multi-element, miniaturized monopole antenna," *IEEE Trans. Antennas Propag.*, vol. 57, no. 1, pp. 72–80, 2009.
- [15] L. Yang, Z. Zhang, G. Fu, Y. Zhang, and Y. Li, "A Novel Low-Profile Quadripod Kettle Antenna with Enhanced Bandwidth," *Prog. Electromagn. Res.*, vol. 144, no. January, pp. 241–247, 2014.
- [16] W. W. Li and K. W. Leung, "Omnidirectional circularly polarized dielectric resonator antenna with top-loaded alford loop for pattern diversity design," *IEEE Trans. Antennas Propag.*, vol. 61, no. 8, pp. 4246–4256, 2013.
- [17] B. Q. Wu and K. Luk, "A Wideband, Low-Profile, Conical-Beam Antenna With Horizontal Polarization for Indoor Wireless Communications," *IEEE Antennas Wirel. Propag. Lett.*, vol. 8, pp. 634–636, 2009.
- [18] K. Lertsakwimarn, C. Phongcharoenpanich, and T. Fukusako, "A Low-Profile and Compact Split-Ring Antenna with Horizontally Polarized Omnidirectional Radiation," 2014.
- [19] R. Gough, A. Morishita, J. Dang, and W. Hu, "Continuous Electrowetting of Non-Toxic Liquid Metal for RF Applications," *IEEE access*, vol. 2, pp. 874–882, 2014.
- [20] H. Lee and C. Kim, "Surface-tension-driven microactuation based on continuous electrowetting," *Microelectromechanical Syst. J.*, vol. 9, no. 2, pp. 171–180, 2000.
- [21] M. R. Khan, C. B. Eaker, E. F. Bowden, and M. D. Dickey, "Giant and switchable surface activity of liquid metal via surface oxidation.," *Proc. Natl. Acad. Sci. U. S. A.*, vol. 111, no. 39, pp. 14047–51, Sep. 2014.
- [22] S.-Y. Tang, Y. Lin, I. Joshipura, K. Khoshmanesh, and M. Dickey, "Steering Liquid Metal Flow in Microchannels using Low Voltages," *Lab Chip*, vol. 15, pp. 3905–3911, 2015.
- [23] S. K. Cho, H. Moon, and C. Kim, "Creating, transporting, cutting, and merging liquid droplets by electrowetting-based actuation for digital microfluidic circuits," *J. Microelectromechanical Syst.*, vol. 12, no. 1, pp. 70–80, Feb. 2003.
- [24] M. Wang, C. Trlica, M. R. Khan, M. D. Dickey, and J. J. Adams, "A reconfigurable liquid metal antenna driven by electrochemically controlled capillarity," *J. Appl. Phys.*, vol. 117, no. 19, p. 194901, 2015.
- [25] J. L. Volakis, *Antenna engineering handbook*. 2010.
- [26] H. Brock, "The open sleeve broadband antenna .," United States Naval Postgraduate School, Monterey, California, 1955.
- [27] B. Yuan, J. Xiong, Y. Fu, P. Liang, L. Yao, and F. Zhang, "A Novel Design Method for Improving Sleeve Antenna Performance," no. 800, pp. 2–4, 2016.
- [28] Z. Bin, L. Qizhong, and J. Yicai, "Research on a novel sleeve antenna and its applications," vol. 1, no. 1, p. 330 ST-Research on a novel sleeve antenna and i, 2005.

-
- [29] K. G. Thomas, N. Lenin, and M. Sreenivasan, "Wide-band dual sleeve antenna," *IEEE Trans. Antennas Propag.*, vol. 54, no. 3, pp. 1034–1037, 2006.
- [30] S. Wang, S. Gong, and P. Zhang, "A NOVEL DUAL-SLEEVE ANTENNA," pp. 205–208, 2010.
- [31] M. Taguchi and S. Egashira, "Sleeve antenna with ground wires.pdf," *IEEE Trans. Antennas Propag.*, vol. 39, no. 1, pp. 1–7, 1991.
- [32] T. Oki, T. Hung, M. Sakuma, and H. Morishita, "Basic Characteristics of Wideband Sleeve Antenna," *Proc. ISAP 2014*, pp. 231–232, 2014.
- [33] T. Liu, P. Sen, and C. Kim, "Characterization of nontoxic liquid-metal alloy galinstan for applications in microdevices," ... *Syst. J.*, vol. 21, no. 2, pp. 443–450, 2012.
- [34] "Mercury-free, analog Clinical thermometer with Galinstan - Geratherm Medical AG, Made in Germany," p. 98716.
- [35] A. Glise, "Application des Cyclo-Oléfine Polymère et Copolymère (COP/COC) pour la mise en œuvre de microsystèmes communicants autonomes et des capteurs associés," *Univ. Bretagne Occident. Brest*, 2015.

Chapter 3 : Electromagnetic simulations

I. Design approach and guidelines for the simulations

We have presented in Chapter 2 the two designs of antenna we have elaborated as well as underlined our preference for the one based on a vertically polarized dipole coaxial antenna. Indeed, this system was deemed more promising in terms of agility and overall beam shaping performances over the one based on a horizontally polarized Alford loop dipole antenna.

We will in this part explore the EM performances of the vertically polarized Yagi-Uda based antenna system presented at the end of the previous chapter and visible on figure 36), with a quick comparison with the horizontally polarized Alford-loop based antenna system. The performances will be explored through electromagnetic computer simulations, realized with the ANSYS HFSS software. All simulations were done on the high performance cluster WINCHYPS2, cluster managed by the TechHyp platform of the Lab-STICC.

The average calculation time for each simulation is 2 hours, with the time of execution ranging from 30 min, like the first simulation presented in this chapter, to 3 to 4 hours, like the last simulation presented at the end of this chapter. The optimization is another aspect of the simulation which is also very time consuming but not detailed in this chapter. It mostly consisted into introducing small geometrical variation to the design following a previously established pattern. We afterwards analyse the results of these simulations, and pick from that results pool the best configuration for us. Given the number of single simulations needed to do in a row, we can estimate the average calculation time of these design optimization simulation sessions between 4 to 10 hours. Every design presented on this chapter has been subjected to that optimization procedure.

As we said before in chapter 2, the main criteria we will look at for the evaluations of the systems are going to be the response time, the power consumption, the EM performances and the cost of the device. Given that the simulations presented in this chapter are only EM simulations, it will mostly give us informations on the EM performances of the device.

We could add that the question of the feasibility of the device is going to be also a very important criteria to take into account for the successive design iterations implemented, as we will see in this chapter. That feasibility takes into account the availability of means in our facilities as well as the one of materials on the market.

II. Progressive validation of the architecture

We will now present and discuss the results of the various simulations which were involved in the system's design process. Our approach regarding to those simulations consisted in implementing gradually the complexity of the design, and at each step, discussing the results and addressing issues that might arise. All modification comes in addition of the previous one, which allow us to see the cumulated impact of all the elements on the initial structure. The goal is to have at the end of that process a simulation as close as possible of the envisioned prototype in order to be able to compare results with the measurements.

In that optic, we will first simulate a system based on the theoretical wire dipole, and we will then replace it with our coaxial (or sleeve) dipole antenna. When this is done, we will gradually add the COP encasing of the fluidic columns with a cylinder based architecture. That architecture being only a theoretical one, we then replace it with another, more fit for realization, based on COP slides. Once we have the general architecture, we will start to add refinement to the model. First we will add the electrolyte inside the previously empty columns, and finally we will introduce the tanks storing the Galinstan when it's not pumped up inside the columns.

1) Simulation of the wire dipole based system

Our first simulation was done to demonstrate the working principle of the 3+1 fluidic Yagi-Uda antenna at 5 GHz. As we said at the beginning of that manuscript, that frequency was chosen due to the good compromise it represents between the size of the antenna & the size of the microfluidic elements. The design chosen is a very simplified design, featuring 2 directors and 1 reflector made of Galinstan columns and a central dipole antenna. This antenna is made of 2 copper rods of a length of 13mm each, with an excitation based on a lumped port placed in between of the two rods. The lengths of the other elements are based on the guidelines established before in chapter 2, extracted from [1] which are reminded bellow:

- The length of the reflectors L_R should be of $0.51 \lambda_{EFF}$ ($>0.5 \lambda_{EFF}$)
- The length of the directors L_D should be $0.41 \lambda_{EFF}$ ($<0.5 \lambda_{EFF}$)
- The spacing of the directors S_D should be $0.3 \lambda_{EFF}$ (min $0.3 \lambda_{EFF}$)
- The spacing of the reflector and the feed S_{RF} should be $0.25 \lambda_{EFF}$
- The spacing between the director and the feed S_{DF} should be $0.3 \lambda_{EFF}$ (min $0.3 \lambda_{EFF}$)
- The diameter of the reflectors & the directors D should be inferior to $0.024 \lambda_{EFF}$

The figure 37) bellow is illustrating these guidelines and there placements for the wire dipole system.

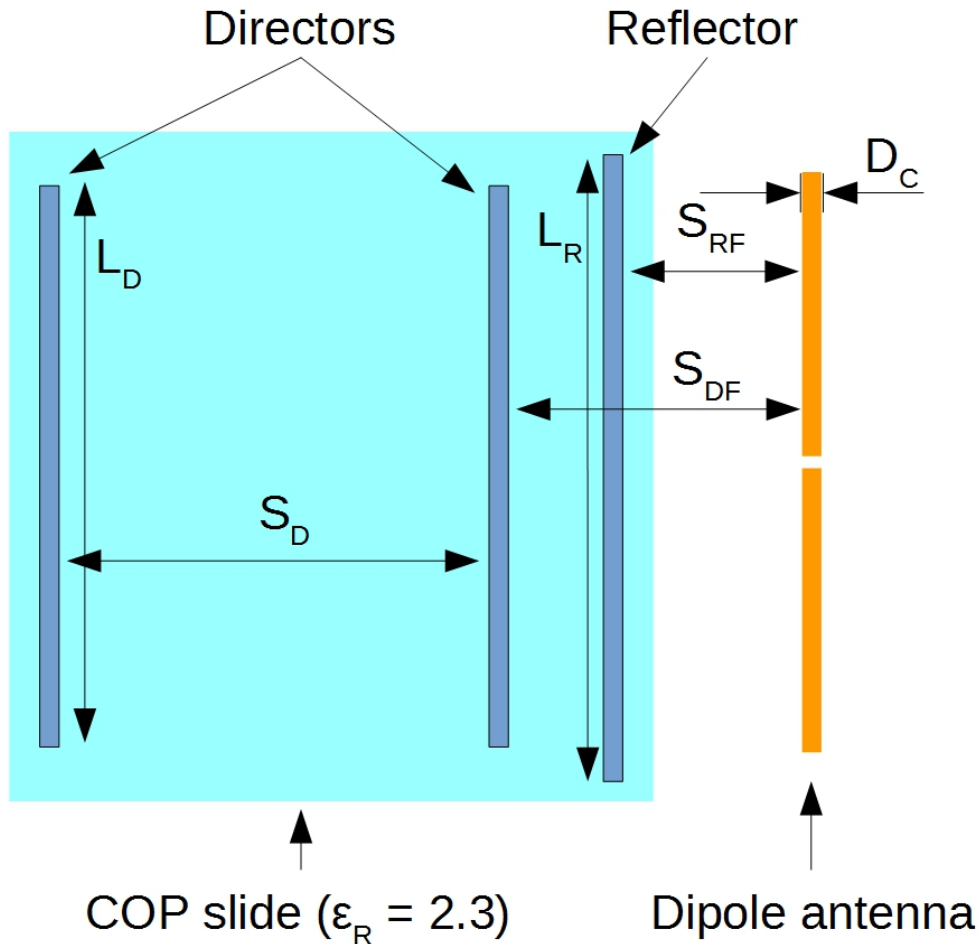


Figure 37 : Illustration of the system's dimensions guidelines

Based on these guidelines, and knowing that at 5 GHz the effective wavelength is 60 mm, we obtain L_R 30.6 mm, L_D 24.6 mm, S_{DF} 18 mm, S_{RF} 15 mm, S_D 18 mm. The length of each rod is 13 mm (instead of 15mm) in order to recenter the antenna resonance peak at 5 GHz. We have chosen here to take the same diameter for the conductor of the dipole & the Galinstan columns, 700 μm .

The properties of the material used for the simulation, which are Galinstan and copper, are the following and will not change throughout all simulations (here just conductivity σ because both are metals):

- **Copper** : $\sigma = 5.8 \cdot 10^7 \text{ S/m}$
- **Galinstan** : $\sigma = 2.3 \cdot 10^6 \text{ S/m}$

We can see that the conductivity of Galinstan (liquid metal) is only one order of magnitude less than the copper one, knowing that copper is a very high conductive metal.

The whole system is simulated in vacuum, and is showed bellow on figure 38).

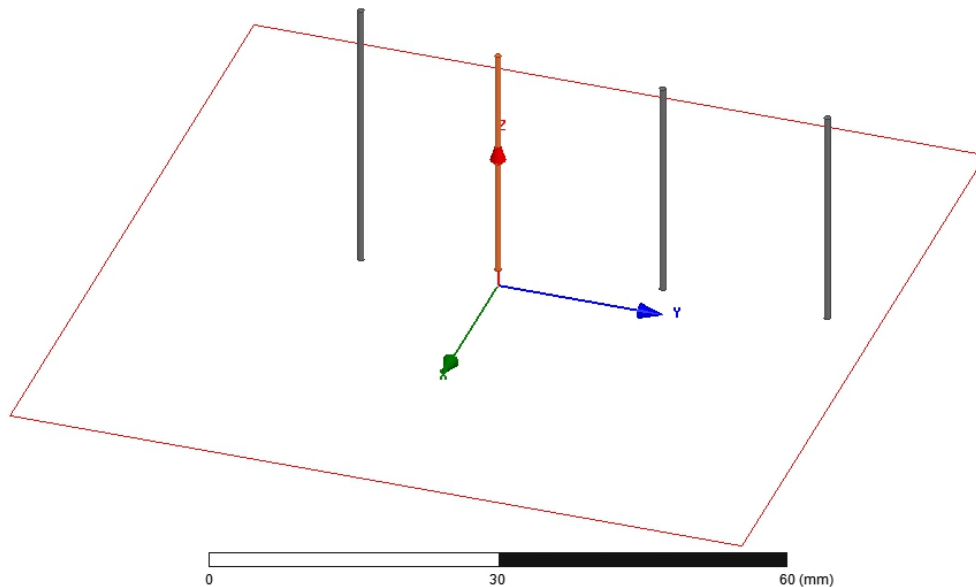


Figure 38 : Wire dipole Yagi-Uda antenna system in a unidirectional “narrow beam” configuration in vacuum (red rectangle figuring the propagation plan)

For the simulation, that structure is encased into cylindrical two “air-boxes”, placed one inside the other. The bigger air-box is used to place on it the far field boundaries, which consists in a radiation boundary used to simulate an infinite space. Its diameter & height is defined by the diameter & height of the second air-box. Indeed its diameter is the addition of the smaller box diameter and half the effective wavelength, λ_{EFF} . Its height is the addition of the height of the smaller box and the effective wavelength. The second air-box have a diameter and a height which is dictated by the diameter of the Yagi-Uda structure placed inside it. Its height is set to have the same value as the maximum height reached by the structure tallest element (which is a reflector or a COP slide). As for its diameter, it is set to leave a distance of 2 millimeters between its limit and the closest element of the structure.

By doing so we are sure to have a spacing between our system and the radiation boundary slightly superior to $\lambda_{\text{EFF}}/4$ inside both the longitudinal plan & the vertical plan. This air-boxes configuration will remain the same for all the further simulations.

We want to obtain the evolution of the reflection coefficient, S11, as a function of the frequency, the evolution of the real and imaginary part of the impedance (Re & Im) as a function of the frequency and also the radiation pattern. For this last one, we want it both in the propagation plan (here in red on the figure 38)) and in 3D. The following figures, 39) to 40), show these results.

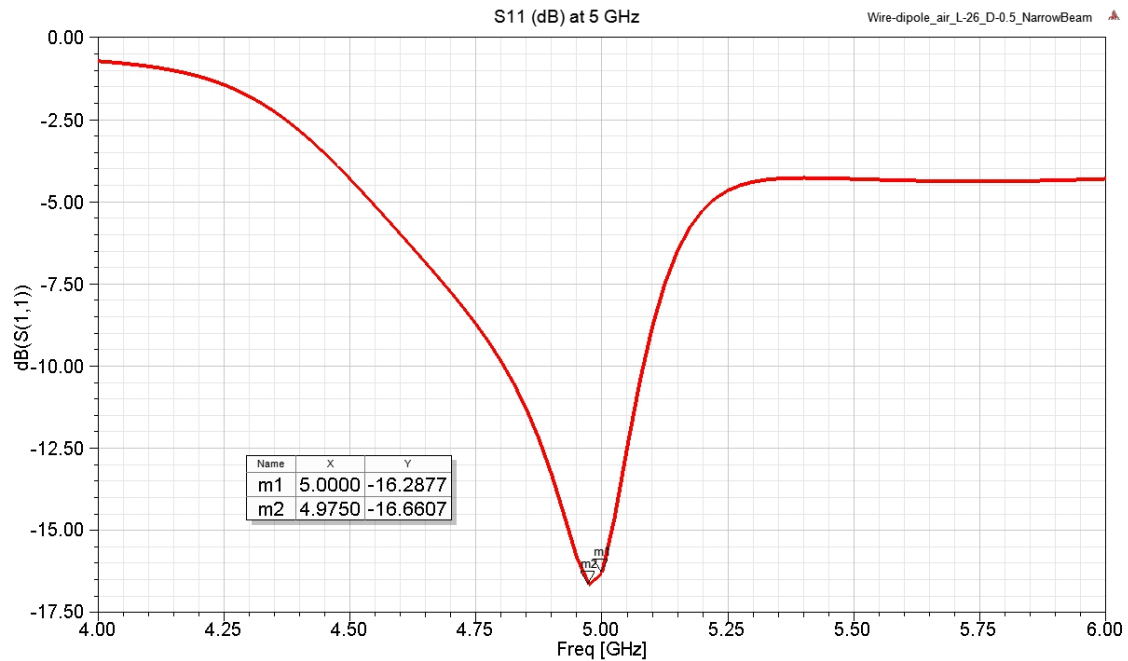


Figure 39 : Evolution of S_{11} of the wire dipole Yagi-Uda antenna system in unidirectional configuration

We can see on this figure 39) the evolution of the S_{11} as a function of the frequency. We can notice that the frequency peak is at 5 GHz, with the min slightly tilted towards the lower frequency (at 4.975 GHz). The value of the S_{11} at 5 GHz is of -15.45 dB.

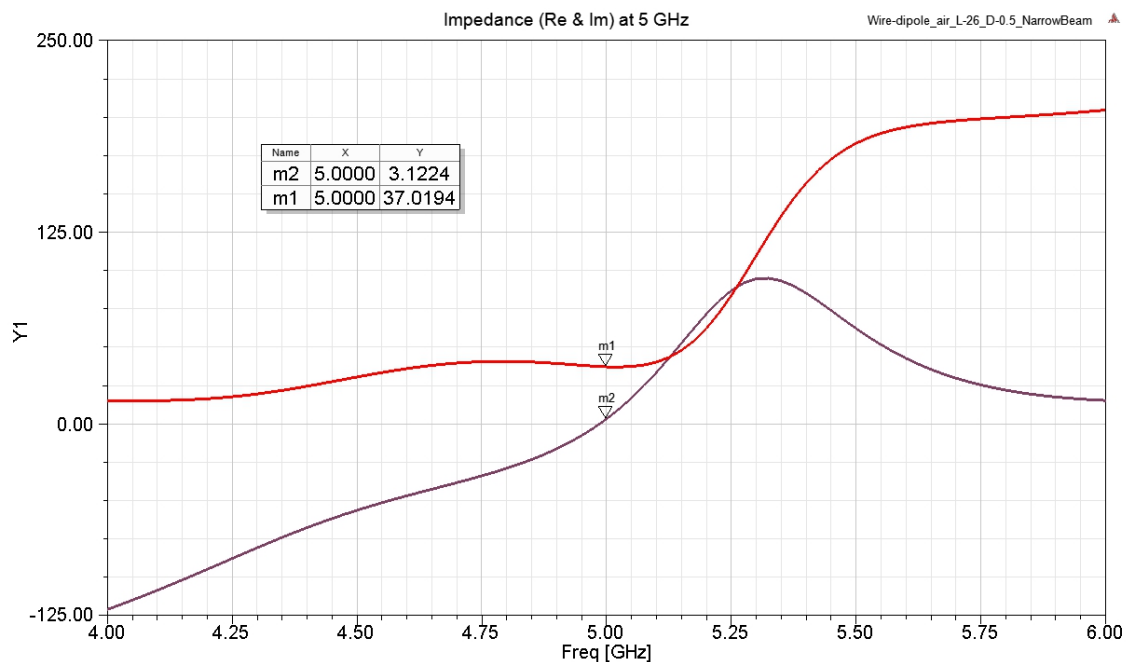


Figure 40 : Evolution of impedance of the wire dipole Yagi-Uda antenna system in unidirectional configuration

We can see on this figure 40) the evolution of the two parts of the impedance (Re & Im) as a function of the frequency. We can notice that the imaginary part is almost nullified at 5 GHz, with a real part reaching 36 Ohms at the same frequency.

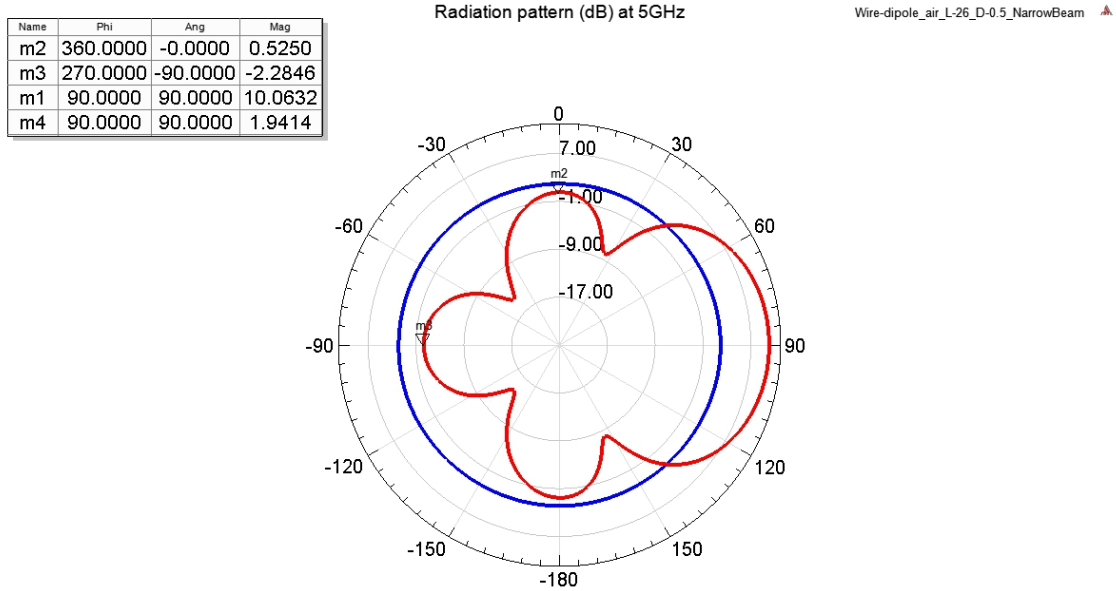


Figure 41 : 2D radiation diagram of the wire dipole Yagi-Uda antenna system in unidirectional configuration

We can see on this figure 41) the radiation pattern of our system at 5 GHz, which is directive, as predicted. The main lobe is going in the direction of the two directors, so towards the right of the figure 38). The realized gain in that direction is of +10.13 dB, when it is of -2.28 dB for the backfire lobe, and +0.52 dB for the side lobe. From these value we can see that our antenna system is working correctly.

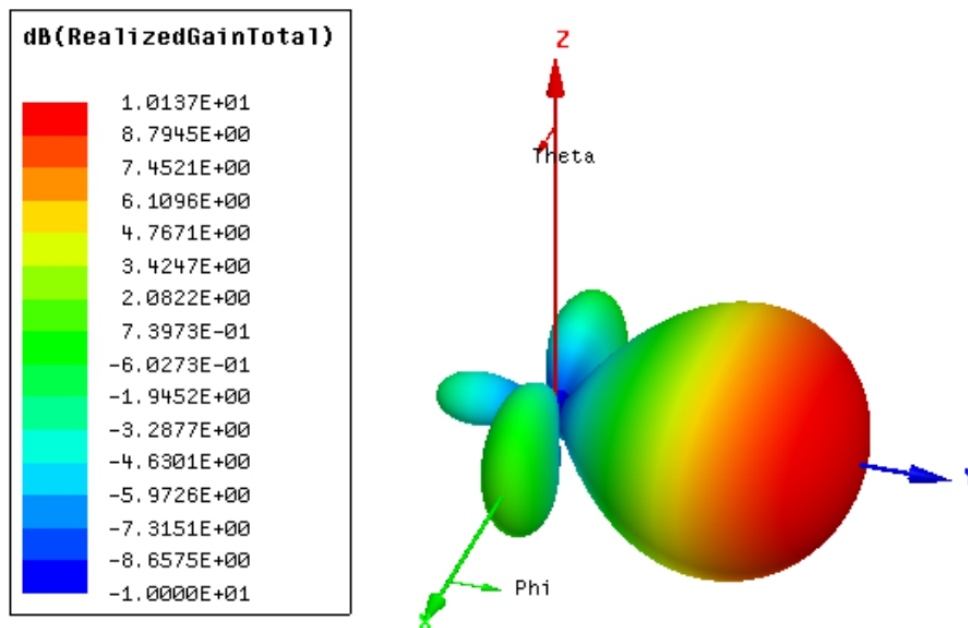


Figure 42 : 3D radiation diagram of the wire dipole Yagi-Uda antenna system in unidirectional configuration

Finally, figure 42) is the 3D radiation diagram of the system. On this figure we can see better the main lobe, as well as the laterals and backfire lobe.

Now that we have demonstrated the working principle of the Yagi-Uda antenna with this “wire dipole” configuration, we will now focus on the behavior and performances of the two configuration presented earlier in chapter 2, respectively the coaxial dipole antenna and the Alford-loop based dipole antenna.

2) Simulation of the coaxial dipole and Alford-loop dipole based system

Architecture of these antennas has been thoroughly explained in chapter 2, and both come from the literature, like in [2] or [3] for example.

We will now compare the performances of Yagi-Uda systems based on these two antennas, a 3+1 Yagi-Uda system for the coaxial dipole antenna, very similar to the configuration of figure 1), and a 2+1 Yagi-Uda antenna for the Alford-loop based antenna. The reason for the difference is the fact that in order to have a simplified fluidic system composed of only one channel, the authors have chosen a configuration with only two parasitic elements, as shown in [3]. They have placed the two elements at same the distance from the antenna, which here is $0.3 \lambda_0$. This constrains their design, and as it is explained in [3], forces them to use a director with a length $< 0.5 \lambda_{EFF}$ and a reflector with a length $> 1.5 \lambda_{EFF}$ because they have chosen to work at the second resonance. The reason for this lies in the fact that the larger the reflector, the better the power reflection. Since they were not limited by height or space problems, they choose to enhance the length of the reflector in order to maximize its efficiency, as it is specified in [4], which compensate a bit the loss of the second director.

For the design of the antennas themselves, their designs are showed on the figure 43) bellow.

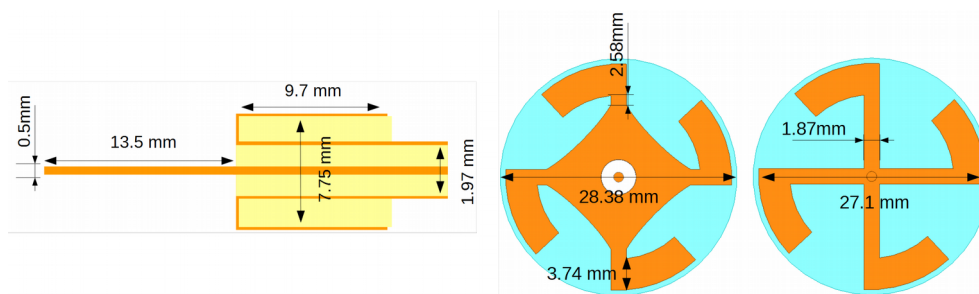


Figure 43 : Dimensions of the central antenna of the coaxial dipole system (left) & the Alford-loop based system (right)

Design rules for the coaxial dipole antenna have been described already in chapter 2. For the Alford-loop based antenna, the design has been established in [4] for a working frequency of 1.8 GHz. Additional work was done by A. Glise during a post-doctoral work in order to adapt the design at the 5 GHz frequency. Both design have also been subject to an optimization work from us in order to work well at 5 GHz.

For the case of the coaxial antenna optimization, the procedure of adaptation is the following:

We multiply by what we call “Sweep Coefficient” (or SwCoef) the initial length of the coaxial antenna defined on figure 43) in order to re-center the resonance at 5GHz. We will consider that the

resonance is reached at 5 GHz if the Im part of the impedance nullify itself at that frequency. In this case, we have $S_{wCoef} = 0.965$, meaning a 3.5% diminution of the antenna's length.

The simulated dimensions of the Alford loop based system are the one displayed on the figure 43) above, and we will not further detailed the process of optimization, it being very similar to the one described above.

Additional materials used in these simulations (in complement of the previous) are the 3D impression polymer (that we will from now on call "3DP-P") used for the 3D printing of the polymer part of the coaxial dipole antenna and the Cyclo-Olefin-Polymer (COP), from Zeonex. Both of these materials are dielectric ones. For the properties of 3DP-P, we chooses a value which was an average value of the characteristics of the dielectric materials commonly used for 3D printing and which were studied in our lab in [5]. This is especially true for the value of the effective permittivity, for the loss tangent we choose a value within the order of magnitude of the calculated average, but purposefully lower than that average to facilitate the simulations.

The properties of these materials are the following:

- **COP** : $\epsilon_R = 2,3$, $\tan \delta = 3.10^{-4}$ at 1 GHz [6]
- **3DP-P** : $\epsilon_R = 2,7$, $\tan \delta = 1.10^{-3}$

The two simulated systems are simulated in vacuum and are showed on the figure 44) bellow:

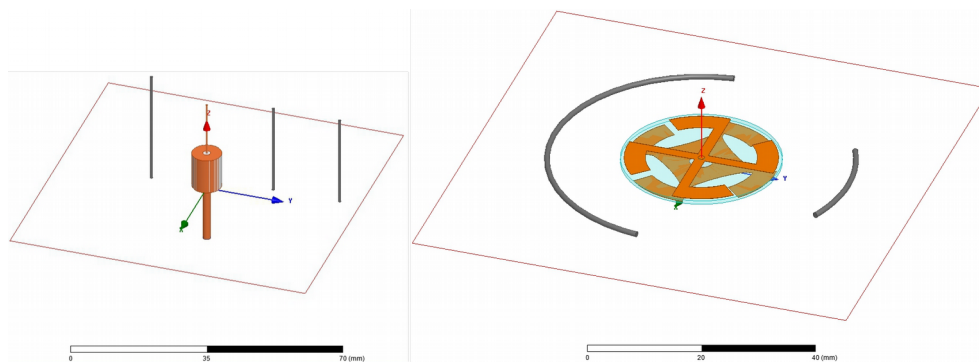


Figure 44 : Coaxial dipole Yagi-Uda antenna system (left) and Alford-loop based dipole Yagi-Uda antenna system, both in unidirectional "narrow beam" configurations

As for the wire system, we want to single out the evolution of the reflection coefficient, S_{11} , as a function of the frequency, the evolution of the real and imaginary part of the impedance (Re & Im) as a function of the frequency and also the radiation pattern. This will be the case for all the following simulations, unless we don't deem necessary to insist on some. Here, we are going to compare on the same graphics the results for the wire dipole system, the coax dipole system and the Alford-loop based system.

The following figures, 45) to 48), show those compared results. For the wire dipole system, they will be in red on the graphics bellow, for the coaxial dipole system in vacuum in blue & for the Alford-loop based dipole system in green.

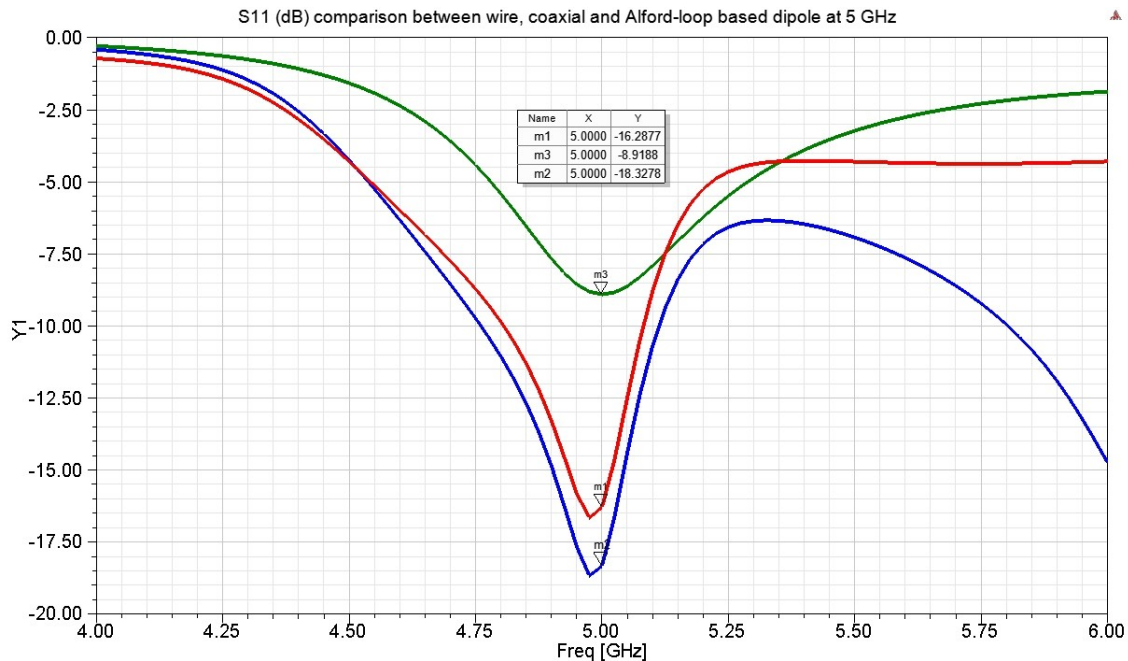


Figure 45 : Evolution of S_{11} of the wire (red) / coaxial (blue) / Alford-loop based (green) dipole Yagi-Uda antenna system in unidirectional configuration

We can see on this figure 45) the evolution of the S_{11} as a function of the frequency for the 3 systems. We can notice that the frequency peaks at 5 GHz, as expected. The value of the S_{11} at 5 GHz is of -18.32 dB for the coaxial system (m2), and at -8.92 dB for the Alford loop based system (m3). It's worth noting that the first system seems to have closer performances to the initial theoretical wire dipole system (it actually have a deeper peak) than the Alford-loop based one when it come to the peak value of the S_{11} at 5 GHz.

The evolution of the S_{11} for higher frequencies seems to behave the opposite way, with the Alford-loop system behavior being closer to the wire dipole system. On the coaxial dipole system, we can spot what could be a second resonance peak around 6.25 GHz, absent from the two other curves.

On the following figure, featuring the evolution of the impedance as a function of the frequency, the evolution of the performances of the wire dipole system will be in shades red, those of the coaxial dipole system in vacuum in shades blue & those of the Alford-loop based dipole system in shades green. The plain curves are for the Re part, the dashed ones for the Im part. This plain & dashed lines for the Re & Im parts will be repeated throughout the whole chapter for impedance charts.

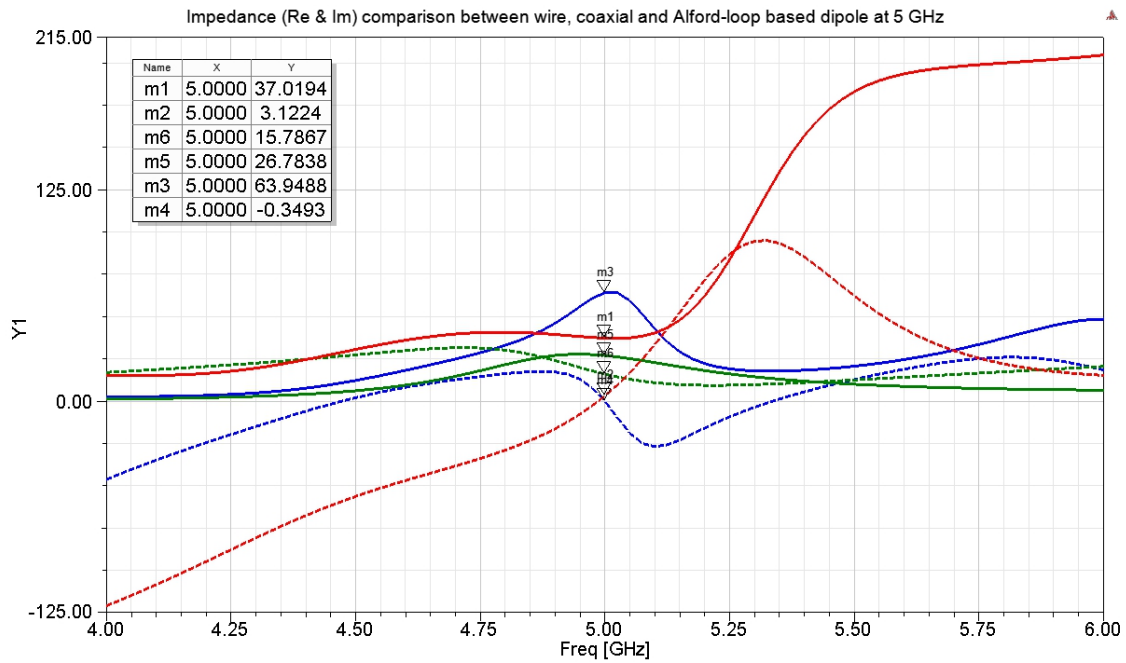


Figure 46 : Evolution of impedance of the wire (red) / coaxial (blue) / Alford-loop based (green) dipole Yagi-Uda antenna system in unidirectional configuration

We can see on this figure 46) the evolution of the two parts of the impedance (Re & Im) as a function of the frequency for the 3 systems. While we can find back the performances of the wire system at 5GHz in m1 (Re) & m2 (Im), we also notice that the imaginary part is almost nullified at 5 GHz for the coaxial dipole system (m4) although that's not the case for the Alford-loop system (m6), even if the value at this point is still low, at 15.78 Ohms. For the evolution of the real part, we find that at 5 GHz (m4), the real of the coaxial dipole system is almost the double of the wire dipole system one (with 63.95 Ohms instead of 26.78 Ohms). It is of 26.78 Ohms at the same frequency for the Alford loop system (m5).

Radiation pattern (dB) comparison between wire, coaxial and Alford-loop based dipole at 5 GHz

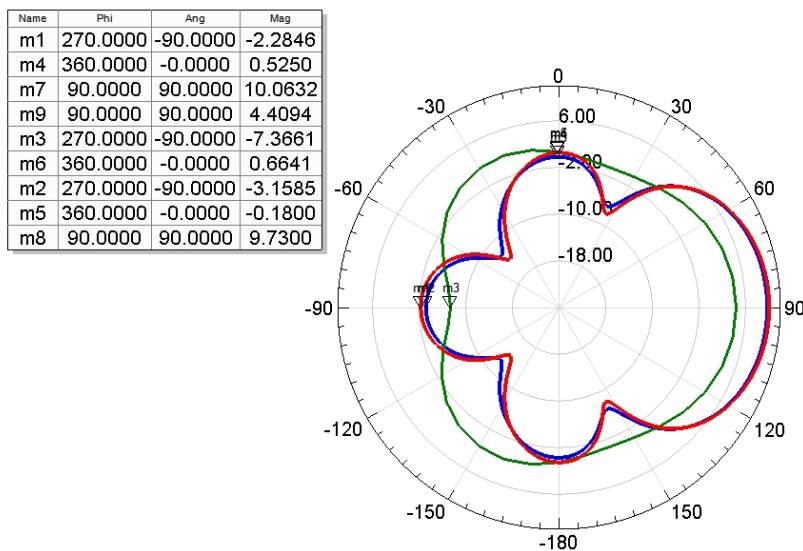


Figure 47 : 2D radiation pattern of the wire (red) / coaxial (blue) / Alford-loop based (green) dipole Yagi-Uda antenna system in unidirectional configuration

We can see on this figure 47) the radiation pattern of the 3 systems at 5 GHz, which are all directive. For all, the main lobe is going towards the right of the figure 38) and 44), as it is expected with this Yagi-Uda configuration.

The realized gain in that direction is of respectively :

- +10.06 dB for the wire dipole system
- +9.73 dB for the coaxial dipole system
- +4.41 dB for the Alford-loop based dipole system

When for the backfire lobe it is of respectively :

- -2.28 dB for the wire dipole system
- -3.15 dB for the coaxial dipole system
- -7.36 dB for the Alford-loop based dipole system

From these values we can formulate a first conclusion, which is that the 2+1 configuration of the Alford-loop based antenna shows inferior performances. Indeed, it has a lower forward gain & a higher level of lateral lobes to the 3+1 configuration of the coaxial dipole antenna, which is its direct competitor for our application. While this is partly to be expected due to the missing director, it is nonetheless a disadvantage for that system. We could add that given the architectural choices made for the Alford-loop antenna design, adding a director would drastically increase the diameter of the system ($+0.6 \lambda_0$). That means that this architecture will always be wider than the vertically polarized Yagi-Uda architecture based system for an equivalent configuration (due to the width of the central antenna (L_a) & because of the mono-tube configuration for director & reflector). But even at the same configuration (same number of elements), its performances would be inferior because its design doesn't follow the proper design rules and place the director and reflector at $0.3 \lambda_0$ (instead of $0.25 \lambda_0$) from the central antenna, degrading the efficiency of the reflector in particular.

Based on other elements in chapter 2, we already concluded that we will focus more on the coaxial dipole antenna, and these simulations are backing up this conclusion. This is especially robust since the results for the Alford-loop system are coherent with those presented in [3], with for example an announced "front to back ratio" (or FTBR) of 10 dB when we have here a FTBR which just come short of 12 dB. As for the coaxial dipole system, we see here that it has very similar performances to the theoretical wire dipole system, which is a very good news for us, and solidify our choice of selecting this architecture for the next steps of this work.

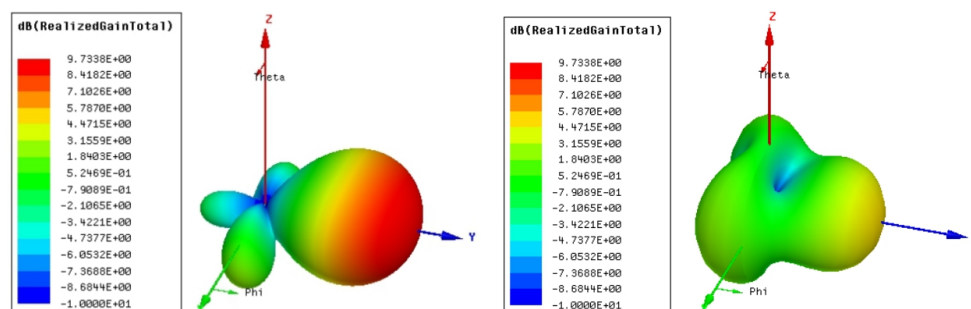


Figure 48 : 3D radiation pattern of the coaxial dipole antenna system (left) & the Alford-loop based dipole antenna system (right) dipole both in unidirectional configuration

Finally, figure 48) shows the 3D radiation diagrams of the coaxial dipole and Alford-loop based dipole systems. We can especially note that on the Alford-loop system, the lateral lobes are significantly more important than what they are on the two other systems. The inability of that system to focus more the beam is rooted in large part in the absence of a second director, in opposition to the coaxial dipole architecture.

Having all these results, what we can conclude is that the EM performances of the Alford-loop based dipole antenna system are clearly not as good as those of the coaxial dipole antenna system. Therefore, it comes in addition of our recommendations in chapter 2, which were to discard this architecture for our final system based on agility concerns and the beam forming limitations inherent to this architecture. So we can say that these simulations are substantiating these concerns by proving them true and are adding the overall lesser EM performances of the architecture.

From now on, we will study more extensively the coaxial dipole architecture, which can from now on be considered adopted as the final general architecture of our system.

3) Simulation of the coaxial dipole based system embedded in a COP cylinder

Having established the coaxial dipole antenna system as the architecture of our prototype, we now need to focus on the feasibility aspect of the conception.

As we presented before in chapter 2, the Galinstan columns are embedded inside COP. So in order to investigate the impact of the polymer on the antenna performances, we have performed a simulation where the columns are embedded inside a COP cylinder, the ones filled with Galinstan, but as well as the empty ones. That rod has a cylindrical hole in its center to give room for the coaxial antenna

Given that the antenna is now radiating through COP and vacuum, we need to update the dimensions of the parasitic elements. Since we know the value of the dielectric constant of COP, $\epsilon_R = 2.3$, we can calculate the new effective wavelength, λ_{EFF} . At this stage, we need to postulate the hypothesis that we can consider the waves as propagating only inside the polymer inside the antenna system itself. With this hypothesis, and knowing the properties of the COP, we have $\lambda_{EFF} = 40$ mm.

By using the previously determined design guidelines and the effective wavelength, we have the following values for the parasitic elements: L_R 20.4 mm, L_D 16.4 mm, S_{DF} 12 mm, S_{RF} 10 mm, S_D 12 mm. Of course, losses have been taken into account in these simulations.

The simulated system is presented on figure 49) below:

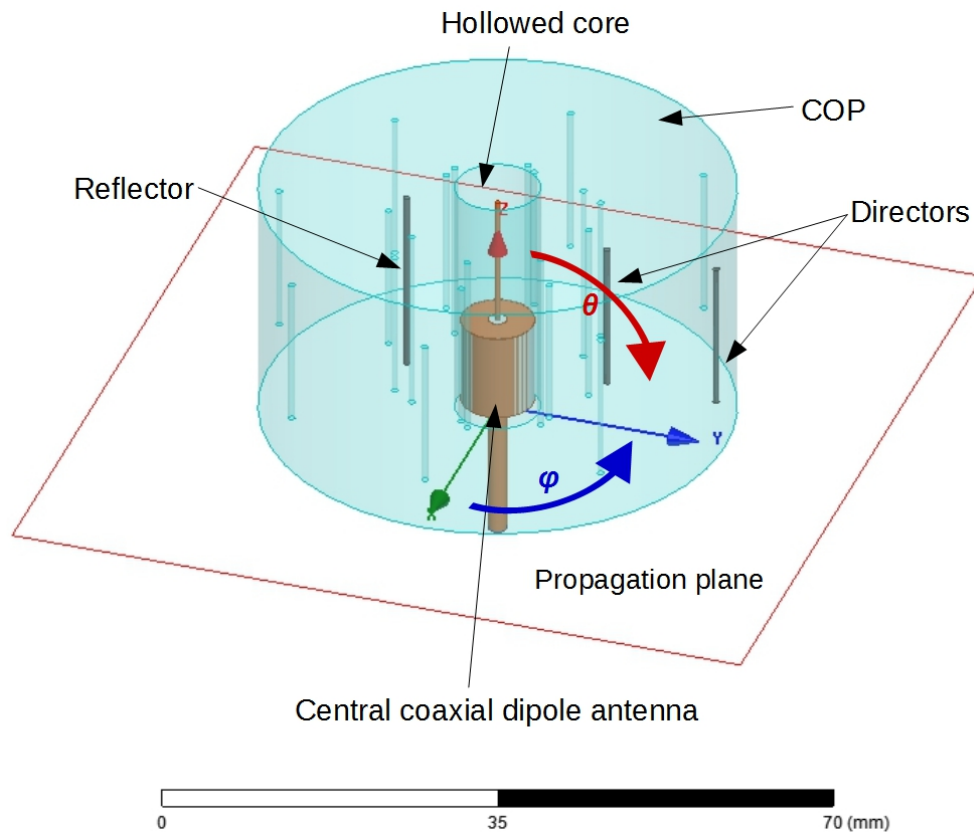


Figure 49 : Coaxial dipole Yagi-Uda antenna system in a unidirectional “narrow beam” configuration embedded in COP cylinder in vacuum

The dimensions of the cylinder of COP are the following: internal diameter of 9 mm, external diameter of 50 mm and height of 27 mm. For the dimensions of the central antenna, we have applied the optimization procedure defined above, and in this case we have a SwCoef = 0.943, meaning a 5.7% diminution of the antenna’s length compared to a system within vacuum.

As for all the previous simulations, we want to extract the performances of the system. In addition, we will here compare these performances with those of the equivalent system in vacuum. The three following figures (figures 50) to 52)) will be the comparison of the S11, the Re & Im parts of the impedance and the radiation patterns of these two systems.

The results & performances for the system in COP will be in red on the graphics bellow, those of the system in vacuum in blue.

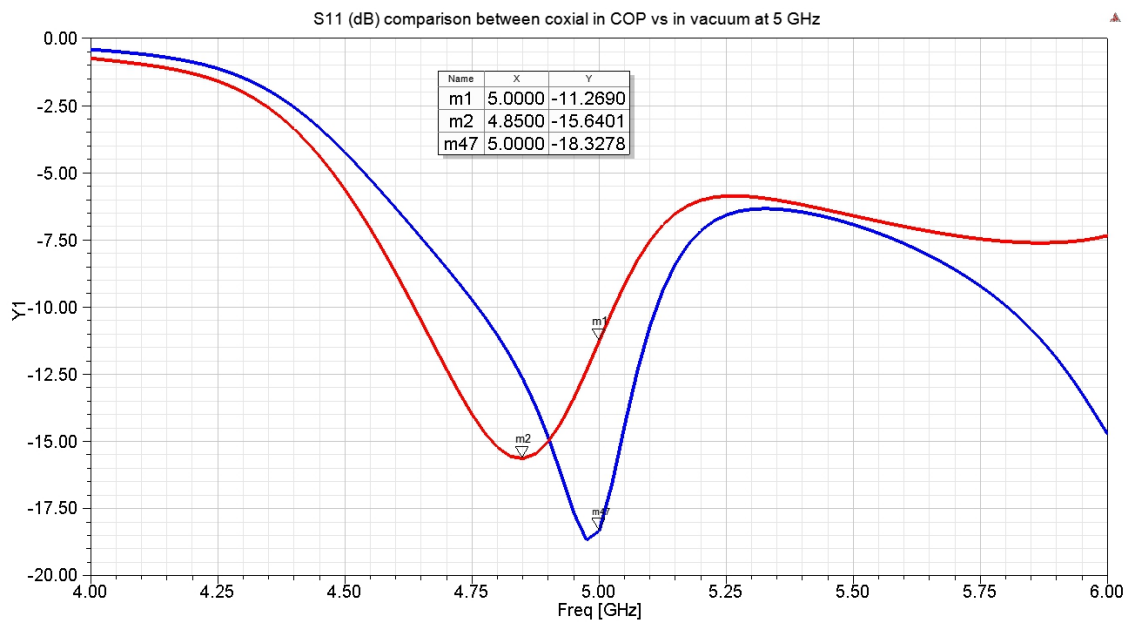


Figure 50 : Evolution of the S11 of the coaxial dipole antenna system in COP (red) & in vacuum (blue) both in unidirectional configuration

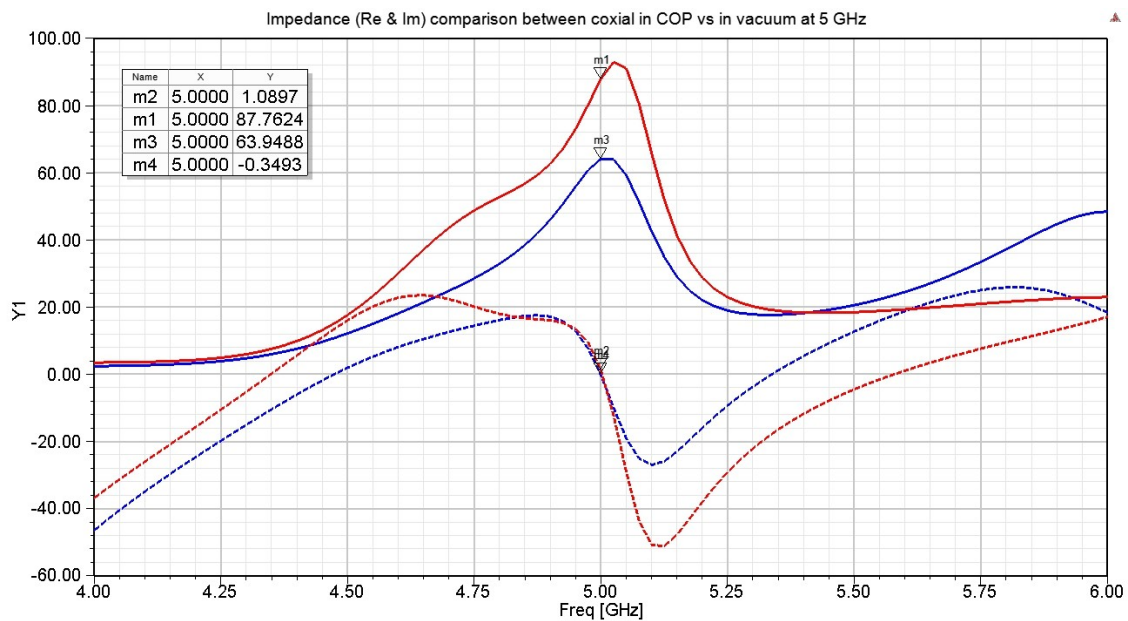


Figure 51 : Evolution of the impedance of the coaxial dipole antenna system in COP (red) & in vacuum (blue) both in unidirectional configuration

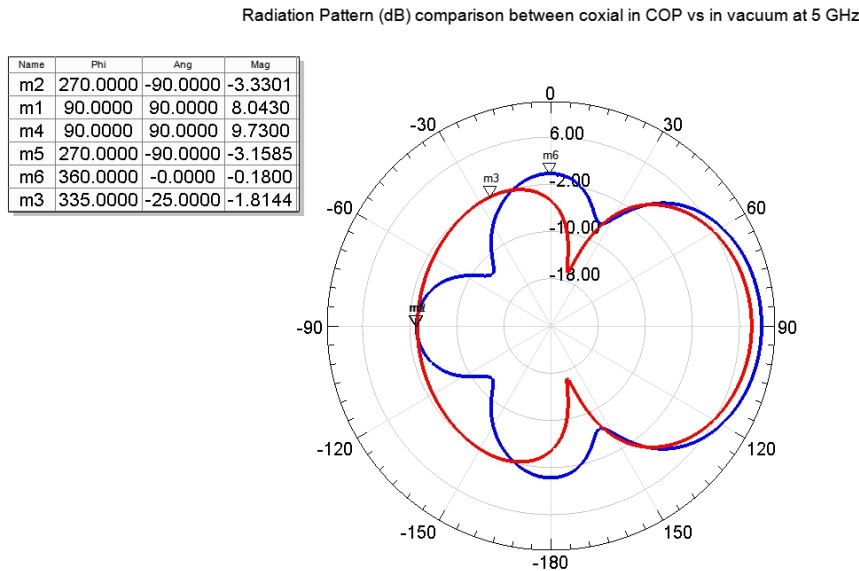


Figure 52 : 2D radiation pattern of the coaxial dipole antenna system in COP (red) & in vacuum (blue) both in unidirectional configuration

With these three figures we can see the impact of the COP cylinder on the behavior of the system. First, we notice a shift of the S11 resonance peak at 4.85 GHz instead of 5 GHz and a diminution of the S11 peak. Second, while we still have an imaginary part nullified at 5 GHz, there is a notable increase of the real part at that same frequency, from 63.95 Ohms to 87.76 Ohms. Lastly, we can observe a notable change in the radiation diagram, with a decrease of the forward gain of the antenna, with respectively, from 9.73 dB to 8.04 dB (so a 1.69 dB decrease). The backfire gain remains more or less unchanged but that lobe has widened, especially at the -30° & -150° angular positions. We also notice a 1.63 dB decrease of the lateral lobes. The comparison of the lateral gains is done by taking the maximum value of that gain on each diagram. This mean that we might compare gain which are not locate at the same ϕ angle value, as we can see on the figure 52) above, with a comparison of the value of the lateral lobes at 335° & 360°.

Overall, besides the diminution of the forward gain which is clearly a drawback of the COP embedding, the performances remains quite close, and there is no major changes to the behavior of our system. The FTBR of the system goes from 13.03 dB to 11.19 dB, with almost no variation of the backfire gain, highlighting the absence of change besides the diminution of the forward gain.

Finally, on the figure 53) bellow, we have the comparison of the 3D radiation pattern of the two systems:

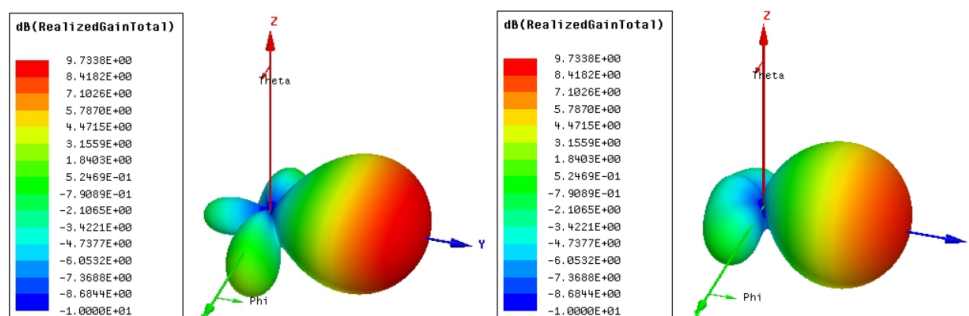


Figure 53 : 3D radiation pattern of the coaxial dipole antenna system in COP (right) & in vacuum (left) both in unidirectional configuration

This figure allows us to visualize the diminution of the lateral lobes of the system in COP as compared to the one in vacuum, as well as the widening of this backfire lobe. We can also notice that the front lobe is of course at an inferior level of gain, but is also less directive.

Now that we have seen the impact of the COP on the system, we need to improve it. Indeed, this system under its present form is not feasible. The reason for that is the unavailability on the market of COP rod of the size we need for it. Therefore we need to adapt our design to available COP supplies. In particular, we are able in our facilities to produce rectangular COP slides of various sizes and thicknesses. This is why the following simulation will present the performances of the new system realized with this specific material supply.

Besides these considerations, we should also try to improve the gain of our antenna, and a system with less COP on the pathway of the propagating waves could decrease the losses inside the polymer and therefore, enhance the final gain of the antenna.

The architecture of that system has been briefly introduced in chapter 2 and consist in a shift from the previously presented cylinder configuration into an 8 COP vertical slides configuration, in which the fluidic channels are embedded inside the slides.

4) Simulation of the coaxial dipole based system embedded in COP slides

Since we will now have a system where the parasitic elements will be embedded inside the slides of COP but where the space between the slides are filled with nothing but vacuum it will have an impact on the effective wavelength. Indeed, that modification of the propagation medium will impact the effective dielectric constant, ϵ_{EFF} , and then the effective wavelength, λ_{EFF} .

In order to determine that new, we have run simulations where we have made variation of that value until the system resonates at 5 GHz. We found that the effective wavelength of the system was $\lambda_{\text{EFF}}=50$ mm, which is in between the wavelength in vacuum and the one in COP ($60 \text{ mm} > 50 \text{ mm} > 40 \text{ mm}$). Of course, losses have been taken into account in these simulations.

Based on this, we designed the simulated system, which is presented just bellow on figure 54):

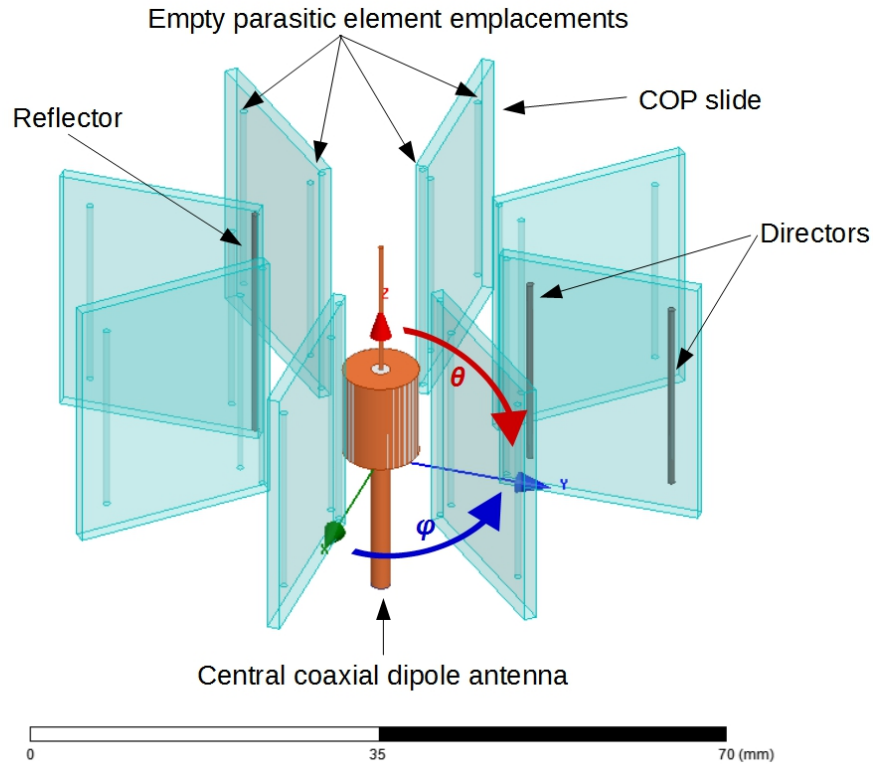


Figure 54 : Coaxial dipole Yagi-Uda antenna system in a unidirectional “narrow beam” configuration embedded in COP slides in vacuum.

The dimensions of the slides of COP are the following: 21 mm x 1.3 mm x 27 mm (length x width x height). Each slide is spaced by 45° from the previous and the next one. Its spacing from the central antenna’s central conductor is 12mm (slightly less than the spacing of the reflectors, at $\lambda_{\text{EFF}} / 4$, or 12.5 mm), in order to encapsulate all channels. For the dimensions of the central antenna, we have applied the optimization procedure defined above, and in this case we have a SwCoef = 0.981, meaning a 1.9% diminution of the antenna’s length.

As for all the previous simulations, we want to extract the performances of the system and compare them to the performances of the equivalent system in vacuum. We will also compare the performances of the system totally embedded in COP in order to see the impact of the architecture modifications. The three following figures (figures 55) to 57)) will be the comparison of the S11, the real & imaginary parts of the impedance and the radiation patterns of these two systems.

The evolution of the results & performances of the system presented in figure 54) will be represented in red on the graphics bellow, those of the system totally embedded in COP of the figure 49) in blue and those of the system in vacuum in green.

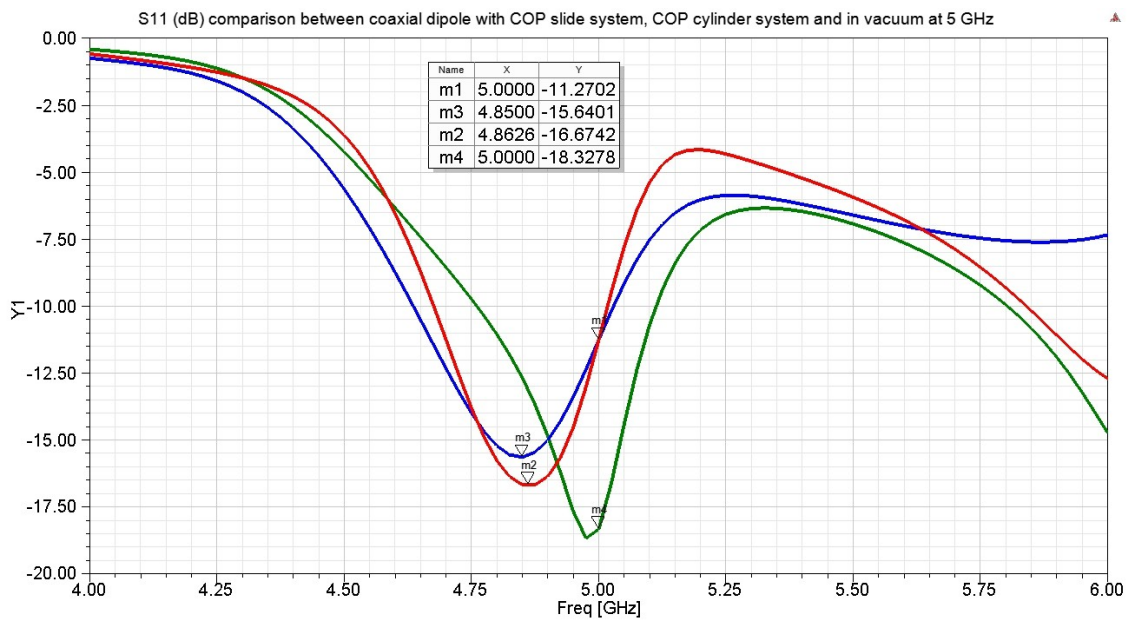


Figure 55 : Evolution of the S11 of the coaxial dipole antenna system with COP slides (red), with COP cylinder (blue) & in vacuum (green) all in unidirectional configuration

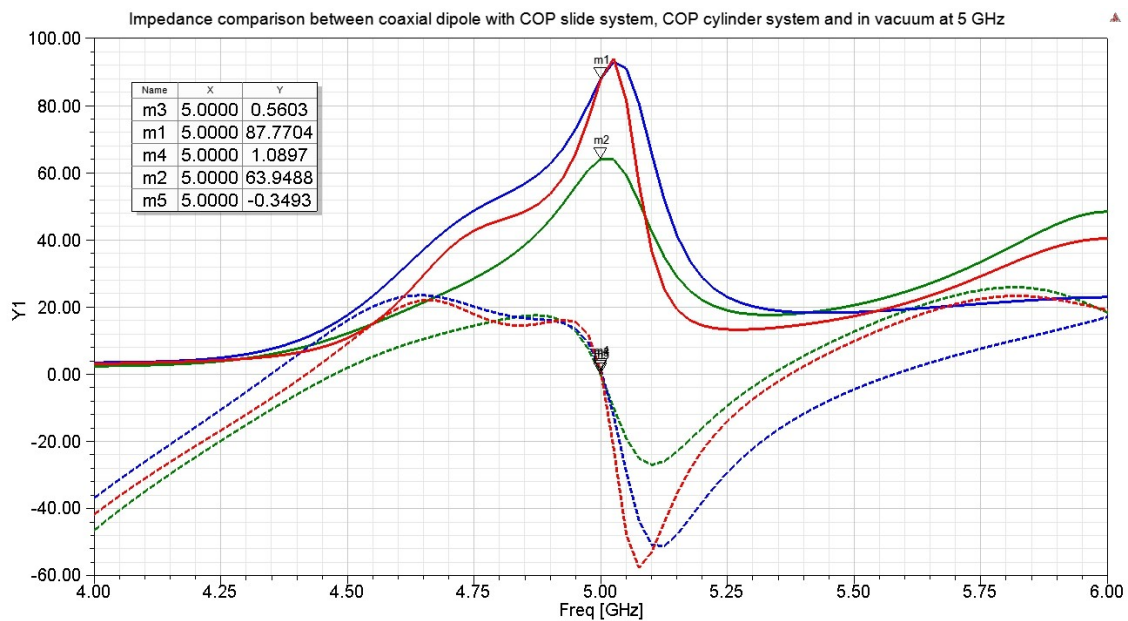


Figure 56 : Evolution of the impedance of the coaxial dipole antenna system with COP slides (red), with COP cylinder (blue) & in vacuum (green) all in unidirectional configuration

Radiation Pattern comparison between coaxial dipole with COP slide system, COP cylinder system and in vacuum at 5 GHz

Name	Phi	Ang	Mag
m1	90.0000	90.0000	9.8043
m2	270.0000	-90.0000	-14.2916
m4	90.0000	90.0000	8.0430
m5	270.0000	-90.0000	-3.3301
m6	335.0000	-25.0000	-1.8144
m8	270.0000	-90.0000	-3.1585
m7	90.0000	90.0000	9.7300
m9	360.0000	-0.0000	-0.1800
m3	354.0000	-6.0000	-1.0625

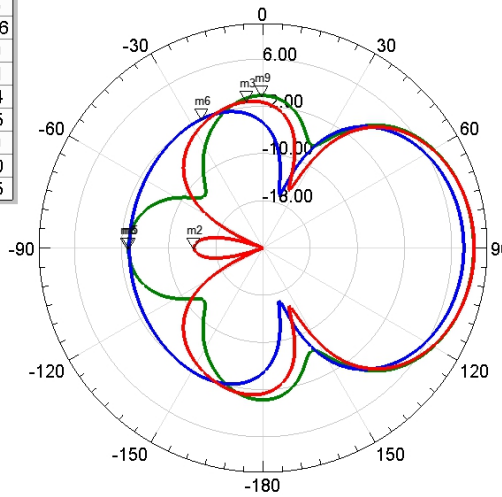


Figure 57 : 2D radiation pattern of the coaxial dipole antenna system with COP slides (red), with COP cylinder (blue) & in vacuum (green) all in unidirectional configuration

With these three figures we can see clearly that the overall performances of the COP slide system are superior to those of the COP cylinder system, especially on the radiation diagram, but its behaviour is very close to it, at least for the S11 and the impedance. For the radiation pattern, its behaviour is closer to the system in vacuum, as well as its performances. This is coherent with the fact that the effective dielectric constant of the COP slide system is lower than for the COP cylinder system, which therefore generates less dielectric losses as the waves travel from the central antenna.

We notice that the shift of the S11 resonance peak around 4.85 GHz instead of 5 GHz is still present for the 2 system in COP & that the two curves are quite similar. Impedance wise, we notice very little changes between those two systems. Finally, their radiation diagrams are also very close at the exception of the backfire gain, which is significantly lower for the slide architecture compared to the cylinder one.

We could add to these figures those of the FTBRs, which are also in favor of the COP slide system. Indeed, we have an FTBR of 24.09 dB for it, against an FTBR of 13.03 dB for the system in vacuum and 11.19 dB for the COP cylinder system. The following figure 58) displaying the 3D radiation diagram of the two systems will also illustrate this fact.

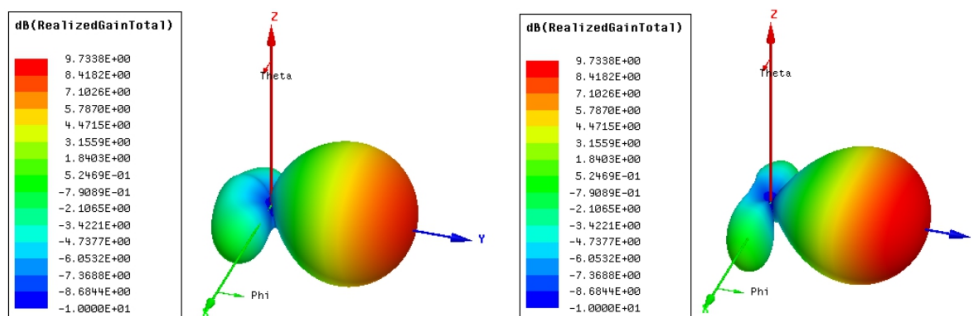


Figure 58 : 3D radiation pattern of the coaxial dipole antenna system with COP slides (left) & with COP cylinder (right) both in unidirectional configuration

As we can see on this figure 58), we notice the almost disappearance of the backfire lobe, which is coherent with the new FTBR we have calculated.

To conclude on this, we can say that the COP cylinder architecture appears inferior to the COP slide architecture in all domains but the lateral lobes, with a difference of 0.78 dB slightly in favor of the cylinder architecture (at -1.81 dB against -1.06 dB). The COP slide system is also superior to the system in vacuum on all points (except that its resonance peak is not centered at 5 GHz), which may come as a surprise, but could be explained by the fact that the emitted waves of the central antenna might get an additional focus through the COP slide to the initial focus of the directors+reflector assembly. That extra focus could be the cause of this small gain boost.

Now that we have seen the impact of the COP slides architecture on the performances, we need to upgrade the realism of our simulation by introducing the electrolyte inside the columns in order to have a more accurate picture of the system's performances.

5) Simulation of the coaxial dipole based system embedded in COP slides with electrolyte

The electrolyte we are going to use is an aqueous solution of NaOH, with a concentration of 1 mol.l⁻¹. In order to add it in our simulation model we need to know three parameters: its conductivity σ , its dielectric constant ϵ_{EFF} and its loss tangent $\tan \delta$.

We can calculate the conductivity with the help of the Kohlrausch law, which is the following:

$$\sigma = \sum_i (\lambda_i * C_i) \quad (12)$$

Where σ is the solution electrical conductivity in S.m⁻¹, λ_i is the ionic molar conductivity of ions i present in the solution in S.m².mol⁻¹, and C_i is the concentration of the ions i present in the solution in mol.m⁻³. Here we have a solution of NaOH with a 1 mol.l⁻¹ concentration (equivalent to a 1000 mol.m⁻³ concentration), which is the same for the two components (Na⁺ & OH⁻) of the ionic compound.

We now from the literature [7] the value of ionic molar conductivity for Na⁺ and OH⁻, which are respectively 5.008 mS.m².mol⁻¹ and 19.8 mS.m².mol⁻¹. Therefore we can calculate the conductivity σ , which is equal to 24.808 S.m⁻¹.

For the two other parameters, it was relatively easy for us to perform a rough properties measurements of the real solution. The measurement was done with a narrow band resonating cavity method, at a frequency between 1 & 2 GHz, and gave us a relatively good estimation of the solutions dielectric properties. The results of this measure gives us two parameters, ϵ' & ϵ'' . Their values are respectively 74.77 and 90.94. We can deduce from there the value of $\tan \delta$ from the following equation:

$$\tan \delta = \frac{\epsilon''}{\epsilon'} \quad (13)$$

So here, we have $\tan \delta = 1.21$. We're going to consider the measured value of ϵ' as the value for the effective permittivity ϵ_{EFF} of the electrolyte, and so we will have the following properties for our electrolyte:

- **1 mol.l⁻¹ NaOH aqueous solution: $\sigma = 24.808 \text{ S.m}^{-1}$, $\epsilon_{\text{EFF}} = 74.77$, $\tan \delta = 1.21$.**

That being established, we will now move on to simulate the impact of the addition of that electrolyte to our model, as it is showed on figure 59) bellow.

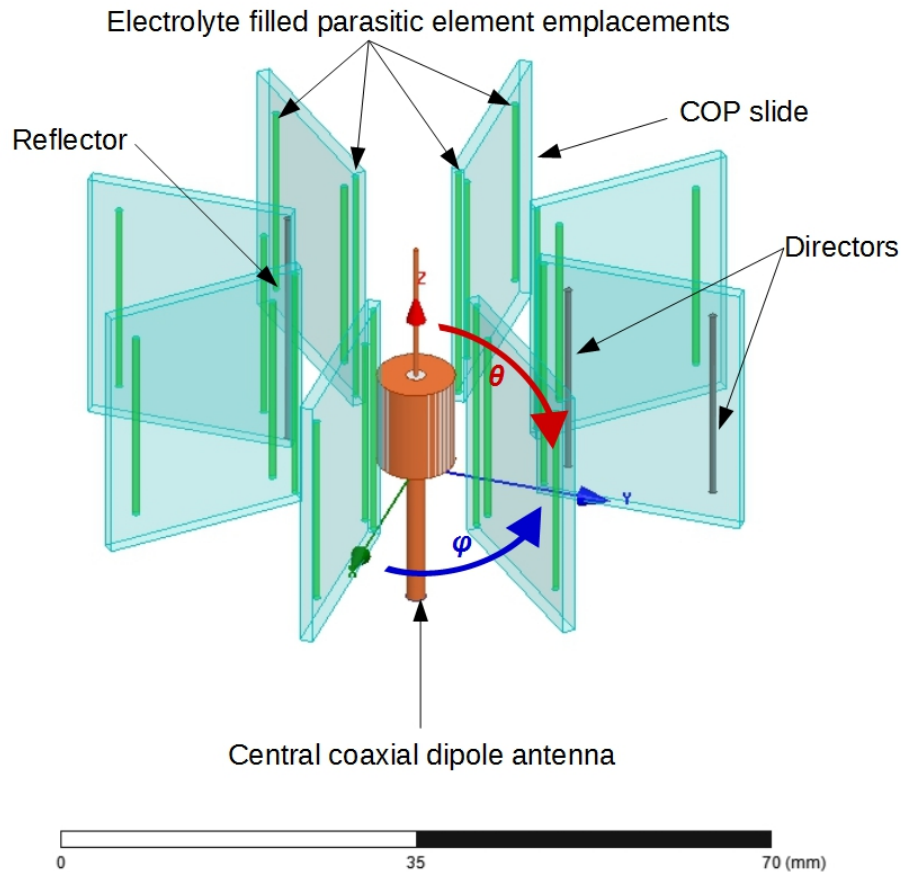


Figure 59 : Coaxial dipole Yagi-Uda antenna system in a unidirectional “narrow beam” configuration embedded in COP slides containing electrolyte in vacuum.

The only initial difference between this design and the previous one is the filling of the previously empty columns with the electrolyte solution. It means this simulation keeps all the previous properties of the system presented in figure 54), in addition of the new ones induced by the addition of the electrolyte. For the dimensions of the central antenna, we have applied the optimization procedure defined above, and in this case we have a SwCoef = 0.981, meaning a 1.9% diminution of the antenna's length.

Here again, we want to extract the performances of the COP slide system with electrolyte and compare them to the performances of the same system without the electrolyte. The three following figures (figures 60) to 62)) will be the comparison of the S11, the Re & Im parts of the impedance and the radiation patterns of these two systems.

The evolution of the results & performances of the system presented in figure 59) will be represented in red on the graphics bellow, those of the one presented on figure 54) in blue.

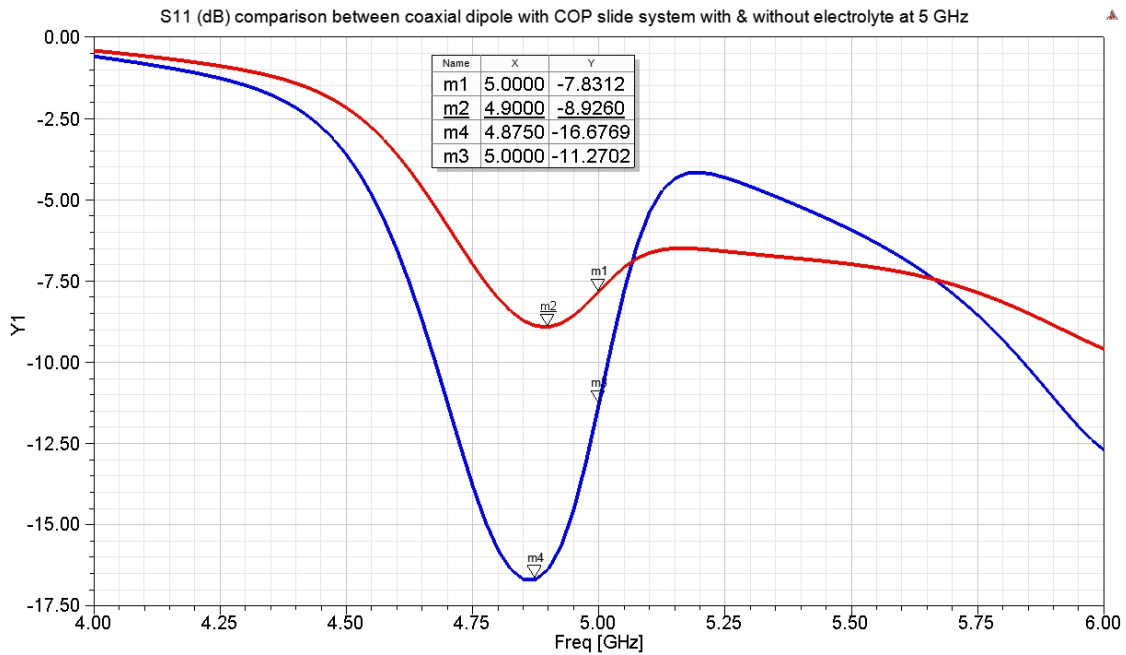


Figure 60 : Evolution of the S11 of the coaxial dipole antenna system with COP slides containing electrolyte (red), without electrolyte (blue) both in unidirectional configuration

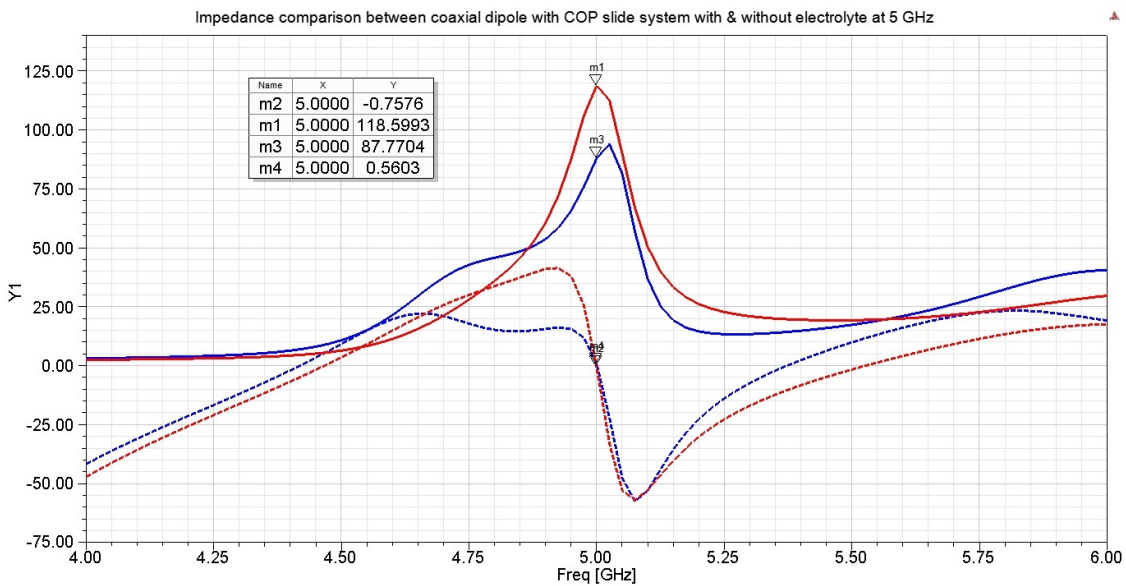


Figure 61 : Evolution of the impedance of the coaxial dipole antenna system with COP slides containing electrolyte (red), without electrolyte (blue) both in unidirectional configuration

Radiation Pattern (dB) comparison between coaxial dipole with COP slide system with & without electrolyte at 5 GHz

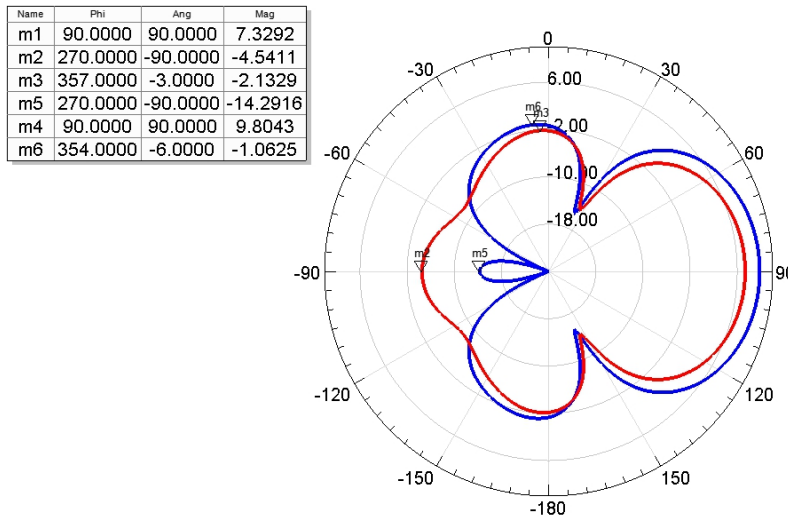


Figure 62 : 2D radiation pattern of the coaxial dipole antenna system with COP slides containing electrolyte (red), without electrolyte (blue) both in unidirectional configuration

With these figures above we can clearly see the impact of the electrolyte on our system's performances. We can see a significant that the two S11 peaks stay aligned but that the addition of electrolyte attenuate it. We observe also an increase of the real & imaginary part of the impedance, but here also the curves stay aligned, which is the result of the optimization realized on this system.

Finally, we notice a diminution of the system's performances in terms of radiation pattern, with an increase of backfire gain & a decrease of the forward gain of 2.47 dB. The only part where the performances seem to be slightly better is the lateral gain, with a decrease of 1.07 dB. That decrease could be explained mostly by the increase of the backfire gain.

That increase of the backfire gain, and the associated decrease of the forward gain can be partly explained by the presence of an electrolyte filled column in the center of the Yagi-Uda 3+1 antenna. Indeed, as we can see inside the red circle on figure 63) below:

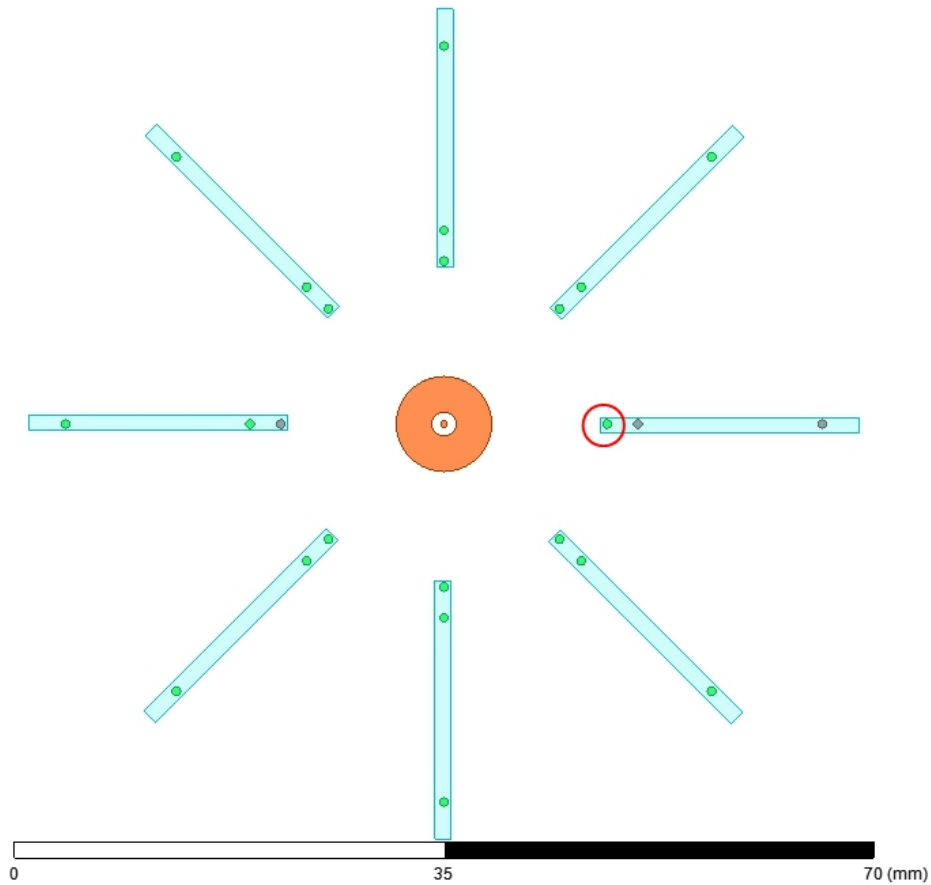


Figure 63 : Top view of the coaxial dipole antenna system with COP slides containing electrolyte

That column of electrolyte placed here have an important impact on the radiation diagram of the antenna, due to the lossy nature of the electrolyte (as it was explained on chapter 2), and its position right in the middle of the Yagi-Uda antenna, close to the central-feed antenna. We can see how it will be interesting for future works to focus on the improvement of the characteristics of the electrolyte properties, by switching to a non aqueous electrolyte for example.

The following figure 64) displays the 3D radiation diagram of the two systems, and will furthermore illustrate the impact of the electrolyte addition to the system in terms of electromagnetic performances.

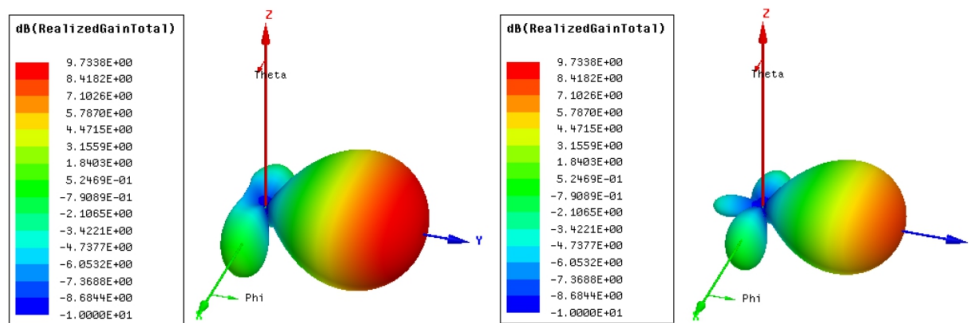


Figure 64 : 3D radiation pattern of the coaxial dipole antenna system with COP slides containing electrolyte (right) & without electrolyte (left) both in unidirectional configuration

We will especially notice here the re-appearance of the backfire lobe, which, as we say above, is most probably in majority due to the presence of the electrolyte filled column in the middle of the antenna elements alignment.

Overall, the lesser performances of the system with the addition of the electrolyte were rather predictable, given the properties of the electrolyte solution. This is fundamentally linked to the actuation mechanism we chose, but it does not jeopardize the concept of our entire system. An analysis of the power consumption and its relation with the gain could tell us more precisely what could be our progress margin if we chose to explore the use of different electrolytes for the fluidic actuation.

We are now coming to the final iteration of the system, the one where we add the tanks into the design in order to see if they're going to interfere with the waves in a way which would lead to a too important degradation of the performances.

6) Simulation of the coaxial dipole based system embedded in COP slides with electrolyte & tanks

The tanks added to the figure's 59) design are cylinders inserted in the slides, which are parallel to their surface. They have a diameter of 4.2 mm, a height of 0.85 mm, and are placed at the bottom of the columns. They are positioned in such way that the bottom of the column coincide with the bottom of the tank in order not to change that length. Indeed, when the Galinstan is going to rise inside them, it will not totally empty the tank, so there will be a metal continuity from the bottom of the tank to the top of the column, like on the example showed on figure 65) below:

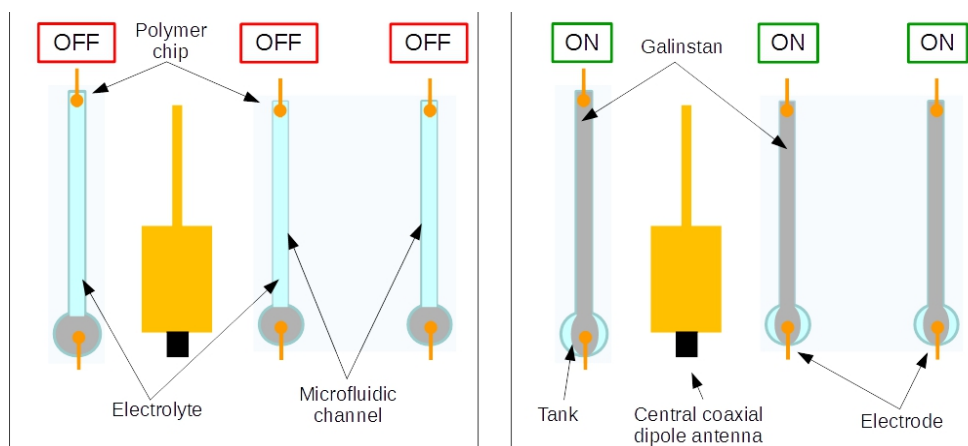


Figure 65 : Illustration of the working principle of the fluidic system

As we can see on the right part of figure 65), the bottom of the column is made of the Galinstan which has not let the tank at the end of the rise. This aspect of the modeling is extracted from the observation we have made on experimentation, as well as from examples of the literature, such as in [8].

The position of the tanks in our design are affected by the fact that we choose to center the parasitic elements relatively to the geometric center of the central coaxial antenna. The previous figures showed configuration where the tanks were well separated from one another. The reason was they were not at the right scale, and were principle schematics. We know from the simulation (which must be at the exact scale & dimensions), that the architecture choice we have made has for consequence the potential overlapping of the first director and the reflector tanks on each slides, as we can see on the following figure 66).

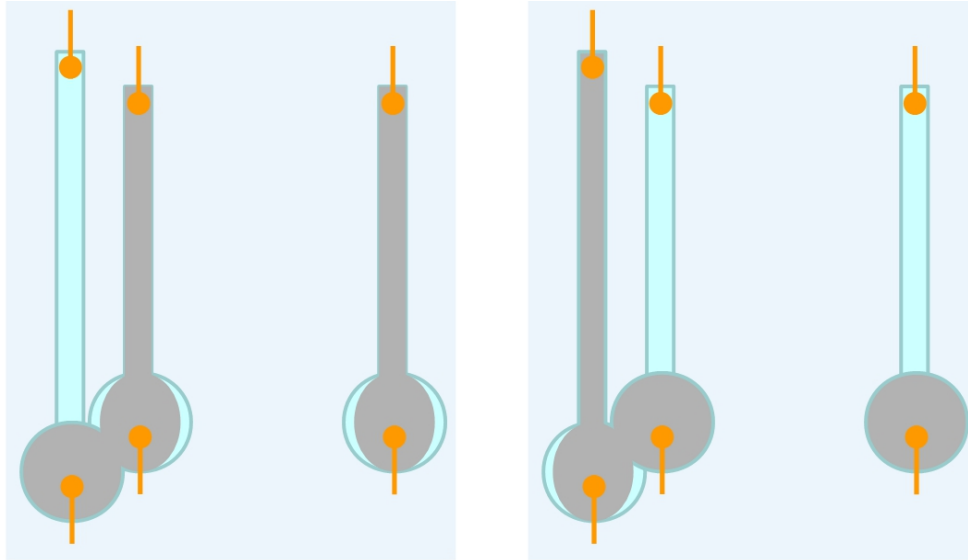


Figure 66 : Illustration of the overlapping tanks in the two “activated” configurations used in the simulation with the two directors ON (left) and the reflector ON (right)

Only those two tanks are susceptible to overlap. The reason is because the design rules state that the spacing between the reflector & the feed must be $0.25 \lambda_{\text{EFF}}$, and $0.3 \lambda_{\text{EFF}}$ between the feed & the first director. Therefore the spacing between the two columns must be of $0.05 \lambda_{\text{EFF}}$, which is a small value and furthermore, which depends on the frequency.

As we saw on previous figures, the tank is not fully emptied during the rise. This implies that it must contain more Galinstan the just enough to fill the channel. Because of this, their radius is very likely to be greater than that $0.05 \lambda_{\text{EFF}}$ value.

No precise rule to define what is the ideal tank diameter has been determined by us. Instead in this simulation we have chosen not to have a column volume superior to 70% of the tanks volume. In this case we have tanks with a 2.1 mm radius and a height of 850 μm for columns which have a diameter of 700 μm & heights of 16.3 mm (directors) & 21.3 mm (reflector).

We are well aware that this is a simplification of the system, but without an extensive test campaign on fluidic chips of various tank size, we cannot settle definitely that question. We should also precise that given the method of fabrication we have developed, it would have been very complex for us to do this campaign of test, because as we will see on chapter 4, we had to fix once and for all the geometry of our chips molds..

Interestingly, we can nonetheless note that the increase of the share of the volume occupy by the COP (for example, through the increase of the slides thickness) would lead to a diminution of the

columns height, and therefore of the volume needed for the tanks. This is due to the fact that the increase of the COP inside the volume of the antenna increases in turn the effective dielectric constant of the system. Given that the effective wavelength is inversely proportional to that value, the effective wavelength will decrease, and thus the height of the columns. On the other hand, this would also diminish the numerical value of $0.05 \lambda_{\text{EFF}}$, and accentuate the overlapping of the tanks, but this might be of no consequences on the behavior of the chips.

Indeed, it must be noted that this overlapping is not expected to be particularly problematic for us, given that we will never have to activate simultaneously the reflector and the director plugged on the same overlapped tanks. Indeed while we might switch ON the two directors, doing the same for the first director and the reflector would be useless since we work inside the horizontal plan and want either to reflect either to focus the beam from a certain direction, and switching ON the two elements would be counterproductive to both objectives.

We should add that even if it was to be problematic, we already have investigated potential alternatives. We have run simulations where the directors are shifted towards the top of the slide in order to suppress that overlapping of the tanks, and thus breaking the alignment of the geometrical center of the ensembles “column+tanks”. These simulations shows a minor negative impact on the performances of the whole system, but not in a magnitude which would prevent us to adopt this solution would it be needed. Indeed, we speak of a diminution of the forward gain of 0.25 dB for the new architecture, and a FTBR which actually gets better at 12.31 dB against 9.74 dB for the configuration presented in figure 66). This is to be kept in mind in order to have a back-up architecture in case where the fabrication and/or the behavior of the fluidic system with the overlapped tanks would appear to be problematic.

This problem being addressed, we can take a look at the simulated architecture (with the overlapping tanks), which can be found bellow on figure 67):

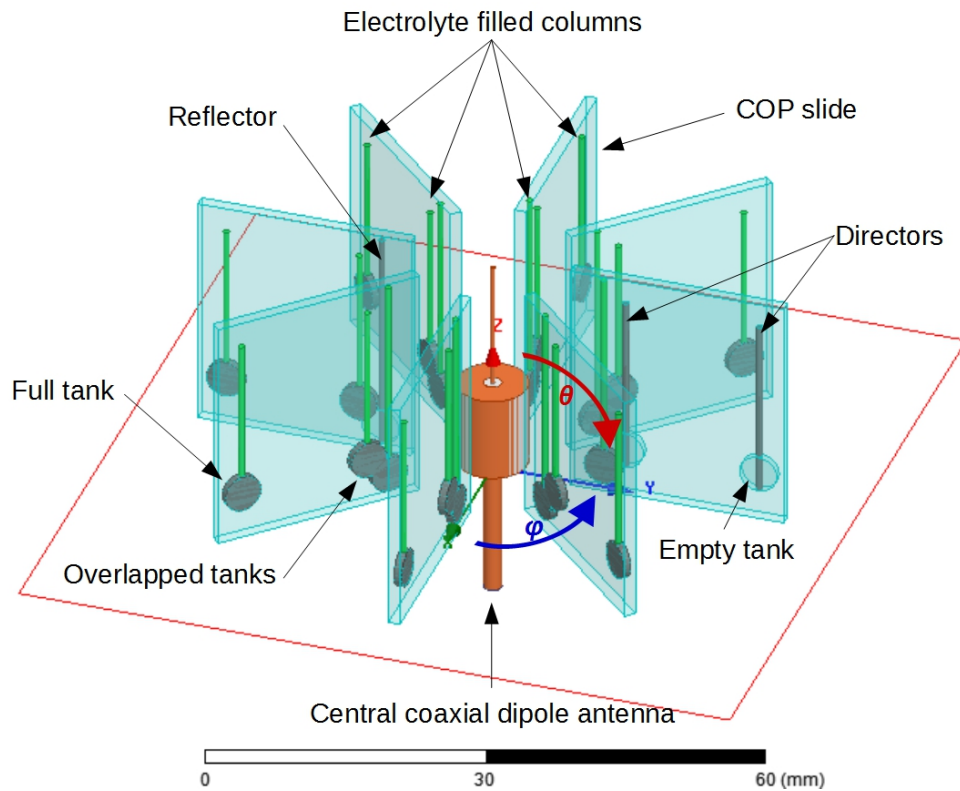


Figure 67 : Coaxial dipole Yagi-Uda antenna system in a unidirectional “narrow beam” configuration embedded in COP slides containing electrolyte and Galinstan tanks in vacuum

The presence of the tanks is the only initial difference between this design and the previous one. For the dimensions of the central antenna, we have applied the optimization procedure defined above, and in this case we have a $S_{wCoef} = 0.965$, meaning a 3.5% diminution of the antenna’s length. This is the same S_{wCoef} value as for the system without electrolyte or tanks placed in vacuum.

In this case, we want to extract the loss of performances due to the addition of the tanks to the system. The three following figures (figures 67) to 69)) will be the comparison of the S_{11} , the Re & Im parts of the impedance and the radiation patterns of these two systems.

The evolution of the performances of the system presented in figure 66) will be represented in shades of red on the graphics bellow, those of the second system, which was presented on figure 59), in shades of blue.

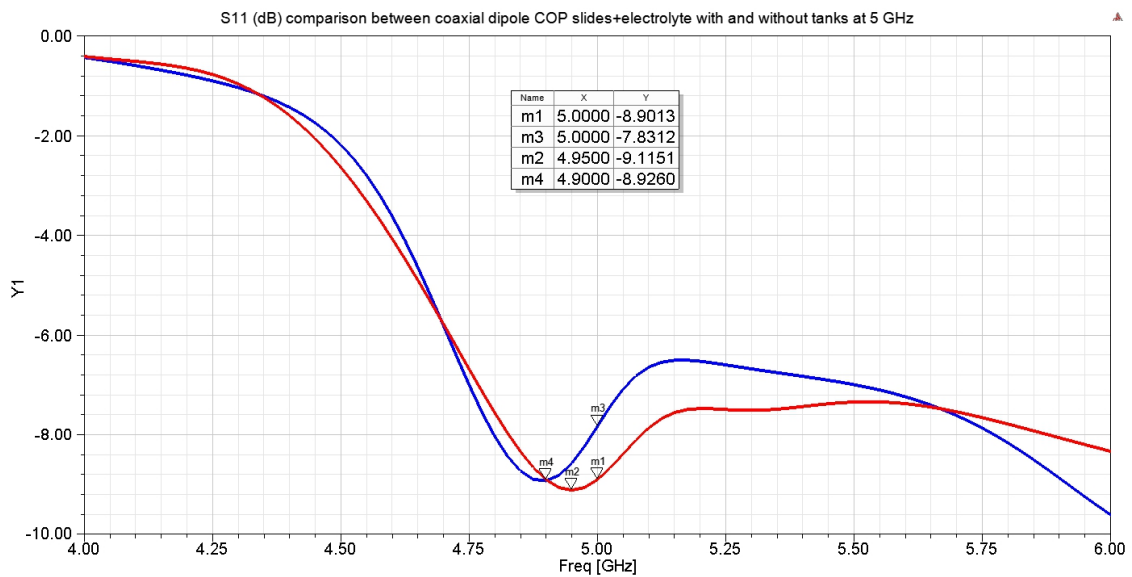


Figure 68 : Evolution of the S11 of the coaxial dipole antenna system with COP slides containing electrolyte and tanks (red), with electrolyte & no tanks (blue) both in unidirectional configuration

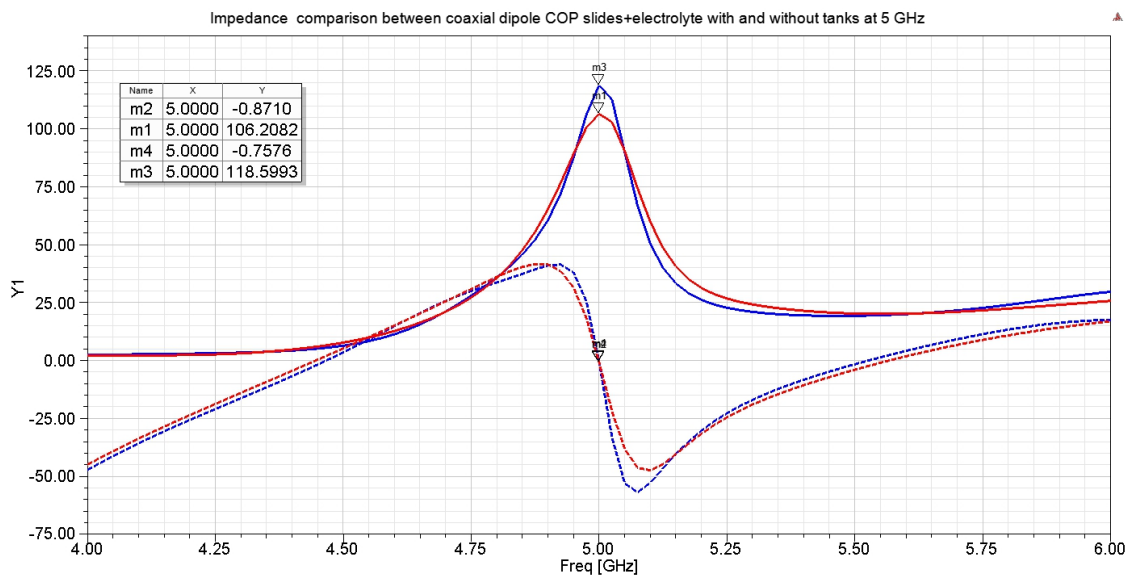


Figure 69 : Evolution of the impedance of the coaxial dipole antenna system with COP slides containing electrolyte and tanks (red), with electrolyte & no tanks (blue) both in unidirectional configuration

Radiation Pattern (dB) comparison between coaxial dipole COP slides+electrolyte with and without tanks at 5 GHz

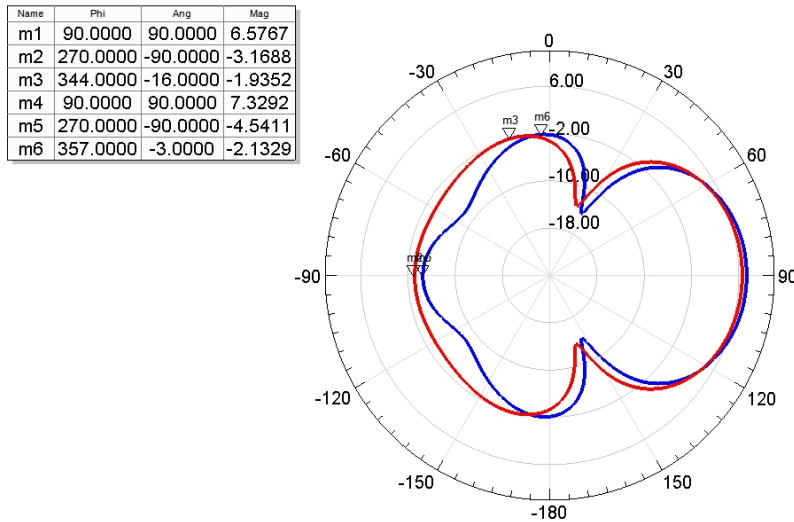


Figure 70 : 2D radiation pattern of the coaxial dipole antenna system with COP slides containing electrolyte and tanks (red), with electrolyte & no tanks (blue) both in unidirectional configuration

Thanks to the three figures above, we are in capacity to assess the impact of the tanks addition on the performances of the system. This impact is overall relatively minor. We can actually notice a small offset of the S11 peak and a 1.07 dB decrease of its depth. The variation of the impedance curves can be qualified as negligible and both curves stayed aligned. Again, we must remind that this fixed position of the Im part being the result of the optimization realized on this system as we said before.

To conclude on these results, we notice a slight diminution of the system’s performances in terms of radiation pattern, with a 1.25 dB increase of backfire gain. The forward gain is a decreased slightly by 0.76 dB, as for the lateral gain, it saw a 0.2 dB increase due to the addition of the tanks.

The comparison of the system’s FTBR is actually slightly at the advantage of the system with the tanks, at 9.86 dB against 9.54 dB without the tanks. But we can notice on figure 69) that beside the main tip of the backfire lobe located at -90°, we also have an increase of the level of backfire gains around that main spike, at 345° for example. This is very clear when we look at the comparison of the 3D radiation pattern of the two systems in figure 70).

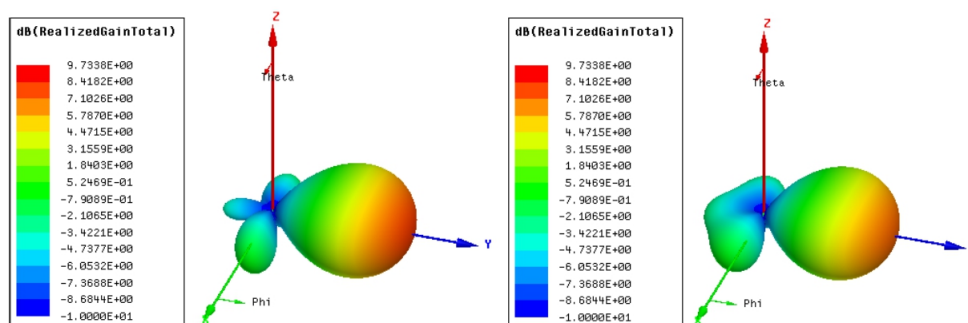


Figure 71 : 3D radiation pattern of the coaxial dipole antenna system with COP slides containing electrolyte & tanks (right) & with electrolyte and no tanks (left) both in unidirectional configuration

On this figure we can clearly see the widening of the backfire gain on the right diagram. Where it was only on spike on the left diagram, it has become larger after the addition of the tanks. We can hypothesize that most of the forward gain losses observed in figure 69) are due to this increase of the backfire gain. This could be caused by the presence of the tanks which might lead to additional parasitic reflections.

Since we have established the impact of the tanks on the behavior of a system architecture close enough to the real system, we can quickly illustrate the possibility of this system in terms of beam forming. As we know, the main objective is to perform a 360° beam steering, but we can add to this the capability of dynamically shaping the steered beam. The figure 72) on the next page is giving an example of four different parasitic elements configurations capable of producing beams of various shapes:

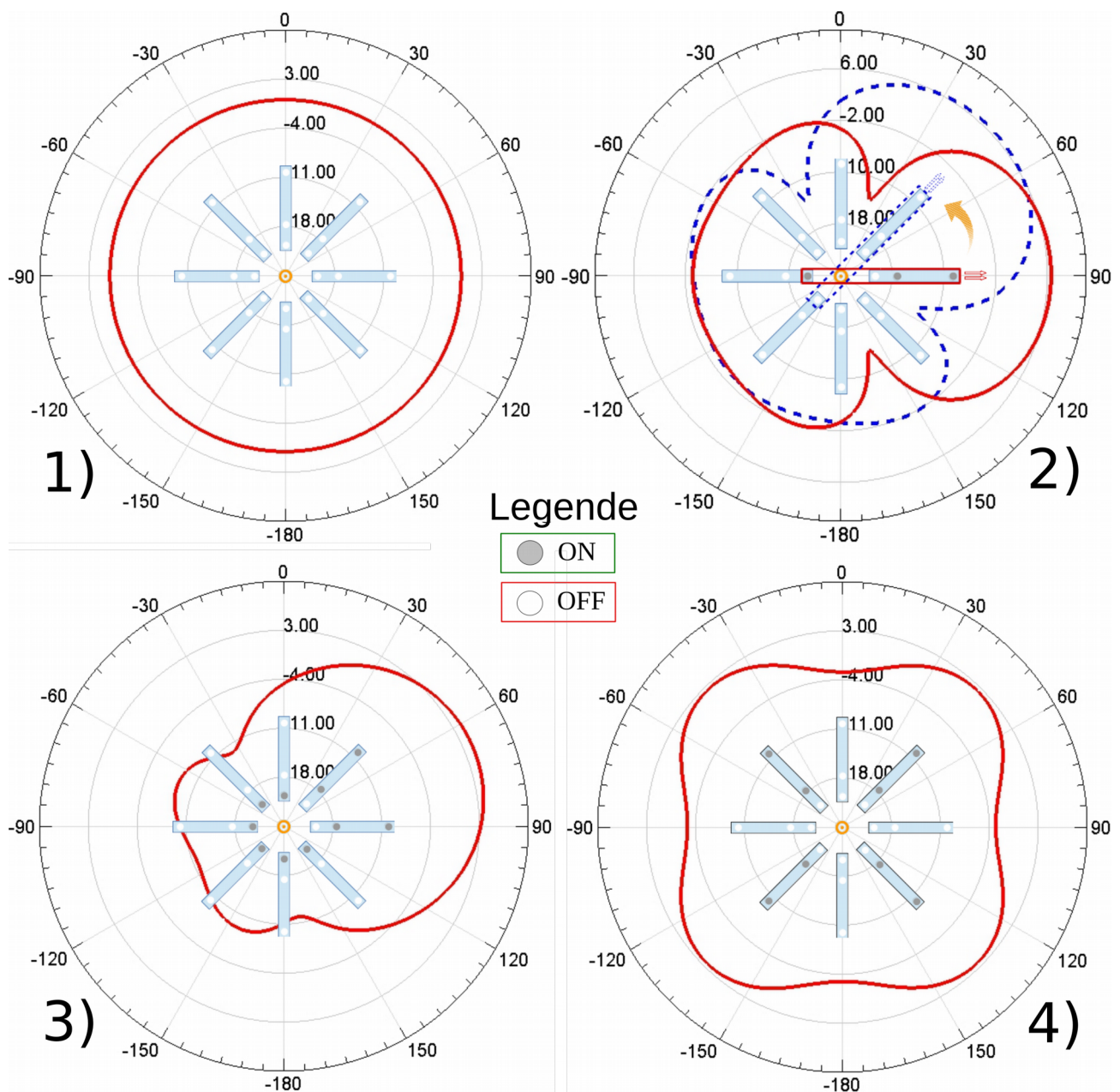


Figure 72 : Radiation pattern for four system's configurations, omnidirectional 1), unidirectional narrow beam 2), unidirectional large beam 3) & four-way multi-directional 4)

As shown on these four figures, we have at the center of each radiation pattern a simplified top view of the system corresponding to the simulated configuration, with in gray the ON columns, and in white the OFF columns.

It must be noted that all of these configuration were simulated on the base of the system's simulation presented on figure 66). One of this figure, configuration 2) was the one presented above, the three additional ones where not presented before. It must be underlined that the optimization process has not been done for the other configurations, meaning that system architecture (COP slides with electrolyte & tanks) is optimized for the configuration 2), considered to be the main one.

Now, as we can see on this figure 72), our system is allowing us to perform a wide variety of beam shaping configurations:

- 1) On this configuration, we see that if we switch OFF all the columns, we have a perfectly omnidirectional beam inside the horizontal plan, which is the propagation plan. That beam is the one of the coaxial dipole, which is expected if the system is fully on a OFF configuration.
- 2) On the second configuration, we recognize the narrow beam configuration of earlier, in red. We can illustrate here in simulation the rotation of the beam with the dotted blue radiation pattern. It was obtained by switching OFF the initial two directors and the reflector present in the red rectangle, to switch ON those present in the dashed blue rectangle. We see that by doing this, we shift the beam's direction by $+45^\circ$ up. We can easily see that if we do this continuously, we will be able to achieve a 360° beam steering, solely by activating and deactivating vertical liquid metal columns.
- 3) On that next configuration, we have achieved a directive architecture but with a wider beam than on configuration 2). This is done by activating all of the reflectors but two, and on the two slides remaining, to switch ON all the directors. This configuration allow us to better control the backfire gain and at the same time to have a wider front lobe. This lobe will of course be of a smaller gain than the configuration 2), due to its increased surface.
- 4) Finally, on the last example of configurations, we have managed to produce a squared beam. This was done by switching OFF two directors every 90° (meaning on 50% of the slides). By doing this we have a radiation pattern with 4 lobes pointing all at 90° from each others.

In terms of comparison of the performances of these designs (looked at the main lobe for the realized gain), we have the following table 3) which sum-up those for the four configuration:

*Table 3 : Electromagnetic performances of the 4 configuration at 5 GHz
(realized gain looked at the main lobe)*

	Realized gain	Directivity	Efficiency
Configuration 1)	+0.2 dB	+2 dB	66%
Configuration 2)	+6.58 dB	+8.32 dB	67%
Configuration 3)	+4.32 dB	+7.2 dB	51%
Configuration 4)	+2.4 dB	+3.6 dB	76%

The main lobe realized gains presented in the table above are extracted from the 2D radiation diagrams presented on figure 72). It is therefore the maximum realized gain on the $\theta = 90^\circ$ plan. The directivity figure is given to us by HFSS, and is the peak directivity value. It is calculated from the far field radiation onto an infinite sphere surrounding the antenna, and is the maximum value of that directivity on the whole sphere.

This table allow us to underline the fact that higher gain is obtained in our main configuration (the number 2)), for which the system is optimized. We can see that it is also the one with the highest directivity. This directivity is due to the 3+1 Yagi-Uda architecture, and therefore changes with the architecture. For example, as we can see if we compare directivities of the first & second configurations, the removal of the parasitic elements consequences is a sharp drop in directivity (-6.32 dB).

The difference between the gain and the directivity can be explained by a combination of the adaptation losses of the antenna & the energy efficiency of the antenna itself. The highest the difference between the two figures, the higher those losses & the lower the overall efficiency of the system to transform the transmitted energy into radiated energy.

If we look at configuration 3), we have a 2.26 dB decrease of the gain compared to the configuration 2). At the same time the directivity has decreased by 1.12 dB, which is only half of the gain losses. From this we can deduce that while the switch from the second to the third configuration has degraded the directivity of the system, it has also degraded its overall efficiency. Finally, we see for the configuration 4) that while we have a 4.72 dB drop in directivity compare with the configuration 2), the overall efficiency of that configuration is actually higher than all the rest of the configurations.

Those assumptions are validated if we look at the third column, showing the efficiency. It is maximal for configuration 4) at 76% and minimal for configuration 3), at 51%. We can see that in the case that interest us the most, configuration 2), it is of 67%, very close to the 66% of configuration 1), hereby showing that the gain increase of configuration 2) over configuration 1) is almost exclusively due to the directivity increase linked to the addition of the parasitic elements.

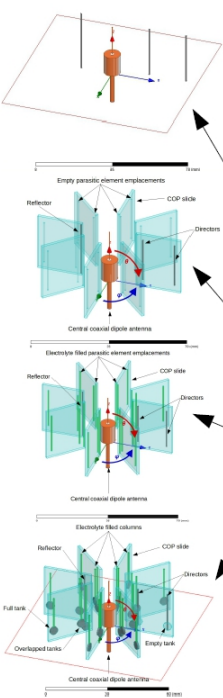
It must be noted that the activation time of all these configurations is different. Indeed, all columns are to be controlled in parallel, but the time of deployment for each system configuration is given by the slowest element. In our case, the slowest is the reflector, because it is the highest column. Therefore all configuration containing at least one reflector will be slower than one comprising even several directors. To take an example, configurations 2) & 3) will have the same deployment time which will be slower than configuration 4). Of course, the more columns involved, the more likely adjustments will be needed, which might enhance slightly the configuration switching time as the number of involved columns rises.

7) Simulation results analysis

Now that we have seen all the developmental steps leading towards the final system's architecture, we can try to analyze what is the impact of each addition on the final design. Clearly, it seems that the electrolyte is the element which take the higher toll on the performances of the system, and would be a point very rewarding to enhance in terms of performances. We can rank the different addition to the design in terms of cost in realized gain, starting from the initial theoretical wire dipole configuration. This mean we will not take into account the Alford-loop configuration nor the COP cylinder configuration, because both have been dismissed from the final design.

The ranking can be seen bellow on table 4), which illustrate the additional losses which occurs for the implementation of each new element of the system.

Table 4 : Classification of the impact on the gain of the system's design modifications



	Forward realized gain	Backward realized gain	Ranking based on losses in forward & backward gain
Initial values for the theoretical wire dipole system	+10.13 dB	-2.28 dB	
Losses due to transition from wire dipole system to coaxial dipole system	-0.33 dB	-0.87 dB	3
Losses due to transition from system in vacuum to in COP slides	-0.07 dB	-10.99 dB	4
Losses due to transition from system without electrolyte to with electrolyte	-2.47 dB	+9.75 dB	1
Losses due to transition from system without tanks to with tanks	-0.76 dB	+0.96 dB	2
Final values for complete coaxial dipole system	+6.57 dB	-3.29 dB	

Electrolyte = majority of the performance degradation
 Replacement of Water ($\epsilon_r = 80.1$) by Ethanol ($\epsilon_r = 24.5$) or Methanol ($\epsilon_r = 32.7$) would lower the losses **but also** NaOH dissolution rate

As we can see on this table, the electrolyte is the most impacting modification, followed from afar by the addition of the tanks. This is the case as well as for the forward than the backfire gain. We can also notice in some case a huge difference in terms of order of magnitude between the variation

of the forward gain and the backfire gain, as for the addition of the COP slide for example. While the impact is almost null and leaning toward the negative side on the forward gain, it is very positive on the backfire gain. Nonetheless, despite these differences, the classification is the same if we based it on the forward or backfire gain, which tend to makes it more reliable.

Interestingly, we can see that the addition of more complexity to the design constantly diminish the forward gain, when the backfire gain does not seem to follow a clear tendency towards more losses neither towards less, and those variations between these two poles present large amplitudes.

This table consolidate the conclusion that we should, if possible, try to enhance the dielectric performances of the electrolyte because it is going to be a high pay move in terms of gain enhancement. However, we have shown above that this would be difficult. An optimization work on the tanks size and placement could also be quite rewarding, even if significantly less than for the electrolyte. Optimization on the antenna might give us some extra gain, but rather few, and finally there is no interest in optimizing the slide system, since their current configuration has no negative impact on the forward gain and a huge positive impact on the backfire gain.

With this, we conclude here the presentation of our work on the simulations we've done in order to ensure of the viability of our design. In the next chapter, some simulations will be presented in order to feature a more accurate model of the fabricated central antenna, but the rest of the system will remain unchanged.

III. Bibliography

- [1] C. Balanis, *Antenna theory: analysis and design*. 2012.
- [2] B. Yuan, J. Xiong, Y. Fu, P. Liang, L. Yao, and F. Zhang, "A Novel Design Method for Improving Sleeve Antenna Performance," no. 800, pp. 2–4, 2016.
- [3] D. Rodrigo, S. Member, L. Jofre, and B. A. Cetiner, "Circular Beam-Steering Reconfigurable Antenna With Liquid Metal parasitic," *IEEE Trans. Antennas Propag.*, vol. 60, no. 4, pp. 1796–1802, 2012.
- [4] D. R. López, "Reconfigurable pixel antennas for communications," Universitat Politècnica de Catalunya (UPC), 2013.
- [5] Y. Arbaoui, V. Laur, A. Maalouf, P. Queffelec, D. Passerieux, A. Delias, and P. Blondy, "Full 3-D Printed Microwave Termination: A Simple and Low-Cost Solution," *IEEE Trans. Microw. Theory Tech.*, vol. 64, no. 1, pp. 271–278, 2016.
- [6] Zeon corporation, "ZEONEX® - Cyclo Olefin Polymer (COP)," Tokyo, 2016.
- [7] P. Vanysek, *Ionic conductivity and diffusion at infinite dilution*, CRC PRESS. 2016.

- [8] M. Wang, C. Trlica, M. R. Khan, M. D. Dickey, and J. J. Adams, “A reconfigurable liquid metal antenna driven by electrochemically controlled capillarity,” *J. Appl. Phys.*, vol. 117, no. 19, p. 194901, 2015.

Chapter 4 : Fabrication, tests & measures

I. Central antenna fabrication architecture

As we saw at the end of chapter three, we have come up with a final definition of our antenna system. The architecture retained is composed of one central coaxial dipole antenna, bottom fed via a coaxial cable, and surrounded by eight COP fluidic chips. These chips are vertical COP slides which all contain three vertical columns, which are acting as the parasitic elements (directors and reflectors) of a Yagi-Uda antenna. That Yagi-Uda antenna is more precisely a dipole 3+1 elements antenna, elements which can be on demand activated or deactivated. Indeed, these columns have at their base a Galinstan tank, and are filled with an electrolyte solution of NaOH.

As explained in the previous chapters, when we apply a sufficient voltage to the column via electrodes placed at the two ends of it, we make the Galinstan rise inside that channel. Being of a specifically calculated length, that liquid metal filled channel now acts as a director or a reflector to the central antenna.

The following figure 73) is a reminder from the previous chapter of the aspect of the system:

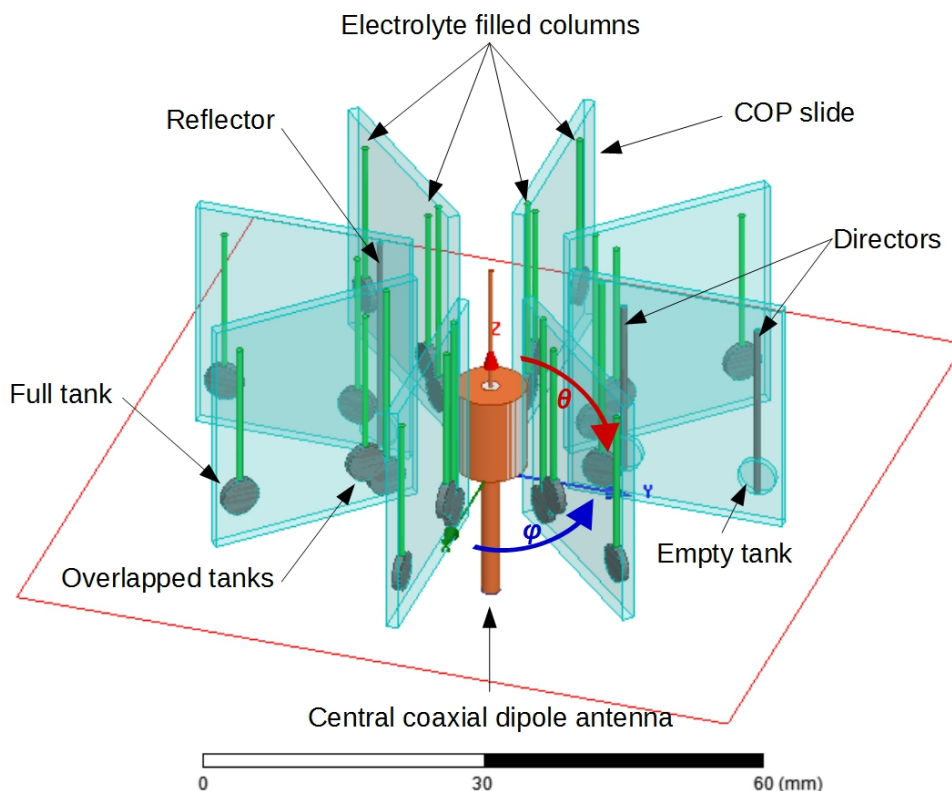


Figure 73 : 360° beam steering capable coaxial dipole Yagi-Uda antenna system actuated by microfluidic technology

Now that we have our design, we must take the appropriate steps in order to fabricate it. Since their conception lies on very different technologies, we are going to split the fabrication study in two, the first part will focus on the central antenna itself and the validation the proof of concept from an RF perspective, the second will focus on the fluidic actuation. For the fluidic part, we are going to focus on the fabrication of a mono-channel fluidic chip which will be our proof of concept for the whole fluidic system. The reason is that since all channel are identical in the complete system (short of the length), we will be able to draw conclusion from the test of just one of the channels and extrapolate from there the performances of the entire system.

As it was stated in the previous chapter, the antenna itself will be fabricated via 3D printing. The metallisation of it will have to be done onto the 3D printed part, which can be challenging. Indeed, surface metallisation is sometimes hard to do selectively and the surface state of the 3D printed material is also often problematically high for such purpose. The centre conductor of the antenna is planned to be a precisely cut piece of copper wire.

The antenna's parts were realized on DASSAULT SYSTEMS SOLIDWORKS in order get them fabricated by a company in UK called 3D alchemy. The dimensions are different of the initial dimensions when it comes to the diameter of the 3D printed parts. The reason is that the characteristics of the 3D printing material used by the contractor is different then the one used in simulation. Indeed, we had the following characteristics:

- **3DP-P** : $\epsilon_R = 2.7$, $\tan \delta = 1.10^{-3}$

We now have these ones, for their material called “Ceramic-like”:

- **“Ceramic-like”**: $\epsilon_R = 3.4$, $\tan \delta = 1.10^{-2}$

These new characteristics will forces us to change some of the dimensions of the parts, and will most likely lead to a decrease of the EM performances, due to the higher loss tangent in particular. Those changes are necessary to keep as much as possible an identical impedance for the central coaxial guide, as well as for the external one.

Indeed, if we simplify, we can consider that the layer of dielectric material sandwiched between the external conductor of the central coaxial line and the external sleeve of the antenna is like a coaxial line. In this case, the sleeve is the external conductor, and the external conductor of the central coaxial line is the new central conductor. The two lines are forming two imbricated coaxial lines.

Since we have designed the previous antenna in such way that the two coaxial lines have a 50 Ohms impedance, we now have to change the external dimensions in order to maintain that value. Given the rise of the permittivity, this will lead to an increase of the diameter of the two lines, when the length will stay unchanged. The figure 74) bellow show the evolution of the antenna's dimensions:

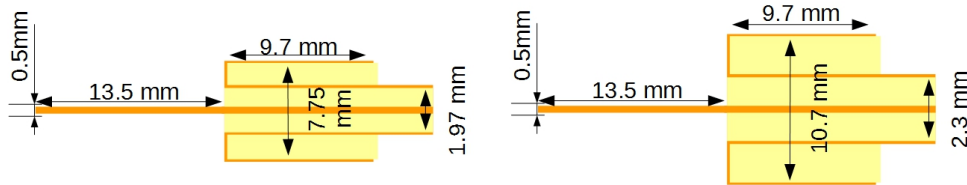


Figure 74 : Evolution of the dimension of the system's antenna before (left) and after (right) recalculation for 3D printing

As we can see here, we have an external diameter increase of 2.95 mm and an internal diameter increase of 0.33 mm while all other dimensions stay the same.

Given these precisions, we can now design the parts we will get from 3D alchemy. We have decided to realise two separate parts in dielectric and then assemble them in order to have an easier manufacturing. It means we will print the “sleeve support” on one hand, and the internal dielectric part of the central coaxial line (or central coating) on the other. The following figure 75) is displaying the CAD (Computer Aided Design) plans of the two parts:

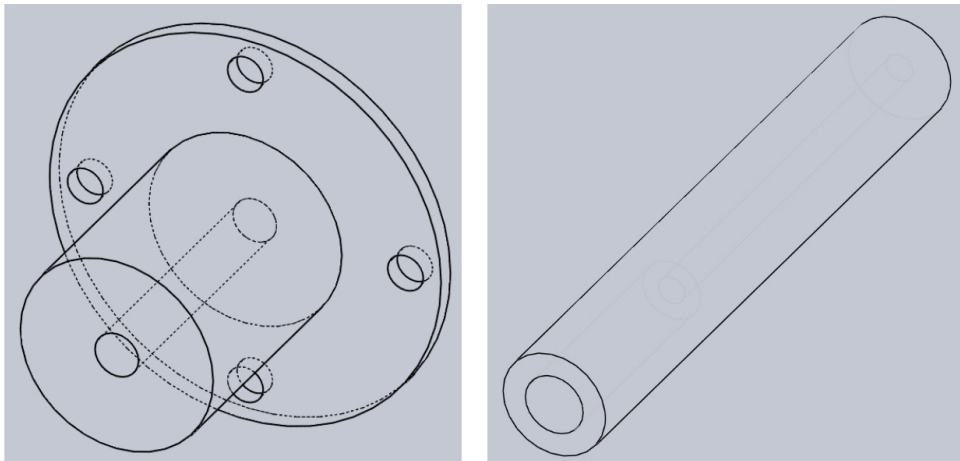


Figure 75 : 3D CAD plans for the “external coating” (left) and “central coating” (right)

We have on the left the sleeve support, or as we call it, the “external coating” and on the right the central coating. As we see, the “external coating” possesses a ring with four holes at his base that was not present on the figure 73). The rational for it is that we need to lock into place the SMA connector needed to power the antenna. This is done by sandwiching the SMA between that ring and a host base which will be shown later on, with the holes serving as passage for tightening screws. That perforated ring is there for that but also to provide a surface which can be metallized in order to ensure the connection between the ground plan of the SMA and the external conductor of the central coaxial line. At the same time the “external coating” is actually longer than the 9.7 mm displayed on figure 74), because of the need for us to embed the jack of the SMA connector.

It is for that reason that the “central coating” part is hollowed in its centre by two different diameters. Indeed, at its base we have a hole of larger diameter realized to host the jack of the SMA, the second diameter corresponding to the central conductor diameter. Of course, the length of the “central coating” part is impacted in the exact same manner by the presence of the SMA jack.

Regarding the hole on the centre of “external coating”, its there in order to slide in the “central coating”. The diameter of that hole is $2.3\text{mm} + \delta$. δ is the assembling clearance which is applied to the hole and which goes from 100 to 200 microns for the whole diameter. The reason behind that clearance is that the 3D printing process is not as precise as other technologies such as micro-machining and we much therefore take our precaution for our parts to be able to fit into one another.

Given that we have spoken of the SMA connector, the next figure 76) is showing the connector as well as the 3D part in which it will be held on pressed against the back of the connection ring of the “external coating”.

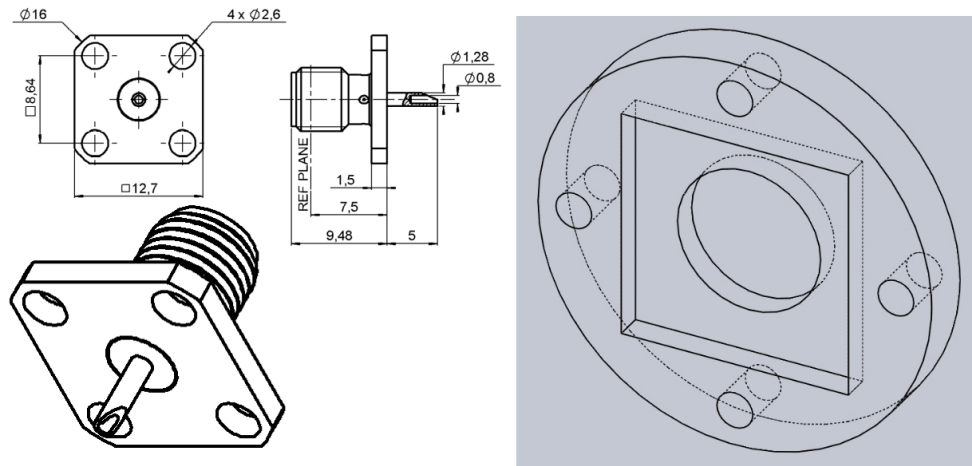


Figure 76 : 2D & 3D CAD plans for the SMA connector of the antenna (from RADIALL) (left) and its 3D printed fitting base (right)

As we can see on this figure the length of the SMA jack is 5 mm, which is from RADIALL (ref: R125.403.000). This means we have to add 5 mm to the length of the “external coating” part, but this additional length is not going to be metallized. This gives us a total length of 14.7 mm. Since the addition of coaxial line length is not going to impact the behaviour of the antenna because the electric field will stay confined into it, it is not a problem.

The diameter of the jack being 1.28 mm, we will therefore have a 1.3 mm diameter hole deep of 5mm at the bottom of the “central coating” part, with a hole with a diameter of 0.5 mm on the 9.7 mm remaining of it.

On the right side of the figure 76) we have the base we designed to host the SMA and hold it in place. It has a diameter of 22 mm and a square cut in the middle which is a square with a side of 12.7 mm long and 1.5 mm deep, just as the square base of the SMA.

In order to sum up all the modifications brought to the design of the antenna to ease fabrication, we can have a look at figure 77) bellow:

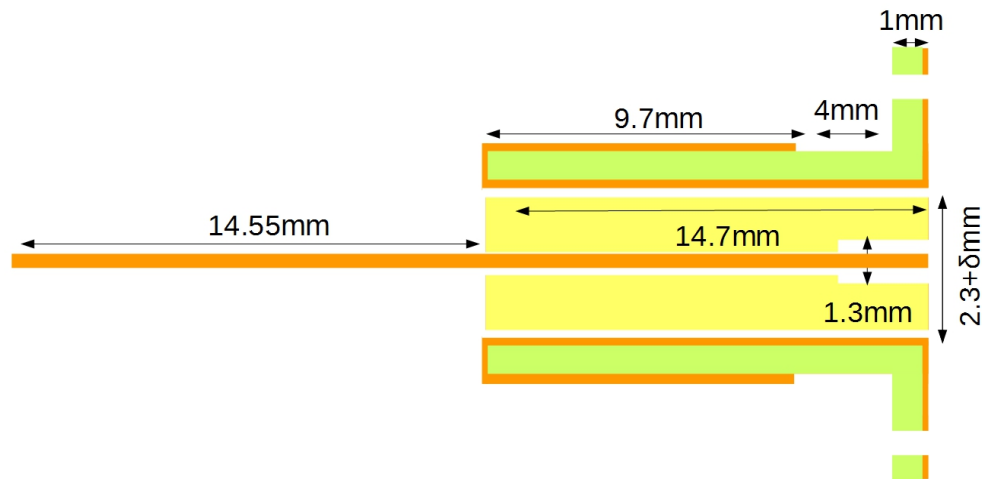


Figure 77 : Sectional schematic view of the assembled 3D printed and metallized antenna

On this figure we can clearly see the two different parts “central coating” in yellow, and “external coating”, in green, as well as all the dimensions needed for fabrication. We also clearly see that the metallisation of the antenna is done exclusively on the “external coating” part (in green), and is represented in orange. That colour is chosen because copper is used for the metallic coating, as it is the case for the material of the central wire. We also clearly see the metallized back of the “external coating” in order to allow the electrical contact between the SMA ground plane and the central coaxial line external conductor.

Once this final schematic presented, we can now look at the end product, both before and after the metallisation, as presented on figure 78) bellow.

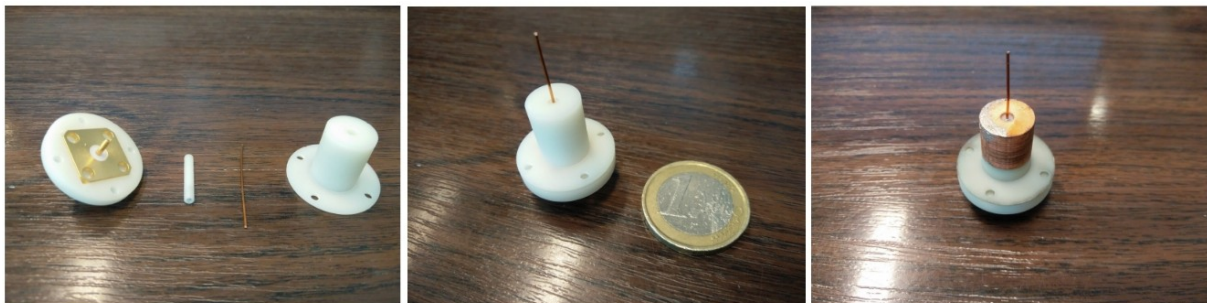


Figure 78 : From left to right, the 3D printed antenna non metallized and disassembled, non metallized and assembled, metallized and assembled

On this figure we can see on the top position the different parts of the antenna after being fabricated. We can see from left to right, the SMA host base with the SMA already embedded into it. Next to it, we have respectively, from left to right, the “central coating” part, the central wire and the “external coating” part. All those parts are not yet metallised as we can see. On the bottom left corner we have the assembled antenna previous to metallisation, next to a 1€ coin for scale comparison. And finally, on the bottom right corner, we have the antenna assembled after its metallisation.

The metallisation itself was performed by the GTID company, in Brest. The process involve a first bath of the part in a palladium solution for a better adherence of the copper, copper which is

deposited onto that layer of palladium compound through electroplating. This technology being not selective, we had to tape-mask the faces of the part we didn't want to metallise, such as the bottom 4 mm of the main cylinder and the top of the perforated ring. This technology was chosen because it gives good results in terms of metallisation of high aspect ratios holes, which is the case of the central hole of the "external coating". Another reason of this choice was that it was readily available in Brest, and the previous positive experience we had about this company.

II. Development of fluidic chip fabrication technologies

1) Introduction to fluidic chip fabrication

We know that the antenna system is made of two sub-systems, the central antenna itself, and the fluidic parasitic elements, which are encapsulated inside COP chips. We have seen above the refinement process applied to the antenna architecture which led to its fabrication. We will now focus on the second sub-system, the fluidic chips. Given that we have already explained that the eight chips surrounding the central antenna are the same, we will actually focus on the study of only one of the chips. We will even further simplify the study, by focusing on a single column chip. Indeed, one slide holds three columns, which are identical in all but length, and in the overlapping or not of their tank. We can consider that these two points of differentiation are minor and that a study of a single column chip will be sufficient to improve the feasibility of our chip design.

The basic design of the chip we will study is composed of a bottom tank, a vertical channel connected to the top of that tank and a smaller tank on the top. The following figure 79) is showing an example of such chip, with top, side and 3D views.

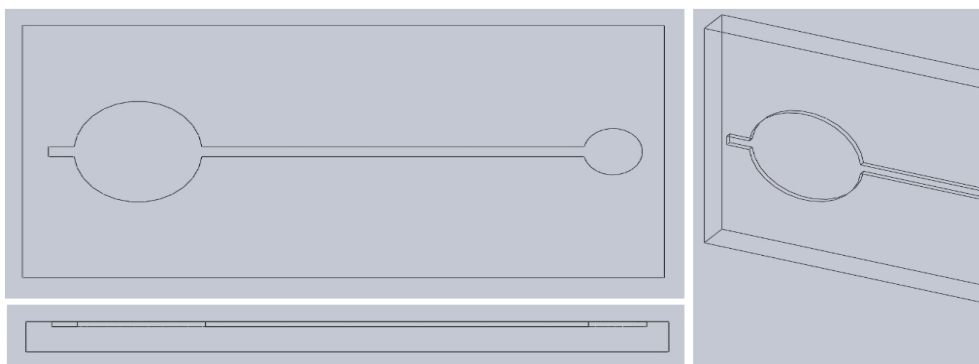


Figure 79 : Basic COP fluidic channel design

This example of fluidic chip is realized with a COP slide as a support. The dimensions of the slide are the following: 50 mm * 25 mm * 3 mm. These dimensions will be an imperative constraint for

us in the development of our chips design and fabrication technologies. Indeed, the length and width of those COP slides are determined by existent injection mold at the laboratory. They are produced by injection molding, from COP granules (Zeonex 480R [1]), which are annealed and injected into a metal mold via a specific injection press. Both the press and the pellets can be seen on figure 80).

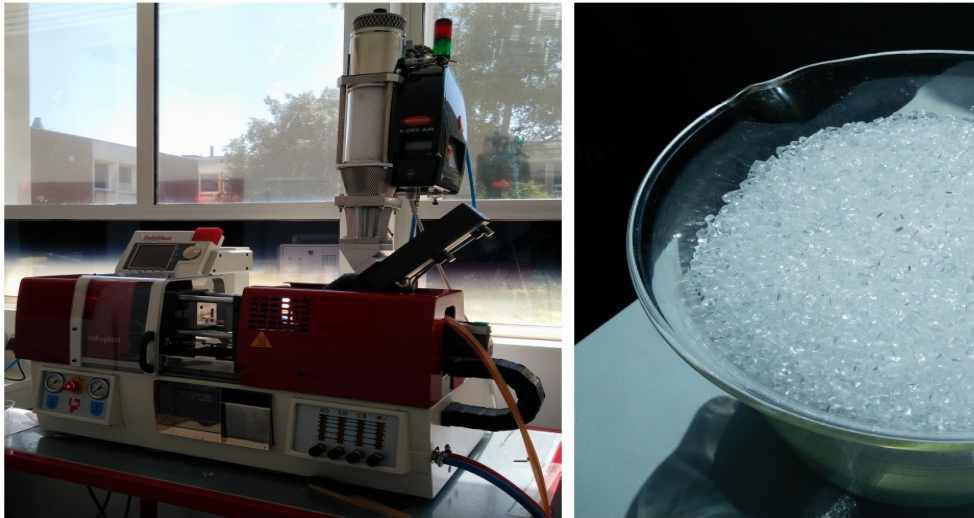


Figure 80 : COP injection press (left) and COP granules (right)

Since it is very expensive to make a new injection mold, and since we are able to make the longer of the columns we will use (which is the reflector column, with a total length of 25.5 mm), we will therefore use these COP slide as the basis of all our developmental work on the fluidic chips.

Since it is also very easy to produce these kind of chips with PDMS, sometimes more than with COP, we will also develop technologies to fabricate chips with this material. While it is not going to be the final chips that we will make out of PDMS, we can still use it as a practical way to realize and test prototypes & to ensure that we will be able to achieve fluidic performances tests. Dimensions of these chips will be the same, at least in terms of width and length in order to simplify their interfacing with the injection devices we will develop on another side a second time for the COP chips.

2) Fluidic channels fabrication on COP substrate

Once we have established the developmental base for the COP chips, we will now look at the different fabrication technologies at our disposal. These technologies can be divided into two categories. The first are the technologies which allow us to obtain a fluidic channel as presented on figure 79) from the COP slide of the dimensions mentioned above. The second category encompasses the technologies which allow us to seal this newly formed channel in order to have a functional fluidic chip.

The number of methods falling into the first category amount to three. While they use all the same COP slide (50 mm * 25 mm * 3 mm,) as a starting point, they differ in the treatment applied to that slide in order to obtain the fluidic channel. These technologies are the following:

1. Micro-machining
2. Laser engraving
3. Hot embossing

We will now present these three technologies and the resulting channels.

a) Micro-machining

In the case of the micro-machining, we use a LPKF S103 CNC to create the desired channel. This equipment is available in Brest, at the UBO, in the Fab-Lab, and can be seen on the left of figure 81). On the right is the channel manufactured with this machine.



Figure 81 : LPKF S103 CNC (left) and micro-machined COP fluidic channel (right)

While this method is relatively fast and easy to deploy (only need the COP substrate and machine time), with a chip realized in less than 15 minutes for a channel depth of 500 μm . The dimensions of the whole microfluidic design are the following: the diameters of the tanks are respectively 10 mm for the bottom tank & 4.6 mm for the top tank. The length of the channel, which is the length between the two tanks, is of 29.8 mm and it has a width of 1 mm. This technology has one significant drawback for our application. Indeed, the micro-machining results in a channel with a high surface roughness. That is problematic for us since moving of fluid and thereby the fluidic chip working will be heavily impacted by the energy for the fluid movement losses due to friction forces on this rough surface. This in turn will slow the movement of the Galinstan inside the channel as well as most likely increase the electric consumption of the device. That's why, despite being a very cost effective and attractive method, we will not use it as our first choice for the realisation of the channel itself.

b) Laser engraving

The second technology mentioned is the laser engraving. This was done using an EPILOG Fusion CO2 engraving & cutting laser. This device was located in the facility of the school of EEE, in the Nanyang Technological University. It accessible to us thanks to the co-supervision of this PhD by Pr. P. Coquet, director of the CINTRA laboratory, in Singapore. That equipment can be seen on the left of figure 82), and on the right, the channel manufactured with this machine.



Figure 82 : EPILOG fusion CO2 cutting laser (left) and laser engraved COP fluidic channel (right)

This technology has the advantage, like for the micro-machining, to allow the update of the design on the fly on a computer just before engraving the channel. The fabrication time is also relatively short, with here a chip realized in 5 minutes, for an identical microfluidic design as the one realised by micro-machining, with a channel depth of few hundred of microns, but with the following parameters: laser travel speed at 80% and laser power at 50%. The lack of precision on the depth of the channel is due to the fact that we only have control on the laser speed and power, but the reaction of the substrate to the laser is depending on the nature of the substrate's material. It must be noted that this machine is usually used for substrate cutting & not engraving. This is why, as expected, the same set of parameters on two different materials will achieve different results. This is the major drawback of this technology, it require a lot of testing to establish precisely the proper set of parameters for each substrate. We also see that the aspect of the channel, while being seemingly slick, also have a lot of waves and is not flat. This is due to the nature of the laser engraving, where the material is melted and vaporized along the progression of the engraving. Here again, it can be a problem for our application.

c) Hot embossing

Finally, the last technology is the hot-embossing technology. This technology consists in pressing into a custom aluminium mold a COP slide of the previously mentioned dimensions, while being heated in an oven. The pressing function is performed by a weight of 20 Kg put on top COP slide. The temperature of heating is of 190°C, which is 50°C more than the glass transition temperature T_G of the COP ($T_G \sim 140^\circ\text{C}$). The mold posses an imprint of the channel we want to have into the COP slide at the bottom of a milled pocket. The bottom imprint is finely machined in order to have a good precision of the transferred imprint on the COP slide. It must also be noted that the pocket dimensions, especially it depth, are adjusted to the COP slide ones. This is done in order that once the imprint is done and the slide has fully entered the pocket, it is not further crushed by the weight, which now rest onto the mold itself.

Those dimensions are the same of the standard COP slide. The dimensions of the machined imprint were initially the exact same as those of the micro-machined microfluidic design, but had to evolve to make the fabrication of the mold possible. The most significant change is the transition between the different bodies of the design, mainly between the tanks and the channel, where angles have been softened, as we can see on the figure 83) bellow. The height of the imprint is 500 μm (deeper than 300 μm because we don't expect the chip to be perfectly deformed up until the bottom of the pocket), for a channel length which remains identical to the previous chip.

This technology was initially developed in the CINTRA facility, where the mold was design and the majority of the development tests conducted. Given the use of very widespread equipment short of the custom made mold, it was then shipped back to Brest for further usage. The following figure 84) is showing the mold & oven installation as well as the end product of the process, which is the chip.



Figure 83 : From left to right, aluminum milled hot embossing imprint, hot embossing process before start & a hot embossed COP fluidic channel

The production time for such chip is significantly higher than for the previously showed technologies, with a 210 minutes heating at 190°C required to produce one chip with our mold. Of course, due to the nature of the process, it is easy to parallelise, by having a multiple cavities mold and a large oven. This is way more complex to realize by the other technologies compared to the previously showed chips, the aspect of the channel seems very slick and display no sharp edges like the micro-machined chip, neither waves like for the laser engraved chip.

3) Fluidic channels fabrication on PDMS substrate

As mentioned earlier, we have also develop in house technologies to fabricate PDMS chips. The reason for it was to use this material for prototyping some chips (because of its simplicity of use) and as a guarantee, in case we would face significant difficulties during the development of COP chips. Here also, the technologies fall into two categories, between the one aiming at fabricating a channel, and those aiming at sealing that channel. We will first explore the technologies falling into the first category, where there is actually only one. Indeed, all our PDMS chips where obtain with the same method.

The PDMS present itself under the form of two component, an elastomeric one and what is called a “curing agent”. Both products are initially liquid, and that is only the combination of the two which render the PDMS into a flexible but solid material after a certain amount of time. That flexibility can actually be adjusted by tuning the quantity of curing agent for a given volume of elastomeric base. Given this mode of preparation, we realize that it is relatively easy to fabricate fluidic channels embedded inside a PDMS slide by pouring the still uncured PDMS mix into a mold similar to the one we use for the COP hot embossing.

We choose that process to fabricate our chips. The PDMS we used is the “Sylgard 184”, from Sylgard [2]. The mold we use is exactly the same (we made two of them) one as for COP hot embossing, we will therefore have the same dimensions for the microfluidic design. We also have add a plastic bridge on to of mold during the curing process in order to create the injection holes of the chip. This, as well as the end product is showed on the following figure 84).

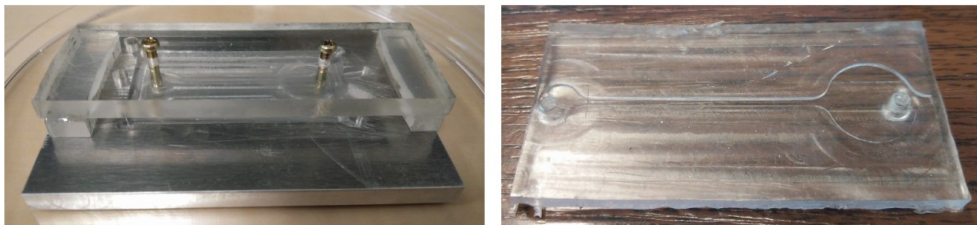


Figure 84 : Aluminum PDMS with the plastic bridge (left) and a molded PDMS fluidic channel

It must be noted that further on, a redesigned 3D printed bridge was realized, in order to have a more reliable injection holes position, to which was also added a perforated plastic slide on its side used to create holes in the chip, as shown on figure 85) bellow.

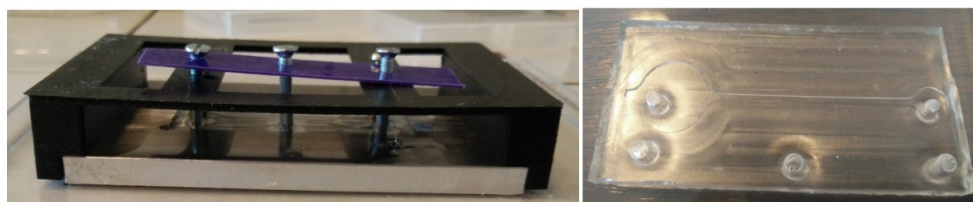


Figure 85 : Redesigned 3D printed PDMS molding bridge with additional purple plastic slide (left) & resulting PDMS chip (right)

The objective of this new PDMS molding superstructure is to ensure a reliable fabrication of PDMS chips with a relatively good control over the injection & electrical contacting holes position (which are needed for us to contact the deposited electrodes), should we need to fabricate PDMS on glass

chips. This precision is important because we consider the PDMS technology to be a mostly a back-up for us if the COP technology doesn't work.

4) Fluidic channels characterization

As we can see on part 2), all these technologies have been tried by us to produce chips and each has its own specificity in terms of channel profiles and surface roughness. In order to compare them we have done a series of measurements of the channel's profile with a profilometer on each chips. The following figure 86) is showing the four measured chips, with, from left to right, COP micro-machined and hot embossed chip, the PDMS chip and finally the laser engraved COP chip.



Figure 86 : From left to right, micro-machined COP, hot-embossed COP, molded PDMS & COP laser engraved fluidic chip

The results of these measures are shown on figure 87) for these four different chips.

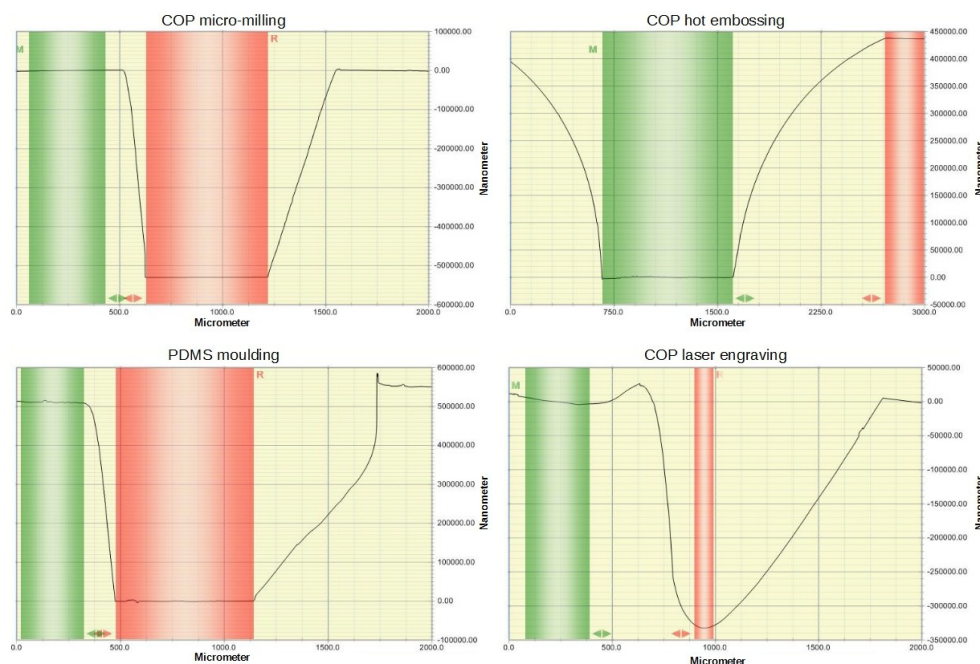


Figure 87 : Profilometer profile of the chips presented on figure 86)

These figures clearly show the profile of the channel is heavily impacted by the fabrication technology chosen. The COP micro-machining and the COP hot embossing technologies are creating channels with relatively sharp walls, more in the case of the micro-machining than the later. In terms of channels depth, the target has a depth of 500 μm . We can see that it's the case for the micro-machined channel, but there is a significant deviation for the hot-embossed chip, where we reached a depth of 430 μm , which is a 14% variation. The depth of the PDMS channel is 500 μm , which is the depth of the mold. We also notice the very sharp hedge of the channel's wall, which is as good as for the micro-machining technology on COP. As for the laser engraving, we have a channel depth 200 μm inferior to the target, at roughly 300 μm for the depth, which is a 40% variation. The profile of this last channel is not symmetrical and highly irregular.

We can also observe some phenomenons which are linked to the fabrication technology, such as the bumps on the side of the trench for the laser engraved chip. This is the effect of polymer heating during engraving and could lead to a degradation. We can also notice on the hot-embossed chip that the channel walls are not as sharp as for the micro-machined one or the PDMS channel.

This, as well as the difference in terms of depth between the mold and the final chip, could be the result of the COP being compacted during the fabrication process. Indeed, the hot embossing technology is the only technology, with the PDMS molding, where we don't remove any material from the initial slide in order to produce the channel. Instead, we press the matter under a large weight to forces it conform itself into a new configuration, with very little space for expansion inside the mold pocket, in whatever direction. Therefore, there is a resistance to that expansion which may build itself during the course of the process, halting the deformation of the COP slide. In the case of the PDMS, although we also don't remove any material from the chip to make the channel, we don't have the same kind of problems we had with the hot embossing of the COP slide. The reason for it is mainly that because the PDMS is liquid when poured into the mold, we poured just the right quantity needed to make the chip. The PDMS chip is then let to solidify without any applied pressure on it, leaving it uncompressed, on the contrary of the COP chip.

All the results of the profilometer measurements can be found on the following table 5), which sum-up the depth measurement shown above as well as various roughness parameters:

Table 5: Fluidic chips profilometer measures sum-up

	COP hot embossing	COP micro-milling	COP laser engraving	PDMS moulding
Channel average depth	361 μm	518 μm	330 μm	511 μm
Channel average roughness Ra	0.49 μm	2 μm	1.36 μm	0.68 μm
Channel average roughness Rq	0.65 μm	2.49 μm	1.65 μm	0.88 μm
Channel average roughness Rz Din	2.2 μm	6.86 μm	2.46 μm	2.83 μm

As we can see, this table sum up various data. We have already spoken of the channels depths for the various technology, but not yet of their surface roughness. In terms of depths, we notice that the COP micro-machining and the PDMS molding are the two technologies which provide the targeted depth value. They are followed by the COP hot embossing and finally the COP laser engraving. In terms of roughness, we have three figures to look at in order to compare every technology: The Ra, which is an arithmetic average of the surface roughness, Rq, the quadratic average, and finally Rz Din. It is the average value of the 10 biggest peak to peak variation. This allow us to get a sense of the frequency of roughness peaks on the surface of the channel, as well as their amplitude.

As it was predictable, the COP micro-machining is the technology which generates the most of surface roughness. It is followed by the COP laser engraving. PDMS molding and COP hot embossing are the ones who performed the best, with the COP hot embossing being the best, even though both are very close. Surface roughness of this two last technologies are mainly related to the roughness of molds.

5) COP & PDMS fluidic chips bonding

Now that we have seen the various technologies on COP and PDMS for creating the channels, we must take a look at the second category of them. Indeed, once we have the chip with the channel embedded inside, we need to enclose that channel. To do it, we have explored three

different technologies with the COP, and two with the PDMS. These methods are depending on the material use to seal the channel. We tried COP & glass for the COP chips, and glass and PDMS for the PDMS chips. One of the constraint is of course the possibility to bond together the two part, but also think of the electrodes addition into the chip.

Indeed, we would prefer to have the electrodes deposited onto the chip's sealing panel, as we will detail later. Therefore, we must be able to deposit the metal onto that panel, and have a bonding technology which will not prevent the electrical contact between the electrodes and the content of the channel. For the sealing slides materials, we have tried COP and glass for the COP chips, and PDMS and glass for the PDMS chips. The glass is an interesting support in a sense that it is widely used for microfluidic applications, and its a material on which the metal deposition is rather easy. On the other hand, it has poorer EM properties than the PDMS or the COP. It's also possible, according to the literature, to deposit metal directly onto PDMS, as in [3][4] & [5] or COP, as in [6] but this is significantly more challenging, especially on PDMS, due to its flexible nature.

The tested bonding technologies are the following for the COP:

1. Mechanical & toluene bonding
2. Thermal bonding

And for the PDMS they are:

1. O₂ plasma bonding
2. Curing agent bonding

We will now present theses various technologies and the resulting chips obtained.

COP bonding technologies

a) Mechanical & toluene bonding

For the case of COP, the first technology used consists in micro-machining the surface of the chip by 500 μm in order to leave only two confinement walls high of 500 μm surrounding the central channel. We then mill the patterns on the sealing slide, which is made out of COP, with a depth of 500 μm as well. Finally, we assemble the two halves, after having deposited Toluene outside of the two confinement walls. The interest of the Toluene is that this solvent will dissolve the COP, creating a local sticking of the two COP slide together. This will render the chip sealed, at the exception of course of the injection port, as well as the electrodes ports. Of course, given the dependency of that technology on the dissolution of the COP due to the Toluene, it was not tested on glass, which is inert to the Toluene. An example of such architecture can be found on figure 88), with the CAD design on the left, and the end result on the right, before and after the Toluene sealing and the addition of the electrodes, which are here made of copper foil.

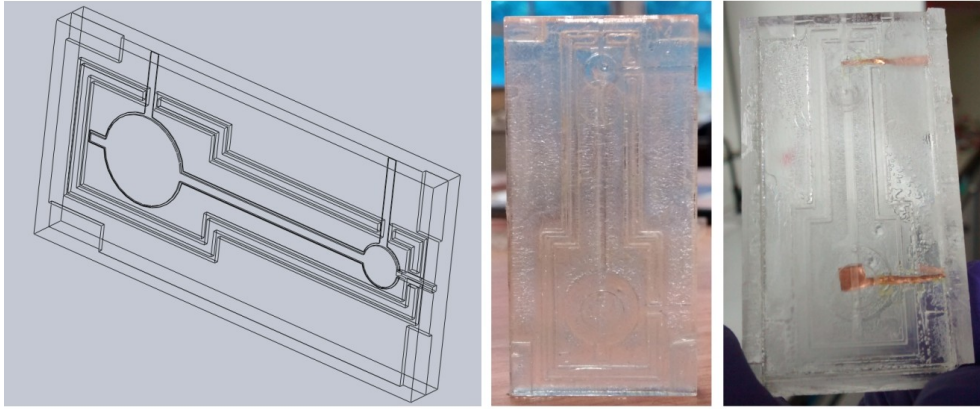


Figure 88 : 3D CAD view of an assembled mechanically bonded COP fluidic chip (left) and two of these same chip after fabrication & assembling (right)

We can see on the bottom right corner of the CAD image the injection port, at the end of the channel, as well as the electrode ports, perpendicular to the channel. The interest of such technologies is that it requires the same equipment as the micro-machined channels. We could therefore produce the chip entirely with a CNC machine & two slide of COP (of course, without the electrodes). We also have a high flexibility in terms of design modification, since we can modify on the fly the chip design and fabricate it immediately.

However, these figures, in addition with the previous study of the micro-machined channels, allow us to see one of the major drawback of these technology. Indeed, aside from its complexity from a manufacturing point of view, it is going to be rather time consuming, because the amount of matter to remove from the slide is important. Otherwise, we have seen cracks in some machined slides, it is probably due to relaxing constraints into molded COP and to initiation and crack propagation during machining step. This is amplified by the fact that the mechanical assembly creates additional constraints.

The Toluene deposition itself is also a process difficult to master, and the risk to spill some by accident inside the channels, and hence dissolving them, is real. If that were to happen, it would render the chip useless. The fact that we must breach the confinement walls to allow the passage of the electrodes and the injection syringe is also a problem, because the Toluene can also pass through these openings. This is increasing the likelihood of problems with the chips due to fabrication. Finally, the necessity to work with Toluene is also a drawback, given that it is a very toxic solvent and therefore require adapted facilities and protection for us to use it.

b) Thermal bonding

The second technology, which is the one we privilege, is the thermal bonding technology. It derive closely from the hot embossing technologies, in the way that it consists in pressing together two COP slide at 190°C, with the help of a weight (here also of 20 Kg) on top of the slides. In order to avoid misalignment problems as well as a complete crushing of the slides, we use a custom bonding support, also made of aluminium. This support is made out of two centring plates, a spacer

frame to place between these two plates and a guiding frame providing alignment to the assembly. Aside this, the recipe is identical to the hot embossing one. The figure 89) shows the opened support, loaded with two slides ready to be bonded, and an example of a bonded chip.



Figure 89 : COP thermal bonding support holding a COP chip before bonding (left) and a bonded chip (right)

We clearly see on the left picture one of the centring plate on the background, as well as the spacer frame placed flat on top of the second centring plate, surrounded by the rectangular guiding frame. We also see that the cover slide of the sealed chip posses two holes drilled into it. These holes are the injection ports of the chip, which were realised via micro-machining (LPKF S103 CNC), but will be detailed further on in this manuscript.

The advantages of this technology is of course its simplicity, the fact that we don't have to bring any additional material to realize the bonding, as well as the fact that it's almost identical to the hot embossing technology, which further simplify the production of the chips and the associated logistics. Minimizing the number of fabrications technologies involved in the making of the chip also further reduce the number of potential fabrication related problem sources, making it more reliable.

It must be noted that this technology was tried to bond together a glass slide and a COP chip, with no success. The testing was extensive, and even include the coating of glass slides with an adhesion promoter, Hexamethyldisilazane (or HMDS), in an attempt to strengthen the bond, but in vain. With or without HMDS, the chemical bonds between the two never resisted manipulation once removed from the support.

PDMS bonding technologies

a) Oxygen plasma bonding

As mentioned earlier, we also explored ways to seal PDMS chips. It exists two possibilities, for the bonding material. The first one we explored is the plasma O₂ bonding technology. The process is rather simple, we used a PlasmaTherm PTI 790 PECV (atmospheric pressure plasma) & RIE (Reactive Ion Etching) dual system to perform a surface activation of the PDMS chip with an O₂ plasma. That equipment was accessible to us in Singapore, in one of the clean room of the school of EEE, thanks to our cooperation with CINTRA. The recipe we used was the following: 180 mTorr O₂, for 90 s at 60 W. After that step, the activated PDMS chip is pressed onto a glass slide and then

the newly sealed chip, which is now sealed. An illustration of RIE system and the chip resulting of the process can be found bellow, on figure 90).

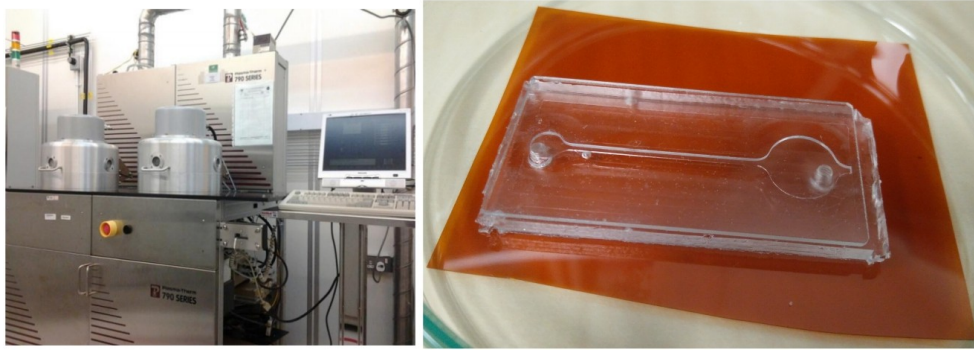


Figure 90 : RIE system used for the oxygen plasma bonding in Singapore (left) and PDMS/glass bonded fluidic chip (right)

This technology works especially well to bond the PDMS chip on glass, since it is providing a rigid support to the chip, preventing mechanical stress due to flexion to the newly formed bond, therefore preserving it. Glass is further interesting for us given that the deposition of metal on it is a particularly well mastered technology, so it will not present a challenge. The same technology can also be applied to full PDMS chips, but this material is more challenging to be metallized.

b) Curing agent bonding

The second technology mentioned earlier is the curing agent bonding. This method can be found in [7], and take advantage of the fact that the PDMS chip production process involve the use of two components, the elastomer base and the curing agent. It consist into depositing a thin film of curing agent on top of the surface of the slide we want to bond with the chip using a spin coater. Once this is done we press the two part of the chip together in order to seal it and re-bake the newly assembled chip for three hours at 65°C. The working principle of this process is that the curing agent deposited on top of the substrate is going to create hard chemical bonds between the coated surface and the PDMS chip, which is mainly made of the elastomer. It is therefore quite reactive to the curing agent bonding properties. An illustration of the process can be found bellow on figure 91).

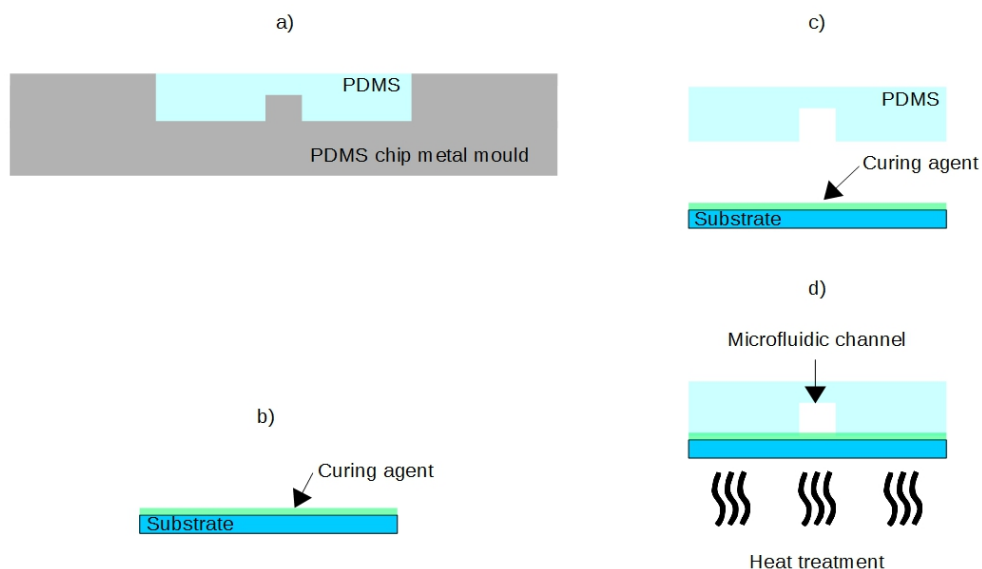


Figure 91 : Illustration of the curing agent bonding process used by us

However, it must be noted that the curing agent method might be problematic in the sense that, as we can see on the figure 91) above, the curing agent is deposited on top of the substrate. The problem is that is also where we usually deposit the metal we use to make the electrodes of the chip. If we cover them with the curing agent, they'll be insulated from the channel content and therefore the chip will not work. It might be possible to flush the newly formed channel with an appropriate solvent afterwards in order to remove the curing agent from the electrodes, but that's not a very reliable technology.

Nonetheless, we have tried this technology anyway, firstly in order to test it, and secondly we could imagine some solutions to obtain non insulated electrodes. For example, the electrodes could be added prior to the chip assembly from a piece of metallic tape or wire. In such case, there is no problem of unwanted insulation of the electrodes. It is also interesting because we can realize chips made of PDMS & glass as well as PDMS & COP, as we can see on the following figure 92).

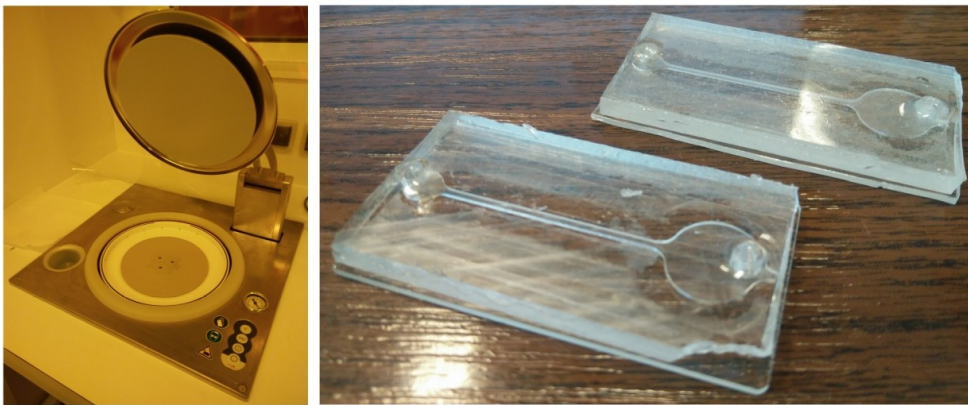


Figure 92 : Spin-coater used to deposit the curing agent on top of glass and COP slides (left) and two PDMS chip bonded on top of glass (right-front) and COP slides(right-back)

This figure shows these two type of chips on the right, as well as the spin coater used to deposit the curing agent on the left. This equipment is available in the Lab-STICC facilities in Brest, which rendered that technology attractive to us as well. The substrate used are a glass slide and a COP slide. The interest of having a mixed PDMS-COP chip is that it will have a lower effective dielectric permittivity than a mixed PDMS-glass chip, since the value of ϵ_{EFF} for COP is 2.3, and is ranging from 3.9 to 5 for glass, depending of its chemical composition. We will therefore have a chip with a relatively low effective dielectric constant while being very easy to manufacture and bond. The downside is that while it's possible to metallize COP, as shown in [6], it is not an as easy & mastered process as for glass.

6) Electrodes fabrication

This bring us to the final aspect of the chips fabrication, which is the electrodes. These could be done through the metallization of the of the two halves of the chip in order to materialize the electrodes, or, an other way, by just introducing small metallic wires inside the chip. It must be noted that if the later solution seems easier to realize, it is no so obvious. Indeed, it is relatively hard

to correctly seal the chip after inserting wires inside, due to the volume occupied by these electrodes. That therefore complicate the chip design, because we need to take into account the diameter of the wire, to dig trenches in the chip to insert the electrodes inside while still being able to close the chip and bond it. But given that it will be impossible for us to dig semi-circular trenches through micro-machining, and because the wire section is circular, it means that there will always be leaks around the electrodes if we don't coat the area around the electrode at the exit of the chip with a seal, as showed on figure 93) bellow.

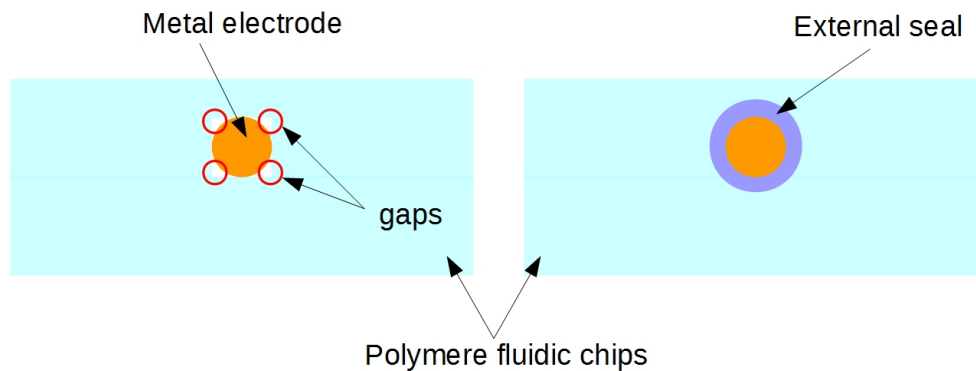


Figure 93 : Illustration of the problem posed by the use of metallic wire as electrodes

That seal can be glue or dissolved polymer, but will in any case be not ideal, and we run the risk of letting some of the sealing material enter inside the chip and obstructing the channel, rendering the chip useless. Another problem is that the surface of exchange of such electrode is smaller than a metallic strip deposited on one of the slide. This smaller exchange surface with the fluid constraint the number of charges departing from that electrode during the chip activation, slowing down the process of changing the surface tension of the droplet. Finally, we have to consider the electrodes material. Given the relatively hostile environment in which the electrodes will be immersed, which is a basic solution containing also an eutectic metallic alloy (Galinstan) susceptible to degrade the electrodes, we have to consider relatively chemically inert metals. A ubiquitous metal in electronic like copper cannot be use for this reason, and we would prefer to use gold or platinum. Gold will be used in this study and will be deposited in thin layers.

As we mention previously, we favour the deposition of metallic electrodes as a thin film on top of one of the two halves of the chip. Despite being more adapted to our objective, this technology nonetheless presents also challenges, even if the previous problem of the chip sealing is absent here, due to the very small height of the electrodes.

Indeed, we must be able to realize a selective metallization, and make sure that this metallization adheres to the substrate. The first step consist into realizing a mask to define patterns. This mask can be made from photoresist if we want very fine levels of details, or more simply, of an adhesive tape capable of withstanding the constraints (chemical or thermal) of the deposition process. This is if a coarser level of details is not a problem, which is our case. In our case we have used both masking methods, with mixed success as we will see.

The second step is to deposit the metal on top of the substrate, with a plain field metallization method, the masking allowing us to nonetheless obtain a selective metallization. This step was

performed by us through three different methods, both on glass and COP substrate, respectively for PDMS-glass and COP/COP fluidic chips. Depositing metal on top of a substrate can be a bit complex due to adherence problems, but this very substrate dependent. For example, deposition on top of glass of various metals is a relatively well mastered process. It becomes more problematic when it come to depositing on top of COP. The literature present some example of such deposition, of gold to be precise, through e-beam evaporation. Indeed, it was demonstrated by Illa et al. in [6], that the deposition of 200 nm thick gold electrodes on top of a COP substrate is possible with e-beam evaporation. Notably this was obtained without any adhesion layer with a standard lift-off technology.

As for deposition on top of bulk PDMS, we didn't tried, although it was demonstrated in [4], by Hage-Ali et al. the possibility of depositing gold electrodes on top of a PDMS substrate through evaporation technology. However, this process require a relatively important number of intermediate steps, making this process rather time consuming, complex and requiring equipment not easily available to us. It must be noted that the reason behind the complexity of the process is the thermal dilatation of the PDMS during the deposition process, which in turns damages the deposited gold patterns. In addition, the flexible nature of the PDMS doesn't make of it a very suitable substrate for electrodes, because they would run the risk of cracking due to the flexion of the substrate's surface, especially during the bonding process.

Having presented the different masking technologies as well as the potential difficulties of these metallization process, we have chosen to use three different electrode fabrication technologies, which are the following:

- 1) Gold evaporation with e-beam on top of photoresist masked substrates
- 2) Gold electroplating on top of selective copper metallization obtained through an autocatalytic process on top of tape-masked substrates
- 3) Gold electroplating on top of selective Au-Pt metallization obtained through sputtering on top of tape-masked substrates

We will now present theses three technologies and the resulting electrodes obtained.

a) Gold evaporation with e-beam on top of photo-resist masked substrates

The e-beam pulverisation consist in evaporating gold from a target to be then deposited on substrate. 200nm was deposited on top of glass and COP slides on which photoresist patterns was coated beforehand in order to use the lift-off method to obtain metallic electrodes The result of the deposition process can be seen on figure 94).



Figure 94 : Results of the gold deposition on top of COP and glass slides (left), with a COP slide (right-top) and glass slide (right-bottom)

The resulting electrodes from the lift-off procedure can be see bellow on figure 95).



Figure 95 : Results of the lift-off and scalpel grinding operations on COP slides (left) and glass slides (right)

As we can see on this last figure, the lift-off was not very successful. It is especially visible for the two samples on the top of each photos, where just the lift-off procedure was applied. The cause of this could be too thin layer of photoresist and thick layer of metal preventing its removal by cleanly breaking the gold layer and leaving the electrodes intact. Instead we have noticed that the gold layer was remaining intact and was not breaking into small flakes, staying attached to the electrodes. Therefore, we have decided to grind of the unnecessary metal with a scalpel blade, using only this technology for the COP slides (on the left) and combining it with acetone applied with cotton swabs for the glass slide (on the right). With that problem in mind, we were nonetheless able to produce 2 to 3 viable COP slides with electrodes, and 3 for glass.

b) Gold electroplating on top of selective copper metallization obtained through an auto-catalytic process on top of tape-masked substrates

This technology was developed in the Lab-STICC and is composed of three steps. The first step is a plain field deposition of a palladium ink which serves as a precursor for the second step. Beforehand, an adhesive tape was used in order to define patterns. This tape masking is applied just

for this first step and remove thereafter. The second step is electroless growth of copper which use the palladium as precursor. Finally the third and last step is an electroplating of gold on copper in order to prevent its oxidation. It should be noted that if we were to realized chips with a longer lifespan, it would be imperative to deposit a layer of nickel between the copper and the gold in order to prevent the solid diffusion of the copper through the gold, which may lead to the deterioration of the electrodes and the failure of the chip. This step was here ignored since the nickel deposition was not readily available to us and because those chips are prototypes designed with a short lifespan. Nonetheless, this method present for us the interest of being available at the lab for multiple testing, and to have already given interesting results in terms of metal deposition, especially on COP substrate. This method was used to deposit electrodes both on COP & on glass. The resulting electrodes after the two first steps can be seen on figure 96).



Figure 96 : COP slides after metallization with copper

The next figure 97) is showing these same electrodes after having being plated with the gold.

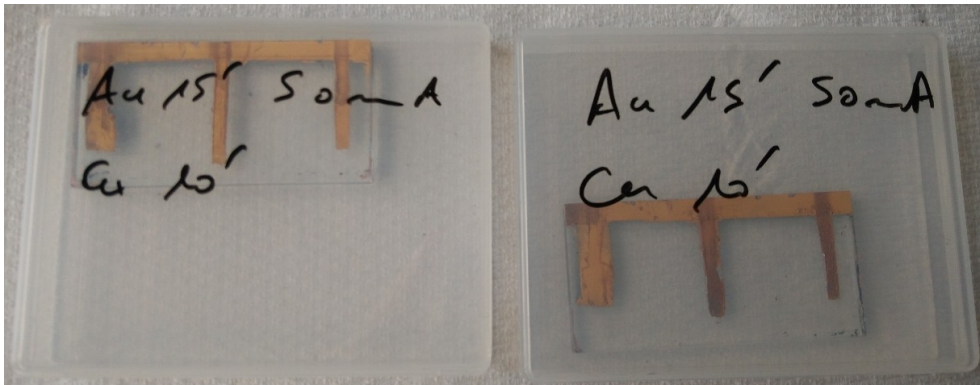


Figure 97 : COP slides with copper electrodes after the gold electroplating

This figure 97) is actually displaying on the top of the containers the time of copper and of gold growth on these electrodes, which is respectively of 10 and 15 minutes. As we can see, this method is reliable in terms of producing the selective metallisation. It must be noted that further improvement are possible, such as depositing the palladium ink directly on top of the slides with a 5 axis dispensing machine. This lead is actually currently studied in our laboratory to be presented in future works.

c) Gold electroplating on top of selective Au-Pt metallization obtained through sputtering on top of tape-masked substrates

Finally, the last technology consisted into a plain field deposition of a thin film of Au+Pt on top of tape-masked COP and glass substrate via sputtering. This step is to be followed with the

removal of the tape mask and the subsequent electroplating with gold of the obtained patterns. Though, with the success of the electroless method, this technology was not explored further, also due to the fact that the sputtered metal is known to not adhere well to COP slides, rendering that technology useless for COP chips realization, which is our main objective.

III. Test of the prototype's fluidic system

In order to characterize the performances of our fluidic system, in terms of power consumption & reaction time, we need to run tests on the fluidic chips. The tests were run on two types of chips, on COP chips and on PDMS chips. The COP chips were exclusively realized by us in the facilities of the Lab-STICC and of CINTRA, while the PDMS chips were realized by us and also by a Spanish company called Micro-Liquid.

1) First COP fluidic chip testing

A preliminary test was run early on the PhD (within the first 8 months) with a full COP chip in order to validate the concept of vertical actuation of a Galinstan column based on electrofluidics actuation, and not electrochemical actuation as in [8], and have a first characterization of the performances of that displacement.

As a reminder of the chip working principle, we can look at figure 98), which sums it up.

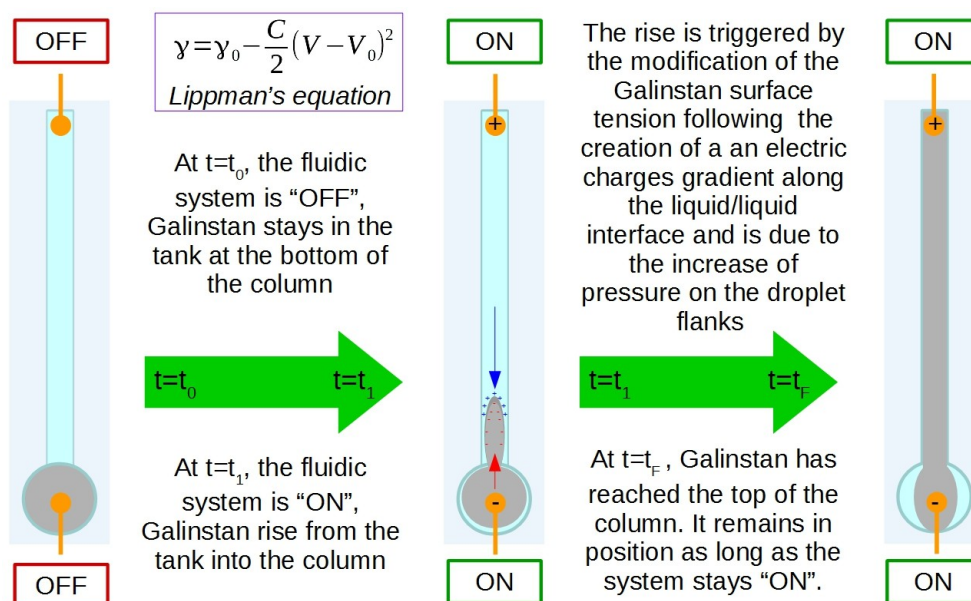


Figure 98 : Summary of the fluidic chips working principle

As we can see the cornerstone of the working principle of the chip is the Lippman's equation, which shows the relation between a variation in the voltage applied to the electrode and the creation of a

surface tension gradient along the droplet surface. Just as a reminder of chapter 1, here γ_0 is the maximum value of surface tension (for $V=V_0$), C is the capacitance per unit area of the liquid/liquid interface, V_0 the initial voltage applied between the electrodes, and V is the applied voltage across that interface.

The chip general architecture, which is the same for all the chips, is composed of a channel with at each extremity a tank, one large at the bottom, and a small one at the top. The top tank is not absolutely necessary for the chip to work, but allows a bigger electrode to be placed in. Indeed, we can see that we didn't retain it for the simulations, like on figure which is extracted from one 73). Nonetheless, it is not a critical point since it is not destined to contain Galinstan. Its presence will therefore only slightly impact the performances. The bottom tank possesses at its bottom a pressure relieve channel, which was documented in [9], and is interesting in order to prevent the build up of negative pressure at the bottom of the Tank. Indeed, that pressure could deform the Galinstan droplet by creating a trail, which would divert a part of the energy injected with the electrodes instead of focusing it to make the Galinstan rise.

The first COP chip tested, as we said above, was realized through micro-machining and enclosed with the mechanical and toluene bonding, because we hadn't developed the other technologies yet. Indeed, that test was done during our first year of work. The COP slides used as a substrate has the following dimensions: 50 mm * 25 mm * 2.5 mm (the previous COP slides were thinner by 500 μm). The diameters of the tanks are respectively 10 mm for the bottom tank & 4.6 mm for the top tank. The depth of the channel is 300 μm , for a length of 29.8 mm, which is the length between the two tanks, and a width of 1 mm.

The following figure 99) is showing the CAD depiction of the assembled chip with its top cover. The holes on it are the two holes for the placement of the electrodes and a supplementary injection hole. On the right of the figure is presented a top view of the channel with its dimensions placed on it.

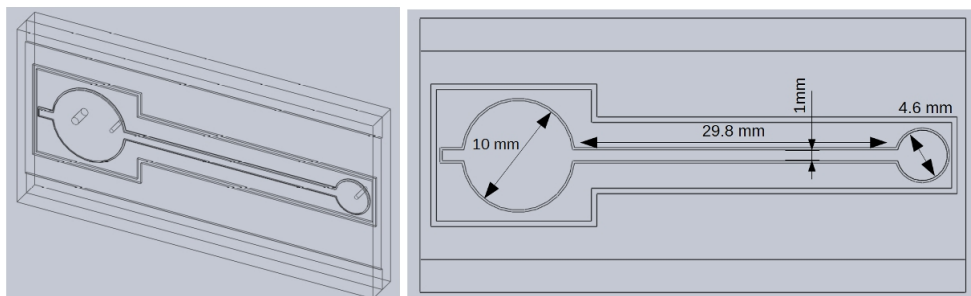


Figure 99 : 3D (left) & 2D (right) CAD views of the first fluidic system test chip

We can see on this figure the containment wall used to prevent the toluene to enter the chip, as well as the presence of a narrow step along the walls of the channel & tanks. That step, which is 100 μm deep, is also something documented in [9] by Gough et al. and is presented there as a recirculation circuit for the electrolyte. Indeed, when the Galinstan rises inside the channel under the effect of an electrical tension, the electrolyte gets pushed back towards the bottom tank under the pressure of the rising Galinstan. The cause of this is the fact that the system is theoretically enclosed and the electrolyte has nowhere else to go. That rapid backflow of the electrolyte is susceptible to create

turbulence along its path, especially along the rising column of Galinstan. Therefore, by adding this small step, we enlarge the path for the electrolyte to come back down, in a try to minimize these turbulences. It must be noted that if the initial backflow is due to that pressure increase, it is then continued by the Marangoni effect documented on chapter 1. Indeed, since the Galinstan and the electrolyte have a high surface tension gradient, once the equilibrium broken, the electrolyte will flee the contact of the Galinstan, hence fuelling its backflow movement, which in turn increase the pressure in the bottom tank. Finally that increased pressure will make rise further the Galinstan, chased away from the tank.

The test on the chip were performed by applying a DC voltage between the electrodes of the chip with a DC power supply. The voltage was applied with the negative sign on the bottom electrode, and the positive sign on the top one, in order to have a chip working with the electrofluidics actuation, not the electrochemical actuation. It's worth noted that the electrodes used here are brass wire, which has actually reacted with Galinstan when we did the experiment. The disposition of the electrode holes on figure 99) was rather indicative, since the top electrode was inserted via the top of the chip, the hole having been used for the filling.

The following figure 100) is showing the experiment setup in terms of distance & wiring:

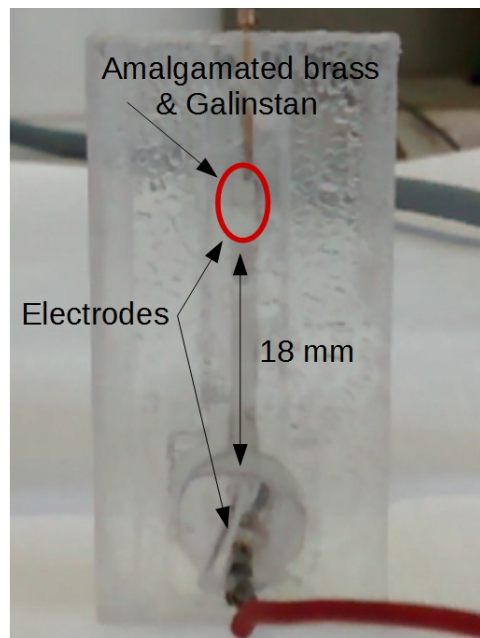


Figure 100 : Detailed view of the experimental set-up of the first chip

On this figure we clearly see the troubled aspect of the COP due to the toluene bonding, as well as the reaction of Galinstan (circled in red) with the brass electrode inserted inside the channel. The next figure 101) is displaying the rise sequence during the test of the chip, with three pictures showing the gradual advancement of the Galinstan inside the channel. From left to right, we have the initial state where Galinstan start its rise from the initial position to the moment the rising droplet touches the Galinstan which as previously reacted with the top electrode.

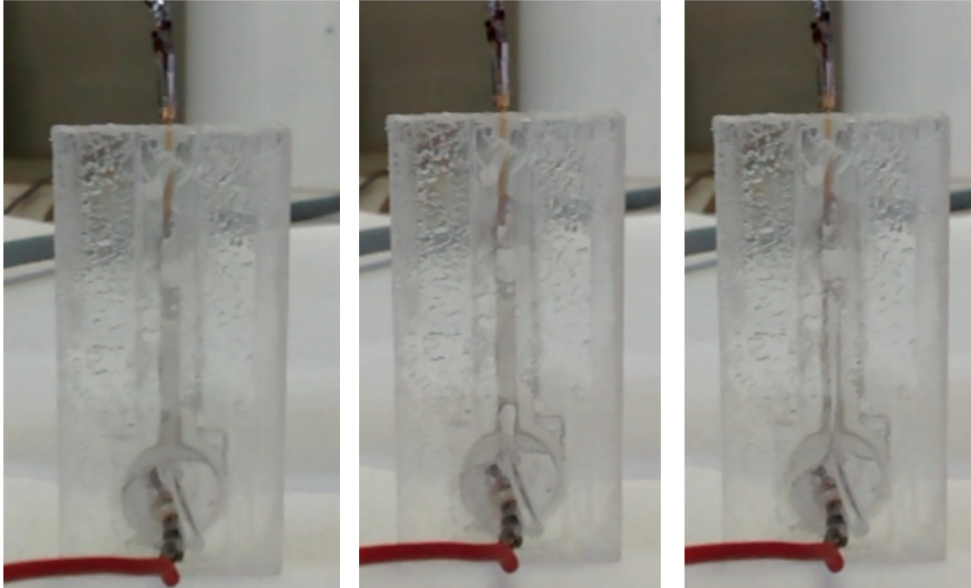


Figure 101 : From left to right, sequential rise of the Galinstan inside the first test chip

The chip has been injected with an aqueous electrolyte solution of NaOH with a concentration of 1 mol.l^{-1} and had its bottom tank filled with Galinstan (imperfectly as we can see). It must be noted that in order to ensure the sealing of the chip, the sides of the chip have been coated with toluene in order to further dissolve the two slide together. As we will see, sealing will be a major preoccupation for us, and we experimented various methods to further perfect it after the initial bonding step.

The pictures of figures 100) & 101) are obtained for an applied voltage of 5 V DC. We can observe a rise of approximately 18 mm in 8 s, which give us a rise speed of 2.25 mm.s^{-1} . When the voltage is shut off, we have the columns which retracts back into the tank in a time we can estimate at less than 1 s. Therefore we have a withdrawal speed that we can approximate it at 20 mm.s^{-1} . The power consumption was not measured, the chip having suffer a critical failure by the end of the measure session. That failure was due mainly to the fabrication technology of the chip and its sealing, and was not questioning its working principle.

We can notice that the aspect of the Galinstan column, from very even at the beginning (second image), degrades as we rise in the chip. Especially the base of the columns is very thin on the last picture. This could be potentially due to fluid turbulences in the return flow of the electrolyte or to a non optimal fluidic flow between Galinstan and the electrolyte.

If we want to compare these results with the ones presented in the literature for similar devices, we can look at the work of Wang et al. in [8], where they have a superior rising speed to ours, at 3.6 mm.s^{-1} but that we have a very superior withdrawal speed than the 0.6 mm.s^{-1} documented in that same paper. These performances are realized for voltage of -7.7 V DC , with an electrochemically actuated vertical device, which is made out of a 0.7 mm diameter glass capillary when ours are realized for an electrofluidically actuated vertical device made out of a square $1 \text{ mm} * 300 \text{ }\mu\text{m}$ COP channel & 5 V DC . While there is not to our knowledge equivalent design with this actuation presented in the literature, we can compare with horizontal design. It must be noted that in our case

the rise of the Galinstan has to fight the gravity unlike when the horizontal devices. That's why our performances will be necessarily inferior for at least that reason.

In [9], Gough et al. have documented a horizontal speed ranging from 30 mm.s^{-1} to 40 mm.s^{-1} for a voltage of 4 V DC & from 90 mm.s^{-1} to 40 mm.s^{-1} for a voltage of 6 V DC. These speeds are for a 1 mm wide channel, $300 \text{ }\mu\text{m}$ deep and 15 mm long and for the electrofluidics actuation in the horizontal plan. They have also documented a horizontal speed of 3 mm.s^{-1} in a $2 \text{ mm} * 300 \text{ }\mu\text{m} * 15 \text{ mm}$ channel for the electrochemical actuation at -10 V DC. In [10], Gough et al. again have documented a speed of droplet elongation of 8.3 mm.s^{-1} under the effect of an electrofluidics actuation and a voltage of 7 V DC. This value is for a droplet inside a 2 mm wide channel, with a depth of $600 \text{ }\mu\text{m}$ and long of 40 mm.

These example allow us to compare the performances of our system to other. We can say that we are predicability slower than the horizontal one by one order of magnitude, which was to be expected due to the fact that we cannot relies on the help of gravity to flatten the droplet. We can also see that while our device is slower than the other vertical system, there are different explanations for this. We use a smaller voltage, we start with the Galinstan in the tank and not in the channel. Finally due to the displacement technology selected, we have a system which is on the whole more reactive but allows smaller Galinstan travel. Indeed, the rise speed of our device is 2.25 mm.s^{-1} and the withdrawal speed is estimated at 20 mm.s^{-1} for a total height of 18 mm. The average rise speed of Wang et al.'s device is of 0.7 mm.s^{-1} , their withdrawal speed is of 3.6 mm.s^{-1} for a total height of 75 mm.

Nonetheless, we have encounter some problems with this first chip, namely, its reliability, which could be dramatically increased, and also with the fact that the electrodes being made of brass, it was a very harsh environment for them. The filling of the chip is also a major difficulty we need to overcome.

First of all, given that it was one of the earliest chip, its fabrication quality was not as good as the micro-machined chip we can do now, as in figure 81) for example. The use of Toluene & mechanical pressing for bonding was also part of the problem. Indeed, this technology creates mechanical stress inside the chips, which, coupled with the additional stress induced by the too harsh machining, end up by generating cracks inside the chips. These cracks of course break the sealing of the chip, and therefore render them unusable. The use of toluene present an additional risk of inadvertently dissolving the channel if there is infiltration, and forces us to add the confinement walls, which in turn require more machining.

Second, we have also noticed that the electrolyte solution is aggressive to the copper, which was predicted by us. The replacement of brass by a more chemically inert material like gold, platinum or tungsten will be necessary for the next chips, but was not done here in order to speed up the realization of this first test. It is also interesting to note that, as it was noted in [11] by Zavabeti et al., we witnessed the phenomenon of amalgamation of the Galinstan to the electrodes. This was not a problem in our case, given the size and volume of the electrodes, but it might become one if the electrodes are just deposited in thin films on top of a substrate. In such case, the Galinstan could potentially seriously damage the electrodes and therefore render the chip useless.

Finally, filling of the chip also present a challenge, because on this case of the configuration of the chip. Indeed, as we can see on figure 100), we bypassed the top electrode hole and directly inserted the electrode inside the channel. The reason for it is that we realized during the filling stage that we absolutely needed to have an air release hole for the injection in the chip. Therefore we placed the two electrodes prior to sealing of the chip and used the top electrode hole as the air release hole. Finally, to ensure a good sealing, we plugged the two injection holes with small COP rods previously partially dissolved with Toluene, instead of plugging them with the top electrode as it was initially planned. It was at this place that the critical failure which damage the chip occurs, with the breaking of the chip sealing and the its content leaking out. We also had difficulties to properly fill the chip due to the lack of depth of the channel which made it difficult for us to inject the electrolyte and Galinstan with a syringe. This last part explain why the tank is not totally filled, which can have an impact on the performances of the chip due to the mechanism of the rise. Indeed the phenomenon we use relies on the build up of the pressure on the flanks of the Galinstan droplet due to electrolyte fast displacement (Marangoni effect). It could in particular partly explained the very uneven aspect of the rising Galinstan column, which seems also very unstable.

2) Second COP fluidic chip testing

With all these observations in mind, and in order to better assess the performances of our system, especially to measure more precisely the parameters such as the power consumption, a second chip was realized and used to test the system performances. Of course, we have tried as much as possible to answer to the problems identified during the first test. The dimensions of the chip can be seen just bellow on figure 102).

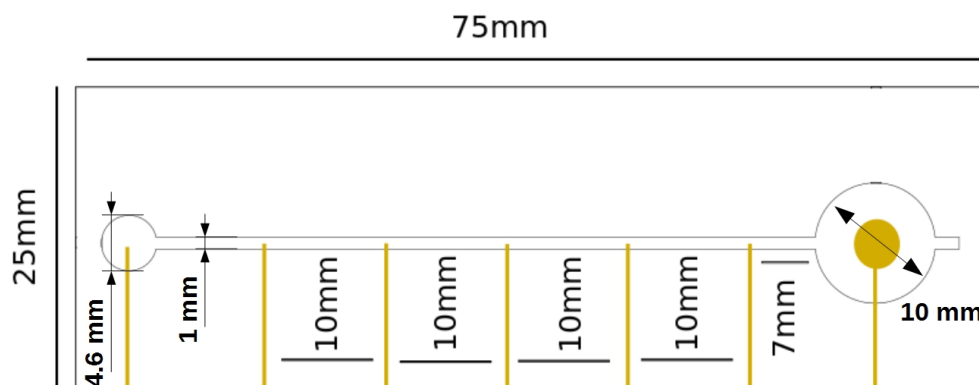


Figure 102 : Schematic top view of the chip design sent to MicroLIQUID for realization

As we can see the chip is longer than the previous one. This was made possible because it was realized externally, as we will see just bellow. It also posses multiple electrodes, the goal here was to be able to tests various height of actuation if need be. The only two dimension not mentioned here is the depth of the channel, which is of 300 μm , and its total length, which is of 53 mm. That length is not that important because we don't expect to be able to reach the full height of it.

As we said, the chip was realized by an external company named MicroLIQUID, based in Spain. It was made out of a PDMS channel topped and sealed with a glass slide. On that slide was deposited the electrodes, which were made out of gold (Au) & platinum (Au+Pt), which will be far more resistant to the electrolyte and also less prone to amalgamation with the Galinstan. The reason why we used PDMS and not COP is because the company didn't have any technologies available for COP chip patterning. The PDMS characteristics are relatively close to those of COP (as we saw on chapter 1), and so we chose to use this material.

The same kind of logic applies to the choice of a hybrid PDMS/glass architecture. Deposition of metal on PDMS is a difficult task, which necessitate an adhesion layer and the electrodes integrity is difficult to maintain overtime due to that flexible nature of the PDMS substrate, as mentioned earlier and documented by Tiercelin et al. in [3] and Hage-Ali et al. In [4] & [12]. This is why we have chosen to go with the hybrid architecture, even though, as mentioned above the glass has poorer dielectric properties than PDMS, and even more COP. Therefore this chip main purpose is to help us define further more the performances of the vertical fluidic system rather than to be integrated inside the antenna system.

Finally, in order to solve the injection problems we have encounter, the chip will be integrated inside a two part holder, realized in transparent polymer through stereo-lithography. This holder, made of two halves screwed together, holds the fluidic connection and electric connection to the chip, therefore avoiding the aforementioned problems with the filling and the electrodes contacting. The chip and the holder from MicroLIQUID can be seen bellow on figure 103), with the chip on the left and the same chip inside the 3D printed holder (fabricated via stereo-lithography by MicroLIQUID) on the left.

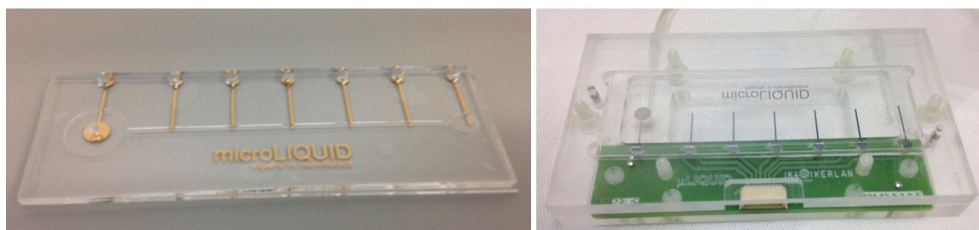


Figure 103 : MicroLIQUID PDMS/glass fluidic chip (left) and inside its holder (right)

The testing of the chip was realized in Singapore inside the CINTRA & school of EEE facilities. The Galinstan needed for it was brought by us to Singapore, and the NaOH used for the electrolyte was made available to us by the team of assistant professor E. Teo. The following figures 104) & 105) illustrate this testing phase, with the full rise cycle illustrated on figure 104) and a zoom on the initial and final sequences on figure 105).

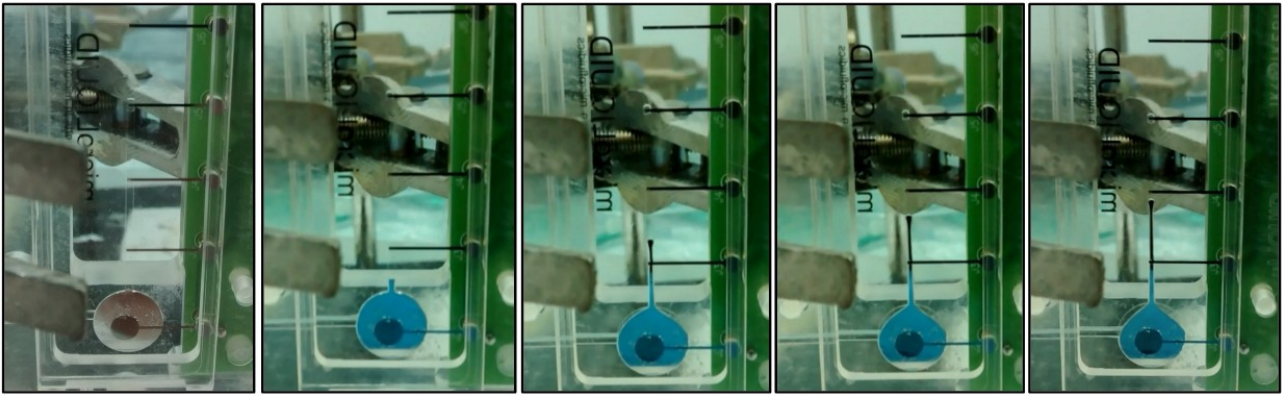
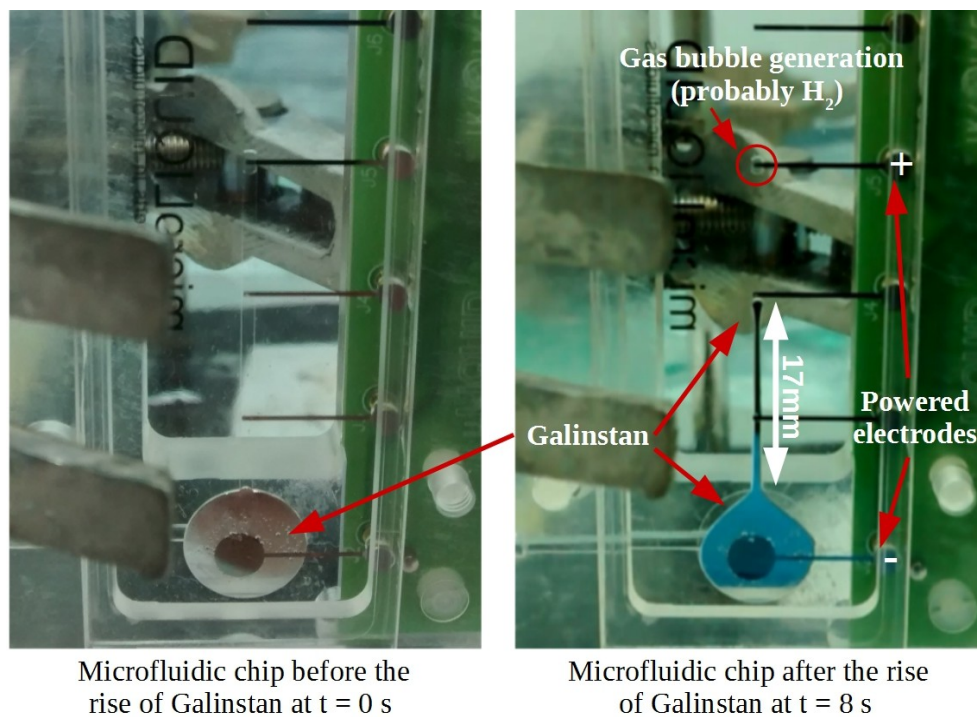


Figure 104 : From left to right, sequential rise of the Galinstan inside the second test chip

As we can see on this figure, we see the full rise step by step, with a total elapsed time between the first image to the left and the last to the right of 8 seconds. The rise occurs for a voltage applied to the electrodes (pin pointed on figure 105) of 20 V DC.



Microfluidic chip before the rise of Galinstan at $t = 0$ s

Microfluidic chip after the rise of Galinstan at $t = 8$ s

Figure 105 : Detailed view of the rise of the Galinstan inside the second test chip

This figure 105) presents the total height of the rise of the Galinstan which is 17 mm. That height is reached in 8 s, which gives us an average speed of $2.1 \text{ mm}\cdot\text{s}^{-1}$, consistent with the speed already measured for the first chip. We can also notice on this chip that there is the formation of a bubble at the positive electrode, with the bubble circled in red. This bubble is likely to be dihydrogen gas, and is most likely due to the water electrolysis. This phenomenon is to be expected given the relatively high DC bias we have applied to the chip. It's worth noting that the occurrence of such gas release at the cathode during the use of CEW like actuation was documented in the literature by Eaker & Dickey in [13].

The aspect of the rising column on this chip is way more even and the rise looks less turbulent than on the previous chip. This could be linked to the fact that the channel & the tank are properly molded & that the last one is completely filled with Galinstan. Indeed, we can see that there is of course a deformation of the droplet inside the tank, but that deformation is more even and limited to the superior half of the droplet. This is likely due to the Marangoni effect, where the returning electrolyte, by entering the tank, pressure the side of the droplet, which in turn expel more Galinstan into the channel.

The power supply of our chip was done through a Chroma 62012P-80-60 programmable DC power supply, which gave us a current output indication during the measure via its front panel. The current display resolution on this panel is of 10 mA, as indicated in [14]. The current values measured at the front display during the rise of the Galinstan were of 140 to 160 mA during approximately 1 s, followed by a current of 1 to 10 mA during the remaining time of the rise, with reserves on that value since we are reaching the limits of the resolution of the display. These values were reached for an applied voltage of 20 V DC.

Among the things worth noticing, there is the significant increase of the DC voltage needed to actuate the chip. Indeed, it went from 5 V DC to 20 V DC, while the channel section dimensions stayed the same, with 1 mm width and 300 μm depth. Among the differences between the chips, we can cite the length of the channel (from 29.8 mm to 53 mm) and the distance between the electrodes, the material of the chips (COP versus PDMS+glass), the material of the electrodes (brass versus Au+Pt). Another difference could also be the fact that the chip is not operating fully sealed, neither at atmospheric pressure, since the injection channels are always connected to the injection syringes (one at each of the two end of the circuit) and given that there is no fluidic valves installed on the holder. That means that the hydraulic pressure inside the fluidic circuit is kept at a higher level than in the first chip, and is constantly hold. That could potentially explain the rise in the actuation voltage from 5 V to 20 V DC, given that the actuation of the Galinstan in our case relies heavily on the pressure action onto the flanks of the droplet which leads to the rise of the Galinstan level inside the channel. Therefore, we would potentially need a greater voltage to create a sufficient gradient to overcome the initial pressure.

Based on the displayed current information, we can calculate a very rough estimation of the power consumption of the chip, which seems to present a spike at 3W during 1 s, but then decrease dramatically and lies between 200 to 20 mW during the rest of the operation time. This gives an energy spend of 4.4 J to make the Galinstan rise 17 mm at 2.25 $\text{mm}\cdot\text{s}^{-1}$.

It must be noted that these values are be taken with caution because we couldn't perform a sufficient number of trials with this chip. Indeed, we experienced a mechanical failure of the chip due to the holder system (namely, the glass cover cracked, therefore breaking the sealing of the chip). This failure has been combined with a phenomenon which prevented us to properly fill the tank of the chip, as we can see on the following figure 106).

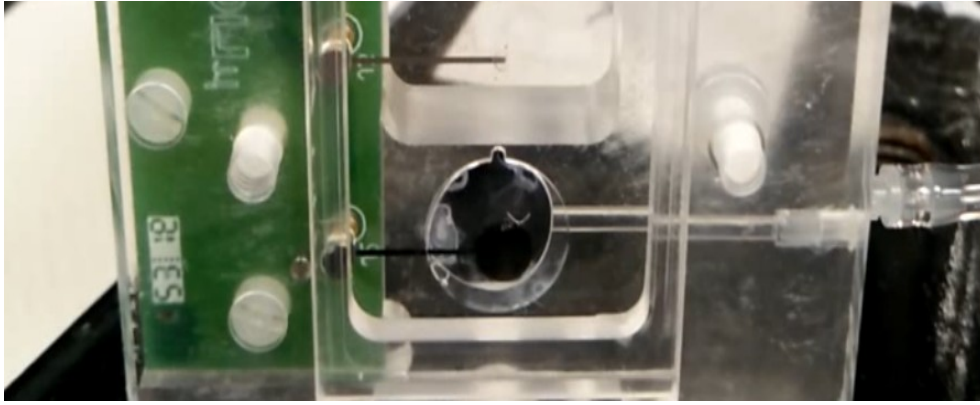


Figure 106 : Example of an incomplete filling scenario of the chip

This improper filling had serious consequences on the ability of the chip to function. Indeed, as we explained above, the rise of the Galinstan inside the channel is largely due to the recirculation of the electrolyte inside the system, electrolyte which play the role of a “pump” to push on the flanks of the Galinstan droplet and therefore “squeezing” it to rise. If the filling of the tank is incomplete initially, there is new directions towards which the droplet can expand, within the tank itself, therefore rendering the chip useless for our purpose.

The reason of this filling problem is not known of us, especially since that problem didn’t seem to occur with the COP chips we will look at in the next part. We can hypothesize that it’s maybe due to the fact that the microliquid chip is the only chip realized in PDMS, which have in particular wettability characteristics very different to the COP. Another observation we can make about this is that the injection hole for the tank is placed in the middle of it and right after a 90° angle in the injection canal, visible on the right of the holder on the figure 106) above. This could prevent the Galinstan to reach the bottom during the injection phase, especially in a situation where the pressure inside the chip is already high and might prevent movements of the Galinstan droplet.

In addition to these two points (the relatively early failure of the chip and the inability to fully fill the chip’s tank), the fact that we are operating in what appears to be a constraint environment (for the pressure inside the chip) plead for a certain distance, especially towards the power consumption results. As we will see on the next part, the measured value here are far remote from the values measured for our in house developed COP chip.

In order to avoid the problems we had here, we are going to implement modification on the architecture of our in house chip. First of all, as we said just above, they are going to be made of COP only, which will suppress the risk of having a fragile chip breaking under mechanical stress. Second, we are going to revise our injection methods in order to be sure not to have an initial overpressure in the chip. Third and finally, we are going to modify the position of the injection hole for the bottom tank, by placing it at its base, so that risk of filling problems like the one observed on this chip will be minimized.

With all these observations in mind, and in order to better assess the performances of our system, especially to measure more precisely the parameters of the power consumption with a greater repeatability, a third model of chip was realized and used to test the system performances.

3) Third COP fluidic chip testing

As we mentioned it above a third series of chip have been made with the help of the technology we developed and presented above to have in house the full chip fabrication process. Those chips were realized by hot embossing of COP slide, which were then drilled to allow their injection & the contacting of the electrodes. Those holes are drilled with a CNC machine available in our lab, a LPKF S103, which was already presented before. An example of such half chip ready to bond can be found on figure 107).



Figure 107 : COP fluidic channel after injection and electrodes access holes drilled through it

Those electrodes were first deposited on top of COP slides through the auto-catalytic bath process described above. This means that the first layer is made of palladium on top of which copper is deposited. In order to protect the copper from the NaOH solution, we have then grown a layer of gold on top of the copper through electroplating. Examples of this process results have been presented above on figure 97).

The half chip obtain through this process is now ready to be bond to the second half containing the channel. This bonding of COP chip is performed along the exact method described in part 4) above, meaning the two slides are compressed together in an oven heated at 190° for 210 minutes. We can see on the following figure 108) an example of a successful result of the bonding process, just after the bonding.

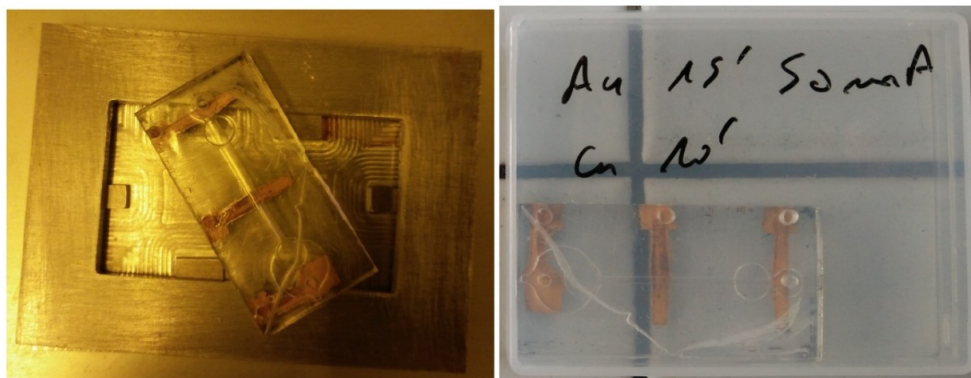


Figure 108 : COP fluidic chip with gold plated copper electrodes after thermal bonding

As we can see, we have a chip architecture with three electrodes, fully made in COP. We can also notice that we have moved the injection hole of the bottom tank (aligned with the channel, visible on the picture on the right of the figure 108)) towards its base, as advised as a consequence of the tests of the second chip.

Now, the final steps in order to produce testable chips are make sure that they are sealed enough to withstand injection & tests and to add the contact wire for the electrodes. Regarding the sealing, we have experienced small leaks from the thermally bonded chips. The reason for it lies in the process of the hot embossing.

Indeed, we are embossing plain COP slide by heating them and pressing them in a mold at the bottom of which is the thumbprint of the channel we want to create. During the process, no matter is removed from the COP slide, it is just displaced. Therefore, while it works to create the channel, the surface of the slide is deformed, and less plane than the original slide. This was already highlighted above on the figure 86). This has an impact on the thermal bonding, because the contact between the two slide to bond is not perfect along the sides of the channel. This weaker & imperfect bonding leads as a consequence to leaks.

A good solution to this problem would be to transition from hot embossing of COP plain slides to injection of COP directly in a mold with the template needed. We would also witness much sharper channels walls, with a profile closer to the PDMS channel's one, as shown on figure 86). It was not done due to the fact that it would require a new mold for injection technology & therefore not hot embossing, which is relatively long, complex & expensive to produce, at the moment for this study.

To answer to this problem of small leaks, we initially decided to film the chips with an adhesive polyimide (commercial name: Kapton) tape, as shown bellow on figure 109). This measure is only intended here for the fluidic trials and will have no consequence on the fluid properties of the chips.



Figure 109 : Kapton (polyimide) film coated COP chip

On those chips were then added the electrodes & the filling tubes. Regarding the electrodes, they were tin soldered to electrical wires.

For the filling tubing sections, they were needed after our decision to move away from the holder solutions after additional trials with a holder we 3D printed at the UBO Open Factory (University's Fab-Lab). Indeed, during those trials it appears that non-permanent fluidic connections could not

guarantee us a sufficient sealing of the chip and weren't actually very practical due to the obligation for us to overcome alignment problems. Those problems arose from the dimensional variation during the printing of the support itself & of the variations of the positioning of the injection holes from one chip to another.

Instead, we have decided to insert polymer tubing inside the chip and glue them into place. Once glued, those tubing were also glued inside larger diameters PVC transparent tubing sections, which allow us, through the use of two fabricated connectors, to adapt specific "Luer-lock" connectors to the chips.

In order to guarantee the sealing of the chip, the electrodes wells containing the soldered wires were topped with a coating of the same glue used for the injections tubes. The following figure 110) is showing the resulting chip with the soldered wire before & after the addition of the tubing.

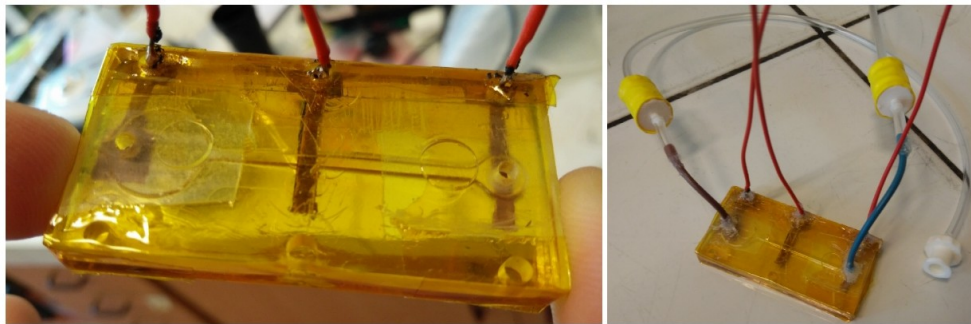


Figure 110 : Kapton filmed COP chip with wires soldered (left) without & with the filling tubing sections (right)

As we can see on the left of the above figure, there is also holes drilled on the other side of the wires. This is only the case on a few specific chip. Those holes have been plugged with the glue.

After a first round of injection testing it was noted that some leaks were still occurring, specifically at the corner of the chips, and that those leaks were channeled under the Kapton. In order to definitely suppress them, we have coated a relatively large part of the chip which transparency was not crucial to us, with the glue used previously. An example of the resulting chip can be seen on figure 111) bellow.

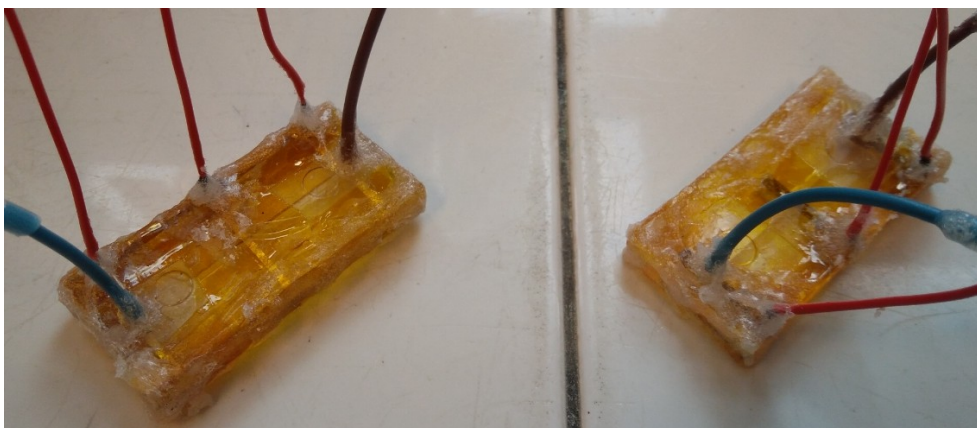


Figure 111 : Kapton filmed COP chips with wires soldered & filling tubing sections after being sealed up by glue

The above figure clearly shows that the coating with the glue is concentrated at the edges of the chips. We can also notice that we have cut of the Kapton coating above the channel because it was not useful here and might block our field of view during the experiments. Those chips were then injected with a mix of Galinstan & 1 mol.L⁻¹ NaOH solution in order to test them on the bench we have installed and that we can see on the following figure 110).

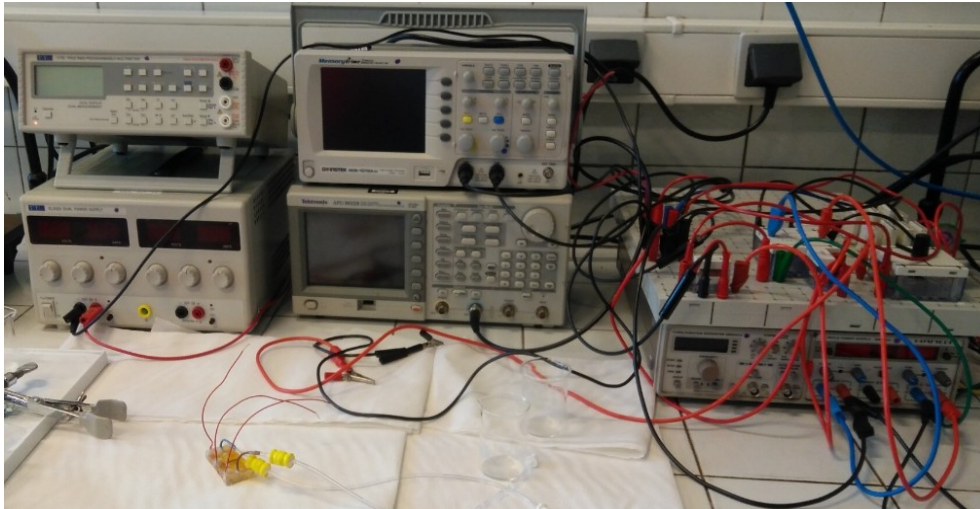


Figure 112 : Test bench of the fluidic chips

This bench is composed of a DC power supply for the chip to work on DC mode, an oscilloscope to monitor the current in the chip (with the help of a measure resistance in series with it), a function generator in order to test the effect of an AC signal on the chip, and finally a second DC power station paired with an operational amplifier used as a non inverting summing amplifier. This final part of the bench is needed if we want to inject AC signals with peak to peak tension superior to the max output voltage of the function generator, or if we want to add a stronger DC bias than the one achievable with the function generator.

The measures were conducted using the chip presented above on figure 109) only using a DC power source. The goal of those measure is to determine the speed of actuation of the chips as well as their power consumption.

The first test we did was to apply a 9V DC voltage to the circuit comprising the chip and the measure the voltage at the terminals of the resistance (needed to get an image of the current). This resistance is 100 Ohms resistance and is in series with the chip. The objective of that first measure is to get a precise value of the I_R current flowing through the chip during the operation. The voltage of the chip can be calculated as the DC voltage minus the voltage of the resistance ($V_R = R \cdot I_R$).

The resulting Galinstan movement can be seen bellow on figure 112), achieved with the chip 3, the third COP fluidic chip testing:

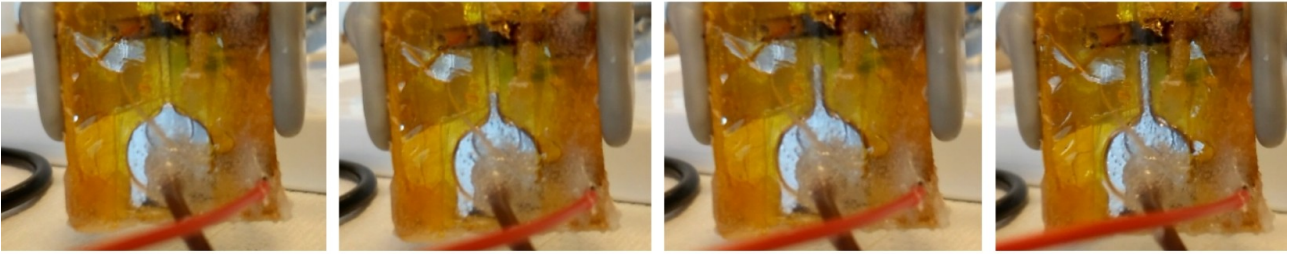


Figure 113 : Rise sequence of the Galinstan inside the chip 3

As we can see on this figure above, we have a rise of the Galinstan between the two connected electrodes. The rise length is 8 mm between the top of the Galinstan filled tank and the bottom of the gold plated copper electrode, as we can see on the following figure 113):

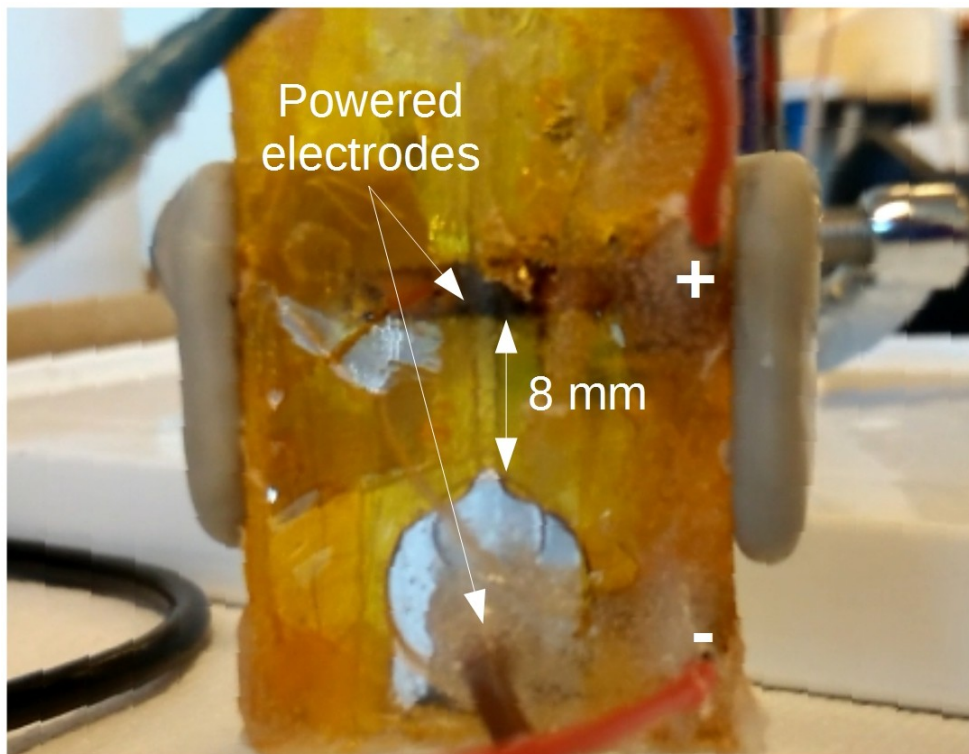


Figure 114 : Detailed view of the initial setup of the chip 3

The rise displayed on figure 113) has taken place in approximately 4 seconds, which means we have a Galinstan speed of 2 mm.s^{-1} . The measured current allowing that rise is a 15 mA DC current. From this value, the value of the resistance as well as the value of the applied DC voltage to the system, we can find back the value of the voltage applied to the chip itself. This value is 7.6 V, which mean the rise of the column necessitate a power of 114 mW.

We have done a more thorough testing of the chip by looking at the relation between the current flowing in the chip as the function of the tension applied to it. Those measures were done with a slightly different setup, because we used a 1 k Ohms resistance to measure the current. The following figure 115) is presenting the results of those measures:

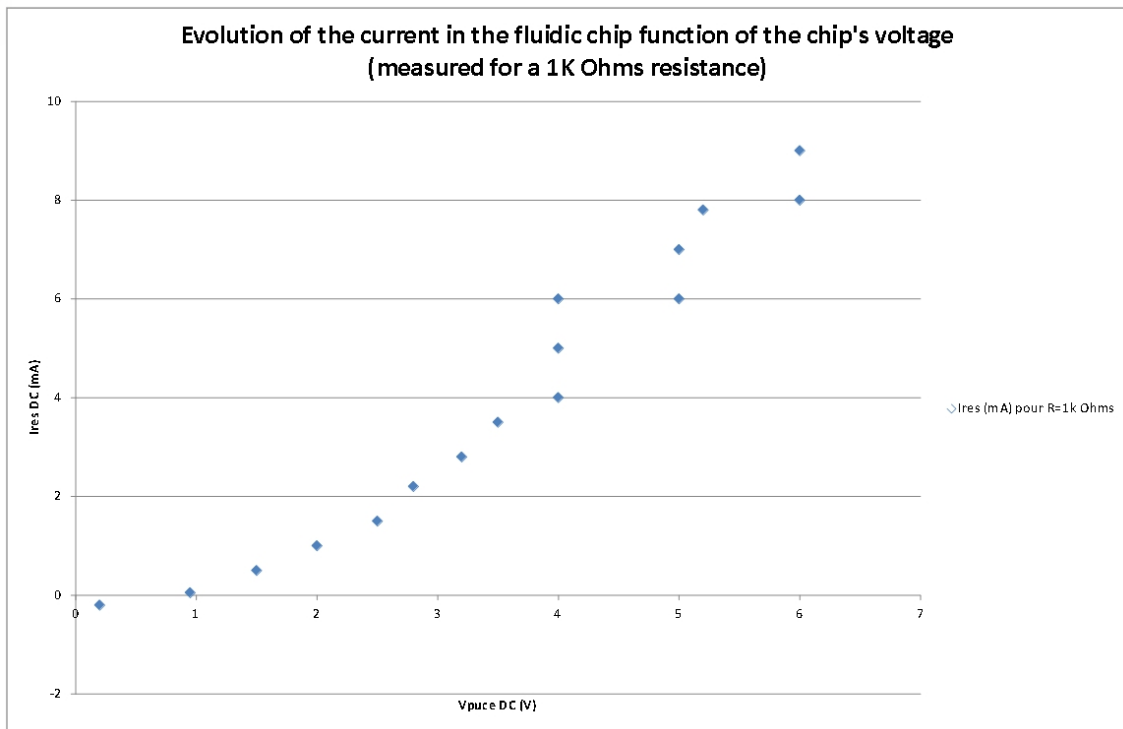


Figure 115 : Evolution of the current in the chip as a function of the voltage applied

As we can see, and rather predictably, the higher the tension, the higher the current flow in the chip. We also notice a “stairs” pattern which seems to appear after 4 V.

If we are to compare the performances reached for this chip to the others, we can first of all notice that despite differences in fabrications technologies & materials, their respective speed are comparable and comprise between 2 to 2.3 mm.s⁻¹ and all those chips have been actuated with DC voltage only. The common element to all these chips is their design which is almost identical to all of them. The depth may varies a bit from the initial 300 μm, especially for the hot embossed chip, but that is all.

We can notice that the height reached in the third chip is significantly lower that what was reached for those chips, with here 8 mm against 17 mm for the glass & PDMS chips & 18 mm for the first chip. The main reason is the spacing between the electrodes, the Galinstan is well mounted up to the top electrode. We could not perform the test using the third upper electrode because it had an electrical connection problem, probably due to the presence of air bubbles inside the channel, disrupting the electrical path.

On the other hand, we can see that the aspect of the rising column is very similar to what we observed on the second chip, with a very stable column and few turbulence observed along the rise, on the contrary to what was observed on the first chip. We can also notice a deformation of the droplet's superior half which here also is very similar in shape to the second chip, with the flanks bended in a typical way.

The actuation voltage is also a source of differences. While in this case we are at 7.6 V, the second chip needed 20 V & the first 5 V. We note that we are closer to the first chip than the second chip in this regard.

Finally, if we look at the injection mode, while the first chip was injected and sealed once and for all, the second was injected with a syringe which stay connected to the chip, with another one at the second extremity of the fluidic circuit. The result of this is that the chip was “pressurized”, operations didn’t took place at atmospheric pressure due to the mode of filling retained. The last chip was also injected through a syringe, but the fluidic circuit was let open at one extremity, which therefore didn’t led to a pressure build-up inside the chip. Nonetheless, the chip was not a fully enclosed circuit as the first chip.

The following table 6) will sum-up the behaviour of the chips for a DC actuation:

Table 6: Sum up of the performances achieved during the chips testing

	Chip 1 (COP/COP –micro- milling & toluene bonding)	Chip 2 (PDMS/glass – molding & O₂ plasma bonding)	Chip 3 (COP/COP – hot embossing & thermal bonding)
Rise speed of Galinstan achieved (mm.s⁻¹)	2.25	2.1	2
Height reached (mm)	18	17	8
Voltage needed (V)	5	20	7.6
Current needed (mA)	-	-	15
Initial pressure & sealing conditons of the fluidic circuit	P_A – sealed	$P_{int} > P_A$ – unsealed	P_A – unsealed

We can already propose a potential lead to enhance the performances of the chip by transitioning from a DC only to an AC command based on a 30 Hz squared signal. Indeed, as it was demonstrated in by Gough et al. in [10], for horizontal displacement, this transition doubled the displacement speed and made the slug displacement smoother. Therefore by applying this type of command to our system, we can hope to also have a higher speed of actuation and maybe to lower (and possibly eliminate) turbulences inside the channel.

IV. Test of the system’s proofs of concept

1) Test of the non-fluidic proof of concept

The final design of antenna having been established earlier and the antenna fabricated, we have run a first test of our system, but a simplified version of it. That version is featuring all the RF functionalities of the final device, without any fluidic. Basically, we have replaced the chips and the

Galinstan columns inside them by vertical copper wire (of course, after having adapted the dimensions). The interest of such system is to validate the working principle of our system from an EM point of view and have a first round of measurements for the antenna. The fluidic system will later be integrated into the system, in order to have a more accurate performances evaluation of the prototype.

Given that we are working in air and not in COP slides, we have to change the absolute (geometric but not electric) dimensions of the system, the parasitic elements ones more specifically. The reason for it is that the effective dielectric permittivity of the whole system can now be considered to be equivalent to 1 (instead of 1.44 for the last simulation presented on chapter 3), which therefore, lead to an effective wavelength value of 60 mm. We have for this “non-fluidic” system the same dimensions for the parasitic elements as the first simulation presented in chapter 3. These dimensions are the reflector length, L_R 30.6 mm, the director length, L_D 24.6 mm, the spacing between the feed antenna & the director, S_{DF} 18 mm, the spacing between the reflector & the feed antenna, S_{RF} 15 mm and finally the spacing between the two directors, S_D 18 mm. These elements were cut to the right dimension from copper wires.

The following figure 116) is presenting a sectional schematic view of the non-fluidic system on the left, with on the right a picture of the real system assembled.

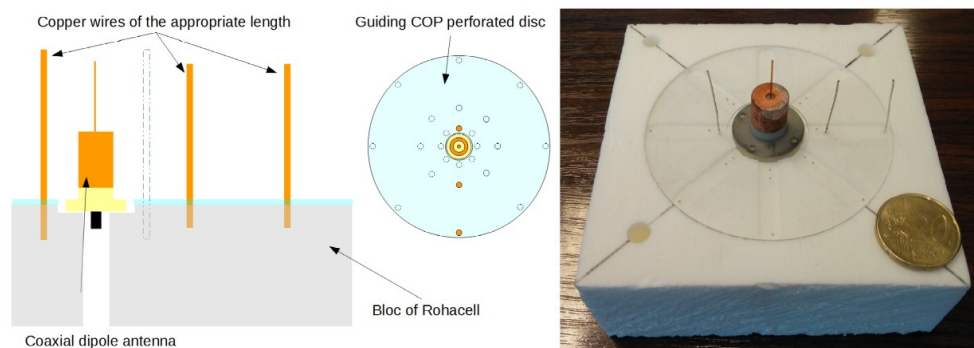


Figure 116 : Schematic view of the non-fluidic proof of concept (left) and picture of the real device (right)

As we can see, the copper wires serving as directors and reflectors are positioned at the adequate distance from the central antenna. Their position is guaranteed by the presence of a guiding perforated disc made of COP, through which the wire must go. The wires are then planted into a bloc of polymeric foam (here Rohacell) placed under the COP disc. This disc, with a diameter of 75 mm and a thickness of 1mm, is made of COP slides manufactured with the help and the equipment of the IRDL laboratory from Zeonex granules. This demonstrates the possibility for us to manufacture large and thin slides of COP. The antenna itself is positioned on top of the Rohacell block, which has been specifically machined to house the antenna and the COP disc in specific recesses. This means that we have a relatively good & repeatable control over the wire positions, because the wire position relative to the COP disc are fixed, and its position relative to the central antenna is fixed also.

Indeed, that block of Rohacell serves a specific purpose, and this material was specifically selected. In order to be able to test the system efficiently inside an anechoic chamber, we have decided to encase the system inside a fully enclosed support which would protect the antenna when we

manipulate the device, and guarantee that the copper wire doesn't fall from the antenna or be bended for example. This support is machined from two blocks of Rohacell, and we can see an example of it on the right of the figure 116) above. This polymer was chosen because it has a very low dielectric constant as well as a low loss tangent, as shown bellow:

- **Rohacell:** $\epsilon_R = 1.106$, $\tan \delta = 16.10^{-4}$

As we said, the Rohacell casing is made of two blocks, with the following dimensions: 100 mm*100 mm*40 mm. Those blocks were machined in order to leave empty volumes to house the central antenna and the parasitic elements. This was done with a CNC machine in the UBO Open Factory of the UBO university. A picture of the system can be found on figure 117) bellow:

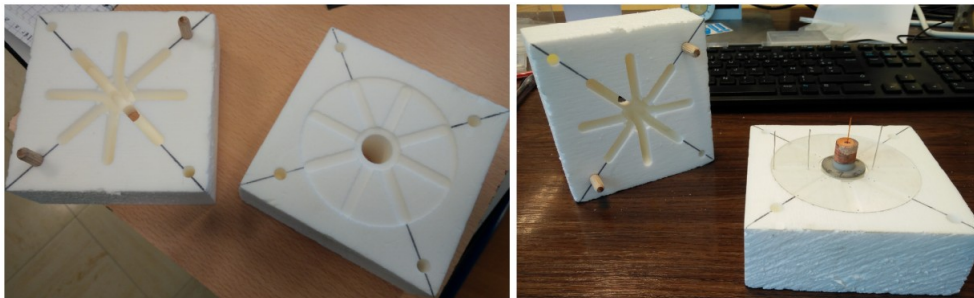


Figure 117 : Pictures of the non-fluidic system Rohacell support without (left) & with (right) the system installed

The first measures done on the non-fluidic system was the S11 measurement of this configuration which was then compared to the results obtained for the simulation for the same system on HFSS. The simulated configuration (and therefore the measure configurations) is the narrow unidirectional one configuration, which is the configuration for which our system is optimized and the one displayed on the right of the above figure 117).

The following figure 118) is showing the simulated system, as we can see almost identical to the tested one. This view also allow us to see a bit more closely the general outline of the configuration measured in order to get the S11 parameter.

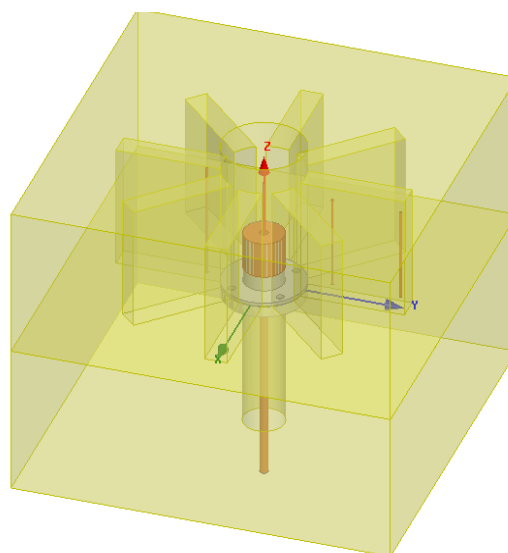


Figure 118 : Simulated non-fluidic proof of concept in unidirectional configuration

We have included the Rohacell support in the simulation, because while its impact should be low, it appears more accurate to compare to the measured system one which is as close as possible, especially given that there is already a notable difference between the two systems.

Indeed, the main difference between the simulated system and the fabricated one is the transition between the coaxial cable and the central antenna itself. As a consequence, it means that the difference is only on the modelling of the central antenna. In the simulation it is considered that there is no discontinuity of the coaxial feed cable, when in reality, there is one. The following figure 119) is showing the difference between the simulated system and the real one with a figure displaying a sectional view of the central antenna of each systems.

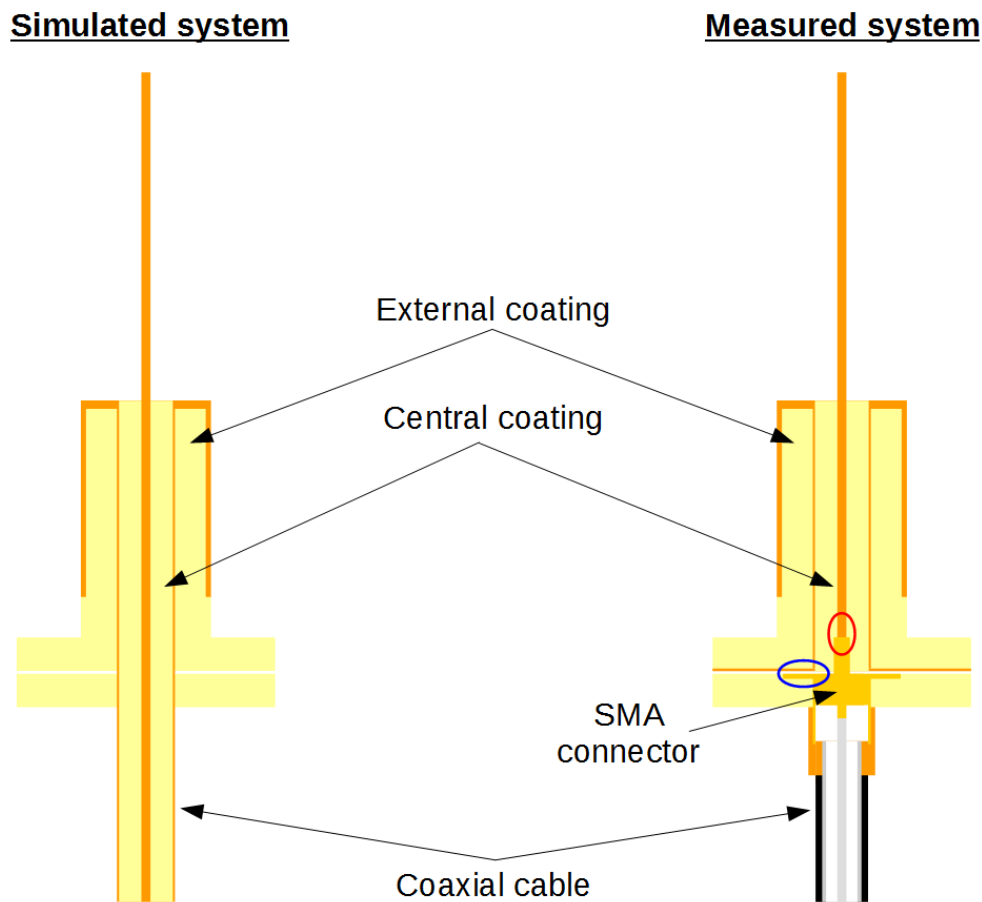


Figure 119 : Illustration of the main simulation/measurement modelling difference

As we can see, on the real system, on the right, we have a SMA connector which terminates the feed coaxial cable. The centre of the SMA is then connected to the central conductor of the antenna (within the red circle part), and the external conductor of the coaxial cable is connected to the main body of the SMA connector. This body is then put in contact with the sleeve of the antenna through the metallized bottom of the 3D printed “external coating”, which ensures the electrical connection, as we can see on the blue circled part above. On the other hand, we can see that on the simulated system, on the left, the central coating and the coaxial cable are in fact the same part, which has been elongated and through which is injected the signal. Due to this choice of modelling, we can expect potential differences in the behaviour of the simulation & the measures

The cause of those differences is not the SMA itself, because it is design to have an impedance of 50 Ohms, so it's not its presence in itself that might induce potential differences between the simulation and the measure. Instead, it is our interfacing work between the SMA & the antenna which could likely cause such differences. We can indeed notice that the introduction of SMA is creating a discontinuity of the impedance, due to the transition from the SMA pin diameter to the central conductor of the antenna itself. Because that transition happens inside the section where the central antenna coaxial section is optimized to have a 50 Ohms impedance for the diameter of the central conductor (which is 500 μm), the increase of that section to 1.28 mm will have for effect to lower the impedance. This impedance will in this case fall from 50 Ohms to approximately 20 Ohms, creating a discontinuity and potential frequency shifts in the antenna's response.

We can also see another potential differences source in the presence of the large metallization ring at the bottom of the "external coating" part and with possible air gaps between that ring and the base plate of the SMA connector. Such gaps would create a parasitic capacitor, which could also potentially impact the frequency response of the antenna.

Those two phenomena in particular have been simulated in the case of that system and the result of these simulation will be discuss further down, when we will present the S11 measure results for the non-fluidic system. It must be noted that these differences should occur in a similar fashion in all designs using the same central antenna which were simulated with the same "No-SMA" model. It means that by comparing measure results of different systems using that antenna, we shall see similarities in the way the simulation & the measure differ.

Now that we have presented the likely source of differences between the simulation and the real system, we can go back to the presentation of the results of the S11 measurement for the system presented in figure 117).

This measure was done with an Anritsu VNA master MS2026C, and its results can be seen on figure 120), which is showing the comparison between the measure & the simulation for the unidirectional configuration. On the following graphic, the measured curves are in dashed lines and the simulation curves in plain lines.

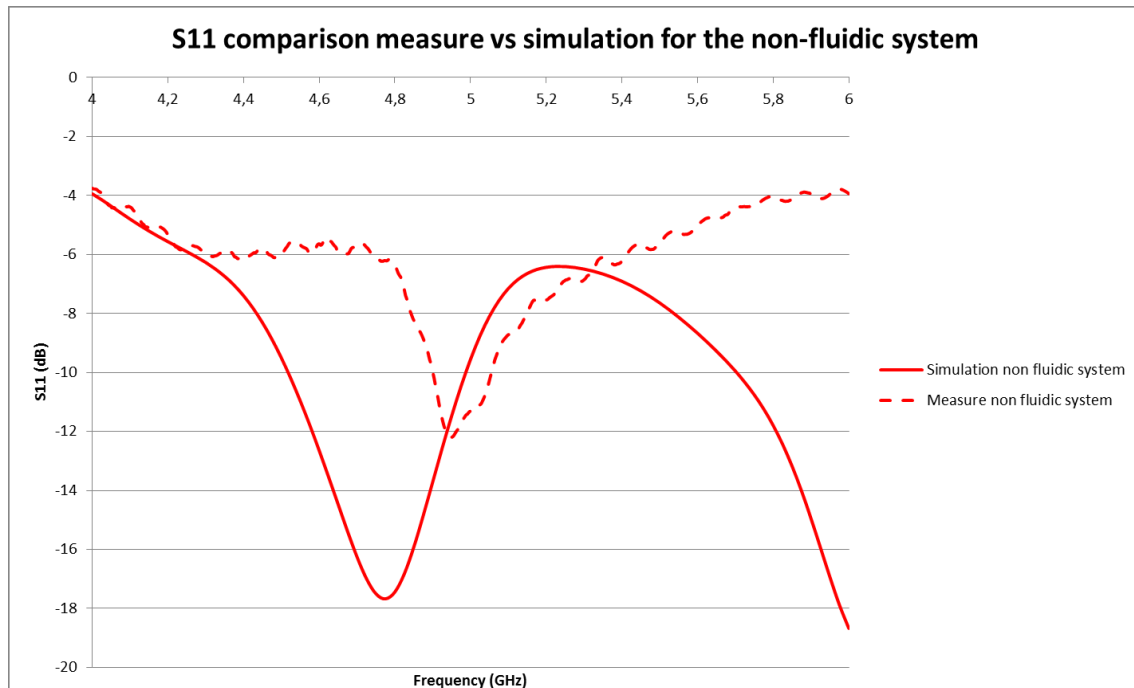


Figure 120 : S11 comparative evolution of the non-fluidic system for simulation & measure

We can observe that there is a difference in terms of resonance frequency between the simulation and the measures. Another difference visible is the level of the resonance peak. The frequency shift towards higher frequency between the simulation and the measure, going from 4.775 GHz to 4.950 GHz, which is a 175 MHz shift (3.5% variation of the theoretical system operating frequency, 5 GHz). In terms of peak levels, we notice that the minimal level for the simulated system is around -18 dB, when for the measure system it is of around -12 dB. This mean a 6 dB difference.

We also notice that there is a second peak towards the 6 GHz frequency which appears in simulation, but not in the measure. Though, given the frequency shift reported on the measured device it is possible that this peak occurs in the measure at a greater frequency, and therefore is not visible on this graphic, the aspect of the curve doesn't seem to indicate it is the case.

As we said above, simulation were done to assess whether the impedance variation due to the SMA to central conductor transition or the presence of the metallization ring could explain this frequency shift. The following figure 121) presents the S11 response for the fabricated system, for the initial simulation (following the modelling presented above on figure 118)) and for three other simulations. Two of those retain the general layout of the initial modelling, but one add a locally enlarged central conductor to model the impedance discontinuity, the other add the same metallization ring present on the fabricated system. Finally, the last simulated system feature a simplified version of the SMA connector present on the fabricated system.

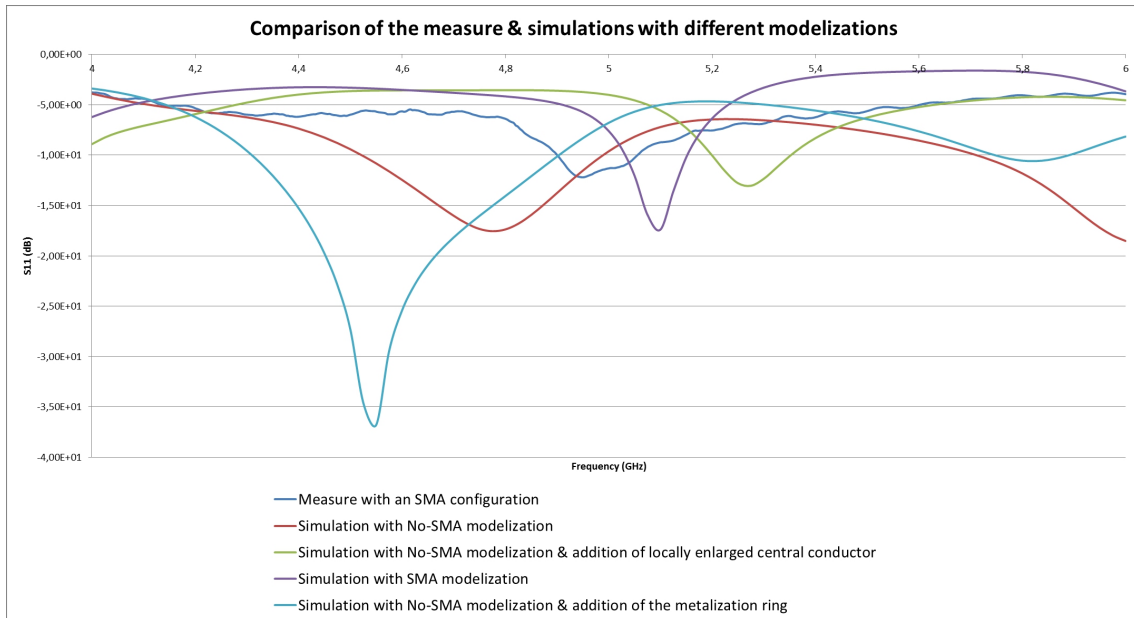


Figure 121 : S11 comparison for the various feeding system models

As we can see, it seems that the effect of the metallization ring is to offset the resonance towards lower frequency (at 4.55 GHz) while the presence of the impedance discontinuity offset it towards the higher ones (at 5.275 GHz). We can also see that the resonance peak for the simulation featuring the simplified SMA has a resonance peak at 5.1 GHz, which represent a 150 MHz shift from the measure own peak, at 4.95 GHz. Therefore, we can propose the hypothesis that the combined effect of the metallization ring and the locally enlarged central conductor of the antenna are the main responsible for the difference in term of frequency of the resonance peak we can notice between measurement & simulation.

In order to further understand the behaviour of the system, it seems necessary to also show the curves of the evolution of the impedance of the system, as shown bellow on figure 122).

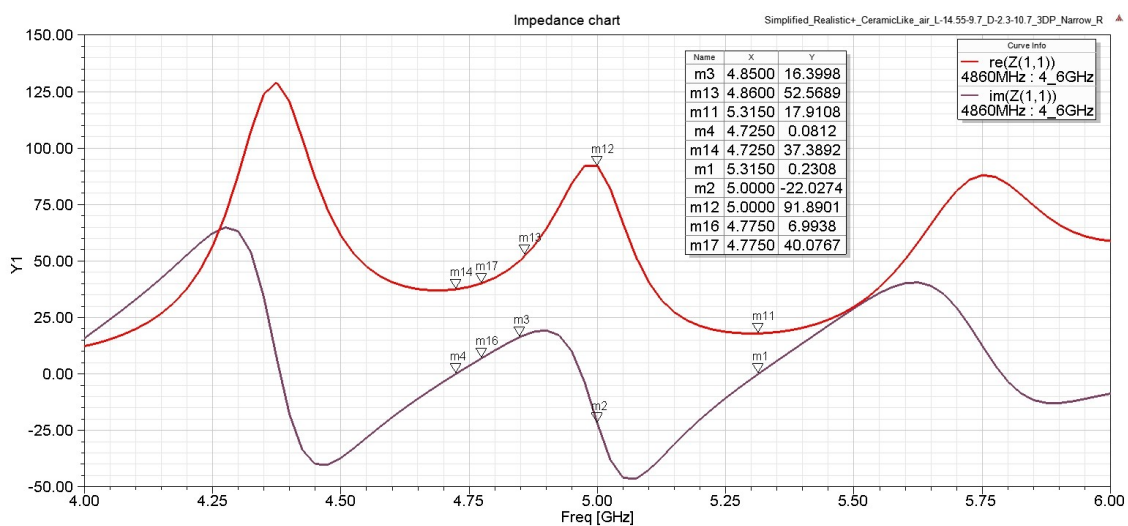


Figure 122 : Impedance evolution of the simulated non-fluidic system

As we can see, there are several points where the Im curve cross the zero line. Now, to get adapted, we need to have at the same time an imaginary part at 0 or close, and a real part at 50 Ohms, or

close. If we look at the figure 120), we can see that the resonance peak is around 4.77 GHz. We can see that on the graphic above that for this frequency we have an imaginary part around 7 Ohms and the real around 40 Ohms. We can also predict from the evolution of the impedance curves that we might have a secondary S11 peak at 6.25 GHz, which is coherent with what we see on figure 120).

In order to get the second part of the RF measurements, the radiation pattern, the system displayed on figure 117) was then placed inside the anechoic chamber of the ENSTA Bretagne, as we can see on figure 123).

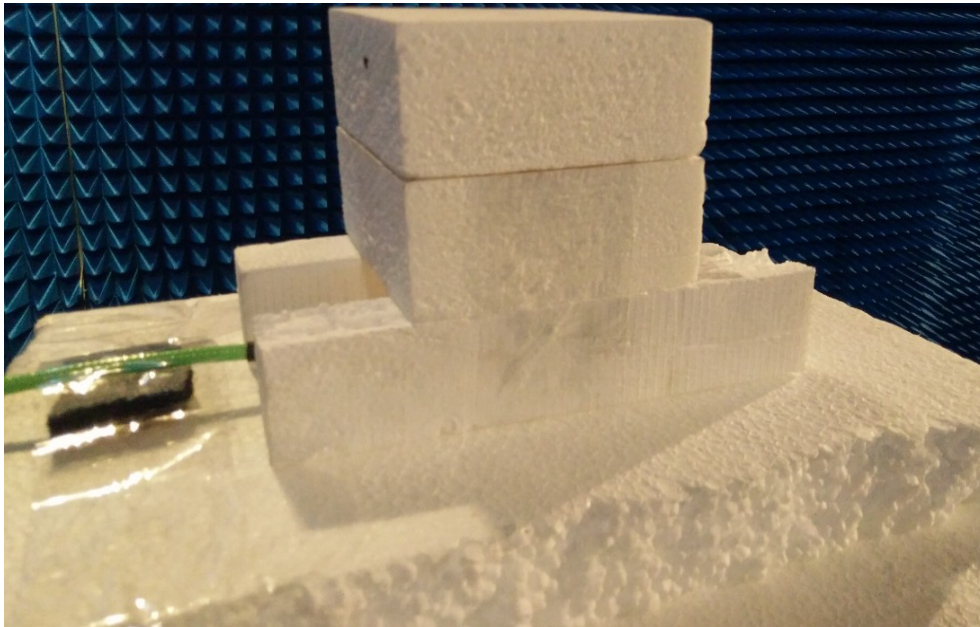


Figure 123 : Picture of the measured non-fluidic system inside the anechoic chamber

The goal is to measure its performances in its unidirectional configuration and then compare it to the simulated system to have a first estimation of its performances. The measure protocol consists in measuring the antenna's radiation inside the propagation plan (horizontal plan on the image above). These measurements are done for a total angular sweep of 180°, from -90° to +90°, with the 0° being the antenna's initial position, which is the case on figure 123). This position consists in the antenna parasitic elements aligned in the direction of the reception horn.

In order to perform the measurements of the antenna's performances, we need to first of all to measure a "calibration" radiation pattern. This is needed to have a known comparison base for the measurement exploitation with the dedicated Matlab code. This calibration measurement was done on a specific horn antenna (ref: LB-187-10) working on the 3.95 GHz to 5.85 GHz band, which was provided to us by A-INFO. This antenna and its characteristics are displayed below, on figure 124).

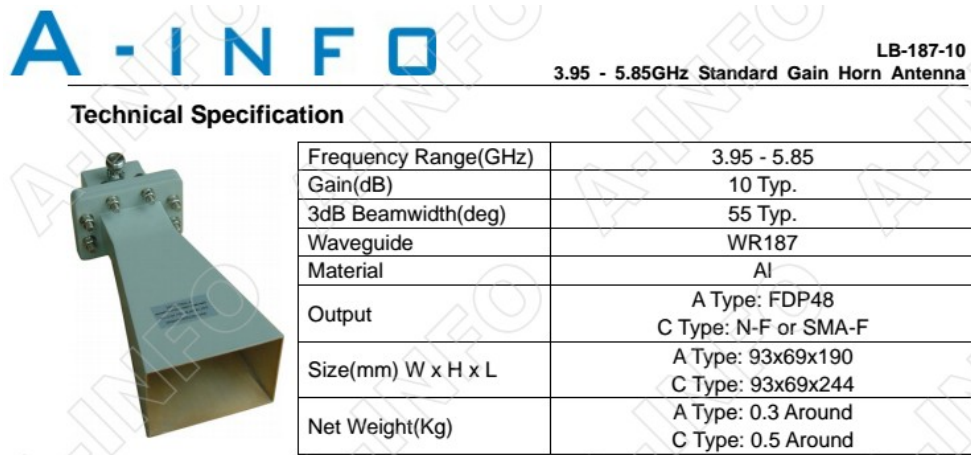


Figure 124 : Illustration of the calibration horn antenna & its properties

In order to be sure of our calibration, a first calibration measure was performed before the measure of the radiation pattern of the non-fluidic & fluidic systems (fluidic system which we will see later on) themselves, and one at the end of the measure session. The goal is to counter any potential shift in the calibration response and taking the better calibration of the two.

The corresponding simulated system to the measured one is exactly the same as the one presented on figure 118). Therefore, the following radiation patterns (polar & rectangular) shown on figure 125) & 126) are corresponding to this system and are showing its performances.

The frequency chosen for the diagram is the frequency at which the measured antenna performed the best (in this case 4.86 GHz). In turn, we have chosen the same frequency to generate the radiation pattern of the simulated system. This way we can compare corresponding responses.

On these graphics the red curves show the performances of the system in the horizontal plan (theta = 90°), while the blue ones show them in the same plan but tilted 10° (theta = 100°).

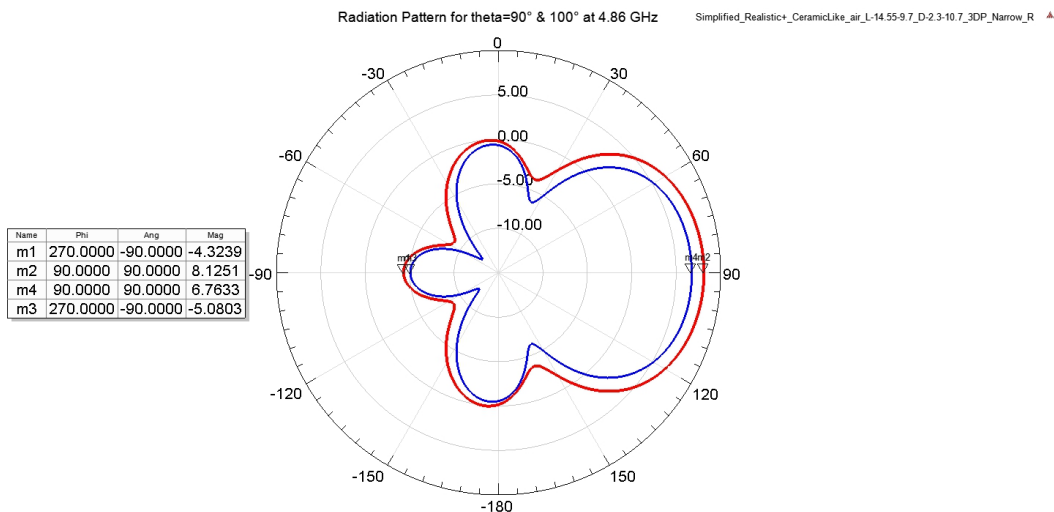


Figure 125 : Polar radiation pattern of the simulated non-fluidic system at 4.86 GHz for a system tilted of 0° (red) & +10° (blue)

The reason why we look the results in two different plans is that the antenna support inside the anechoic chamber was tilted on this particular measure. We want to compare the measure results

with the corresponding simulation configuration's performances, therefore we need the blue diagram for this. In the mean time, we also need to asses the performances of the system in its nominal configuration, which explain the red curve.

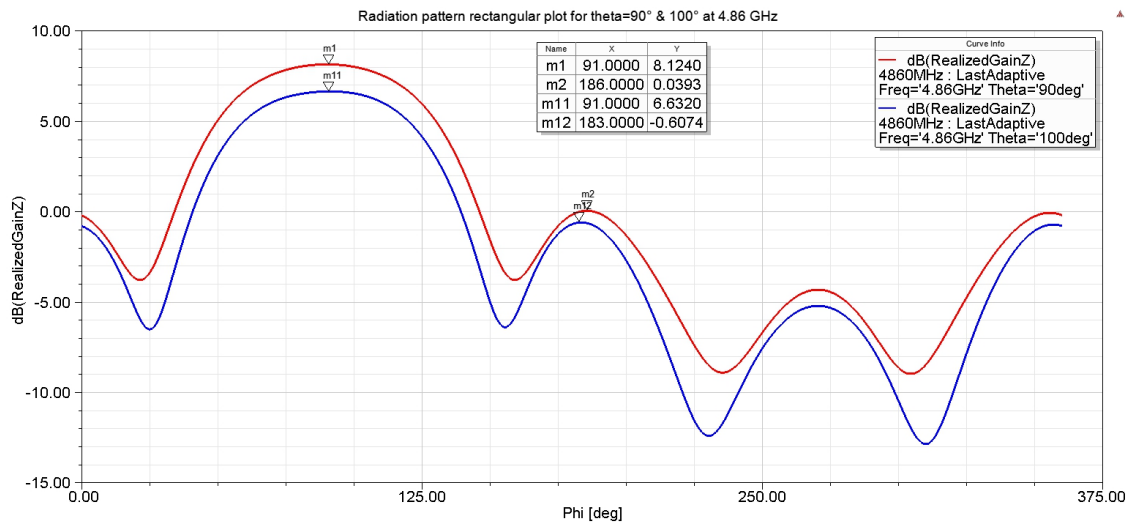


Figure 126 : Rectangular radiation pattern of the simulated non-fluidic system at 4.86 GHz for a system tilted of 0° (red) & +10° (blue)

As we can see on those two figures, the tilting of the antenna has for effect to decrease the max gain by 1.49 dB but does not affect the general profile of the radiation pattern, which just generally diminish while retaining its aspect. Given that we know about the antenna tilted support, we will directly compare the measured results with the corresponding simulated radiation pattern, as we can see on the figure 127) below:

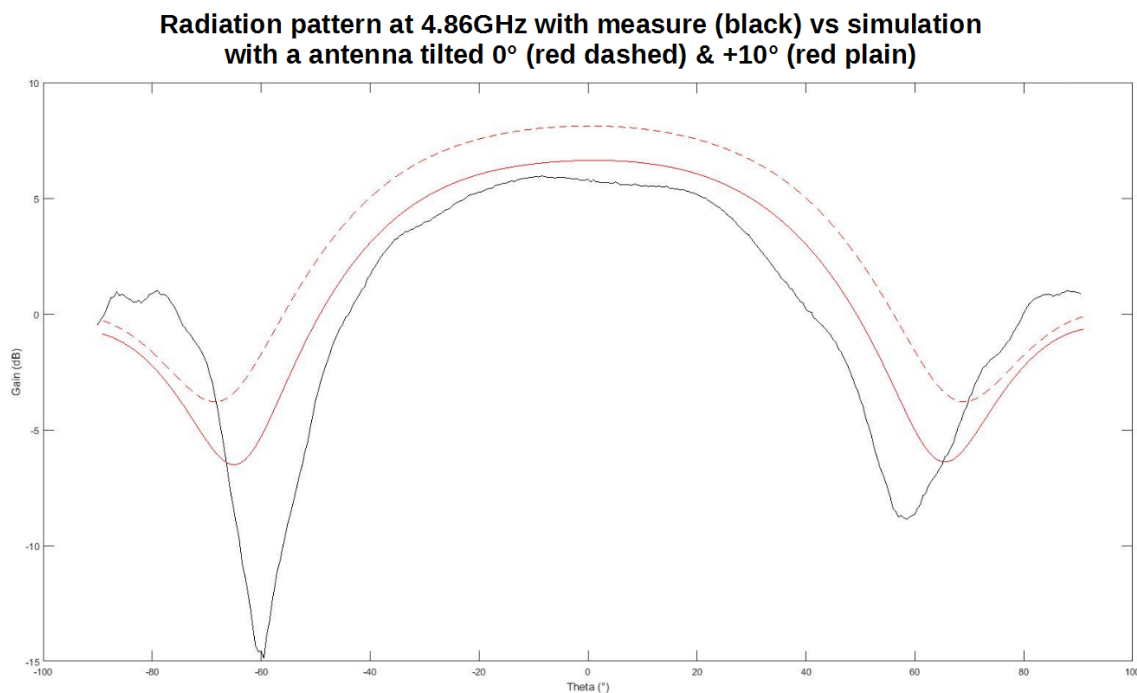


Figure 127 : Comparison of the rectangular radiation patterns of the non-fluidic system at 4.86 GHz for measure & simulation

Obviously we will compare on this graphic the results for the tilted configurations. The dashed red line, which is the simulation result for the non tilted antenna, is here just to illustrate the difference

between the tilted & non-tilted antenna. Now, if we compare the results of the measure and the simulation for the tilted antenna, we can note several things. First of all we can see that the levels of gain at the peak are lower in the measurement than in the simulation. The difference is of 0.79 dB in favour of the simulation, with a peak at 6.63 dB against 5.84 dB. As it appears clearly on the figure above, it is even more the case for the non-tilted simulation, though it is absolutely normal.

Second, we can see that the “zeroes” are deeper than on the simulation and their positions are slightly shifted. Indeed, the beam seems a bit narrower on the measured system than on the simulated one, with its zeroes at 60° against 65° for the simulation. The angular difference between measured and simulation zeroes is therefore of 5° .

Finally, we can also notice that the level of the lateral lobes is higher on the measured system than in the simulated one, with an average maximum difference of 1.75 dB in favour of the measured system. From this point, we can tell that our measured system is a bit less directive than the simulated one, but we need to keep in mind the difference of coaxial line transition highlighted above, which could explain part of the difference between the two systems behaviour.

Overall, we can say that the fitting between measure and simulation on this particular non-fluidic system is satisfying. We can therefore validate the underlying concept, and move on to the next system, which is based on the same general concept and architecture. The critical difference is that the parasitic elements are this time embedded in COP slide and made of Galinstan, rendering it closer to the complete system in terms of RF behaviour.

2) Test of the fluidic proof of concept

As we have said above, in order to better evaluate the RF performances of the complete system, we have also fabricated and tested a system in which we retain the general architecture presented above, but where the copper wires are replaced by Galinstan filled microfluidic channels embedded inside COP chips. The figure 128) bellow is illustrating this concept.

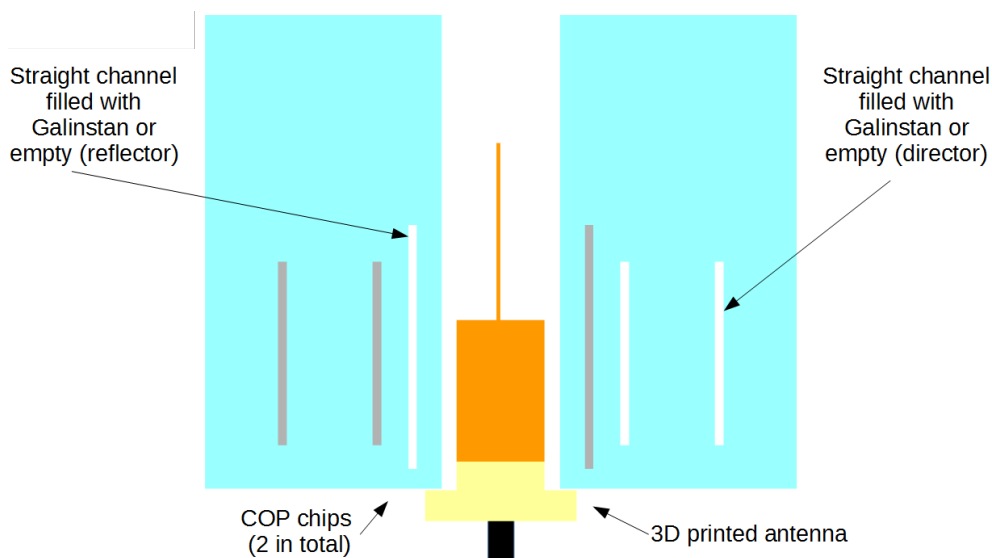


Figure 128 : Illustration of the general architecture of the fluidic proof of concept

In order to fabricate that system, we first of all need to know its dimensions. We already now that we are going to use thermal bonded COP chips, which give us slides with the following dimensions: 50 mm * 25 mm * 6 mm. Since we are going to re-use the central antenna of the previous system, we just need to design the “parasitic elements” system. The re-design of these elements will be done by using once again the Yagi-Uda design rules outlined in [15] by C. Balanis.

Obviously, given the absence of electrodes & electrolyte within the chip, these Galinstan channels cannot be commanded. But the RF behaviour of the system will allow us an even more precise estimation of the performances of the complete system, as well as a good illustration of its size, given that it is realized in the same materials as the complete system would be.

It must be noted that in order to have a more accurate simulation of the behaviour of the complete system we have also added six COP slides to the two used for the housing of the parasitic elements around the central antenna (one every 45°). This in order to have a more homogeneous dielectric constant for the waves travelling medium.

We have used the simulations in order to determine the precise positions of the channels within the slides and their length. For this we had to elaborate a new simulated system, different than the system presented above on figure 118). Indeed, we had to integrate the COP slides and replace the copper wires with Galinstan. Given the fact that the COP is now the main travel medium of the waves leaving the antenna, instead of air as it was the case for the system presented on figure 118), we had to change the λ_{EFF} of the design. As a reminder, λ_{EFF} (effective wavelength) is the parameter which is going to impact the parasitic element positions and dimensions. By successive simulation iterations, we have found that the appropriate value for this parameter in order to have a working system is $\lambda_{\text{EFF}} = 41.2$ mm. This is this value that we have used to fabricate our system.

We can note here that a system fully enclosed in COP would have a λ_{EFF} of 40mm. This value of 41.2 mm is therefore proving effectively that the waves mostly travel inside the COP.

Since we need to hold the COP slides in the air, we are here also going to use a Rohacell support in order to keep the slide at the right position. The use of such support seemed a good compromise for us, because due to the relatively good “EM transparency” of the Rohacell, the support shouldn’t drastically affect the system’s performances. The following figure 129) is showing the simulated system we have modelled (in its final configuration) and which will be also used for the comparison with the measured radiation pattern of the fabricated system. The support, as it was the case previously, was also machined, this time to house the COP slides & the central antenna.

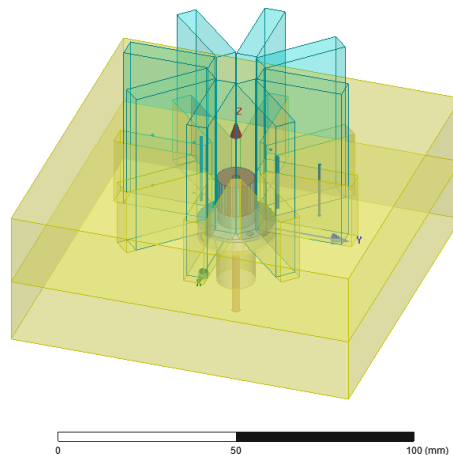


Figure 129 : Simulated fluidic proof of concept in unidirectional configuration

The fabrication process to realize the system presented above in the simulation is relatively simple. We need mainly to fabricate the channels and the support, the rest was already existing. These channels are first machined inside a COP slide (three on each slides, two directors and one reflector) with an S103 LPKF micro-machining machine (figure 81)). This slide is then topped with another one on which corresponding injection holes have been drilled, using the same machine. These two are then sealed by thermal bonding, using the same equipment & technologies we presented earlier on this chapter. The following figure 130) is depicting the CAD models of the two slides as well as an assembled view of them.

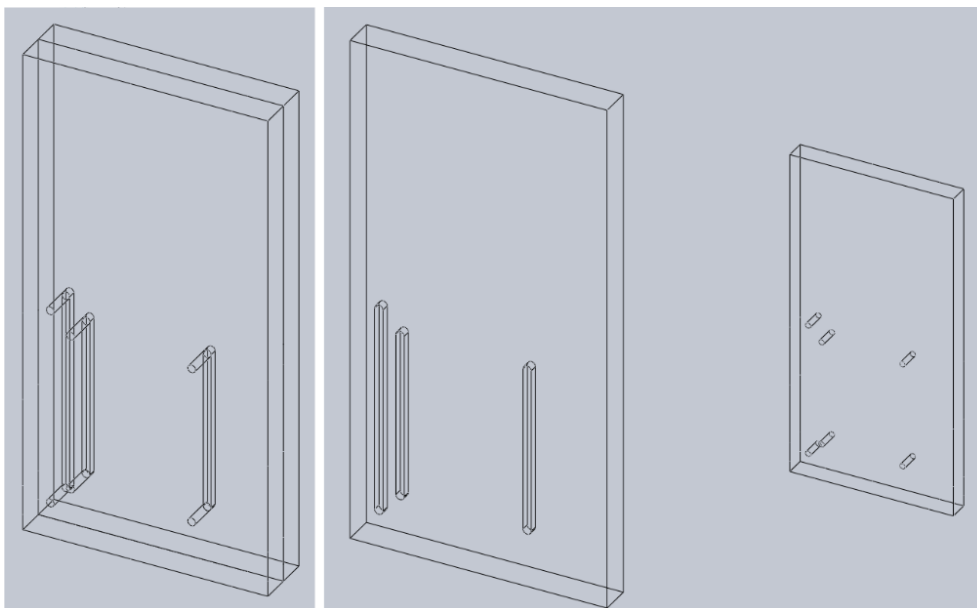


Figure 130 : CAD views of the COP slides assembled (left) & disassembled (right)

Once the sealing is done, the Galinstan is then injected with a syringe inside the channels. The Galinstan is injected without NaOH in order to allow it to get oxidized and therefore to stay inside the channels. The idea is to counter the tendency of the Galinstan to “jump out” the channels due to

its high surface tension by letting the oxidation take place. Due to the oxide surfactant properties, the Galinstan surface tension is lowered and it stays in the channel during the final phases of the fabrication.

After the injection of the Galinstan inside the chip, a thin COP slide (from the same supplier than the previous COP guiding perforated disc) on which toluene has been deposited is pressed on top of the injection holes. This definitely sealed up the chip thanks to the toluene induced local dissolution of the two COP slides which create a strong bond between the two. This technology, which was already experimented previously and shown in this chapter, was retained because it is simple, efficient and in the present configuration there is no risk of blocking the channels with Toluene infiltration. Indeed, the Galinstan was already injected inside them before the sealing and its movements are limited by its oxidation. The final chips can be seen on the figure 131) below.

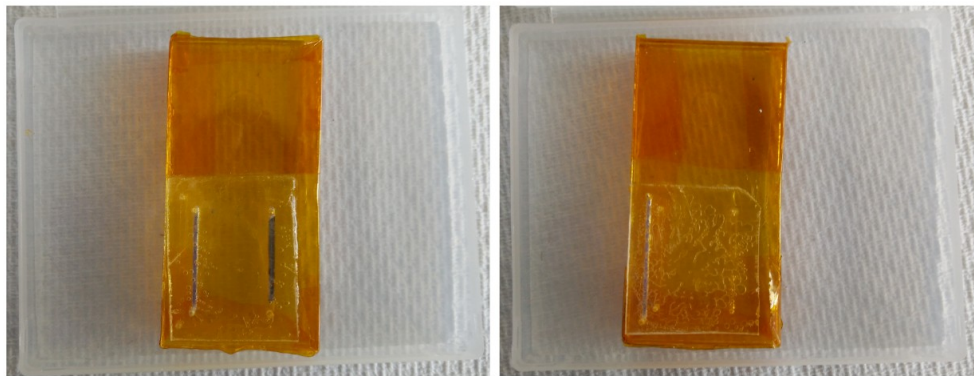


Figure 131 : Pictures of the fabricated, injected & sealed slides with two Galinstan directors (left) & one Galinstan reflector (right)

As we can see on this figure, the chips have finally been filmed with an adhesive Kapton, in order to maintain a good sealing and to protect the thin COP cover during manipulations occurring for the measures, especially the insertion of the chip inside the Rohacell support. This filming prevent also Galinstan spilling outside the chip in case of a breach of the sealing.

The following figure 132) shows this support we designed and machined from a block of Rohacell of identical dimensions as the ones used for the non-fluidic system (100 mm*100 mm*40 mm). It was machined by the same way than the previous ones, also at the UBO Open Factory.

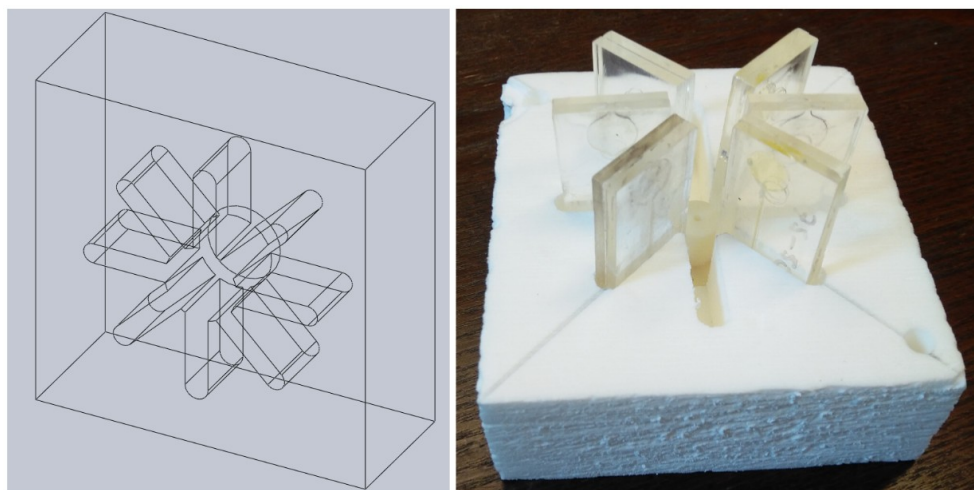


Figure 132 : CAD view of the fluidic system Rohacell support (left) & picture of the same system post-fabrication (right)

Now that we have presented the difference components of the system and its general architecture, we can present the results of its S11 measurement.

This measure was done with an Anritsu VNA master MS2026C, and its results can be seen on figure 133), which is showing the comparison between the measure & the simulation for the unidirectional configuration. On the following graphic, the measured curves are in dashed lines and the simulation curves in plain lines.

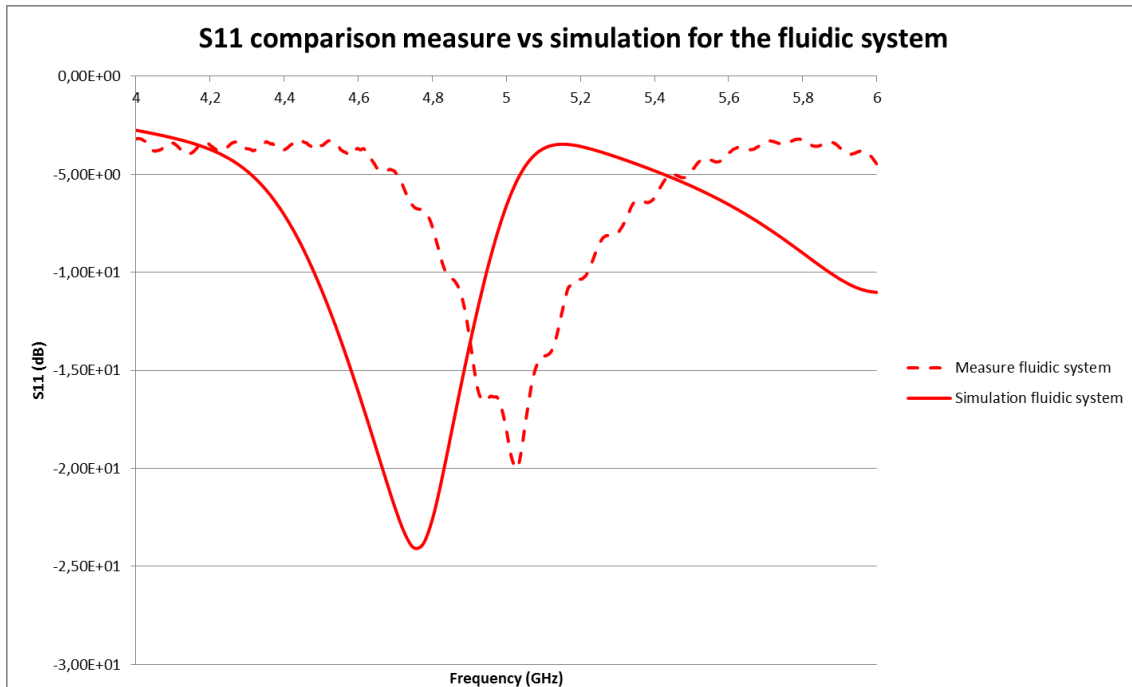


Figure 133 : S11 comparative evolution of the fluidic system for simulation & measure

We can observe that here also there is a difference in terms of resonance frequency between the simulation and the measure. A difference in the level of the resonance peak is also present.

Indeed, we have a similar frequency shift towards higher frequency between the simulation and the measurement, going from 4.75 GHz to 5.02 GHz, which is a 270 MHz shift (5.4% variation of the theoretical system operating frequency, 5 GHz). In terms of peak levels, we also notice that the minimal level for the measured system is a bit less good than for the simulated system, with an increase from -24 dB to -20 dB. This mean a 4 dB increase.

In order to further understand the behaviour of the system, it seems in this case also necessary to show the curves of the evolution of the impedance of the system, as shown bellow on figure 134).

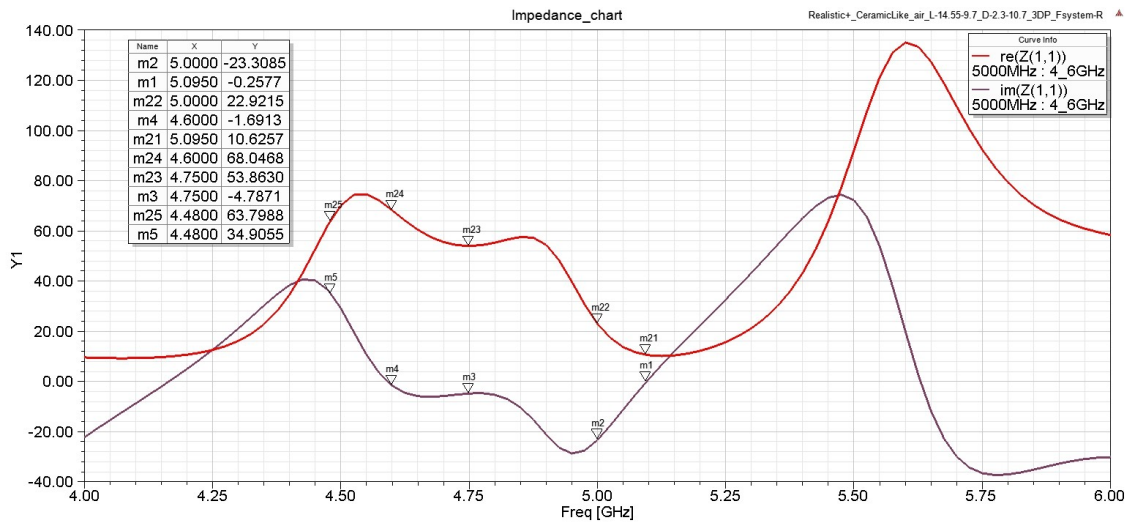


Figure 134 : Impedance evolution of the simulated fluidic system

If we look at the figure 133), we can see that for the fluidic system, the resonance peak is around 4.75 GHz. We can see that on the figure 134) above that the Im value is around -5 Ohms and the Re value around 55 Ohms for this frequency.

Given the apparent similarities between the two graphics of figures 120) & 133), that is why they were plotted together on the following figure 135) in order to better compare them, with the fluidic system curves in red and the non-fluidic curves in blue, the measured curves in dashed lines and the simulation curves in plain lines.:

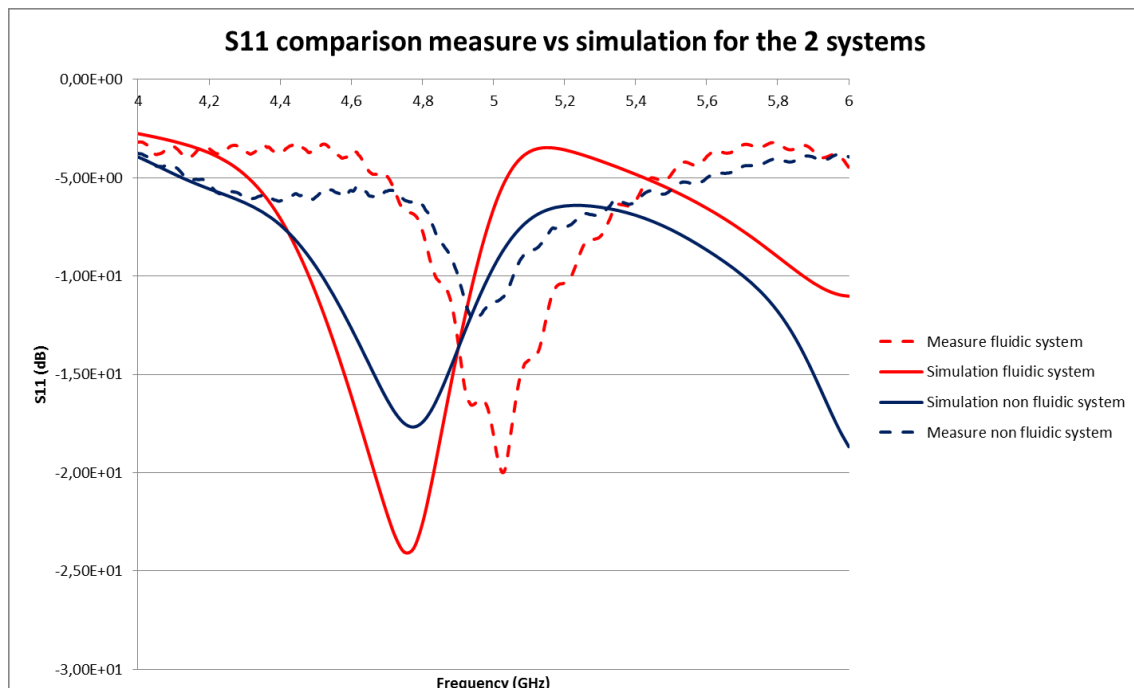


Figure 135 : S11 comparative evolution of the fluidic & non-fluidic system for simulation & measure

We can see that the frequency shifting between simulation and measure is almost identical on both systems (fluidic & non-fluidic). Therefore we could hypothesize that it is mainly due to the difference between the model and the fabricated system in terms of connection between the coax cable and the central antenna, difference which was highlighted on figure 119). The difference in dB

between the simulations & measurements peaks level is also quite comparable on both systems (6 dB for the non fluidic system, 4 dB for the fluidic one). This might be indicative of the fact that those level differences are due to fabrication & measure characteristic and defects and not due to modelling problems.

In order to get the second part of the RF measurements, the radiation pattern, the system displayed on figure 132) was then also placed inside the anechoic chamber, as we can see on figure 136).

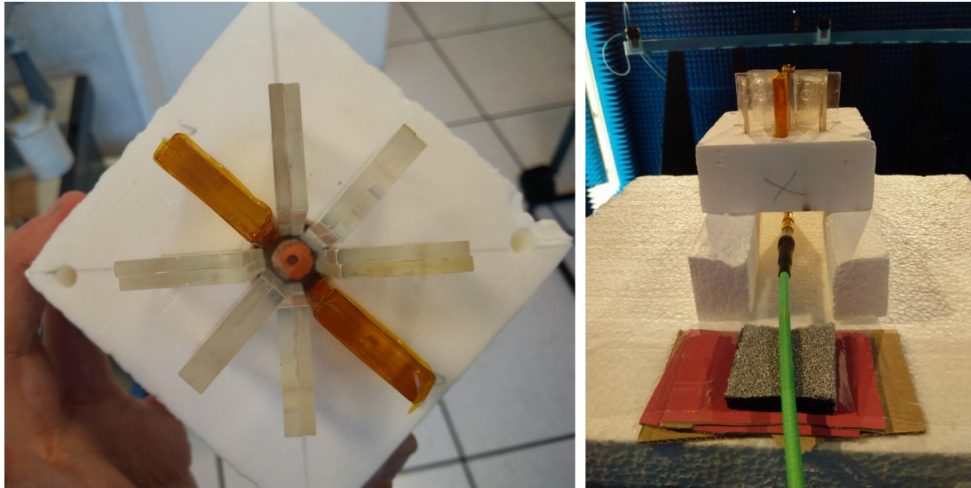


Figure 136 : Picture of the measured non-fluidic system assembled (left) & inside the anechoic chamber (right)

The measure protocol is identical to the one presented for the non-fluidic system. This measure allow us to have a more refined estimation of the complete system. Indeed, short of the electrolytes and the tanks, this system is identical to it.

As for the previous measurement, we also need to do a calibration. Since we measure in the exact same condition than the first antenna, on the same day, therefore we used the same calibration radiation.

The simulated system was already presented above on figure 129). Its performances in terms of radiation pattern can be found bellow, on figure 137) & 138), with the two radiation diagrams, in rectangular and polar plot.

The frequency chosen for the diagram is the frequency at which the measured antenna performed the best (in this case 4.48 GHz). In turn, we have chosen the same frequency to generate the radiation pattern of the simulated system. This way we can compare corresponding responses.

On these graphics the red curves show the performances of the fluidic system, while the green ones show those of the previous non-fluidic system presented above (with the performances taken at the same angle $\theta = 90^\circ$). We will first focus on the red curves only.

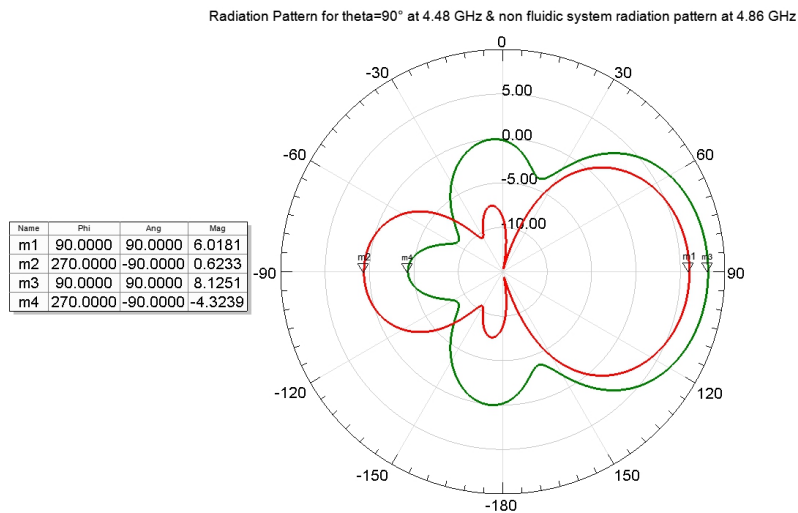


Figure 137 : Polar radiation pattern of the simulated fluidic system at 4.48 GHz (red) and for the non-fluidic system at 4.86 GHz (green)

We can see on these diagrams that we consider the radiation pattern in the horizontal plan (theta = 90°). The reason for not looking in the +/- 10° plans is that in this case the proof of concept was not tilted during the measurement.

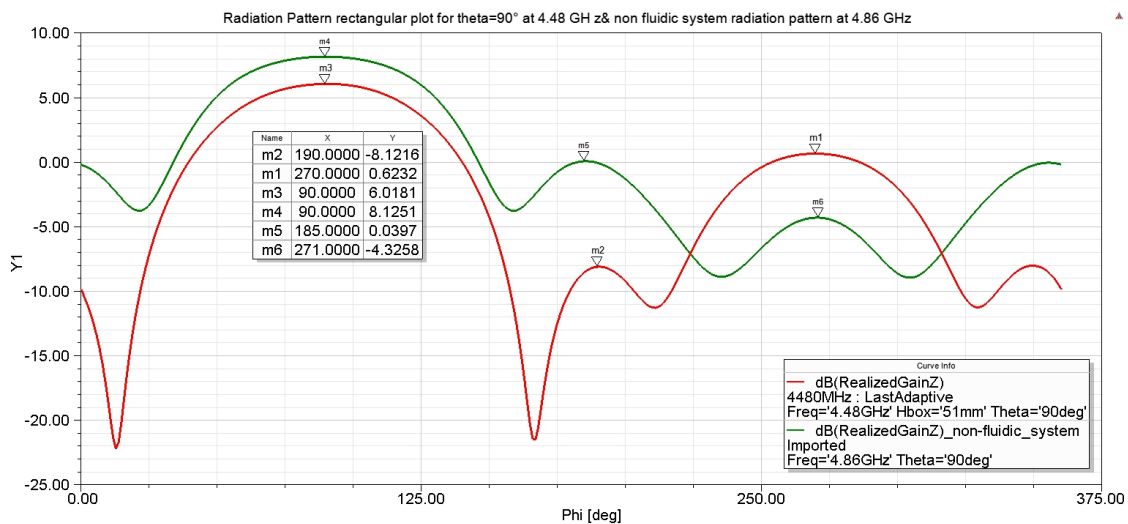


Figure 138 : Rectangular radiation pattern of the simulated fluidic system at 4.48 GHz (red) and for the non-fluidic system at 4.86 GHz (green)

As before, the next step is to directly compare the measured results with the corresponding simulated radiation pattern, as we can see on the figure 139) bellow:

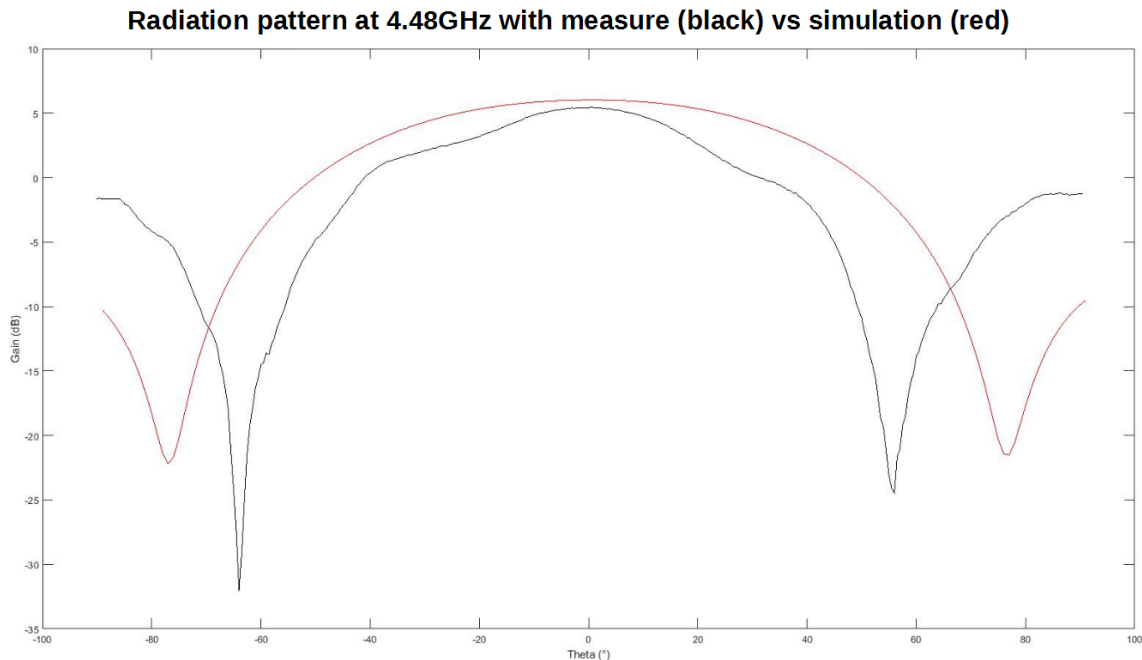


Figure 139 : Comparison of the rectangular radiation patterns of the fluidic system at 4.48 GHz for measure & simulation

If we compare the results of the measure and the simulation, we can note several things. First of all we can see that the levels of gain at the peak are lower in the measure than in the simulation. The difference is of 0.61 dB in favour of the simulation, with a peak at 6.02 dB against 5.41 dB.

Second, we can see that the “zeroes” are deeper than on the simulation and their position are frankly shifted. Indeed, the central beam seems clearly narrower on the measured system than on the simulated one, with its zeroes at 64° & 56° against both at 77° for the simulation.

We can also extrapolate from this that the measured system is maybe offset by a few degrees inside the horizontal plan and doesn't face perfectly the reception horn antenna. From the angular position of the zeroes, we could estimate the total value of the offset at 4°, which would place the zeroes at 60° if we were to recentre the curve. In such case, the angular difference between measured and simulation zeroes would be 17° on both side of the central 0.

Finally, we can also notice that the level of the lateral lobes is also frankly higher on the measured system than in the simulated one, with an average maximum difference of 8.46 dB in favour of the measured system. From this point, we can tell that our measured system is less directive than the simulated one. This was also highlighted by the comparison between the red & green curves of figures 137) & 138).

The reason for such differences could lies in the alignment of the parasitic elements with the central antenna and in fabrication tolerances.

Indeed, it appeared after the Galinstan injection inside the chips that channel where not perfectly filled with Galinstan, as we can see it on figure 131). In one of the two directors channels, the Galinstan droplet was 2 mm shorter than it should be. The droplet inside the reflector channel was 3 mm shorter than it should be. The reason for this is that it is still difficult to handle Galinstan and especially to confine it into small volume with high aspect ration, like a channel. Therefore the

filling process is not yet as repeatable as we would like. This difference definitely has an impact on the performances of the system, and we can explain partly the difference in terms of radiation pattern with this.

The second source of possible differences in performances could be the alignment and positioning of the COP chips in the support. Indeed, while the distances between the channels inside the chip are fixed, we are then positioning them inside the housings machined inside the Rohacell support. The precision of this machining is reasonable, but not very high. Similarly, to position the slides at the exact same distance then in the simulation is an extremely complex task. Hence, this alignment and positioning cannot be guarantee, and might also impact the results.

Additionally, we need to keep in mind the difference of coaxial line transition highlighted above on figure 119), which could also explain part of the difference between measure and simulation.

If we want to compare now the measurements of the two systems, we can look at the following figure 140) bellow, where the non-fluidic system response is in dark blue and the fluidic system response is in red.

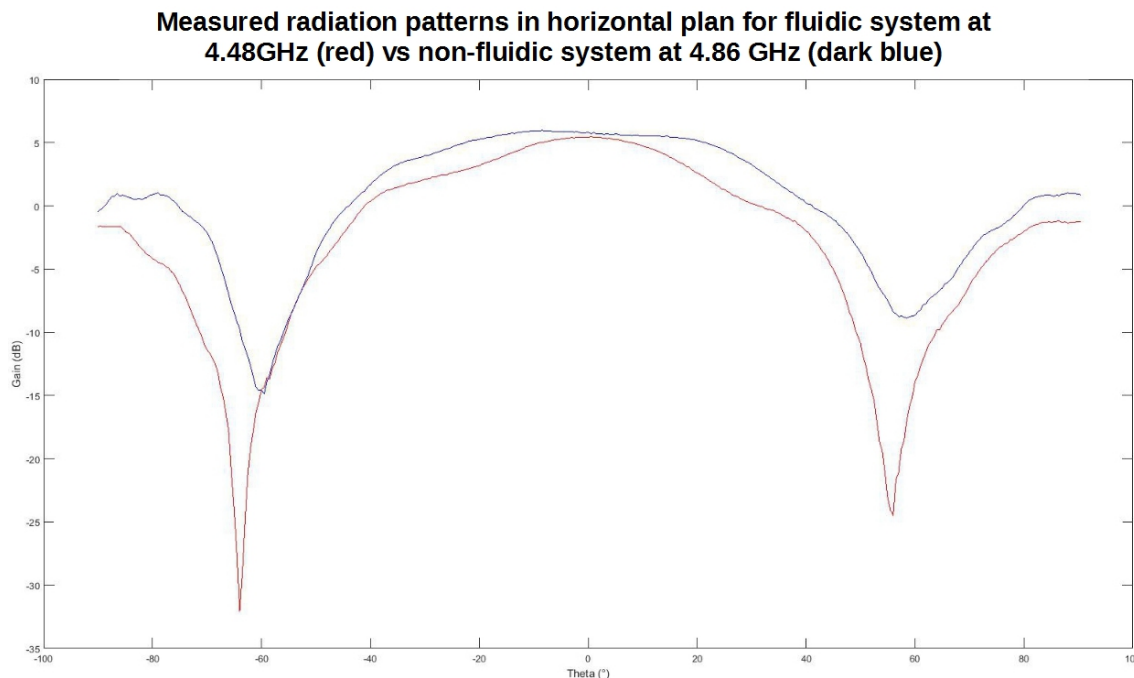


Figure 140 : Comparison of the measured rectangular radiation patterns of the fluidic system not tilted at 4.48 GHz & of the non-fluidic system tilted +10° at 4.86 GHz

First of all, it is important to keep in mind that given that the two measures are not taken in the same plane (red: theta = 90° & blue theta = 100°), we cannot directly compare the levels but more the general aspect of the curves.

Now, as we can see, the offset of the fluidic system (red) towards negative theta is very visible on this graphic, especially when we look at the position of the zeroes compared to those of the non-fluidic system (dark blue). We can also notice that aside from this point, the two curves are quite similar, in terms of shape and of levels. For this last point, it is most likely coincidental, the level

inside the plan $\theta = 90^\circ$ can be expected higher for the non-fluidic system (blue) based on the simulations.

The key point to notice from this comparison is that the transition of the parasitic elements from copper wire in air to Galinstan filled channels encased in COP seems to only change superficially the system's response, especially in terms of aspect, which remains the same.

To sum-up, first, the system we designed and fabricated has a response corresponding to the simulation, which means that we can also have a relative confidence in the more advance simulations results (comprising the electrolyte & the tanks), and that the approximations we have done during the modelling are acceptable.

Second, the function of the system was maintained through the change of material architecture, a change that we engineered with the intent to keep an identical function while trying to preserve performances, or at least keep them at an acceptable level.

The fact that this has been achieved means that our understanding of the design and its working principles is solid enough. It also mean that our fabrication technologies are also mastered enough so that there is no major difference during the conception to realization transition. Nonetheless, as we have seen above, we still have fabrication flaws. Two examples of it could be the problem of the leaks of the fluidic chips due to the bending of the COP slides during the hot embossing process, or as in the case of the figure 131), the incomplete filling of the channels with Galinstan.

To conclude on the RF measurement part, we can say that the simulation/measure fitting is satisfying for both systems. We notice that while the performances in measure are a bit lesser than in the simulation, especially in terms of forward gain, this doesn't reach a point where it would be critical. This performances drop can be explain by several factors, among which: the difference in coaxial transition modelling inside the central antenna (less efficient than the simulated solution), the fabrication tolerances for the parasitic elements of the antenna (incorrect element length and variation in elements positioning...), the fabrication tolerances of the central antenna (potentially leading to looser fittings, air gaps...) & the quality of the central antenna's metallization (potential oxidation, defects in metal layer uniformity...). With this overall result, we can therefore definitely say that, at least from an RF point of view, the concept & architecture of the microfluidic actuated Galinstan Yagi-Uda like microwave antenna is validated.

V. Microfluidic actuation system applied to an autonomous system

In order to better evaluate the relevance of our technological solution in regards of the applicative frame we have selected at the beginning, which is the integration of our solution within an autonomous system, we have decided to do a case study of such integration, from the fluidic system point of view. We considered the power consumption of our fluidic actuation system which

allows our antenna to reach a continuous beam steering capability. We have tried to evaluate the energy needs of such systems and did a rough estimation of the volume occupied by our solution.

First of all, we realised an “emulator” of our fluidic system based on the data we gathered from our experimentation on the different fluidic chip in terms of response time & power consumption combined with all the informations we gathered from the RF simulations of the system.

The “emulator” is in fact a table, in which we enter the desired frequency of the system as well as the number of active segments. This emulator works for every design based on the architecture which can be embedded on the same COP slides configuration displayed bellow, on figure 141). This is a simplified version of the system, embedded in two Rohacell foam support for integration (dimensions are a diameter of 70 mm for a height of 38 mm). It is a simplified version because it is just here to give an idea of the dimensions, the tanks & the electrolyte are not represented.

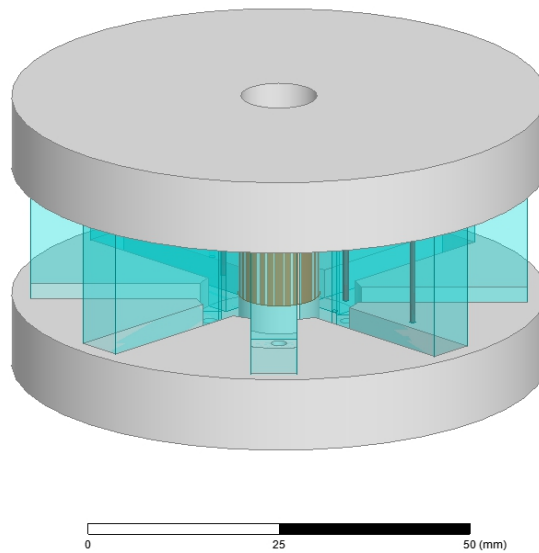


Figure 141 : Simplified embeddable antenna system

From this configuration, we can chose to activate a certain number of segments (with a max of 8), or to change the size of the elements within the slides, but without changing the dimensions & position of the slides themselves. Indeed, this would has for consequence to change the effective wavelength inside the system and therefore changes the calculation of the parasitic elements positioning & dimensions.

The following table 7) is the emulator of this system:

Table 7: Fluidic system's performances emulator

System's parameters		
Frequency (GHz)	For an 8 slides COP made system	Number of segments used
5,0		8,0
Current during rise for one column (mA)	Voltage during rise for one column (V)	Number of columns for each segment
14,0	7,6	3,0
Current during retreat for one column (mA)	Voltage during retreat for one column (V)	Power needed for the rise of one column (mW)
0,0	0,0	106,5
Current needed for one segment activation/deactivation	Voltage needed for one segment activation/deactivation	Power needed for the retreat of one column (mW)
42,0	7,6	0,0
Length reflector column (mm)	Length director column (mm)	Power needed for 1 segment activation/deactivation (mW)
21,0	16,9	319,6
Reflector's tank height (mm)	Director's tank height (mm)	Speed of rise (mm/s)
7,0	5,6	2,0
Reflector's retreat time (s)	Director's retreat time (s)	Speed of retreat (mm/s)
0,5	0,4	30,0
Reflector's rise time (s)	Director's rise time (s)	Time needed for 1 segment activation/deactivation (s)
7,0	5,6	7,5
Time needed for a full revolution (s)	Energy needed for a full revolution (mJ)	Energy needed for one segment activation/deactivation (mJ)
59,8	19107,5	2388,4

As we can see on this table, we need to provide to the system 42 mA & 7.6 V (or 320 mW) if we want to activate one segment of 3 columns, as it is the case on the previous figure 141). We can also see that in the case of an 8 active segments configuration, we need 1 minute to perform a full revolution (with eight 45° steps). We can also see that one segment need to be powered for 7 s and that is the time need for the slowest element to rise, element which is the reflector.

One aspect of the design of the system is that we can tailor the height of the tanks to minimize the rise the Galinstan has to make inside the column, and therefore enhancing the system's reactivity. The downside of that technology is that it implies a potential degradation of the radiation pattern shape and of the gain at the main lobe. In this case we have chosen a tank height of 1/3 of the total needed length of each parasitic element, a choice which is based on what was that ratio for the second chip (10 mm height/diameter of tank for a maximum total metal length of 27 mm).

Now we can apply the data obtain through that simulator to our case study. We want to power our fluidic system so that it performs a continuous rotation 24/7 while being energy autonomous. We will therefore need a way to harvest energy and store it. Solar is the most efficient and easy way to perform that energy harvesting task and that's why we will go for this technology. Nonetheless, solar cells are not able to harvest energy constantly, only during the day. We can consider a range of 8 hours a day during which our solar panels would be able to give us that power output of 320 mW.

There is also the need to consider batteries to power our system outside of that 8 hours ranges, at night. We will need batteries which are capable of delivering 42 mA for 16 hours, which give us a capacity of roughly 680 mAH. We need these batteries to be at a voltage of at least 7.6 V.

If we look at batteries, a simple 9V rechargeable battery like the Tenenergy NiMH 9V [16] offers a typical capacity of 250 mAH. It means that a block of three batteries in parallel would offer us a capacity of 750 mAH at 8.4 V. The data-sheet of that battery stated that we need a 36 mA current to charge it in 7 hours. The dimensions of each battery is 45 mm*30 mm* 18 mm.

Therefore we need an output of the solar cell of 42 mA for the fluidic system itself, plus 3*36 mA for the charging of the batteries, which gives us 150 mA output.

If look at solar cells capable of supplying our system enough power, we can two solar KS-M8080P modules from China Solar [17] and used them in series. Each of them has an output current of 160 mA at 5 V, the series arrangement allow us to have 160 mA at 10 V. The dimensions of those cells are 80 mm*80 mm*2.8 mm.

If we look at what is the occupied area of solar cells and volume of batteries versus the size of our system, we can look at the following figure 142).

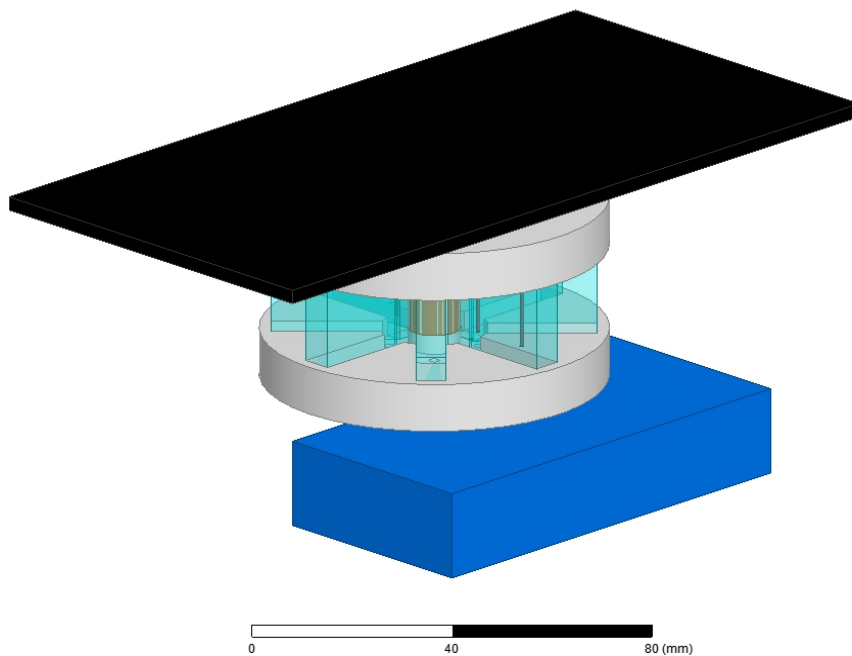


Figure 142 : Simplified system with on top the solar cell array and at the bottom the battery pack needed for a continuous 24/7 actuation of the fluidic system

As we can see, we need more than three time the surface of our system in solar cell and half its volume in terms of battery to render it completely autonomous. Of course, we are only talking here of the fluidic system. The other part which is going to have a high power consumption is the RF part of the system, in particular the 5 GHz power amplifier.

While the surface of solar cell needed is big, it is not large & bulky enough for rendering our system non-embeddable while being and autonomous, which is a good news for us. It means that our targeted application is still within our reachable possibilities. We should add that those

performances are those of a severely non-optimized system. It is obvious that with an optimization work on the design of the channels, the tanks, on the fabrication of the channels (we can think of a PTFE coating to render them slicker as in [18]), on the sealing of the chips & finally on their filling, we could obtain better performances. While it is difficult to say how much exactly can be gain, tendencies seems to show that a better sealing lower the voltage needed to actuate the chip (and so the power consumption), and a better filling seems to generate a more even Galinstan rise, with less turbulence. This would probably increase the chip reliability as well as the speed of rise.

VI. Bibliography

- [1] Zeon corporation, “ZEONEX® - Cyclo Olefin Polymer (COP),” Tokyo, 2016.
- [2] Dow Corning, “Sylgard ® 184 Silicone Elastomer,” 2014.
- [3] N. Tiercelin, P. Coquet, R. Sauleau, V. Senez, and H. Fujita, “Polydimethylsiloxane membranes for millimeter-wave planar ultra flexible antennas,” *J. Micromechanics Microengineering*, vol. 16, no. 11, pp. 2389–2395, Nov. 2006.
- [4] S. Hage-ali, N. Tiercelin, P. Coquet, R. Sauleau, H. Fujita, V. Preobrazhensky, and P. Pernod, “A Millimeter-Wave Microstrip Antenna Array on,” vol. 8, no. c, pp. 1306–1309, 2009.
- [5] S. Pacchini, A. Togonal, S. Hage-ali, N. Tiercelin, and P. Pernod, “Inkjet-printed elastomeric millimeter-wave devices,” pp. 3–6.
- [6] X. Illa, O. Ordeig, D. Snakenborg, A. Romano-Rodríguez, R. G. Compton, and J. P. Kutter, “A cyclo olefin polymer microfluidic chip with integrated gold microelectrodes for aqueous and non-aqueous electrochemistry.,” *Lab Chip*, vol. 10, no. 10, pp. 1254–1261, 2010.
- [7] B. Samel, M. K. Chowdhury, and G. Stemme, “The fabrication of microfluidic structures by means of full-wafer adhesive bonding using a poly(dimethylsiloxane) catalyst,” *J. Micromech. Microeng. J. Micromech. Microeng*, vol. 17, no. 17, pp. 1710–1714, 2007.
- [8] M. Wang, C. Trlica, M. R. Khan, M. D. Dickey, and J. J. Adams, “A reconfigurable liquid metal antenna driven by electrochemically controlled capillarity,” *J. Appl. Phys.*, vol. 117, no. 19, p. 194901, 2015.
- [9] R. C. Gough, A. M. Morishita, J. H. Dang, M. R. Moorefield, W. A. Shiroma, and A. T. Ohta, “Rapid electrocapillary deformation of liquid metal with reversible shape retention,” *Micro Nano Syst. Lett.*, vol. 3, no. 4, pp. 1–9, 2015.
- [10] R. Gough, A. Morishita, J. Dang, and W. Hu, “Continuous Electrowetting of Non-Toxic Liquid Metal for RF Applications,” *IEEE access*, vol. 2, pp. 874–882, 2014.

-
- [11] A. Zavabeti, T. Daeneke, A. F. Chrimes, A. P. O'Mullane, J. Zhen Ou, A. Mitchell, K. Khoshmanesh, and K. Kalantar-zadeh, "Ionic imbalance induced self-propulsion of liquid metals," *Nat. Commun.*, vol. 7, no. May, p. 12402, 2016.
- [12] S. Hage-ali, S. Member, N. Tiercelin, P. Coquet, R. Sauleau, S. Member, V. Preobrazhensky, and P. Pernod, "A Millimeter-Wave Inflatable Frequency-Agile Elastomeric Antenna," vol. 9, pp. 1131–1134, 2010.
- [13] C. B. Eaker and M. D. Dickey, "Liquid metal actuation by electrical control of interfacial tension," *Appl. Phys. Rev.*, vol. 3, no. 3, 2016.
- [14] CHROMA ATE INC., "CHROMA PROGRAMMABLE DC POWER SUPPLY MODEL 62000P SERIES." .
- [15] C. a. Balanis, *Antenna Theory Analysis and Design*. 2005.
- [16] Ternergy Corporation, "TENERGY 9V 250mAh NiMH Battery," pp. 1–10, 2009.
- [17] China Solar LTD, "KS-M8080P - 5V 160mA Mini Photovoltaic Panel," p. 1.
- [18] R. C. Gough, J. H. Dang, A. M. Morishita, A. T. Ohta, and W. a. Shiroma, "Frequency-tunable slot antenna using continuous electrowetting of liquid metal," *2014 IEEE MTT-S Int. Microw. Symp.*, pp. 1–4, Jun. 2014.

Conclusions & perspectives

I. Conclusion

The work carried out during this PhD is a continuation of the COCORICO ANR ASTRID DGA project. It deals with beam steerable antenna, liquid metal (Galinstan) & microfluidics. It starts with an original idea which is that we could achieve a 360° beam steering with an antenna through a microfluidic based liquid metal actuation. This technology would then offer a credible alternative to the today well known mechanical and electronic beam steering antenna technologies. The developed micro-system is based on the use of a Cylo-Olefin Polymer (COP) in order to be able to obtain a fluidic system which is as less lossy as possible from an RF point of view, easy to produce & relatively low cost.

The bibliographic study of the thesis is focused on the documented technologies to displace liquid metal inside the fluidic system and to use this displacement for RF purposes. We tried to single out from the literature the best fitted displacement technology for our needs, which were to design a micro-system with that beam steering capability. From this study, we were able to compare the advantages and inconvenience of every technologies and chose among them. We have finally selected the electrofluidics actuation as the most adapted technologies for the development of a fluidic actuated RF micro-system.

From this choice of technology, we have designed our micro-system in order to maximize the use of available volume to us. This constraint led us to privilege the use of a vertically polarized antenna over a horizontally polarized one, because it allow the system more potential agility for a given surface area. We selected a Yagi-Uda architecture for our antenna due to the fact that the simple shape of the parasitic elements render it easy to partially convert it into a microfluidic antenna. We also decided to use a dipole antenna as the central antenna of our Yagi-Uda architecture due to the parasitic elements design simplicity it would enable, simplicity which again, facilitate for us the task of integrating microfluidic into the system. This choice of the antenna's type led us to a more precise definition of its own design. To simplify the design of the system, we have decided to use a coaxial dipole antenna, which is coaxial fed from the bottom. This has for consequence the evacuation of the feed line out of the antenna's line of sight. All those choices led us to narrow down the field of application of our system, (by excluding applications such as electronic warfare or airborne & spatial systems) based on the conclusions of the bibliographic study & the general outline of the system's design.

Once the RF design was established, we have switched to a campaign of finite element computer simulations on ANSYS HFSS in order to refine the general antenna architecture. This allowed us to validated the vertically polarized dipole base Yagi-Uda architecture. Through successive simulations we have added complexity to the design, from a theoretical dipole Yagi-Uda

wire based architecture to a feasible coaxial dipole/Galinstan Yagi-Uda architecture, partially embedded into a COP slide construction. This approach allowed us to look at the impact of each element of the system in terms of RF performances.

In parallel to this work, we have developed fabrication technologies & process to realize the fluidic system and the central antenna itself. The work regarding the antenna was done relatively fast because it relied on already industrialized solutions (3D printing & metallization) and the time needed from the design to fabrication could therefore be minimized. Consequently, its design was directly optimized through the simulation before its fabrication. For the fluidic system, the development was longer because the tooling necessary to its realization was non-existent. A development effort was done (through a series of tests of the various channel forming, chip sealing & electrodes deposition technologies) in order to come with a solution enabling us to produce a functioning fluidic chip to further validate the concept of our system's actuation. The concept was already partly validated through the test of a first chip in the first year of the PhD, but its realization was crude and its performances hardly reproducible. The conclusion of the development effort, conjugated with the use of the service of an external company allowed us to realize additional validation of our system's concept. The realization of our own chip had for consequence the characterization of our system's performances. Alongside those developments, we also fabricated and tested proof of concepts (both non-fluidic & fluidic) of the antenna system in order to experimentally validate their RF performances and the underlying concept of the whole system. We ended up this chapter with a case study of the integration of our fluidic system into an autonomous device to evaluate its performances in terms of power consumption and to judge of the relevance of our solution in regards of the envisioned application.

II. Perspectives

In short term, the realization of a fully functional prototype would allow us to confirm the evaluated performances in terms of power consumption & response times. Those two parameters are indeed critical, the first to allow the integration into an autonomous system, the second to have a credible alternative to propose against the mechanical beam steering, which we think is our main competitor given the range of application we aim for.

A certain number of part of this work can be subjected to further in depth studies, studies which can be independent from one another. In particular on the fluidic aspect of this work, a study of the impact of the shape & size of the tank & channel on the performances in terms of response time and power consumption could bear very significant fruits in terms of gains in those two aspects. This study could be done first by simulating one chip with a dedicated fluidic simulation software (like ANSYS FLUENT) or with a multi-physics software with the appropriate add-on (like COMSOL MULTIPHYSICS). The conclusions drawn from those simulations could then be compared with the results of the tests of several chips with different sets of characteristics from the simulations, with an approach similar to what we did for the elaboration of the central antenna's design.

It is also obvious that a work centered on the development & improvement of COP hot embossing & thermal bonding technologies would also had great potential. We can also think of investigating the impact of the direct injection of the COP into patterned molds on the deformation of the resulting slide. Indeed, a lower deformation and a better surface state would definitely improve the quality & the efficiency of the thermal bonding process. This particular process could also be greatly improved by the use of a heating hydraulic press instead of the use of weights and an oven, has presented here. This would greatly improve reliability of the process and most likely the strength of the resulting bond.

On the RF aspect, some adjustments of the antenna design could easily be done (improvement of the SMA/antenna transition for example). We must also investigate the impact of the addition of the electrodes of the fluidic system onto its RF performances, especially the gain of the main lobe. This could be done by simply realizing simulations of the prototype to observe the impact on the radiation diagram. Of course, the fabrication of the prototype and subsequent RF measurement inside an anechoic chamber would also be very helpful in this regard.

This bring us to another point which could be done, once the prototype is realized, which is the realization of the same autonomous system presented in the case study at the end of chapter 4) to see if our sizing is accurate. This would also be the occasion to see if our system is able to function reliably for an extended period of time and investigate potential failures which might happen, in order to correct them. We can already point several potential weakness of the fluidic system such as; the progressive degradation of the electrodes over time (due to the action of the electrolyte & Galinstan & probably the electrical current as well), the potential build up of pressure inside the chip due to the production of dihydrogen gas (from the water electrolysis) which might lead to a breaking of the chips sealing or also the potential gradual bulk oxidation of the Galinstan which would render the actuation of the chip impossible due to the high adherence of the liquid metal to the walls of the tank.

Finally, it could also be potentially interesting to realize the horizontally polarized system presented on chapter 2) to compare it's size & performances with our prototype. Indeed, while the two systems relies on very similar technologies (and in this regards, the manufacturing processes have already been developed through this work), they have very different architecture and will likely have different performances. Maybe the trade-off we made in favor of agility and reconfigurability might be problematic for certain application (which might need lower response time for example). Therefore the technology developed here could allow us to realize systems capable to address different needs with that same antenna liquid metal based fluidic actuation.

Conception d'une antenne orientable dotée d'un actionnement par métal liquide

L'apparition des objets connectés intelligents dont nous sommes les témoins depuis quelques années a généré un besoin croissant d'antennes à bas coût et énergétiquement sobres. La capacité d'effectuer à la volée une mise en forme du faisceau ou sa reconfiguration est une propriété particulièrement intéressante, qui pourrait permettre à l'objet intelligent d'effectuer des tâches telles que la surveillance de zone par exemple ou bien d'optimiser son bilan de liaison en ne visant qu'une seule direction de l'espace. Cela pourrait également mener à un accroissement de l'autonomie de l'objet, via une diminution de sa consommation énergétique, voir à le rendre totalement indépendant s'il devient suffisamment économe pour envisager son alimentation via des systèmes de récupération d'énergie. C'est dans ce contexte que proposons ici une nouvelle architecture d'antenne reconfigurable, capable d'un balayage de faisceau sur 360° degrés et basée sur l'utilisation de métal liquide au sein d'un système d'actionnement microfluidique.

Dans le premier chapitre, nous ferons une rapide présentation des deux principales technologies de balayage de faisceau utilisées aujourd'hui avant d'étudier les diverses techniques de déplacement de métal liquide utilisées et documentées dans la littérature. L'objectif de ce travail est de sélectionner la technique la plus adaptée à nos besoins.

Dans le second chapitre, nous proposerons les deux designs d'antennes envisagés pour notre système, basés sur l'architecture Yagi-Uda. Nous discuterons des avantages et inconvénients de chacun afin d'en sélectionner un qui sera examiné plus en avant dans le chapitre suivant.

Dans le troisième chapitre, nous étudierons, à l'aide de simulations électromagnétiques, les performances du design d'antenne sélectionné dans le but de justifier notre choix. Cette étude se concentrera sur l'implémentation graduelle de la complexité du design retenu, en partant d'un système très théorique pour aboutir à une émulation très proche de ce que pourrait être un prototype final.

Finalement, dans le quatrième & dernier chapitre nous considérerons deux preuves de concept du système complet ainsi que leur différentes techniques de fabrications. Étant donné le fait que chaque preuve de concept se concentre soit sur l'aspect RF ou fluidique du système, nous étudierons aussi leurs performances respectives. Nous détaillerons également le développement de certains procédés de fabrication spécifiques utilisés pour réaliser les briques de base, en particulier les objets micro-fluidiques. Ce chapitre nous permet de conclure positivement cette étude de la faisabilité du concept proposé et développé dans ce travail.

Mots clés: Hyperfréquence – Antenne reconfigurable – Balayage de faisceau – Microfluidique – Métal liquide – Galinstan – COP

Steerable antenna design based on liquid metal actuation

The advent of autonomous connected smart objects we are witnessing since a few years has generated a growing need for low cost and energetically sober reconfigurable antennas. The ability to perform on the fly beam shaping and re-configuration is a particularly interesting property which would allow the smart object to perform task such as area surveillance for example and to optimize its link budget by targeting a specific direction of space. This could also allow the increase of the object's autonomy, through a diminution of its power consumption, or even to render it fully autonomous if it become sober enough to envision the use of energy harvesting systems. It is in this context that we propose here a novel reconfigurable antenna architecture, capable of 360° beam steering, based on the use of liquid metal within a microfluidic actuation system.

In the first chapter, we will do a quick presentation of today's two main beam steering technics used for antennas before studying the various used and documented technics of liquid metal displacement used in the literature for RF applications. The objective is to single out the better suited one to our requirements.

In the second chapter, we will propose the two antenna designs envisioned for our system, based on the Yagi-Uda architecture. We will discuss the advantages and drawbacks of each in order to select one design which will be more closely investigated on the following chapter.

In the third chapter, we will study, with the help of electromagnetic simulations, the performances of this selected antenna design in order to justify our choice. This study will focus on the gradual complexity implementation of the chosen design, from a very theoretical system to one very close to what a final prototype would be.

Finally, in the fourth and last chapter we will consider two proofs of concept of the complete system and their various fabrications technics. Given that each proof of concept focus either on the RF or the fluidic aspect of the system, we will investigate their performances. We will also detail the development of some of the specific fabrication processes used for the basic building blocks, especially for the fluidic objects. This chapter allow us to conclude positively this study on the feasibility of this concept which was proposed and developed in this work.

Key words: Microwave – Reconfigurable antenna – Beam steering – Microfluidics – Liquid metal – Galinstan – COP